RMIT UNIVERSITY

Development and Optimisation of a Chronic Single Unit Carbon-Based Electrode Array for Neural Interfacing

A thesis submitted in fulfilment of the requirements for the degree of Doctor of Philosophy

Simon James Higham

Bachelor of Science, The University of Melbourne

Bachelor of Engineering (Biomedical Engineering) (Honours), RMIT University

https://orcid.org/0009-0008-3955-7179

School of Engineering
Biomedical Engineering
RMIT University
Melbourne, Australia

Submitted July 2024

Declaration

I certify that except where due acknowledgement has been made, this research is that of the author alone; the content of this research submission is the result of work which has been carried out since the official commencement date of the approved research program; any editorial work, paid or unpaid, carried out by a third party is acknowledged; and, ethics procedures and guidelines have been followed.

In addition, I certify that this submission contains no material previously submitted for award of any qualification at any other university or institution, unless approved for a joint-award with another institution, and acknowledge that no part of this work will, in the future, be used in a submission in my name, for any other qualification in any university or other tertiary institution without the prior approval of the University, and where applicable, any partner institution responsible for the joint-award of this degree.

I acknowledge that copyright of any published works contained within this thesis resides with the copyright holder(s) of those works.

I give permission for the digital version of my research submission to be made available on the web, via the University's digital research repository, unless permission has been granted by the University to restrict access for a period of time.

I acknowledge the support I have received for my research through the provision of an Australian Government Research Training Program Scholarship.

Simon James Higham Submitted 30/07/2024

Acknowledgments

Firstly, I would like to thank my very supportive supervisors, David Garrett, Wei Tong and Shaun Cloherty. They were the perfect help for the completion of my project and really allowed me to fully enjoy and thrive during the time of my thesis. I would especially like to thank David for funding me and being a big motivating factor in me wanting to complete a PhD after my undergrad. Further to this id like to acknowledge everyone I worked with, specifically Sorel and Jason who made most of my project possible and definitely more enjoyable.

I would also like to thank my beautiful partner Amy, who acted like a fourth supervisor especially during my write up. Having someone that had been through the same thing made me question a lot less when trying to complete my thesis. I'm happy I got to share much of this work with you and I'm sorry I couldn't grow you a ring.

I have to give credit to the boys here as well, for keeping me grounded during this entire process. I'm sorry I could not do the experiments that you wanted me to do. Ill also shout out Jordan for bouncing off ideas most days at lunch, Don Tojos almost needs a mention here as well.

I would also like to thank my family, who are always supportive in everything I do. Especially Shane, who very often sat and listened to me explain my day not following a thing I'm saying but it was always more supportive than you probably realise. Lastly, and most importantly I would like to thank my Mum and Dad, as they are the reason I have been able to achieve everything I have. They are the reason I have had so much opportunity in life, and I could never express how lucky I am to have them.

RMIT UNIVERSITY

Contents

RMIT UNIVERSITY

Abstract

Much progress has been made in the field of neuromodulation implants in recent years. These devices aim to improve the diagnosis and treatment of neural pathologies such as chronic pain, epilepsy, and Parkinson's disease. This progress would not be possible without continued advancement in biomaterials that are stable and well tolerated within the brain. However, these devices are still limited primarily due to the inability of current implantable electrodes to interface with meaningful numbers of individual neurons long-term. Interfacing with many single units long term allows for complex and localized interventions for these diseases. Advancements in flexible, micro scale electrodes have improved the effectiveness of neural electrodes with more work still required to create a fully implantable chronic array of electrodes. A material that shows promise in overcoming many of the current limitations is carbon fiber. This is due to the flexibility, robustness, biocompatibility, conductivity, and size of the material. Work has been conducted recently to demonstrate carbon fiber micro electrodes viability for chronic single unit recordings that could expand on the ever-increasing field of neural interfacing. Currently no high-density electrode arrays have been constructed that could fully capitalize on this promising material's potential. The overall aim of this project is to develop methods to fabricate, optimize and assess carbon fiber electrode arrays for chronic neural interfacing applications.

This thesis includes the fabrication and assessment of a carbon-based microelectrode array which comprises a diamond substrate to house the array of carbon fiber electrodes in a novel configuration. Research was conducted to electrically connect these devices and create a fully functional neural implant. This involved numerous novel techniques for fabrication and treatment of the devices to produce chronically implantable arrays. Each aspect of the construction and performance of the devices were validated through various techniques, including electrical testing, surface characterization, mechanical analysis, and imaging techniques. Complete devices were implanted into both acute and chronic animals for extensive *in vivo* validation. These results showed the electrical performance of the electrodes and their ability to record single unit neuronal cell signals. The chronic stability of the implant within the tissue was assessed using imaging techniques. The safety of the implant and the associated impact on neural tissue was confirmed using immunohistological staining, implying that this device configuration has much potential as a chronic solution for neural interfacing.

Carbon fiber electrodes still possess some limitations. Chronic recording and stimulation from the electrode tips require additional coating applied to these sites. Commonly used coating materials for improving the electrode performance possess electrical and stability limitations long term. These coatings are only applicable for neural recording and lack the chronic ability for alternative neural interfacing processes like those used for neurotransmitter detection. An alternative to electrical signal acquisition from neurons has seen promise in the treatment and detection of a broader range of neural pathologies. In this thesis, research was also completed on expanding the utility of these devices by developing a Boron-doped Nano Crystalline Diamond (NCD) coating onto carbon fibers for neurochemical sensing. Collaborative work was completed to establish the potential benefit such a coating would have for dopamine sensing. Finally, the ability to translate this novel coating onto the proposed carbon fiber array configuration was also explored. This aimed to highlight the potential of the device proposed and the future promise of further development with these technologies. Bridging the gaps in technology that are currently limiting neural disease treatment, diagnosis and understanding will improve the outcomes for those suffering from such pathologies. All work in the following thesis was performed by me, unless specifically otherwise stated.

List Of Acronyms

BCI	Brain Computer Interface
BDD	Boron Doped Diamond
CNW	Carbon Nano-Wall
CV	Cyclic Voltammetry
CVD	Chemical Vapour Deposition
DBS	Deep Brain Stimulation
DI	De-Ionised
EDS	Energy Dispersive Spectroscopy
EELS	Electron Energy Loss Spectroscopy
EIS	Electrochemical Impedance Spectroscopy
FBR	Foreign Body Response
FIB	Focused Ion Beam
LFP	Local Field Potential
MCD	Micro-Crystalline Diamond
MEA	Micro-Electrode Array
NCD	Nano-Crystalline Diamond
PBS	Phosphate Buffer Solution
PCB	Printed Circuit Board
PCD	Poly-Crystalline Diamond
RIE	Reactive Ion Etching
SEM	Scanning Electron Microscopy
SNR	Signal to Noise Ratio
TEM	Transmission Electron Microscopy

Chapter 1: Introduction of neuromodulation devices and current limitations

1.1 Chapter Aim

This chapter first summarizes the state-of-art interfacing technology and their limitations in long-term, high-resolution applications. The associated theory of neuroanatomy and function is then discussed. In the end, this chapter focuses on carbon fiber technology in the context of current neural interfacing technology and explores potential approaches for improvement.

1.2 Current Neural Interfacing Technology

1.2.1 Current Neural Implants

The first neural interfacing device controlled by neurons was developed in the 1970s [1]. This device was able to control a cursor on a screen using EEG data collected from the patient looking at the screen. Such devices are referred to as Brain Computer Interfaces (BCIs). These possess the ability to analyse, record and in some cases control the propagation of neural signals using a connected computer [2-4]. Brain computer interfaces aim to leverage the vast advancements in computing power to understand and modulate neural signals like never before. Much of the limitation therefore lies in the complexity and resolution of the neural signals obtained and highlights the potential of what can be done with ever improving neural interfacing devices.

Neural interfacing devices are also emerging as a viable treatment of neurological diseases such as Parkinson's Disease, Epilepsy and Dystonia. A commonly used treatment for some of these disorders is Deep Brain Stimulation (DBS). As the name suggests, this involves the stimulation of neural structures deep within the brain. Such stimulation has been an effective intervention in these diseases for decades [5-8]. For DBS applications, the stimulation current required for a therapeutic outcome is high. To safely deliver high stimulation currents, large (>1 mm diameter) electrodes are required. These larger electrodes cause more localized damage to surrounding tissue than smaller electrodes. This damage is a result of acute trauma caused during insertion and chronic scar tissue forming at the electrode interface over time. To overcome the developing scar tissue, the voltage required for stimulation must be increased over time. This allows the device to outlast tissue damage and inflammation that would render smaller electrode devices unusable [9].

value in mA?

Examples of devices that utilizes Deep Brain Stimulation are the Medtronic Activa^{tm} RC, Abbott Infinity, PINS Medical and Boston Scientifics Vercise™ DBS [10-12] (Figure 1.1 and 1.2). These devices have proven an ability to chronically interface with the patient's tissue by both recording and stimulating the target tissue in real time to provide a treatment of Parkinson's disease [13]. DBS implants consist of 4-8 platinum iridium ring electrodes at the end of a polyurethane lead (Figure 1.1 and 1.2). These devices are surgically implanted into deep regions of the patient's brain using imaging to identify the target location before insertion [14]. The implant location can be refined by using a reduction in the patients' symptoms as a means of establishing correct implantation location [15]. Often multiple insertion attempts are required before a therapeutic location is found. Variability of deep brain stimulation can be produced by the positioning of the electrodes and as such is an important consideration for treatment intervention. These devices have shown viability as chronic implants for decades. This is made even more impressive due to

the device being able to both stimulate and record, as stimulating devices tend to increase scar formation which can interfere with recording performance. [16]. Despite the low electrode number, DBS devices can successfully treat the target pathologies in a manner that greatly improves the lives of their recipients.

Figure 1.1: Medtronic ActivaTM RC DBS device [16].

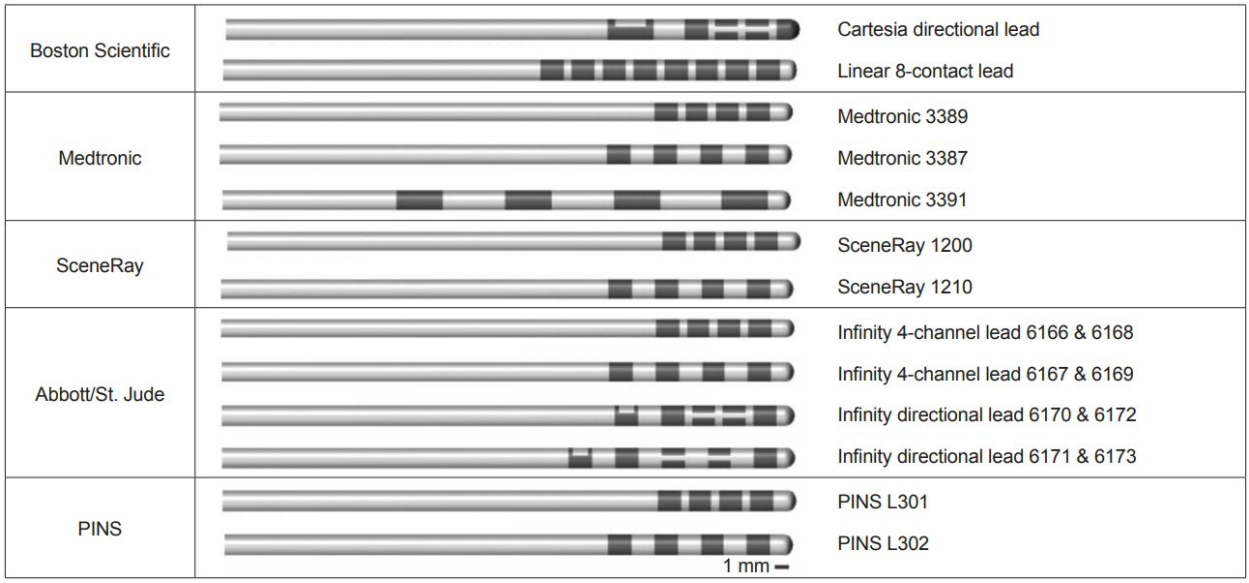

Figure 1.2: Commercially available DBS electrode leads [10].

One of the oldest approved neural interfacing devices, and the only commercially successful sensory recovery device, is the Cochlear Implant [17]. Figure 1.3 shows an illustration of the implanted component of cochlear device and a close up of the electrode array in situ. This device is implanted within the cochlear of a patient to restore hearing in the recipient. The implant works by triggering auditory sensations through directly stimulating the auditory nerve as a replacement for damaged inner ear hair cells. The length of the electrode array is up to 30 mm to coil around the cochlear that is between 6.53 mm and 8.30 mm in diameter (Figure 1.3) [18]. These arrays contain 22 evenly spaced platinum electrodes (~250 µm long) to stimulate different regions in the cochlear corresponding to different frequency bands in the auditory spectrum. The cochlear implant has proven to be an incredibly robust neural interfacing technology often lasting the duration of the lifetime of the recipient with most revision surgeries being a result of infections resulting from the implant. The surgical insertion of these implants is well developed and slight variations in the implantations have proven unlikely to compromise the performance of the implant [19].

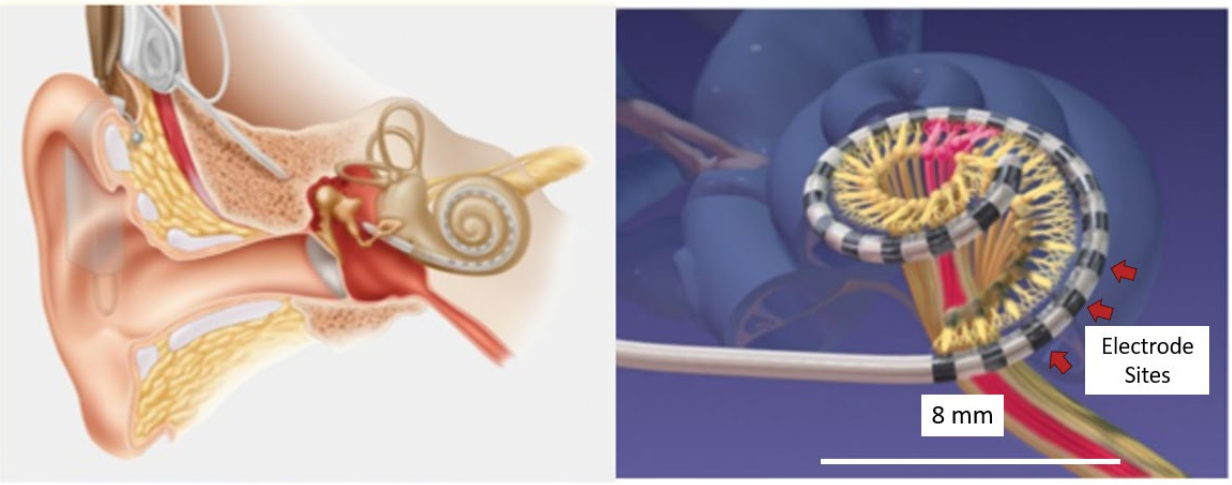

Figure 1.3: Cochlear Implant shown implanted within the human cochlear [17]. The working electrode sites (shown in black) correspond to the different frequency ranges of the intact auditory architecture. These provide stimulation to stimulate the normal working function of the system.

Interfacing directly with the still functioning systems of a damaged neurological system is a promising technique as exemplified by the cochlear implant. The same concept is being explored in the visual pathways as a treatment for retinal diseases. An encouraging device using this concept is under development by Pixium as the PRIMA retinal implant [20]. This device is a Subretinal prosthesis that is surgically inserted between the retinal epithelium and the retinal cell layer [20]. Like the cochlear, this device requires the intact architecture of the rest of the visual neural pathway and targets conditions that result in degeneration of the light-sensitive neural elements in the retina. Retinitis pigmentosa and macular degeneration are the two most pertinent pathologies for retinal implant devices. The PRIMA device has proven to be a successful treatment for the patients that are recipients of the implant for up to 3 years, with *in vitro* accelerated stimulation tests showing minimal pixel loss for up to 10 years. This device can stimulate surviving retinal cells to mimic what would occur in a healthy visual pathway. A benefit of the surgical location is the lower degree of foreign body response experienced in this location [21, 22]. The larger challenge for retinal implants is the corrosive environment in which they are implanted. This means material selection is tailored to these conditions instead of limitations arising from the foreign body response. The other primary failure method for the device is overstimulation. Despite the difficulties stimulating electrodes face, this device is again a testament to the potential benefits successful neural interfacing may elicit.

A unique method for neural interfacing has been developed in the Synchron Stentrode [23]. This device is an endovascularly implanted brain computer interface. This device capitalizes on the already well-developed technology of endovascular stents, by using them as an avenue for implanting an electrode interface into accessible areas of the brain, such as the motor cortex. This method has been utilized in similar technology already implemented in pacemakers and defibrillators [24]. The Stentrode consists of eight 8, 750 µm diameter, platinum disc electrodes connected to leads that are inserted through the jugular vein. The stimulator is position in the chest in a similar location to that used for cardiac pacemakers (Figure 1.4). This technique is very promising as it is implanted without the need to breach the blood brain barrier and this avoids the nervous system's foreign body response, the primary failure mechanism in many neural

interfacing devices [25]. The endovascular surgical approach, however, does limit the number of viable implantation locations, and leads to other limitations for the device. The device may only record in areas proximal to that of the vasculature, meaning some of the intervening tissue is inaccessible to the recording electrodes. This is somewhat mitigated by the incorporation of electrodes into the vessel walls to help limit the distance between the target neurons and the electrodes. The spatial resolution is further limited by the low number of electrodes the device contains. The device can potentially however record over a larger area compared to some other implants due to its size, albeit at a lower spatial frequency. This device has been proven in human trials where patients with limb paralysis were able to regain limited control of digital devices upon implantation [23, 26, 27]. This device is not fully approved for human use but has demonstrated great promise in interfacing chronically with a patient's neural tissue for a diverse range of neurological disorders.

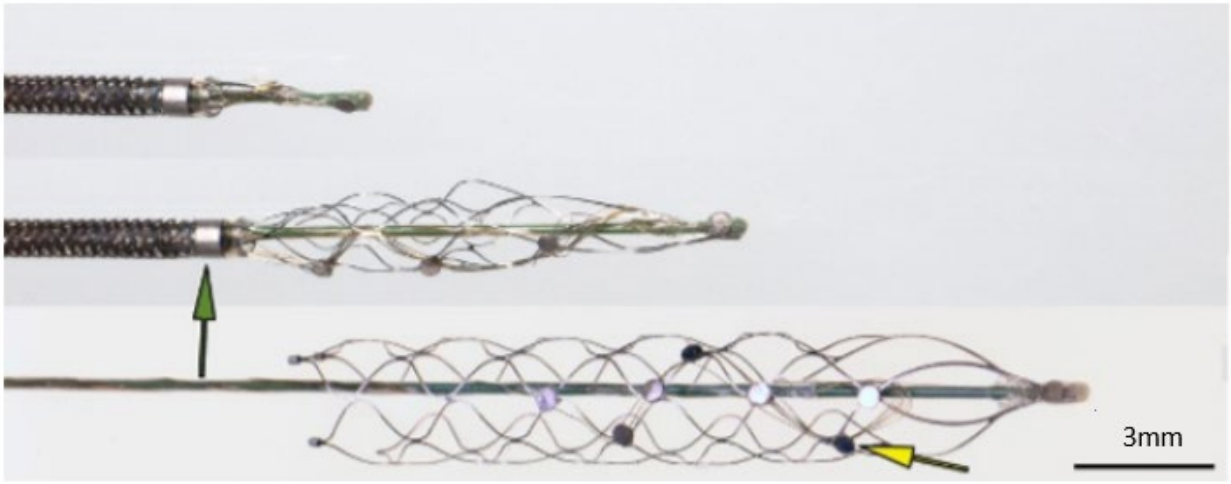

Figure 1.4: Synchron Stentrode device including the platinum disc electrodes (yellow) and the insertion catheter (green) [23].

Another emerging neural interfacing device that has shown great promise recently ~~of late~~ is the Saluda Evoke © closed-loop Spinal Cord Stimulation system. This device targets the dorsal root ganglion within the patient's spinal cord as a means of treatment for chronic pain. This innovative device can stimulate and record its own Evoked Compound Action Potentials (EPAC) [28]. This detectable feedback system allows the device to modulate its output and provide a greater refinement for treatment compared to other implants [29]. This is incredibly important in the treatment of chronic pain, as each patient at a particular time requires a specific amount of stimulation. If the stimulation is too little, no effect is seen, too great, and there is an increase in the patient's discomfort or pain. This feedback system allows this balance to be maintained chronically to match the specific requirements over time. Other devices require either the patient to describe sensations or for pathological differences to be measured to determine the therapeutic range of the implant. The device itself contains two leads with 12 Platinum Iridium electrodes. This is an appropriate level of spatial resolution for this purpose while the two leads allow for the recording of the other leads EPAC for treatment refinement. Due to the functional importance of the junction at the dorsal root ganglion, safety studies are imperative, and extensive safety testing has been performed and will continue to be developed for this electrode type [30]. The device is inserted into the dorsal root ganglion using an epidural needle and utilizes the ECAP measurements of the closed-loop system to obtain the optimal placement. Like DBS techniques, this implant can overcome some FBR issues of chronic applications using larger stimulating voltages and larger electrodes. The Evoke records at a low spatial frequency signal, however, which is suitable for this specific application.

ECAP

ECAP

(define)

One of the newest devices that has garnered an increased amount of media attention is the Elon Musk Funded Neuralink Project. This device contains 96 small flexible electrode threads over 32 arrays for a total of 3072 recording sites [31]. Neuralink boasts a larger number of potential recording sites than similar technology and like the Stentrode system, it is fully implantable. The Neuralink electrodes are also very small, allowing them to interface with single neurons in some cases. This increases the potential of this technology to perform more complex analysis and therefore expands its potential use cases, unlike devices built to target specific neurological conditions. The electrodes themselves consist of gold with a conducting polymer (PEDOT:PSS) and Iridium Oxide coating as a means of lowering impedance and increasing their effective charge-carrying capacity required for electrophysiology [32]. The insertion of this device has been well developed and utilizes a complex surgical robot capable of detecting and avoiding blood vessels which helps reduce complications and limitations that arise from penetrating the tissue with a probe (Figure 1.5). The device is notable as it aims to optimize many aspects of technology that has already been developed and shows the potential for improving current neural devices. A photograph of the Neuralink surgical robot is shown in Figure 1.5. Much work is still required to completely show the chronic safety and performance of this device [33].

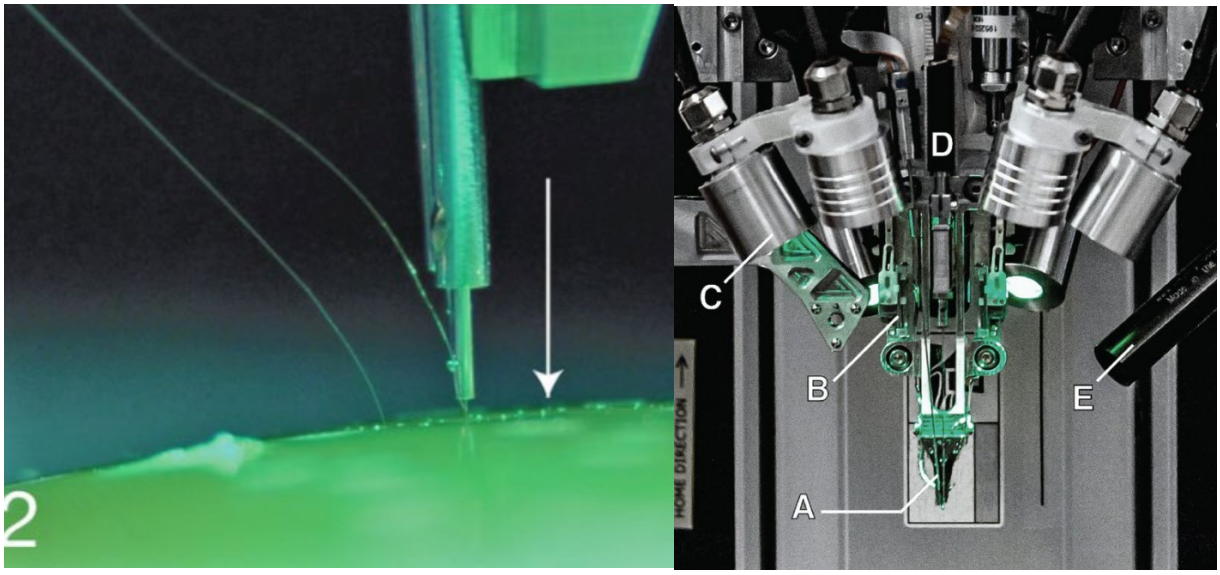

Figure 1.5: Neuralink probe insertion (left) and surgical insertion robot (right) [32].

The most successful device to date in terms of electrode number and chronic performance is the Neuropixel device. This implant is primarily made of silicon and boasts a shank electrode design with 1000 recording sites outfitted with on board amplification and digitization [34]. This device (Figure 1.6) shows the best ratio of device size with increased channel count. Newer versions have multi shanks with upwards of 5000 electrode sites boasting recordings for up to 300 days post implantation [35, 36]. Successful human acute recordings have also been demonstrated across multiple experiments, further demonstrating that this is the current gold standard neural implant [37, 38]. Much of the success is owed to the data acquisition system, as the scalable recording of numerous parallel channels presents a large concern for implantable devices. The current version still requires external connection to be able to process the vast amount of data presented from the system, showing that there is a balance between device feasibility and the amount of actionable data collected [39].

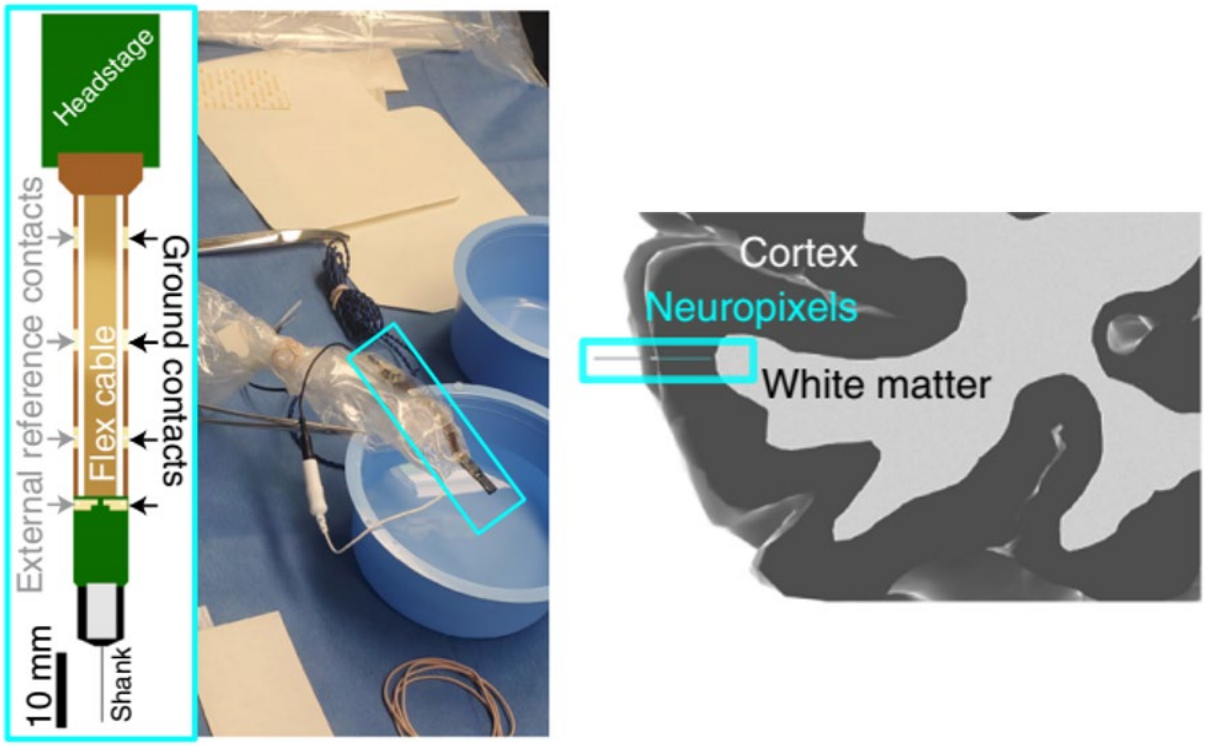

Figure 1.6: Neuropixel probe for human implantation showing the shank and full device size as well as insertion potential into human neural tissue [37].

More common interfacing devices consist of electrode arrays that are primarily utilized for research purposes. These include the Michigan/ Neuronexus and Utah (Blackrock Microsystems) arrays. The Michigan array is a shank electrode with recording sites along the length of the shaft whereas the Utah array consists of multiple individual electrodes (Figure 1.7). The Michigan style electrode is insulated with silicon and Parylene-C and has shanks that are 3.8 mm long, 5 microns thick and 50-100 microns wide [40, 41]. Due to the increased size of the electrode shank, the Michigan style electrode tends to perform poorly when chronically implanted, with signals degrading after only a couple of weeks [42]. Effort has been made to improve the viability of the electrodes including the use of conductive polymers such as PEDOT to improve the electrochemical characteristics for recording [43]. The current Neuronexus array contains either 16 or 32 recording channels with a shaft length of 5mm (Figure 1.7). These devices may be either shank or Utah like, with the smallest of which being 5mm long and 33x15 µm at the tip. The increase in options for this style of electrode is quite unique and therefore provides greater versatility for potential uses.

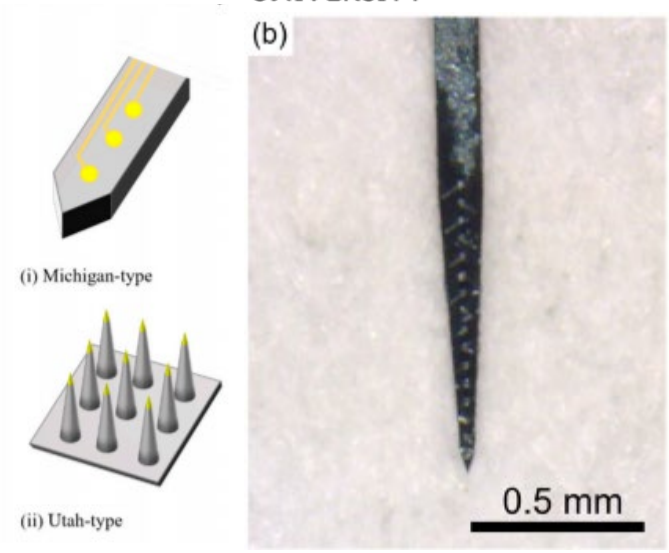

Figure 1.7: Examples of current electrode implant variations currently used, including the Michigan-type and Utah-type (left) and the Neuronexus (shank) array (right) [44] [45].

The Utah array consists of a 10 × 10 electrode array (100 total electrodes) on a 4×4 mm footprint. The electrodes themselves contain 35-75 µm recording tips and show an impedance of 100-500 KΩ (at 1 kHz). Due to the inflexibility of the silicon used, this array is limited to electrode lengths of 1.5mm. This renders the Utah array ineffective for certain treatments, including deep brain stimulation due to the inability to reach neural layers below that of the cortical level. The Utah Array has shown mixed preliminary results in human trials [46]. Stimulating electrodes showed tip degradation in the majority of electrodes, however this did not correlate to a reduction in recording quality. Unlike the Michigan electrode array, the Utah Array has been proven to perform well chronically for recording periods of up to 3 years [46-50]. More recent studies suggest that this time length may be higher, however, this was performed with a low sample number and requires further validation [46]. Although better than the alternatives, the 6-month time frame is not suitable for a chronically implanted device for clinical use. Open brain surgery is high risk and even annual replacements would be considered too risky. Utah arrays have also been shown to produce a larger amount of acute vascular damage in the tissue than Michigan style arrays [25]. This increase in vascular damage is caused by the larger array footprint, meaning it is more difficult to avoid vascular architecture in the tissue during insertion. This drawback is outweighed by the increase in spatial frequency this array type provides and the fact that each individual electrode causes less damage upon insertion resulting in a net decrease in inflammation [51]. The tissue damage is also different depending on the depth of the tissue, with majority of the inflammation caused at the base of the electrodes [46]. This level of tissue inflammation is not as relevant as it will not impact the ability of the electrodes to record if damage is not localized at the electrode tip. Even with the reduced inflammation of the Utah Array, no current electrode array technology can present an incorruptible implant-tissue interface with single neurons [52].

1.2.2 Limitations and Failure Modes of Neural Interfacing Devices

Despite the success of some of the current neural modulating technologies, there are still many improvements needed to achieve higher density chronic neural interfacing devices. The cochlear and Pixium devices are adequate at treating specific pathologies but still require intact audiological and visual pathways, respectively, for successful treatment. DBS and Stentrode treatments are subject to spatial-resolution limitations, and the newer technologies have yet to be proven to interface chronically with single neurons. The Neuralink and Neuropixel project shows there is much benefit to be made from further development beyond what has already been achieved with traditional techniques and materials. This highlights the importance of optimization in the neural interfacing field, and the multitude of avenues wherein this could occur. Developing a device that can capture chronic recordings over a patient's lifetime, for a diverse range of single neuron units, would provide an avenue for treatment of a multitude of neurological disorders, potentially improving the lives of many people.

Interfacing directly with neural tissue presents inherent risks and difficulties, to both the patient and the implant. These issues are mostly the result of acute and chronic inflammation that leads to changes in electrode performance over time (Figure 1.8). Much of the patient's limitations result from the tissues Foreign Body Response (FBR) [51, 53]. The FBR is an immune response within the host tissue that produces what is known as glial scarring. This is the production and mobilisation of immune cells made up primarily of astrocytes and microglial cells [54-56]. This scarring creates a barrier around the electrode that renders them electrically isolated from the adjacent neurons, reducing signal quality. The size and shape of the electrodes is the principal predictor of the level of this host immune response [51, 57]. Inflammation is exacerbated by the insertion trauma experienced by the tissue upon implantation [58, 59]. The mechanical property of the electrode also plays a large role in this damage. Through matching of the implant's mechanical properties to that of the tissue, you may reduce the chronic damage experienced by the tissue [57, 60]. This mechanical mismatch can be compounded by the tethering of the implant to the skull, as the implant is not able to comply with the normal motion of the neural tissue causing mechanical stress and continuous chronic damage [51, 61]. Tissue damage is not the only factor impacting the long-term viability of an implant. Material or electrical failure of the implant itself also adds to the degradation observed in chronic recording [43, 47, 62]. The limitations for material choice is further limited by the availability of biocompatible, non-cytotoxic, non-biodegradable materials that are mechanically able to be inserted into tissue [63].

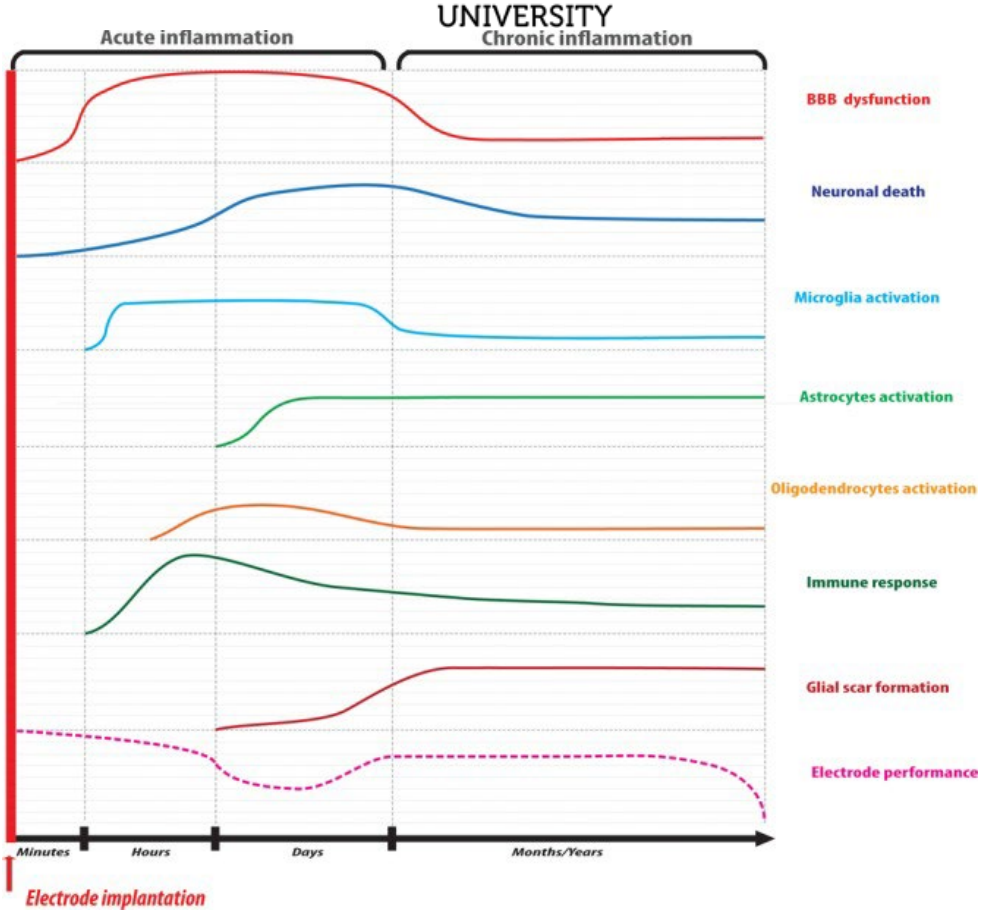

Figure 1.8. Timeline depicting the acute and chronic phases of the tissue response and electrode performance upon implantation into neural tissue [64].

This caption needs expanding greatly, with each of these failure modes explained.

As computing and electronic technology advances, so to do does the potential of neural interfacing devices. The signals gathered from interfacing devices can be complex and therefore require high level analysis to elicit meaningful interventions [65-67]. More complex pathologies, such as epilepsy, require higher fidelity recordings and, hence, more complex signal analysis systems [13, 68]. This means that higher spatial frequency is required which necessitates implants with a larger number of active electrodes. This can be achieved by using multiple implants or larger implants. The use of larger implants presents a problem as increasing implant size will increase the degree of tissue damage and limit the chronic viability of the implant [51, 57, 69]. Multiple electrode implants have shown success; however, this increases the complexity of surgery and device fabrication [25]. Multiple implants also have the potential to reduce vascular damage that occurs during implantation, as it would be possible to implant around vascular architecture in the tissue, reducing inflammation. With these limitations in mind, it is important to start to consider a wider variety of materials for an implantable neural electrode. Such a material would need to be conductive, able to be fabricated into a micro electrode array, flexible and workable into a functional device. To be able to fabricate a device of such a material into a multi-channel neural interfacing array could drastically improve the potential therapeutic benefits of Neural implantable devices.

1.2.3 Metal Micro-Wire Electrodes

Biocompatible metals are the most commonly used material for micro-wire electrodes. These metals include tungsten, platinum, and iridium [52, 70-73]. Metal micro electrodes can be fabricated at the micrometre scale required for single unit recordings, and possess innate stiffness that allows for their insertion into neural tissue. The electrical properties of these materials vary but can be further improved through electroplating or processing methods to improve their electrochemical properties for neural applications [74, 75]. Metal micro-wire electrodes still, however, possess the chronic issues that are associated with the FBR [76]. This is exacerbated by the potential corrosion concerns for some materials as well [70]. The stiffness to insert the metal microwires is still too large to avoid the chronic tissue damage from the mechanical mismatch between the tissue and the implant. Some thinner metal electrodes have been developed with flexible backing to minimize the stiffness of the electrodes, but require guides to be inserted [77-80]. Often in these cases, the inserter guides themselves produce much of the insertion trauma that the electrodes are aiming to avoid. These are a potentially viable route for an implantable chronic neural interfacing device. However, because of the complexity of fabrication and design limitations, alternative materials are worth investigation.

1.2.4 Carbon Fiber Neural Devices

Carbon fibers are the most prevalent carbon-based micro-electrode being developed for neural interfacing [81-83]. These individual fibers are electrically conductive and possess mechanical properties that are conducive to electrode insertion [84]. Carbon fibers have also exhibited good biocompatibility and a reduced degree of tissue inflammation primarily due to their innate flexibility [85-87]. Although the diameter of the fiber can vary, typically 7 µm diameter fibers are used for neural electrodes.

As a result of their conductivity, the electrodes must therefore be insulated to obtain individual unit recordings. The most common of these insulators is Parylene-C. Parylene-C is a vapor deposited polymer commonly used in the implant industry. It has proven biocompatible properties and biostability [88-91]. Carbon fiber materials have also shown the ability to electrochemically record neurotransmitters, further increasing their versatility as a neural interfacing material [92]. Carbon fiber electrodes possess a flexibility that more closely imitates neural tissue than other array alternatives, such as platinum. The flexibility of the electrodes is vitally important, as neural tissue will move along with normal bodily motion; if the implant is unable to move along with the tissue, wear will be experienced at the interface. Despite the low mechanical stress of Parylene-C (1GPa) and Carbon Fiber (~400kPa), the mechanical stress of brain tissue is still lower (100kPa) [93, 94]. They show robustness and a penetrative ability not shown with other carbon-based materials that is conducive to depth electrodes up to 2mm [95]. Through the use of insertion guides this can potentially be even deeper [96].

Conductive polymers have been shown to improve the electrochemical characteristics of carbon fibers for neural recording. One such polymer, Poly (3,4-ethylenedioxythiophene) (PEDOT), has proven to reduce the impedance of the electrodes whilst simultaneously improving its charge injection capacity required for neural stimulation *in vivo* [97-99]. Despite its potential, PEDOT has yet to be proven for long term stability past that seen in other devices, such as the Utah array [45]. Additives and alternative dopants have been shown increased chronic stability [100]. An alternative electrochemically deposited tip modification to PEDOT is Iridium Oxide [101]. Like PEDOT, Iridium Oxide has been shown to improve the electrochemical characteristics of carbon fiber micro electrodes [102, 103]. The benefit of electrochemical deposition is the ability to apply the conductive polymer strictly on the interfacing tip of the electrode. This allows for a much more controlled deposition required for electrode manufacture at scale.

Carbon fibers provide an avenue to produce a flexible, viable Utah style array that shows great potential for chronic single unit neural interfacing. The highest channel count array that has been achieved thus far with this technology is 16 electrodes (shown in Figure 1.9) [104]. The electrode geometry is conducive to single neuron recording as tip geometry will mimic the size of single neurons. The electrical properties allow for both stimulation and recording with further work being done to increase this ability for chronic applications [16, 105-108]. There are, however, no commercially available carbon fiber-based arrays, principally due to a lack of engineering solutions for bonding and forming reliable, high count, electrical connections to carbon fibers. Despite its promise, more work is needed to fully capitalize on this emerging technology.

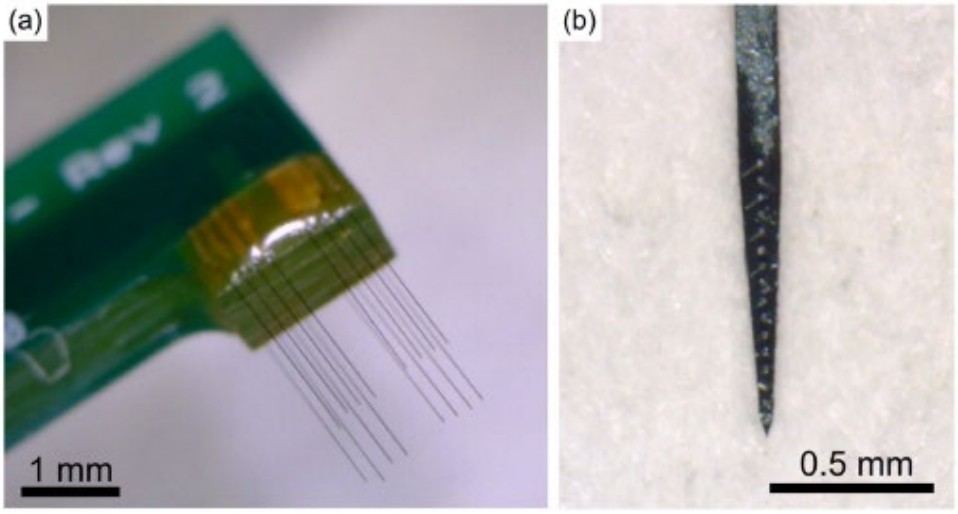

Figure 1.9: A comparison of a carbon fiber (A) and Neuronexus array (B) [45].

1.3 Neuronal Interfacing

1.3.1 Neuronal Communication

To control the development of neural devices, more insights into the complex workings of the neural systems is required. Neural cells (called neurons) communicate through the propagation of electrical and chemical signals. The structure of the neuron consists of a cell body, dendrites, and an axon. These are connected to one another via extracellular spaces known as synapses [109] (Figure 1.10). The dendrite receives the signal from the presynaptic neuron which carries it along the cell down the axon to the next cell in the signal pathway. The axon can pass signals over a range of 0.1mm to 2m with a speed of 1 to 100 m/s. Neurons may be unipolar, bipolar, or multipolar depending on the number of processes that the specific neuron conveys. Unipolar cells have one process, whereas bipolar have two. Multipolar cells are the most common type of neuron in mammals and allow for more complex neural communication between cells. The electrical signals that pass through the neurons are called action potentials. The action potential is caused by a depolarization of the membrane potential [109]. This potential passes along the membrane between nodes of Ranvier, exposed membrane gaps between insulating myelinated Schwan Cells [110]. The nodes of Ranvier contain a higher density of the sodium/ potassium ion channels required

for the regeneration of the membrane potential, so it remains constant along the length of the axon. The signal travels along the length of the neuron until the synaptic junction at the end of the axon.

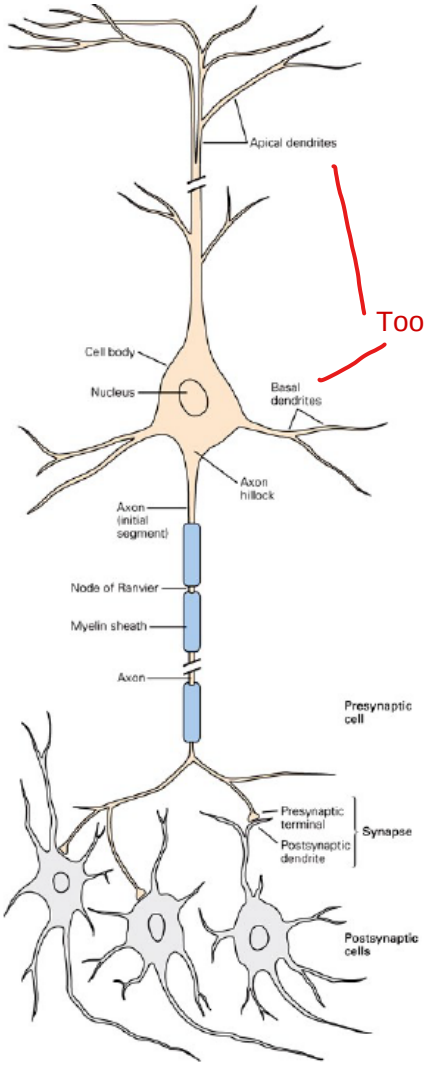

Figure 1.10: Image of a pluripotent neuron showing the myelin insulated cells and nodes of Ranvier along the axon of the presynaptic neuron [109]. The presynaptic axon connects to the postsynaptic dendrites to provide an avenue for signal propagation across the synapse.

The depolarization of the action potential is passed along to postsynaptic cells using ion channels [111]. In majority of nerve cells, these ion channels are activated using signalling molecules known as neurotransmitters [112]. These are predominately acetylcholine molecules (such as dopamine) that have receptor ion channels on the post synaptic neuron surface [109]. This transfer takes less than 100 µs and occurs over a distance of less than 200µm. Neurotransmitters are released at the axon terminals of the presynaptic neuron and bind to receptors on the postsynaptic neuron [113, 114]. These receptors are calcium ion channels that depolarize the membrane potential causing an increase in voltage towards 0mV. Once this voltage exceeds the activation threshold (around -55 mV) the voltage gated Sodium channels open further increasing the membrane potential (up to 30mV). This produces the characteristic spike of an action potential that are recorded by neural electrodes (Figure 1.11). The resting potential is repolarized through combined passive movement of potassium ions out of the cell and active transport

of sodium and potassium by the sodium potassium pump. This exceeds the resting potential of the membrane, causing a hyperpolarized state preventing the neuron from firing again instantaneously. This hyperpolarization is called the refractory period and is what causes the time delay between single neuron unit spikes [115]. If the synapse is sufficiently small (<20nM), the depolarization may be passed directly between the membranes of two neurons [116, 117]. These types of synapses are called gap junctions and voltage-gated ion channels. The gap junction provides a direct connection between the cytoplasm of the pre and post synaptic neurons [109]. The voltage-gated channel passes the action potential along the synapse directly regenerating the transferred signal.

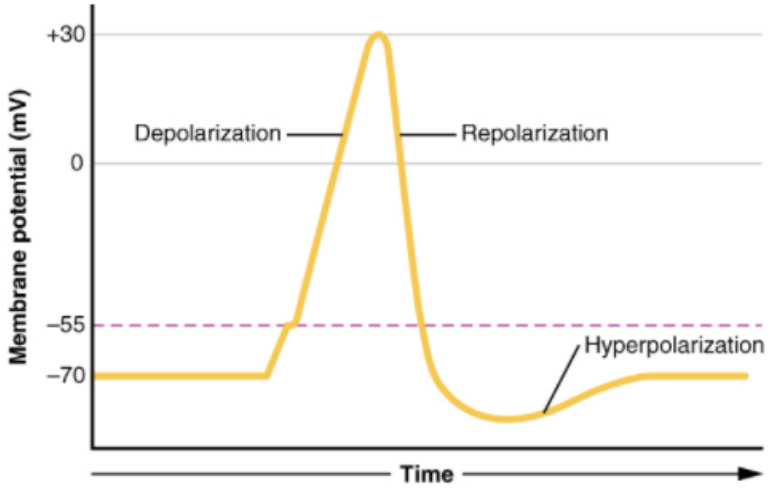

Figure 1.11: The characteristic shape of an action potential. This includes the depolarization and repolarization of the membrane potential. The hyperpolarization observed occurs due to the decreased potential of the refractory period caused by the passive movement of potassium ions out of the cell [118].

The number of these neuronal connections varies between animals as well as in different parts of the brain meaning that different areas of the brain will display different characteristics that need to be considered for neural implants. The neural density of a human cortex is among the highest in the animal kingdom, an important point for translating any animal studies into their human applications. Neuron density is an important characteristic of the nervous system. Brain size has been shown in the past to scale with body size [119]. However, it has also been shown that neuronal density and the number of connections between these neurons that has the biggest implication in terms of processing power [120-122]. This has implications on device design and the ability of electrodes to interact with the largest number of signals. Devices must be as small as possible and cover a wide enough spatial area in order to obtain the most accurate picture of these connections. This provides further evidence for the use of micro-electrodes for neural device design. Implants that are able to detect more of these vast and complex signals could provide much more insightful information about the neural system.

1.3.2 Neural Electrode Double-Layer and Electrode Impedance

The crux of neural interfacing is the ability to present a material to the tissue that can detect changes in the environment that indicate the presence of localized action potentials. The area of electrolyte immediately adjacent to the electrode will not inherently mimic that of the bulk tissue [123]. For neural electrodes this effect can be seen in the Electric Double Layer (EDL) that is present at the electrode/tissue

interface. An electric double layer is dependent on the accumulation of ions at the interface between a conducting material and the surrounding electrolyte, in this case the neural tissue [124]. Counter ions are adsorbed at the surface due to electrical attraction of opposing charges. For electrodes this will be directly affected by the size and shape of the electrode recording site. The movement of opposingly charged ions adsorbing to the recording electrode create a region of charge that is not representative of the surrounding tissue. The diffuse layer of ions closest to the electrode can be thought of as the dielectric layer of a double-layer capacitor (Figure 1.12) [125]. One plate of the capacitor is the recording electrode, and the other plate being the nearby neural tissue. Like all capacitors, a change in the distribution of charge on one of the capacitor plates will result in a voltage change across the capacitor. In neural recording, the neural tissue will cause a change in local ionic concentrations during an action potential. This in turn will cause a change in voltage at the electrode. It is this change in voltage over time that can be amplified and plotted to represent depolarising of a nearby neuron. The challenge is to tune the electrochemical properties of the recording electrode such that the voltage change on the electrode is large enough that it can be successfully amplified and recorded.

The electrochemical characteristics of this double layer capacitor is all important in capturing small charge fluctuations such as those produced by neurons during a depolarisation. The main effect of the double layer capacitor is changes in electrode reaction rate and the introduction of noise due to capacitive and faradaic current introduced into the system [126]. This will have a direct impact on the Signal to Noise Ratio (SNR) of the recording and hence the ability to extract meaningful neural signals above the noise floor [127]. This may change the charge transfer rate on the electrode and as such impact on the electrode recordings. Faradaic reactions at the electrode/electrolyte interface involve the reduction or oxidation of species on the electrode surface introducing noise into the signal in the form of these faradaic currents [128]. This mechanism although can be leveraged with some forms of neural sensing relying on the reductive and oxidative currents produced from faradaic reactions to detect the presence of neuro-transmitters [129].

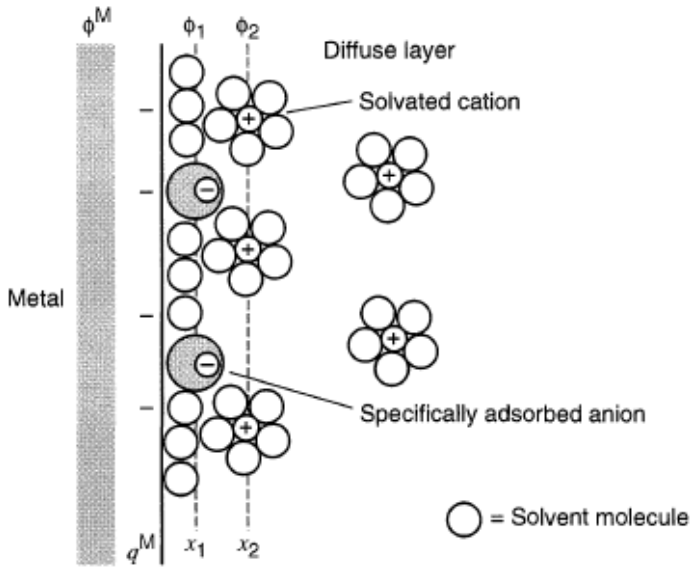

Figure 1.12: Model of the double layer region of electrodes showing the adsorbed ions on the surface of the electrode [125]. This accumulation of ions at the surface is not indicative of the bulk area around the electrode and hence will introduce inconsistencies when measuring especially at the micro scale of neural tissue.

Another important electrochemical characteristic defining the viability of neural interfacing electrodes is electrode impedance [73, 130]. Electrode impedance refers to the resistance to current transfer in an alternating current system like those seen in biological signals. An increase in impedance will reduce the SNR of the signal and hence reduce the quality of the recordings [131]. The impedance is an important measurement as it will show the ability of the electrode to detect the electrical signals at different frequencies. Due to neurons firing at rates between 200 and 1000 Hz (the base width of the average action potential is 1ms), most papers cite the electrode impedance simply at the 1kHz range [127]. This is not necessarily indicative of electrode viability as the impedance will be different for different spike rates and hence different frequencies. For this reason it is often beneficial to plot the impedance magnitude as well as the phase over the entire frequency range [132]. The measured impedance for electrodes is not the entire picture as the impedance of the electrode/tissue interface will differ slightly to normalized impedance spectroscopies in PBS solution [133]. The specific location of the recording and reference/ ground electrodes (these are often shorted during *in vivo* electrophysiology recordings) will influence the electrode impedance *in vivo* [134]. Electrode impedance will also change over time due to glial scarring and the FBR changing the electrode/tissue interface [135]. As such, electrode impedance is an important characterization that needs to be evaluated over several conditions to assess and compare the viability of recording and stimulating devices.

(define)

1.3.3 Action Potential Detection

Action potentials can be detected in multiple ways including electrically and chemically. The most common of these is the electrical recording of the potential difference between the electrode and the extracellular matrix surrounding the neurons. Electrical signals can either be spontaneous in nature or driven. Driven signals involve using a supplied stimulus to correlate with the signals in time, for instance providing images on a screen whilst recording in the relevant location in the visual cortex. Spontaneous signals can be recorded in the absence of a stimulus (Figure 1.13). These signals can be recorded by neural electrodes as burst or single spikes and local field potentials. Monitoring Bursts of neuronal spiking is a reliable method for showing neural activity and are vital to elicit meaningful information [136]. These bursts last at most 25 ms and can show between 2 and 6 action potentials occurring at 200Hz. The spike amplitude typically reduces during the duration of the burst. The burst is a result of the slow depolarization wave of multiple axonal spikes as a result of an interaction between multiple synaptic inputs [137]. Spontaneous spiking can occur as a non-driven signal and are not indicative of a neuronal response to a stimulus [138]. This spontaneous spiking is caused from pacemaker cells with an unstable membrane potential that modulate the rhythmic bursting in surrounding neurons [139]. Spontaneous signals are often seen as single spikes and will not be correlated in time with any stimuli. When recording a neuronal signal, it is therefore important to discern the difference between these spiking patterns as this will indicate the meaningfulness of the signals recorded.

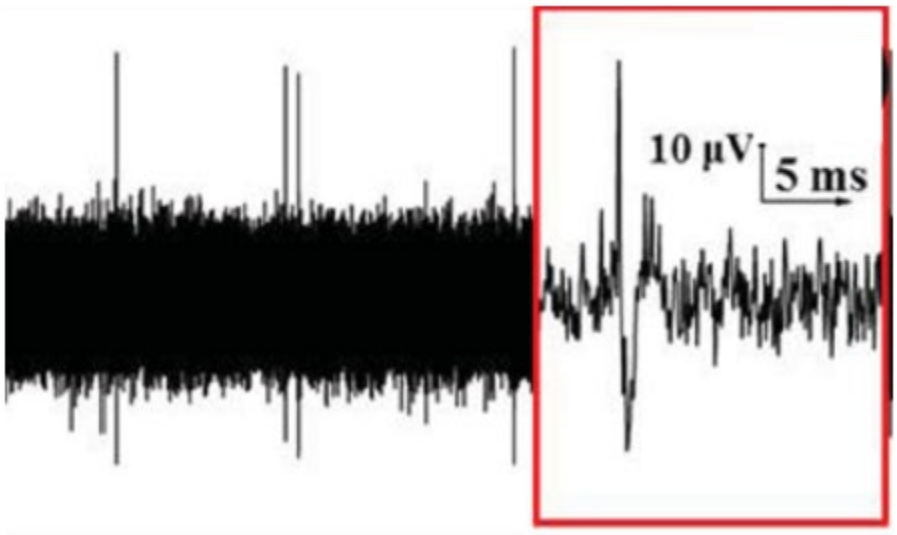

Figure 1.13: Spontaneous neural spiking depicting single action potentials in tissue recorded with carbon fiber electrodes [140].

Local Field Potentials (LFP) represent the accumulation of potentials from a region of neurons. LFPs provide an alternative to single unit detection. These are often detected using larger surface area electrodes. This information is less informative than single units, however, these can be detected despite the accumulation of the glial sheath around an electrode from the FBR [141]. This provides an avenue for signal analyses when the single unit recordings are lost. Further work is being made on modelling the single unit contribution to these fields to elicit meaningful analysis from previously unusable signals [142-144]. Specific signal recordings will vary with positioning of neurons within the tissue. The positioning of electrodes will depend on the purpose of recording and the species in which the recording takes place. For example, depths required for effective epilepsy treatment will be much larger than the depth required for recording from visual cortex regions [145-147]. Electrode length and geometry is a large determinant in the signals that will be recorded. The length of electrode will be affected by mechanical and material properties of the electrode as well as potential insertion mechanics [148]. The ability to access specific tissue is therefore a great limitation on producing signal recordings from relevant tissue.

environment?
tissue?

in

1.3.4 Stimulating Neurons

Stimulating neural tissue requires an electrode to inject enough charge into the vicinity of a neuron to excite an action potential propagation. This proves challenging for single unit recordings, as this must be large enough to elicit a response in the targeted neuron and not in the surrounding tissue [149]. The stimulation must also not damage or produce unwanted electrochemical effects in any of the surrounding tissue. This factor is a major limitation in retinal prosthesis designs [20]. Stimulating and recording simultaneously is a complicated process due to the feed forward effects of stimulating with a signal that is magnitudes higher than those being detected [13, 150]. Stimulating a neural signal requires many of the considerations that recording does. Tip geometry will also have a great effect on the ability to stimulate targeted neurons due in both the charge delivery and the area that this charge will be delivered over [16]. Therefore, the stimulation of neurons depends specifically on the tip geometry and electrochemical properties of the electrode, including the impedance of the electrode interface and its charge injection capacity [151]. The charge injection capacity required for electrodes and any faradaic changes caused by stimulating electrodes are material specific [135].

charge
but
in
to

1.3.5 Neurochemical Sensing

Another form of neural signal detection in tissue is neurotransmitter detection. These work by detecting a change in the presence of neurotransmitters above basal levels, indicating a wide variety of neural signalling. Current techniques measure dopamine levels using a serum technique, where fluid is extracted via micro-dialysis and tested for the presence of dopamine [152-154]. This is slow and laborious and requires large probes that cause much damage upon insertion. These measurements provide a very limited snapshot view of the overall dopamine pathways and lack any real spatial resolution. New methods are being developed that use the electrical detection of neurotransmitters *in vivo* using microelectrodes. This is performed using Cyclic Voltammetry (CV), a common electrochemical measurement. In practise, the dopamine or acetylcholine of interest will be oxidised and reduced at the electrode surface. This produces a current that can be recorded. For neurotransmitter detection specifically, a variation of CV is used known as Fast Scan Cyclic Voltammetry (FSCV) [155-157]. This measures changes in Acetylcholine levels from the baseline levels as a method to detect neural activity. This provides an avenue to explore a greater number of biological processes occurring in the neural tissue. However, due to the background subtraction methods being used, only changes in dopamine can be detected. An emerging technique known as MCSWV is also being developed to measure tonic or baseline levels [158]. The expansion of these techniques to neural recording devices is an idea that is currently being explored in particular for carbon fibers [104]. This highlights the broad avenues for electrodes to interact with the brain and hence the work that still needs to be done to create neural devices.

1.4 Neural Implant Improvement

1.4.1 Methods for Array Optimization

Electrode array optimization may be achieved in several ways. This includes simply increasing the number of recording sites or by increasing the number of implants in the network to increase spatial frequency. However, care must be taken when considering avenues for improvement as opportunity costs may be associated with certain improvements. For instance, increasing the number of recording electrodes may increase the spatial frequency however this has also been shown to increase the tissue damage upon insertion [25]. Array optimization must therefore be carefully considered for any unwanted effects when aiming to improve upon current designs.

1.4.2 Material Selection

Material selection is a major avenue for improvement of recording devices. Improved insulating coatings are beneficial for implantable devices as this will both increase the longevity of implants as well as potentially improve electrical characteristics. This has been done in many devices already utilizing silicon and Parylene-C (Figure 1.14) [62, 159]. Combining coatings also enables different coating characteristics to be achieved as well as providing an avenue for the alteration of the recording sites that may not be producible with only one insulating material [160]. Again, the complications of increasing insulation thickness need to be considered, as increasing the thickness of coating and the utilization of different materials will impact the implants stiffness, potentially increasing tissue damage upon implantation.

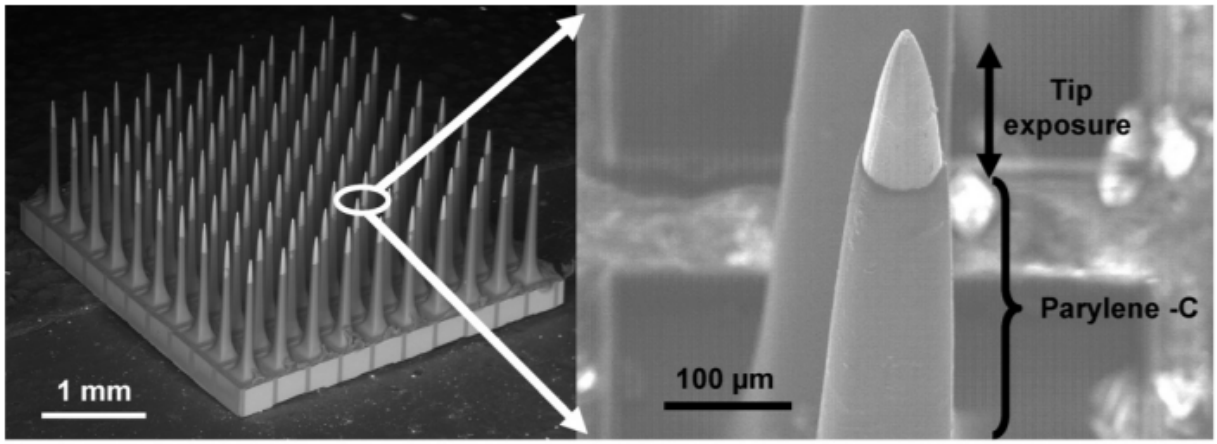

Figure 1.14: Scanning electron microscope image on a Utah Array modified with Parylene-C [159].

Carbon fiber electrodes are a prime example of replacing current technology with materials more conducive to chronic neural recordings. This material is further improved using insulating coatings and conductive polymers for single unit recordings [88-91, 128]. Alternative electrode coatings include the use of Ultra-Nano Crystalline Diamond (UNCD) coatings [92]. This improves the electrochemical characteristics of the device, especially for neural stimulation. Metal coatings such as platinum have also been explored for similar reasons [161]. These highlight a direct avenue for improvement of an already promising electrode material.

1.4.3 Electrode Geometry Optimization

Altering array or electrode geometry is another potential route for increasing device viability. This has been demonstrated in the Neuronexus devices wherein they provide both shank and 'Utah-like' options. The benefits and drawbacks of each can be assessed to ensure the appropriate design is used for a specific purpose. The Utah like geometry will increase spatial coverage over potentially different areas of the brain whereas shank electrodes are better able to record from single cortical columns of neurons or sample different depths of neural tissue more efficiently. This geometry can be further tailored for specific recordings that are required as geometry will dictate the locations in the tissue that can be reached. This indicates that an electrode array design that can be easily manipulated for different purposes could be more advantageous due to increased utility. Geometry constraints are also still limited by material as the mechanical properties of different materials will impact on the length of electrodes inserted as well as other fabrication concerns [162, 163].

Electrode tip geometry can also be optimized to aid in insertion of the electrode and improve electrode performance. Carbon fiber micro electrode tips have seen improvements for inserting longer fiber lengths using laser deinsulation and fire sharpening methods [42, 164, 165]. These methods have shown mixed results with fire sharpening having difficulty to constrain tip geometries due to the size scale of the electrode tips. It does, however, show an increase in insertion success for longer electrodes which is the major drawback of using flexible neural probes. Current laser deinsulation methods have only been developed for single electrode devices and are not proven for 'Utah-like' arrays. Despite this, the technique demonstrates the creativity that can be used for improving current devices and materials for the optimal neural interfacing device.

1.4.4 Electrode Treatment Options

Surface treatment options allow for improvement on electrode characteristics whilst potentially not impacting the size, shape, or manufacture procedure of the devices. Simple treatment options include the use of plasma etching to improve on the electrochemical characteristics of implants [166, 167]. Oxygen plasma modifies the surface morphology of many common insulating polymer materials, including Parylene, for another avenue of device modification [168-170]. Exploring a variety of surface treatment options could be a fruitful endeavour in the improvement of commonly utilized neural interfacing devices.

1.4.5 Device Hermiticity

Hermiticity is an important characteristic when considering devices for chronic implantation. Hermiticity refers to an implant's resistance to leakage, especially to water [171]. This is either through a porous material or through joints or interfaces between different material, like those that are realistically used when creating a complex device. Leakage is particularly important for devices implanted within the body, as this can stop the leaking of potentially toxic materials housed within the implant into the surrounding tissue as well as inhibiting the leakage of fluid that could compromise the electrical performance of a device [172]. As such, hermiticity is a vital safety concern when considering an implant or electrode material. Many developing implants have focused on substrates and materials that are conducive with producing minimal leakage [173-176]. Conventionally, leak testers are used to test hermeticity. This involves a gas passing through a sample with a corresponding to show whether or not and in what quantity any of the gas is able to pass through [177].This gas is generally Helium due to its lower molecular size compared to water and chemical inertness. The subsequent water leak rate can be calculated from these values [178]. The hermiticity value will inform how long a device may be potentially implanted. Materials that can show high levels of hermeticity will be a strong determinant for creating a more effective chronic neural implant. Demonstrating hermiticity in a implant will therefore be vital in improving on current array designs that are unable to be chronically implanted.

? missing word?

Chapter 2: General Materials and Methods

2.1 Chapter Outline

This chapter will outline the general materials and processes that were used in the fabrication and characterization of the electrodes and implants developed in this thesis. This chapter will cover the processes involved in the creation of the diamond substrate that houses the multiple carbon fiber electrodes in the array configuration. This includes the creation of electrical connections ensuring isolation between channels. The electrochemical methods used to characterize these electrodes will be outlined. These include different variations of CVs and EIS. This chapter will also explain the processes involved in the creation and characterization of CVD growth of Boron Doped Diamond on the surface of carbon fibers, including electrochemical, optical, and imaging processes to confirm the morphology of the coatings and their applications.

2.2 Materials

2.2.1 Carbon Fiber

The carbon fibers used in this thesis are 7 µm diameter polyacrylonitrile (PAN) based fibers purchased from Goodfellow. These fibers have a tensile modulus of 230 GPa and a tensile strength of 1.4 MPa. The volume resistivity of the fibers is 900 ~~Ohm~~ cm^{-1}.

(use Omega symbol)

2.2.2 PCD Diamond

The Polycrystalline-Diamond (PCD) substrates used in this work were 10mm by 10mm plates of 0.3mm and 0.5mm thicknesses. These were single sided polished thermal grade (TM100) polycrystalline CVD diamond (PCD) sourced from Element six Ltd, UK. TM100 PCD is electrically insulating and possesses thermal and mechanical properties to withstand many of the proposed manufacturing processes.

2.2.3 AU Braze

Gold Active Braze Alloy (Au-ABA) paste (96.4%Au, 3%Ni and 0.6%Ti) purchased from Morgan Advanced Materials was used to create electrical connections in features fabricated in the insulating PCD. This material has been proven to be biocompatible and suitable for use in combination with a PCD substrate [87].

2.2.4 Parylene-C

Parylene-C Dimer was purchased from Special Coating Systems (SCS). This material is electrically insulating and also presents high levels of flexibility without delamination. The system used to apply uniform coatings throughout this work is a PDS 2010 (SCS, Specialty Coating Systems). Samples ~~can be~~ were loaded into the chamber for uniform coating on all surfaces. Deposition thickness ~~is~~ was determined by the weight of Parylene C dimer used. The standard coating performed in this work was 4.0g of dimer and produced completely uniform coatings between 2.4 and 2.8 µm thick (as confirmed with optical profilometers ~~ad~~ and SEM).

2.2.5 PEDOT

Polyethylene-Dioxythyophene (PEDOT) is a conductive polymer that improves the electrochemical properties of a sample by improving its effective surface area. This material can be applied electrochemically to an electrode surface using electrochemical methods to ensure application to the working site of an electrode. It has been shown to improve the ability of carbon fibers for neural interfacing [100, 179]. The PEDOT used was acquired from Sigma Aldrich and was doped with Poly-Styrene Sulfonate (PSS).

2.3 Fabrication Processes

2.3.1 Laser Milling

Various laser machining techniques exist as a subtractive method to create features or cuts in materials. This technique allows for the surface modification of samples as well as machining holes, trenches and other features that are not possible with alternative techniques. Lasers used on the surface of diamond can ablate the bulk diamond away, leaving an electrically conductive graphitic layer on the surface of milled features. A 2.5W Nd:YAG, 532 nm wavelength, nanosecond pulsed laser micromachining system (Oxford Laser) was used to mill predesigned electrical circuits and through-holes in diamond substrates. The inbuilt stage used is capable of movements with 0.0001mm precision. The spot size of the laser was able to cut features as small as 5 µm on the diamond surface. These parameters allow for the creation of through-holes, wire tracks and electrical pads with micrometre precision.

2.3.2 Furnace Brazing

Brazing is a process wherein high temperatures are used to set metal pastes within cavities in a substrate. This can establish electrical connections between filled features and create hermetic seals. A MTI brazing furnace (GSL-1500X-OTF) was used to braze an Au-ABA paste (Refer to 2.2.3) into features that were previously milled into a PCD substrates using a laser. For the gold to adequately wet the diamond surface and optimally fill the features, an intermetallic sputtering layer is required. This was conducted by sputtering 200nm of both Molybdenum and Niobium (in that order) using an Intlvac Nanochrome AC/DC Sputter System. The diamond samples are loaded within a 50mm diameter quartz tube on a graphite holder. The furnace temperature was ramped slowly according to a previously described recipe to a maximum temperature of 1100 degrees Celsius for a period of 30 minutes [180].

2.3.3 Polishing

A result of the brazing process is the presence of excess braze that accumulates and protrudes above the features of interest. A Coborn PL3 rotary or Buhler polisher was used to remove excess braze, by mechanically removing gold that is not confined within the machined features on the PCD. Silica carbide abrasive papers (Gemworld) with grits ranging from 400, 800 and 1200 were used sequentially in this order. The lower grit was used to remove majority of the bulk braze and lower grits were used for more controlled removal to limit the amount of excess gold removed from within the features of interest.

2.3.4 Acid Boiling

In order to restore the insulating surface of the diamond after processing, graphite was removed from the diamond surfaces using an established acid boiling technique [181]. 3mL of 1M H_2SO_4 (Sulfuric Acid) and 300mg of $NaNO_3$ (Sodium Nitrate) mixture boiled over a hot plate for varied times between 10 to 30 minutes. Samples were sequentially rinsed in Acetone, Isopropanol and DI water for 5 minutes each.

2.3.5 Oxygen Plasma

Controlled ion bombardment of a surface using a plasma cleaner allows for surface modification of samples and films. Parylene C has been shown to become hydrophilic, improve adherence to neuronal cells and exhibit enhanced biocompatibility, when treated with an oxygen plasma [168, 182-184]. In this work a Zepto M2 plasma cleaner from Diener Electronics using a gas mixture of 90% Oxygen and 10% Argon was used. This produced plasma for the alteration of the Parylene C surface of electrodes and implants using a power of 40 mW and a pressure of 0.7 Torr for periods of up to 3 minutes. Cleaned samples were optically tested for carbon fiber degradation and a contact angle measurement confirmed hydrophilicity.

2.3.6 Parylene-C CVD Deposition

Parylene-C was applied to all samples using a PDS 2010 LABCOTER™ 2 Parylene Deposition System (Parcoater). Using 4.00g of the Parylene-C dimer at a furnace temperature of 690 degrees Celsius and a vaporizer temperature of 175 degrees Celsius. This is done at a pressure of 15 mBar to maximize the uniformity of the coating. The coatings produced were between 2.3 and 2.9 µm as confirmed by optical profilometer and SEM.

2.3.7 Pretreatment of Carbon Fiber for UNCD Growth

To allow for optimal CVD growth on the surface of the carbon fibers, pretreatment steps are required. The first step is the addition of amino phenyl groups to the carbon fiber surface using an electrochemical method [87]. The 3-electrode electrochemical cell (Explained further in 2.4.3) was set up using a Gamry Potentiostat (Interface 1000E). An Ag/AgCl and a Glassy Carbon electrode were used as the reference and counter electrodes, respectively. Two separate solutions were used for these processes. Firstly, an acetonitrile solution containing 0.1 M of tetrabutylammonium tetrafluoroborate (purchased from Sigma) and 1mM nitrophenyl diazonium tetrafluoroborate (purchased from Sigma) was used. Five cycles were performed between 0.2 and -0.6 V at a scan rate of 200 mV/s were performed to form a nitrophenyl film at the carbon fiber surface [185]. Samples were rinsed with acetone and DI water. The second solution used was 0.1M H_2SO_4. Five cycles were performed again with voltages between 0.5 V and -1.5 V at the same scan rate of 200 mV/s. This left aminophenol groups at the surface of the carbon fiber. The samples were rinsed sequentially again in acetone and DI water.

2.3.8 Diamond Nano-seeding of Carbon Fiber

The aminophenol groups added to the carbon fiber surface allow for the adhesion of seeded nanodiamonds for CVD growth. The nanodiamond solution is described elsewhere and was prepared by a collaborator [186]. The solution contained a concentration of 8.47 x 10^7 particles/ml with an average particle size of 35-40 nm [105]. The pretreated fibers were soaked in the Oxygen terminated nanodiamond

solution for 24 hours within 48 hours of CVD Growth. The fibers were rinsed with DI water and subsequently dried using nitrogen gas.

2.3.9 MWP-CVD Nanodiamond Growth

Microwave enhanced plasma chemical vapor deposition (MWP-CVD) is a technique for the growth of nanodiamond and other carbon containing films onto a sample. MWP-CVD can produce higher quality diamond films compared to alternative CVD methods [187]. The MWP-CVD creates attenuated plasma fields over the sample for the chemical growth of diamond and similar materials. Growth time, power, temperature, plasma attenuation and gas mixture dictate the properties and thickness of the coating. A gas mixture of H_2, CH_4 and Trimethyl boron (TMB) was used to create Boron Doped Diamond (BDD) and Carbon Nano-Walls (CNW). Samples were grown in different configurations with varying recipes that will be discussed in later chapters (Chapter 5 and 6).

Gas suppliers, purities?

2.3.10 Additive Manufacturing

Additive manufacturing (3-D Printing) involves the creation of 3-Dimensional structures from base materials typically done in layers. These layers are printed sequentially and bound to the layer below, to create bespoke parts that have been designed using computer software (Solidworks). This technique allows for rapid fabrication of designs for more efficient prototyping. Common materials used in this form of manufacturing are polymers and some metals. Polymers can be either in the form of melted and extruded plastics or UV-curable liquid resins. Metallic materials (such as Titanium) can be welded together from a powder bed to create configurations or geometries that are difficult to achieve for these materials using conventional methods. This technique allows for easier prototyping, as single part manufacturing is relatively quick and easy compared to common forms of manufacturing or machining. In this work, many bespoke holders and jigs are created to increase the ease of handling and transporting samples, improve the performance and reliability of measurements as well as creating holders for novel fabrication techniques. The two 3-D printers used in this work were the Anycubic photon mono 4k for UV-curable micron scale prints (25μm resolution) and the SLM Solutions 250HL system for titanium printing of holders for Chemical Vapor Deposition applications. Unless stated otherwise, 3D-printed holders and parts were made from Anycubic High Clear Resin.

2.4 Electrical Characterisation Techniques

2.4.1 Electrochemical Cell

Cyclic Voltammetry (CV) and Electrode Impedance Spectroscopy (EIS) are used to establish the electrochemical properties of electrodes and materials [188, 189]. These were performed on fabricated electrodes using electrochemical cells in solutions. This cell consists of three electrodes: the working, the counter, and the reference. The reference electrode has a well-defined potential and is used as a measurement to reference and hence measure the potential of the working electrode (the electrode of interest). The counter electrode is used to complete the circuit for reactions to take place (between the working and counter electrode). The three-electrode cell is connected in a solution to a Potentiostat that applies a voltage to the working electrode and the circuit is closed at the counter electrode. The three electrode cells used for EIS and CV were performed with a Gamry Potentiostat (Interface 1000E). An Ag/AgCl reference electrode and a Glassy Carbon counter electrode were used as standard in these processes.

2.4.2 Electrode Impedance Spectroscopy (EIS)

Electrode Impedance Spectroscopy (EIS) is an electrochemical process that measures the charge transfer resistance between the interface of an electrode and solution [190]. This measurement can estimate important characteristics including Impedance and Double Layer Capacitance (C_{dl}). Impedance measures the resistance to electrical current in a material at different frequencies. Many neural electrodes simply state the Impedance at 1 kHz as a means of comparison between electrodes due to the good signal to noise ratio at this frequency as well as it correlating to the 1ms base width of an action potential [127]. Impedance values are also visualized using Bode and Nyquist Plots to display the resistance (ohms) or phase (degrees) at specific frequencies (Hz). The C_{dl} is an indication of the ability of the surface of the electrode to store charge. The capacitance is determined from the EIS using equivalent circuit models fitted to the Nyquists plots. These circuit models represent common electrical circuit elements including resistors, capacitors, and inductors to represent the equivalent circuit for the material properties. The C_{dl} of an electrode will impact its capability as a neural electrode as this will directly impact the ability of the electrode to withstand voltage potentials during stimulation or other neuromodulation techniques. For neural electrodes much of the electrochemical properties are dominated by the surface characteristics of the materials and hence why electrochemical methods are important to characterize such devices. EIS performed in this work uses the electrochemical cell described with a 0.1M NaCl solution.

(italic C)

2.4.3 Cyclic Voltammetry (CV)

CV is a technique where an applied voltage is cycled and the corresponding current is measured by the system [189]. CV primarily measures the capacitive charging of the working electrode in the system. It may also measure REDOX processes wherein one species gains electrons (cathode) and the other loses electrons (anode). This allows for characterization and alteration of an electrode surface. The important characteristics that relate specifically to electrodes are the capacitance, water window and charge transfer mechanics [191]. The water window describes the range of voltage between the reduction potential (cathodic limit) and the oxidation potential (anodic limit) of water molecules at the electrode surface [192]. This is considered the safe limit for stimulating electrodes and limits the voltage range for characterization purposes without degrading the electrode or producing toxic species within the solution.

CV can be used to add material to an electrode surface or remove it using REDOX processes. A relevant example is the activation of carbon fiber electrodes through cycling the electrodes through voltage ranges outside of the electrodes water window [193]. This oxidises the surface, making the electrode rough and increasing the external area of the electrode surface and adding oxygen containing functionalities to the surface. This increases the capacitance and reduces the impedance of the electrode. This was conducted using a voltage range of -2.5 to 2.5 volts for 5 cycles at a scan rate of 100 mV/s in a 0.1M NaCl solution. An additive CV process for carbon fibers includes the use of conductive polymers such as PEDOT. In this example the PEDOT solution (Refer to 2.2.5) is deposited at the carbon fiber cathode to improve electrochemical properties. A potential of -0.5 V to 0.9 V for 15 cycles at a scan rate at 100 mV/s was used for deposition. All electrodes used in CV were rinsed with DI water as a final preparation step.

2.4.4 Fast Scan Cyclic Voltammetry (FSCV)

As the name suggests, Fast Scan Cyclic Voltammetry uses a traditional CV method but at a much faster scan rate. The increase in scan rate allows for higher sensitivity for detection of REDOX active analytes in

solution. Current amplitude scales with scan rate, so the signal peaks can be observed over the large background current as well as a drastic increase in temporal resolution. The higher scan rate leads to a much larger background current (the capacitive charging at the electrode interface). Background currents form as the ions gather around the electrode as the potential is applied and is therefore proportional to surface area. This limits the materials available for FSCV as the surface area and capacitance of the electrodes must be within the limits suitable for this technique. In order to detect these small oxidative peaks, the background needs to be removed from the signal. This process of background subtraction allows for higher sensitivity measurements, although means that the technique can only be used to detect changes in concentrations over time [194]. For these reasons, FSCV is a useful tool for the detection of neurotransmitters, such as dopamine and serotonin [179, 195]. The sensitivity of traditional CV is not appropriate for the concentrations of these neurotransmitters found *in vivo*. The dopamine oxidation peak detected will increase linearly with scan rate [196]. FSCV for dopamine detection commonly uses a voltage range of -0.4 to 1.3 V at a scan rate of 400 V/s. These parameters have shown the highest effective sensitivity. Carbon fiber, specifically, has been shown to adsorb many neurochemicals, and also possesses the material characteristics conductive for FSCV [197].

To establish the dopamine detection capabilities of the electrodes, a Pinnacle FSCV system was used. A Ag/AgCl reference electrode was connected to a 3D-printed flow cell. 0.1M PBS was flown through the cell at a rate of 0.1mL/s to record the background current. The optimal parameters of a voltage range of -0.4 to 1.3 V at a scan rate of 400 V/s were used for each measurement. The active measurement was conducted by pumping through a known concentration of Dopamine in PBS solution during a cycle and the current peak of the oxidation was recorded. Successive background cycles were conducted between measurements to ensure complete removal of dopamine from the flow cell chamber as well as the electrode surface. The sensitivity measured for each electrode was normalized to the surface area of the active portion of the electrode.

2.5 Characterisation Techniques

2.5.1 Scanning Electron Microscopy (SEM)

A very common technique to observe the surface morphology of a sample is Scanning Electron Microscopy. This technique uses an electron beam generated from a filament (typically Tungsten) that is scanned along a sample. A detector measures the reflected electrons from the sample to generate a grayscale image with nanometre resolution. SEM images obtained in this work used a FEI Quanta SEM. The accelerating voltage and spot size of these images were attenuated for the specific materials imaged ranging from 10kV-30kV and 3.0-5.0 nm respectively.

2.5.2 Transmission Electron Spectroscopy (TEM)

Like SEM, Transmission Electron Spectroscopy (TEM) uses an electron beam to generate nanometre resolution images. This time the electrons that are measured travel through the sample to produce an image on the detector underneath to provide more information of the bulk material of thin samples [198]. The TEM used in this work to assess cross sections of nanometre thick prepared samples was the JEOL 1010 TEM.

2.5.3 Focused Ion Beam (FIB)

Focused Ion Beam (FIB) is a technique using a similar electron filament method to other imaging techniques that is able to remove material from a sample using a targeted ion beam (typically from a Gallium filament) [199]. This technique can be controlled using masks and fine control of the beam to alter the morphology of a sample on a nano scale. This was used to create cross sections and tunnel through sections of materials to help characterize the interfaces and bulk properties of materials in this work. This was conducted using a FEI Scios FIB SEM.

2.5.4 Energy-Dispersive X-Ray Spectroscopy (EDS)

Energy-Dispersive X-Ray Spectroscopy (EDS) is a technique used to characterize the elemental composition of a sample surface [200]. This collects secondary electrons produced from other imaging processes to produce mapped location of elements within a sample. This was used to show the elemental composition of samples before and after treatments as well as those machined using FIB. The EDS used was the FEI Quanta SEM QFEG.

2.5.5 Optical Profilometer

The optical profilometer used was the Bruker ContourGT. The optical profiler was used to measure parylene deposition thickness, depth of milled features in diamond substrates and the amount of gold braze removed from within features of machined samples.

2.5.6 Raman Spectroscopy

Raman Spectroscopy is a technique that can characterize the bonding structure of a material. This is commonly used in carbon-based characterization by showing the proportion of diamond like bonding (sp^3) and graphitic like bonding (sp^2) in CVD grown films. These are represented by the height and position of the D peak (1350 cm^{-1}) and G peaks (1580 cm^{-1}) respectively. A Renshaw InVia Raman 532nm was used to characterize carbon-based CVD grown films on carbon fibers.

see comments

2.5.7 Hermeticity Helium Leak Tester

The hermeticity validation used in this work was performed using an Adixen ASM310 helium leak detector with a detection limit of 10^{-11} mbar Ls^{-1}. The samples for testing were sandwiched between O-rings and clamped together so that the only leak path available was through the sample to the detector. The system was tested for leaks between O-rings and the surrounding welds before each test to ensure no unwanted leaking occurred during tests. The presence of helium could be used to establish the leak rate of the sample and indicate the potential dew point, predicting the appropriateness of samples for chronic implantation.

Chapter 3: Fabrication and optimization of a carbon-based neural array for recording

3.1 Chapter Outline

This chapter will outline the fabrication techniques used in the development of the carbon fiber array housed within a PCD substrate. This includes all fabrication processes starting from the PCD diamond plates through to the fully electrically connected neural device. The success and limitations of the processing steps and the specific materials used will also be explored. This will cover characterising the performance of the electrodes both physically and electrochemically.

3.1.1 Chapter Acknowledgements

Some work in this chapter was collaborative. The development of the PEDOT coatings and electrical connections were performed with Dr Sorel De Leon Vergara (RMIT University). Dr Vergara was involved in the design of the PCBs used for the electrical connection of the devices. Some of the electrical validation and some of the imaging performed was also performed either alongside or by Dr Vergara. All other work completed in this chapter was conducted by me.

3.2 Introduction

To leverage the potential benefits of carbon fibers for chronic neural interfacing, many considerations have to be made in order to create a device that is practical to implant long term into neural tissue. The device must be biocompatible, manufacturable and be able to be inserted into the target tissue without damage. This renders material selection vitally important at all stages of development. A suitable substrate that can house the carbon fibers and be electrically connected to an external system for signal analysis is the first primary challenge. Groups have explored the use of simple printed circuit boards (PCBs) or silicon as a substrate for carbon fiber arrays [45, 94]. These arrays however were limited chronically due to material selections and the associated fabrication constraints (e.g. sizes and biocompatibility). The geometries of the Patel et al. device [45] also limited the spatial resolution of the device. These experiments did however highlight the potential of a high-density carbon fiber microelectrode array by producing consistent signals over the life of the electrodes. This demonstrates a requirement for future development and exploration into finding suitable materials and fabrication methods to design a chronically implantable, high density neural implant.

3.2.1 Substrate Selection

The creation of an array of carbon fibers that can interface with a clinically significant number of neurons chronically still presents a monumental challenge. The array must be able to electrically address each individual carbon fiber electrode, house them securely to ensure chronic performance whilst also orientating the fibers for insertion into neural tissue. All of these challenges must be met whilst using biocompatible materials and techniques. Substrate selection for the implant is therefore an important decision. Silicon or ceramic substrates have been explored for similar potential devices however their processing has proven difficult and currently no implants have continued to perform well long term [45, 94, 173]. Flexible arrays made of polymers such as Parylene, although promising for chronic implantation presents several added difficulties for insertion, handling, and fabrication [201-203]. A potentially viable

alternative substrate material is diamond. Diamond is mechanically robust, electrically insulating, biocompatible and able to withstand a wide array of manufacturing processes [204-206].

3.2.2 Electrical Addressing Strategy

Potential routes for providing electrical connections to the carbon fibers include lithography or brazing [207, 208]. Producing a stable, biocompatible connection is challenging. Brazing is a promising option as it has the potential to both fix the carbon fibers in place whilst achieving an electrical connection. This will also create hermetic seals in the feedthrough holes as gold has already been shown to do so when used in conjunction with diamond [175]. Previous work has already demonstrated the ability to braze gold into laser milled features on the diamond surface, meaning it is possible to construct electrical circuitry alongside the brazed through holes [175, 209, 210]. These brazed features also enable for an external connection to be made to the array to provide continuity to an external recording system.

The second main concern is the connection of a lead wire from the electrical pads on the diamond circuit board external devices. Solder bumps could potentially be used on this scale; however, this requires specialised equipment and was deemed outside the scope of this work. Another option is the connection of wires and/or PCBs using solder or electrically conductive pastes to brazed electrical pads. These materials have biocompatibility concerns as solder and many conductive pastes are cytotoxic [211, 212]. However, these connections could be fully encapsulated with the diamond surface providing longevity for the implant. A final device would require a hermetic package in which to protect not only the circuitry within the device but also protect the implanted tissue from the leakage of potentially toxic materials.

3.2.3 Electrode Optimisation

The most important aspect of the device is the proposed carbon fiber electrodes. This includes the insulating layer down the length of the electrode and the electrically exposed interfacing tip. Commonly Parylene C has been used as an insulating layer for carbon fibers [45, 104, 213]. Parylene can be selectively removed to allow for a controllably exposed electrode tip. Due to the chemical inertness of Parylene the most appropriate deinsulation methods involve either flame or laser ablation. Laser deinsulation could allow for the cutting of the fibers to length as well. Due to the low micron scale dimensions of the arrays employing either of these methods is technically challenging. The development of novel or optimisation of existing techniques to control fiber length and create controlled tip exposure is therefore required.

3.3 Fabrication Methods

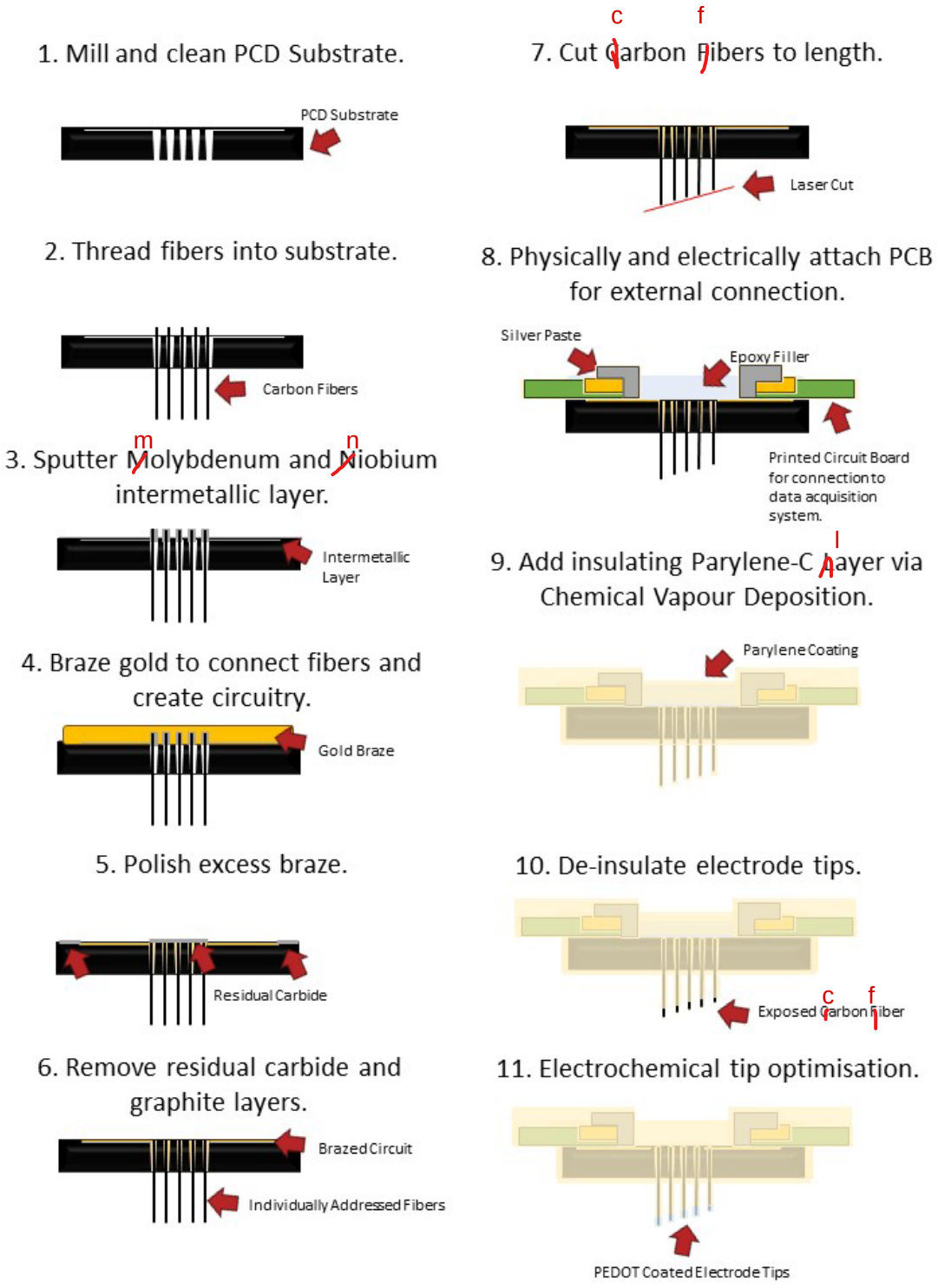

Figure 3.1. Process flow of entire device fabrication from milled PCD substrate through to fully functionalised device.

3.3.1 Array Fabrication

For the creation of the arrays 10mm by 10mm plates of 0.3mm thick single side polished TM100 polycrystalline CVD diamond (PCD) was sourced from Element six Ltd. These were machined using a 2.5W Nd:YAG, 532 nm wavelength, nanosecond pulsed laser micromachining system (Oxford Laser). The machining involved drilling of holes through the diamond for the fibers to be placed through, as well as circuit patterns on the rear of the sample to establish external electrical connections. The circuitry was also milled in various configurations, with the depths of pads and tracks being less than 30 µm.

The diamond substrates were cleaned using an acid boiling process (Refer to 2.3.4) for 30 minutes in a solution of $NaNO_2/H_2SO_4$. Once cleaned the arrays were placed within a 3D printed holder to ensure fibers and arrays remained intact for transport between subsequent processing steps (Figure 3.2). A bundle of carbon fibers (PAN-based, 7 µm diameter purchased from Goodfellow) were cut into 3mm lengths. These were teased out and manually threaded into each of the holes in the substrates. This allowed for 2mm to protrude through the underside of the diamond within the holder with some left above the substrate to help the fiber remain intact until fixed in place with the braze. Once all fibers were threaded, the samples in the holder were sputtered with a bilayer of 200nm Mo and 200nm Nb using an Intlvac Nanochrome AC/DC Sputter System to aid in the subsequent brazing processes [209]. Sputtering deposition thickness was verified using profilometer measurements on reference silicon samples.

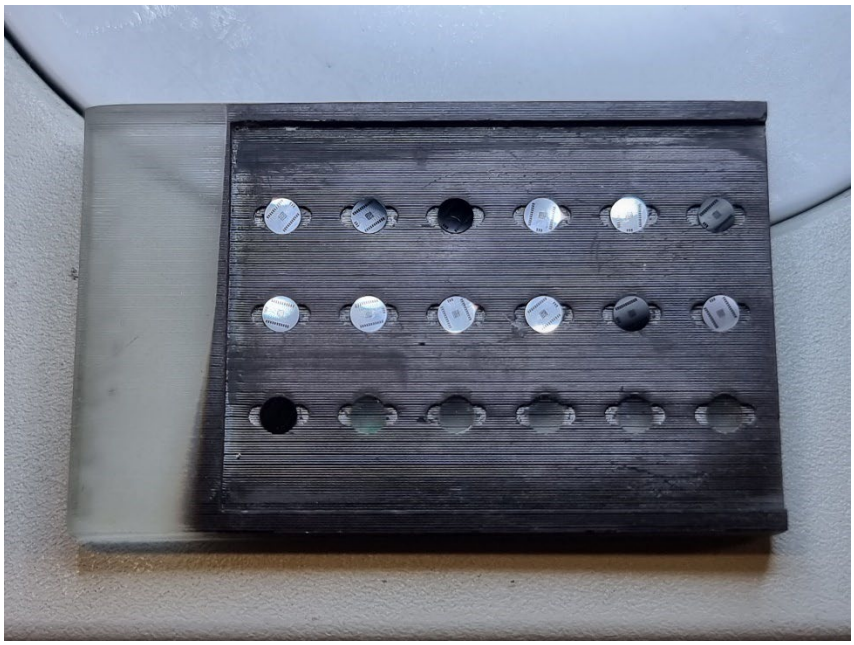

Figure 3.2: Milled PCD substrates in a 3D printed holder for positioning during Ni/Mo sputtering.

Once sputtered, the arrays were transported to a bespoke graphite holder for brazing. Gold Active Braze Alloy (Au-ABA) paste (96.4%Au, 3%Ni and 0.6%Ti) purchased from Morgan Advanced Materials was placed on the top side of the array using a probe, ensuring the paste was pressed into the patterned features whilst not disrupting the fibers placed in their holes (pressing on the fibers with the probe resulted in them being pushed through the other underside of the substrate and a reduction in yield). The braze paste binder was evaporated on a hotplate at 110°C for 15 minutes. The samples were brazed at 1100°C for 30 minutes with a ramp up time of 360 minutes and ramp down time of 600 minutes in a quartz tube under

a vacuum of better than 10^{-5} torr. The samples were inspected for retention rates of carbon fibers and to establish successful wetting of the braze on the diamond surface (Figure 3.3). The straightness of the fibers at this stage was also noted.

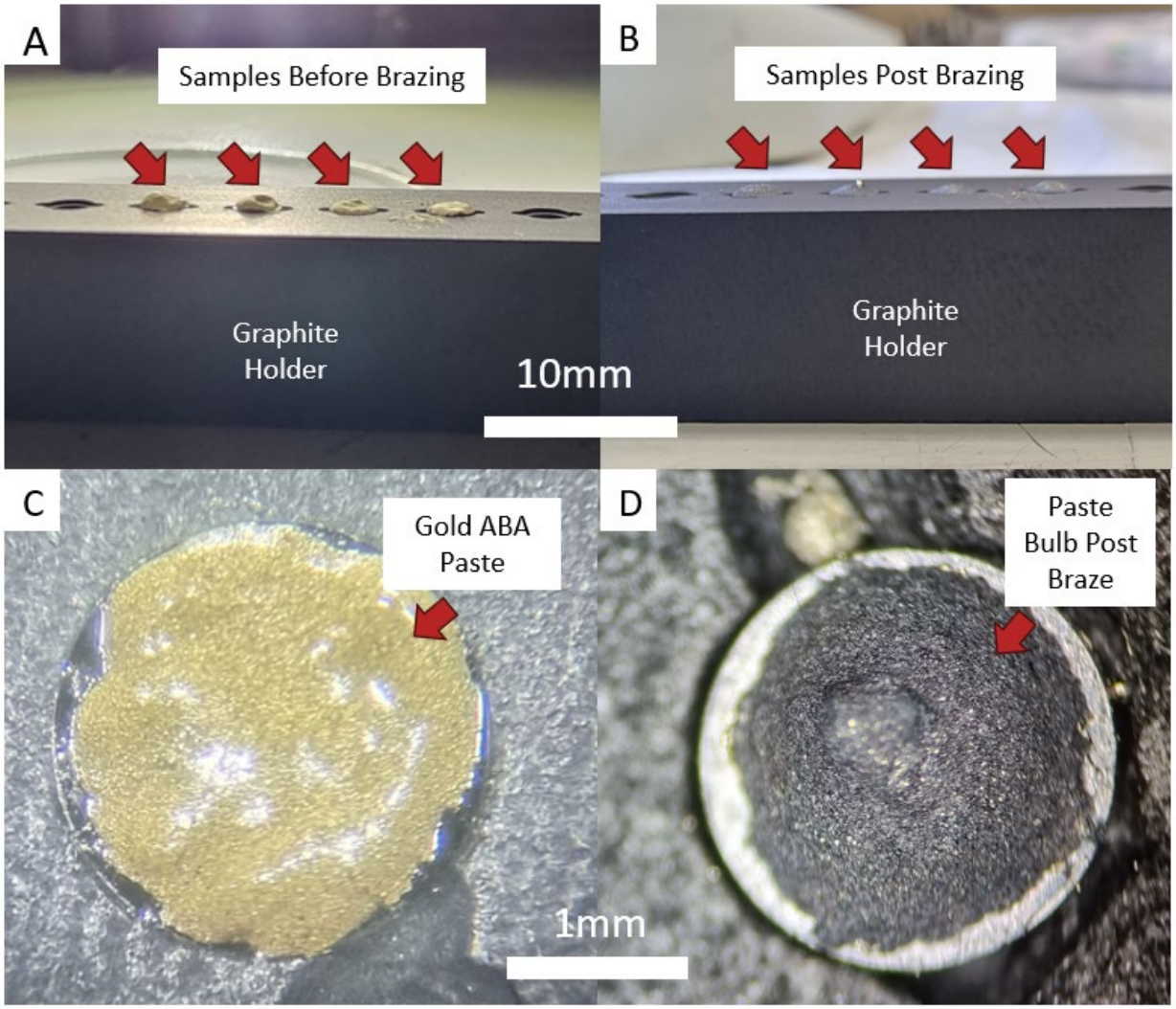

Figure 3.3. Diamond array contained in graphite holder after gold ABA paste application (A, C). and after subsequent brazing (B, D).

The samples were polished (Refer to 2.3.3) using a Bhueler or Coborn PL3 rotary polisher to remove the excess braze and to expose the patterned circuitry (Figure 3.4). The samples were placed into bespoke stainless steel polishing stubs to protect the fibers from the mechanical abrasion. These were secured by heating the stubs to 130 ~~degrees~~ °C and applying crystal bond to the edge of the diamond to be left to cool. To release the arrays the stubs were soaked in acetone until all crystal bond had dissolved.

The PCD diamond surface undergoes a phase transition at temperatures required for the brazing under vacuum wherein a nanometre scale thick layer of graphite forms creating an electrical short [214, 215]. To remove this an acid boiling method is used. A hot plate in a fume hood was heated to 260 ~~degrees~~ °C ~~Celsius~~. 300 +/- 30mg of $NaNO_3$ (Sodium Nitrate) was weighed out and added to a 100mL beaker. The

polished arrays were added (fibers side up) to the bottom of the beaker. 3mL of 1M H_2SO_4 (Sulfuric Acid) was pipetted into the beaker. A drop is ~~first~~ placed over each array first to ensure the arrays remain in place and ~~do~~ not sit on top of the solution surface (due to surface tension). The beaker was placed on the hot plate for 8 minutes, removed, and allowed to cool. Deionised (DI) water was pipetted slowly to ensure a safe dilution of the acid mixture. The solution ~~can~~ be poured out and further diluted until the solution has undergone a 100 times dilution. At this point the arrays were removed and placed in rinsing solutions of ~~A~~cetone, Isopropanol and DI water for 5 minutes each (in that order). Arrays were dried, and the number of fibers noted. A multimeter was used to confirm the removal of graphitic shorting on both sides of each array. If inner holes were large enough it was also possible to perform a preliminarily continuity measurement between the holes, tracks, and pad. SEM images were obtained to confirm the process did not degrade the carbon fiber electrodes (Figure 3.5).

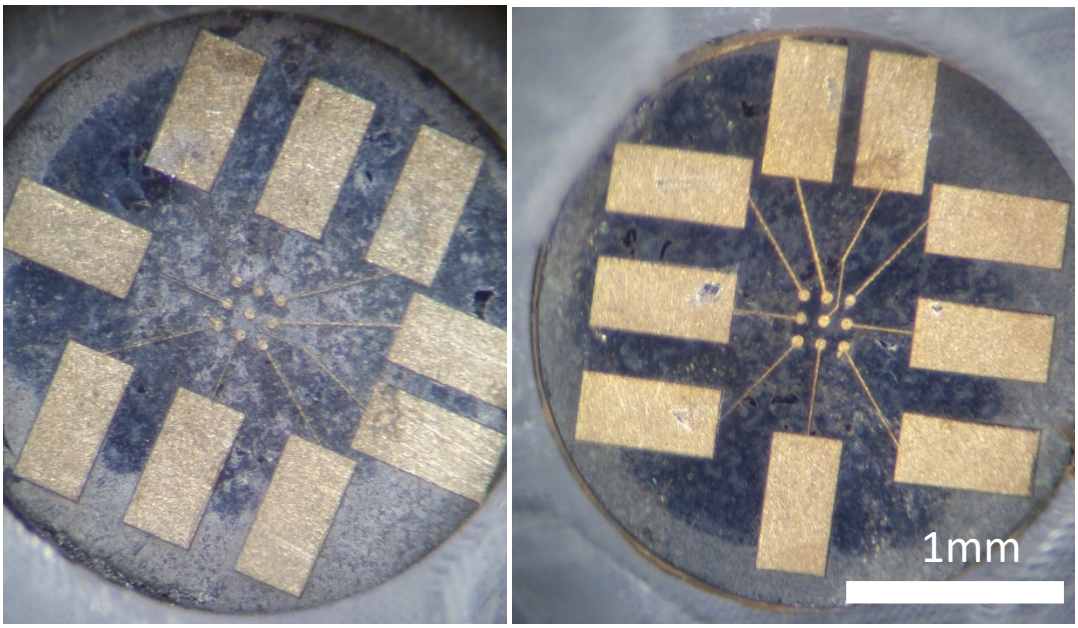

Figure 3.4: Gold brazed PCD substrate after polishing (Left) and after Acid Boiling (Right).

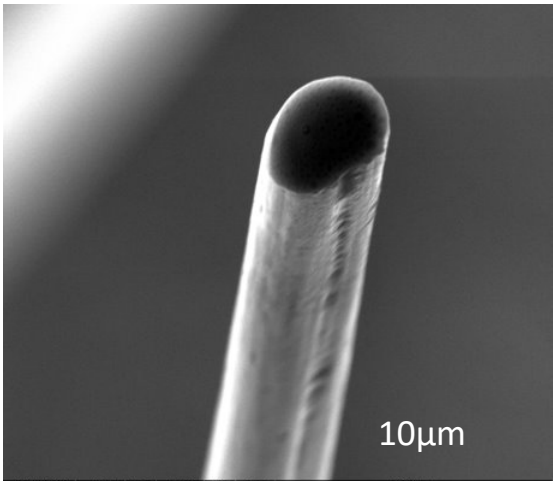

Figure 3.5: SEM image of carbon fiber post acid boiling showing no evidence of degradation.

process involved

The final fabrication cutting the electrodes to length (typically a 1mm to 1.5mm taper). The arrays were placed within a 3D printed holder to position the fibers perpendicular to the laser cutter system (Oxford laser). The fibers were orientated so that an entire row was in line to ensure each row was cut to the same length (Figure 3.6). Once the fibers were positioned the laser was focused onto the middle row of fibers. A double pass laser cut was used to cut every fiber in the array. Different fiber lengths or configurations were created by altering the laser path. The laser camera was used to verify a successful cut. If unsuccessful, subsequent runs at varying focus lengths could be used.

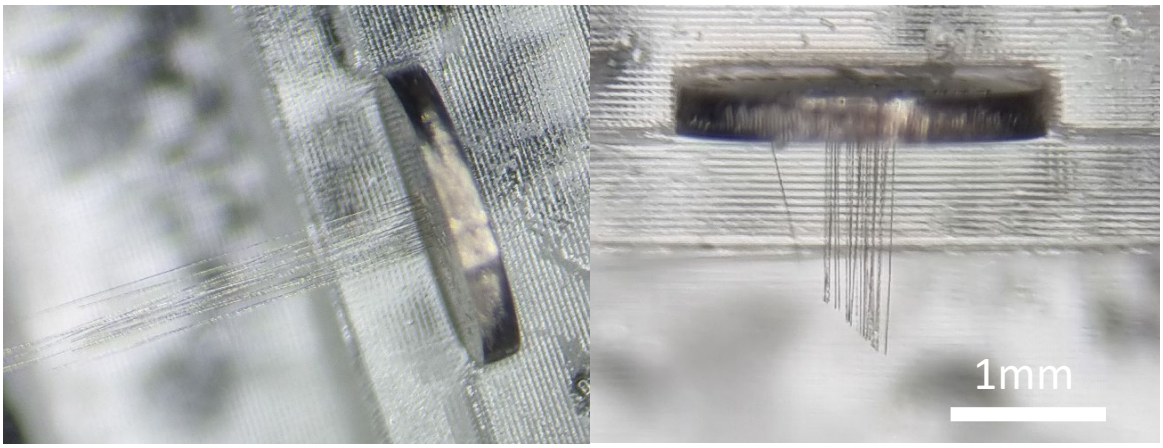

Figure 3.6: Processed carbon fiber array in 3D Printed holder with carbon fibers. Before (Left) and After (Right) fibers cut to length with laser.

3.3.2 Lead Wire Connection

To complete the lead wire connection to the carbon fibers, Printed Circuit Boards (PCBs) were used. These were connected to the larger gold pads on the periphery of the diamond substrates. Different versions of these (9,12 and 16 channel) PCBs were developed to allow for connection to different array configurations. Connections were made with silver paste (Sigma Aldrich) (Figure 3.7). A fine needle was used to apply silver paste to bridge the pads between the PCB and substrate. A 3D printed holder was used to aid in alignment. Once applied the paste was baked at 125 °C for 1 hour until solid. Once connected, a 2-part epoxy was used to reinforce the mechanical connection between the PCB and substrate whilst also providing encapsulation. This was performed in multiple stages to ensure complete encapsulation and to reduce the likelihood of the epoxy coating unwanted areas. The final application of epoxy involved securing a 3D printed holder to the back of the PCB to facilitate handling the completed device (Figure 3.7B). A completely connected 9 channel sample can be seen in Figure 3.8, showing the individual channel pins on the PCB to allow for connection to individual fibers.

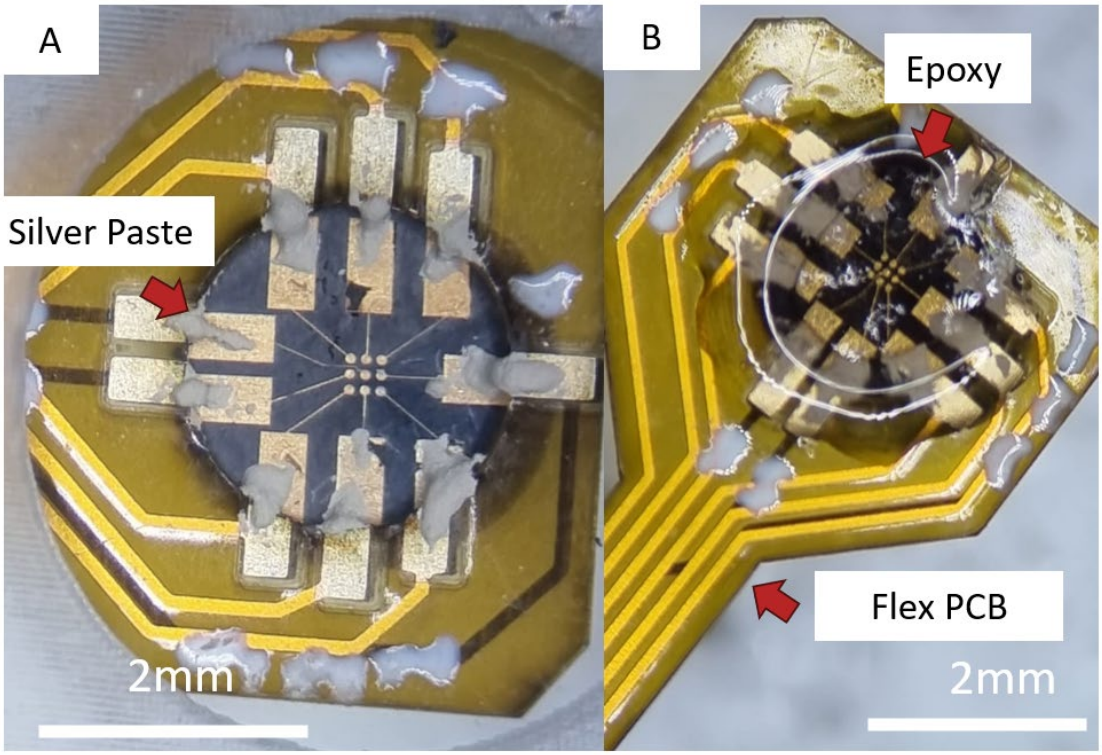

Figure 3.7. Silver paste provides an electrical connection from the gold brazed circuitry to the pads on the Flex PCB (A). A layer of insulating epoxy was applied to coat these connections as a first layer of isolation as well as to establish a rigid physical connection for device durability (B).

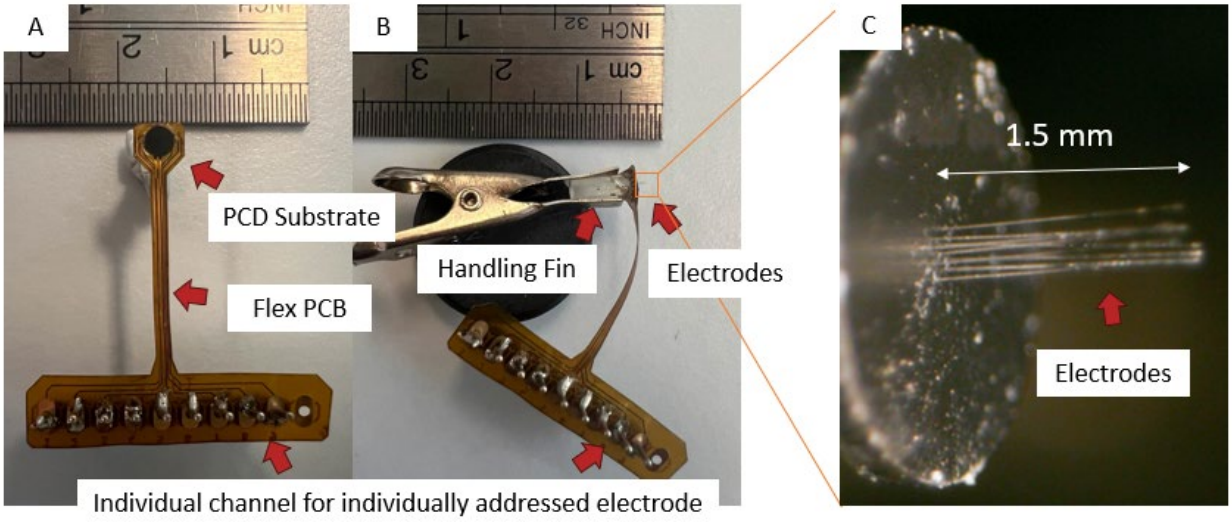

Figure 3.8. Entire construction of a flex PCB device. Showing the length of the device with the connector pins to allow for separate channels to individually address each electrode (A, B). Optical image of the attached Substrate with intact electrodes shown in C.

3.3.3 Electrode Tip Optimization

Samples were loaded into the parylene coater (PDS 2010 LABCOTER™ 2 Parylene Deposition System Parcoater) chamber on glass slides (Figure 3.9). The system was loaded with 4.00g of parylene dimer (Refer to 2.2.4) and activated to conformally coat the sample. Samples were removed from the chamber and optical profiling (Bruker ContourGT Optical Profilometer), using an exposed parylene edge on the glass slide, was used to verify the thickness of the deposition. Typically, 2 µm for 4 g of parylene dimer.

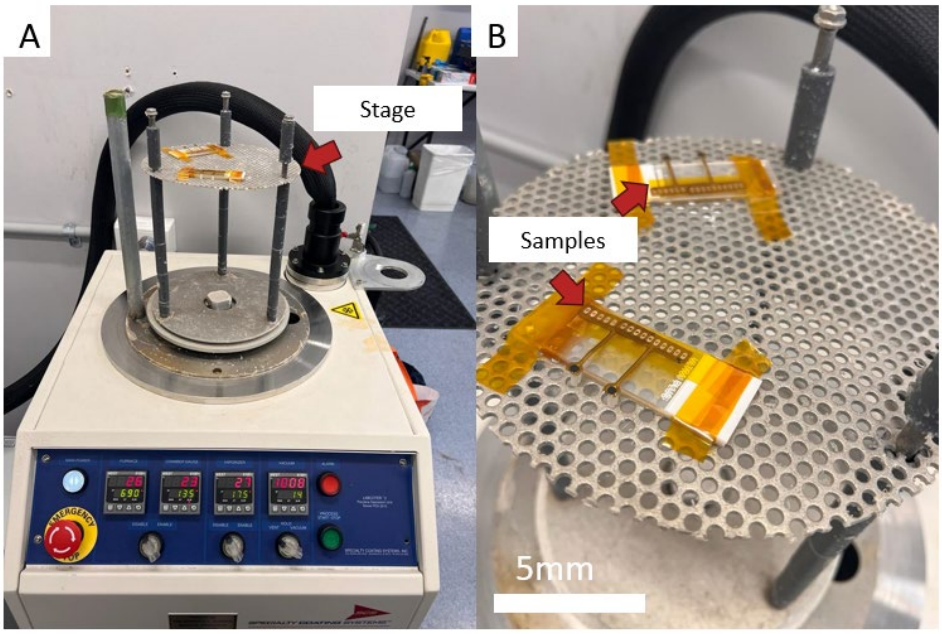

Figure 3.9. Configuration of the CVD coater stage for Parylene coating of Electrode Arrays.

If the parylene coating was deemed successful, electrode tip exposure was performed. To aid in this step, the hydrophilicity of the parylene coating was improved through an oxygen plasma treatment. The arrays were placed within the oxygen plasma cleaner chamber for 2 minutes at 45 mW power and 0.7 torr. This exhibited no bulk etching of the parylene or carbon fibers (verified by SEM). The samples were placed within a bath of DI water for deinsulation. DI water is added/removed so that only around 50 µm of the fibers protrude from the water surface. A camera with a macroscopic lens was used to visualise this exposure length. A butane torch flame was applied to the fiber tips for 1 second. An orange tinge can be seen on the fiber tips if this is performed successfully. The samples were rinsed in DI water and inspected under an optical microscope to confirm parylene removal. Exposure length and uniformity was characterised by SEM.

The impedance of the electrodes was determined using EIS (initial frequency of 500 kHz and a final frequency of 0.2 Hz with 10 points per decade) in 0.1M NaCl solution. The impedance at 1khz was noted and the electrodes rinsed with DI water. To reduce the impedance to levels conducive to neural recording, a coating of PEDOT was electrochemically added to the electrode tips. This was performed sequentially for each individual fiber using a CV electrochemical deposition method. 15 cycles between -0.5 to 0.9 V were performed using the Gamry Interface E1000 in a PEDOT: PSS (1:2) solution at a scan rate of 100 mVs^{-1} using a Ag/AgCl reference and a Glassy Carbon counter electrode. The EIS of the fibers is performed again to provide final impedances as well as confirm PEDOT deposition. SEM was also used to confirm PEDOT deposition and provide images of the arrays prior to implantation.

3.4 Array Fabrication Results and Discussion

A diamond substrate with carbon fibers held electrically and physically using gold braze was successfully created. Arrays were able to be created wherein the fibers were threaded through the substrate and remained in place through each of the processing steps. This included the connection to the PCB and complete electrode tip preparation. Most of the manufacturing challenges were overcome as multiple complete devices were constructed. Each step of the processing was characterized and tested to show effectiveness of the fabrication process whilst still highlighting any remaining limitations. This was particularly challenging as testing downstream issues was difficult as these were affected by any upstream processes.

3.4.1 Substrate Fabrication

Substrates were milled from PCD wherein holes of the magnitude of the carbon fibers were created and able to secure the carbon fibers in place for processing. An optimal array would have holes that protruded through the sample that are slightly larger than the carbon fibers themselves. This allows for them to be placed and held into position within the substrate. In practise this proves quite difficult as the spot size of the laser used is of the same order of magnitude as the carbon fibers themselves (5 µm and 7-8 µm respectively). To mill through the substrate the laser needs to mill in steps, changing focus deeper into the substrate after each cut. This refocuses the beam for efficient power transfer as the beam focus range is around 10 µm. The shape of the beam will result in deeper cuts creating a shadowing effect on the substrate above. This means laser power is transferred onto the surface around the hole and less is transferred to the milling region focused on the bottom of the hole. For this reason, cuts known as kerfs (passes immediately adjacent and parallel to the feature of interest) are used to widen a cut, allowing a higher proportion of the laser power to penetrate deeper into the region of interest. In practise, this means for the optimum 10 µm hole, a kerfed hole of 60 µm diameter is produce with this laser configuration (Figure 3.10). This creates a cone or triangular shaped hole. This is not inherently an issue as it may aid in the brazing of the gold into the features however this will affect how the fiber is secured in position and the orientation that it will be fixed in. This resulted in the fibers being not perfectly perpendicular to the substrate when they protrude through the underside (Figure 3.10C). The variance seen in fiber straightness did not adversely affect the utility of the final arrays as shown through the *in vivo* results explored in Chapter 4.

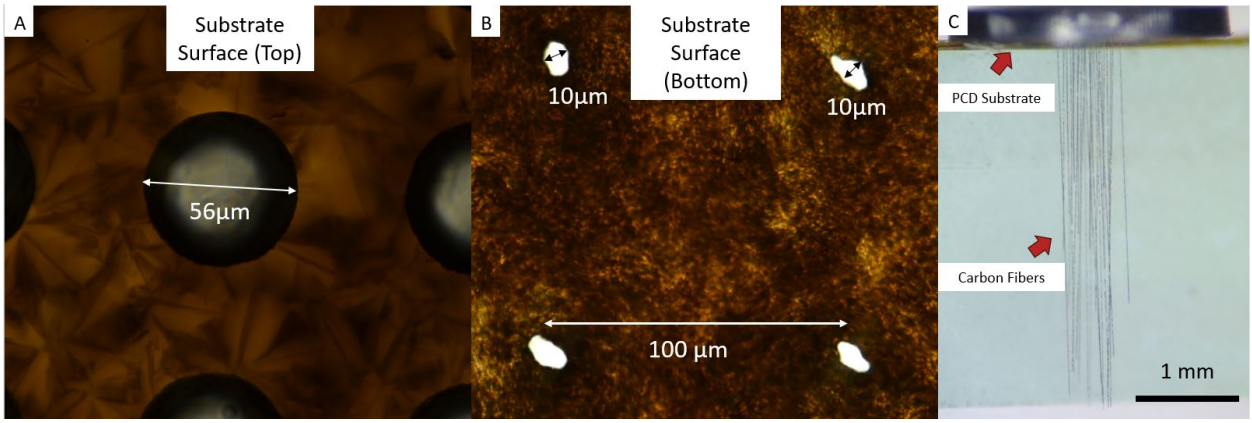

Figure 3.10. High magnification light microscope images of the top (A) and bottom side (B) of the PCD substrates after laser milling and acid boiling. The orientation of the fibers once threaded through the conical holes of the substrate (C).

The performance of the substrate and braze to mechanically hold the fibers was observed at the end of each of the processing steps. This was performed by counting the number of fibers still in place within the holes using a microscope over a batch of arrays (n=12). The yields were noted after fiber threading, gold brazing, polishing and the acid boiling steps. The average percentage yield of carbon fibers remaining intact upon completion of the steps are as follows; fibers threaded into holes 88.9%, fibers intact after brazing 91.9%, fibers in place after polishing 98.8% and fibers intact after acid boiling was 91.3%. This in isolation appears as a very promising result, however due to the cumulative effects this does have many downstream implications of the electrode yield on producing arrays with a meaningful number of electrodes. Of the 108 carbon fibers across the 12 arrays, only 79 remained in place upon the completion of these steps. This is further exacerbated when considering handling errors and other issues arise due to the size and delicacy of the fabrication steps. The cumulative effects of these fabrication and handling concerns will have a strong impact on the overall efficacy of this design. This can be seen in the *in vivo* work where the maximum number of active electrodes on an array was 6.

SEM images were taken to observe the filling of the gold braze within milled features in the substrate Figure 3.11). This included the use of Focused Ion Beam (FIB) to evaluate the encapsulation of the carbon fibers within the braze. The images showed complete filling of all holes and tracks, with only features positioned close to the outer extremities of the substrate not showing complete filling in some instances. The method of applying the braze paste without disrupting the carbon fibers had no discernible effect on the brazing of features. The polishing method employed did result in excess gold being removed below the surface of the diamond. This depth was found to be about 10 µm through SEM and optical profiler measurements (Figure 3.12). Variance was seen between samples due to the manual nature of the polishing process. No further work demonstrated that this excess braze removal influenced the yield of any downstream connection processes, so this was deemed acceptable.

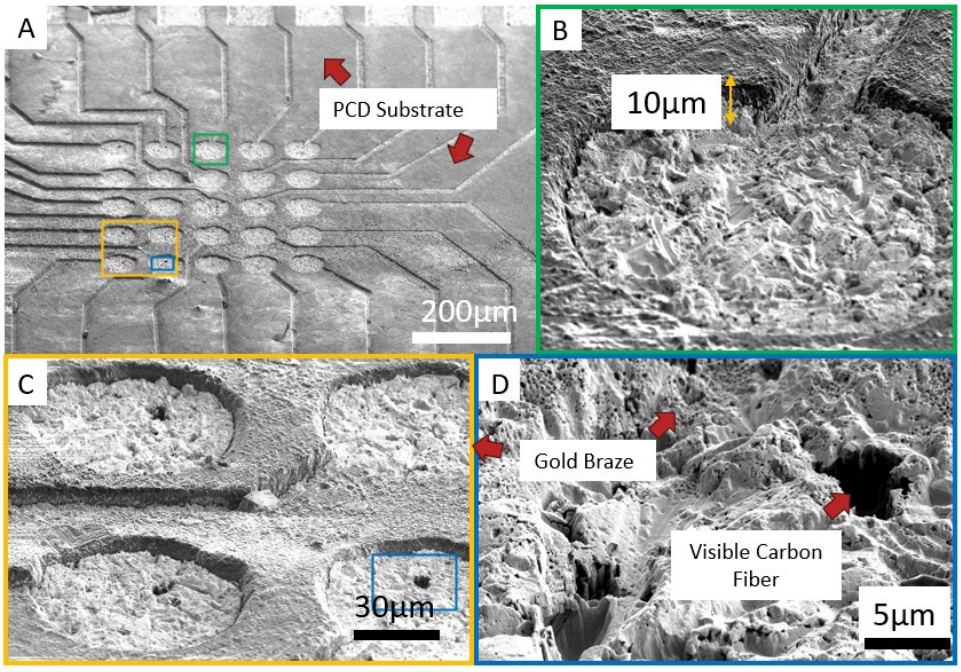

Figure 3.11: SEM images showing the Braze filling in a diamond substrate within a 5 by 5 array configuration (A). The complete filling of the braze within the hole under 10 µm from the surface (B). The presence of carbon fibers is evident on the surface of the brazed holes (C and D).

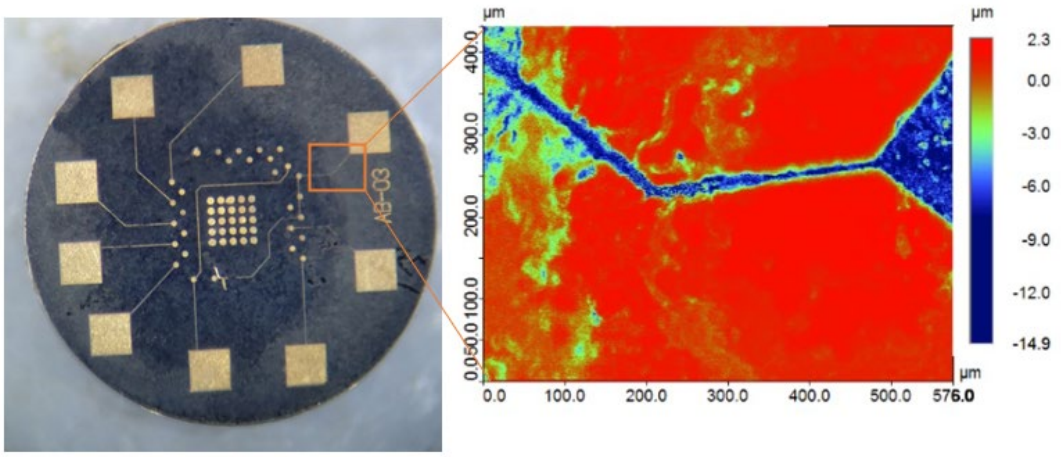

Figure 3.12: Optical Profiler measurements showing the depth of the braze below the PCD surface.

The shape and size bulb of excess gold that was formed on the substrate immediately after brazing was a good indication of the wettability of the gold. As there was some variance between samples this was an important early indication of the braze filling the features of interest. This is more important as the features (specifically the pads) on the outer sections of the diamond were less likely to fill if the wetting or the braze paste application was not optimal. This can clearly be observed in Figure 3.13. In the majority of the fabrication rounds full wetting and complete feature filling was observed, however the braze process itself did show some inherent variability so this could not be quantified. The ability of the braze to fill the samples was not impacted by the diameter of the PCD substrate. 4.5 mm diameter patterned circuit boards were also constructed (Figure 3.14). These samples displayed similar wetting and feature filling characteristics as the smaller (2.5 mm diameter) substrates. This provided further evidence of the versatility of the device design for future applications.

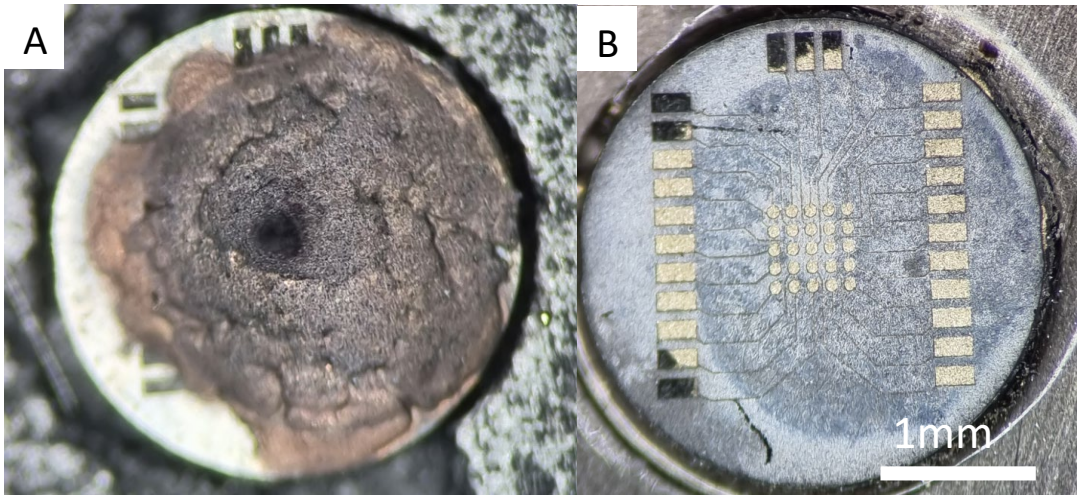

Figure 3.13. Braze before (A) and after (B) polishing showing features not filling where gold has not wet the diamond surface.

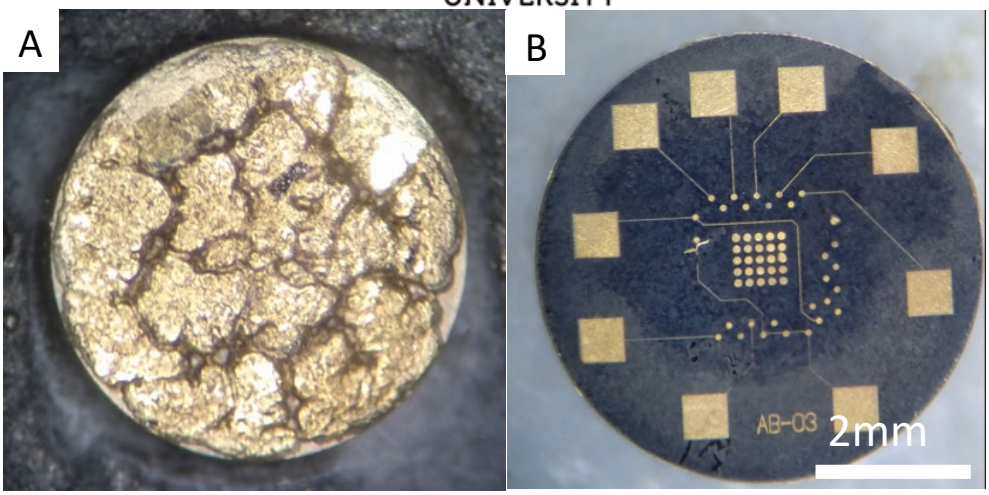

Figure 3.14. 4.5 mm Diameter patterned circuits with excess braze (A) and after processing (B).

An important issue that arose during the fabrication process was the cracking of the diamond substrate after brazing. This was observed mainly in samples that appeared to contain excess braze paste. This was not entirely confirmed as the braze paste application is a manual process with inherent variability. The paste is applied using a probe and it is simply spread over the surface manually under a microscope. This means the exact amount of paste applied is inconsistent beyond manual control. This does suggest future work into a more controlled braze paste application would be critically beneficial to the development of this technology. Cracking is observed to propagate through the milled through holes, an obvious weaker point in the diamond structure. The cracking was observed regardless of the number of holes milled, implying this would not be more of an issue as holes increased (Figure 3.15). The cracking is proposed to be caused by the large ball of the gold pulling on the diamond surface as the gold cools and contracts. The coefficient of expansion of gold is 14.2×10^{-6} K^{-1} whereas diamond is only 1.1×10^{-6} K^{-1}. This difference in expansion coefficient means that the gold expands and contracts as changes temperature to a greater degree than the diamond will under the same temperature range. The adherence of the gold on the diamond surface as it cools pulls on the structure of the diamond to a point of mechanical failure. The strength of this adherence is observed in the difficulty to remove the intermetallic carbide layer that forms from the sputtering and brazing process [216]. Substrates that exhibited cracking could be further processed and showed no evidence of shorting between channels. However, this clearly would have an impact on hermiticity of the devices although no samples could be produced to prove this.

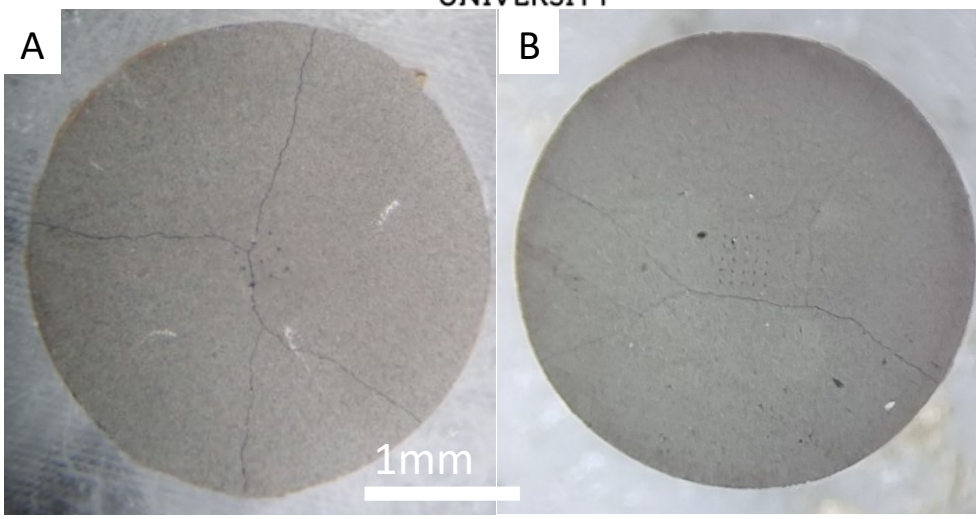

Figure 3.15; PCD substrates post brazing that exhibit cracking in the substrate. A 3 by 3 array (A) and a 5 by 5 array (B) indicating the cracking is not a direct result of an increased number of holes.

The success of the feature filling and diamond wetting was dependent on the amount of braze paste applied. If less paste was applied incomplete wetting and feature filling was more likely to occur. On the other hand, as shown, excess paste results in the cracking of the substrate. This shows an important balance of the amount of paste for optimum performance of the brazing. Due to the viscosity of the paste and size of the nano particles there was no reliable way to apply a controlled amount of braze. By ensuring complete coverage of the surface with braze as seen in Figure 3.16, majority of the surface can be successfully brazed with minimal to no cracking of the substrate.

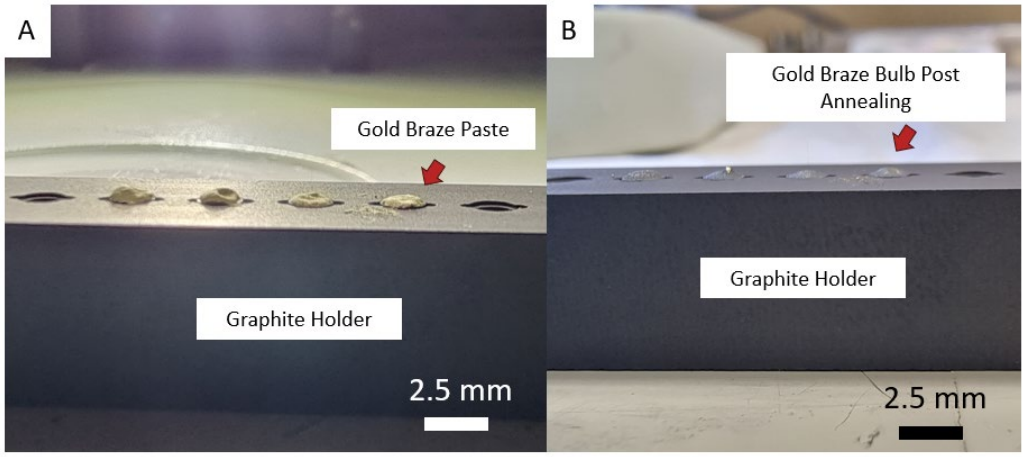

Figure 3.16. The braze paste application (A) and subsequent braze bulb produced (B) after annealing when using the optimal amount of paste.

When initially threaded, the carbon fibers protruded through the holes and excess fiber sat above the top surface of the PCD substrate. This reduced the chance of fibers pushing through and out of the bottom of the holes upon braze paste application. This meant that they were brazed in place with the fibers protruding through the excess braze above the surface. When the polishing was conducted the top of the fibers were sheared off as the excess braze was removed. This can be seen as the fibers are still in place

within the braze under SEM (Figure 3.11). A rare example of a hole not filling completely but still containing a fiber can be seen in Figure 3.17. This nicely demonstrates the positioning of the fiber within the braze, however as this was only ever seen once on a single hole out of at least 100 devices, it is considered an outlier.

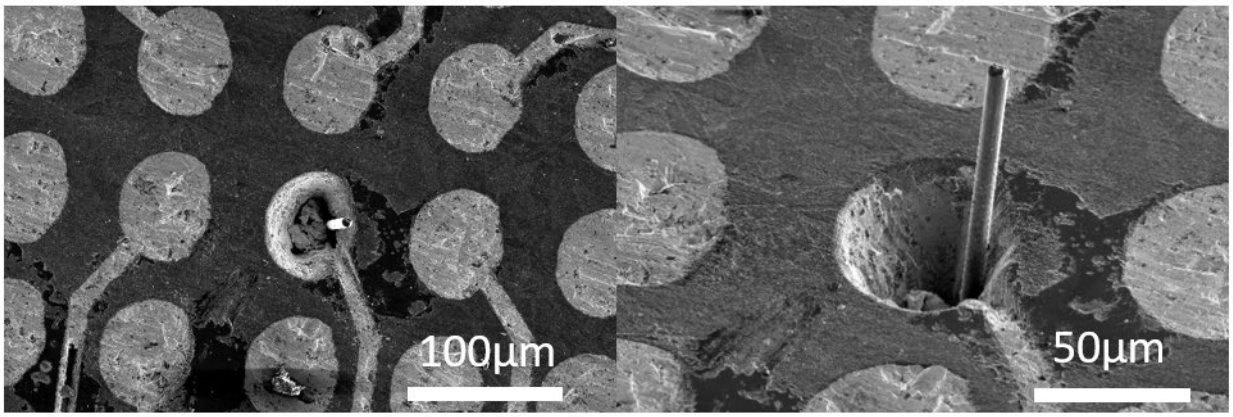

Figure 3.17. SEM images showing a rare instance of incomplete braze filling in a hole, with intact carbon fiber protruding above the surface.

To evaluate the interface between the carbon fiber and the gold braze, cross sections of the fibers were created in place using FIB. Due to the of size constraints this process, a maximum depth of 20 microns was achieved. This only showed the fiber braze interface at the surface. This is potentially not indicative of the entire fiber as it could have been disrupted during polishing, especially when the carbon fiber above the surface is removed. The braze appears to fill closely to the carbon fibers. With voids being seen along some sections of the fiber (Figure 3.18 and 3.19). Complete filling is not necessarily required, however this could impact the mechanical strength of the interface, conductivity of charges from the fiber through the rest of the circuitry and potentially the hermiticity of the device. The elemental composition of the interface was also confirmed using EDS. This was performed with a TEM sample that was prepared using FIB (Figure 3.20). This produced expected results with the carbon fiber sections showing only carbon. There was expected Tin and Nickel within the Gold braze as this was the composition of the braze paste. No Titanium, Molybdenum or Niobium were seen close to the fiber. This suggests there was no carbide formation at the interface, meaning the bond may not be as strong as it is at the diamond interface. Note that because this is a destructive process, voids seen could have been produced from the process itself, however this was deemed unlikely in this circumstance.

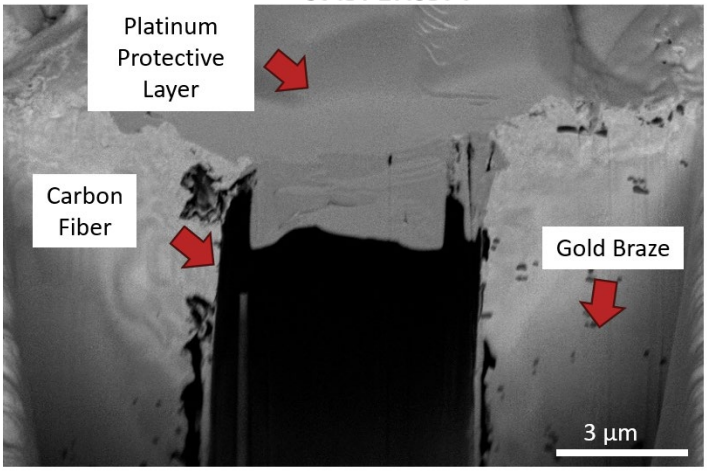

SEM g

Figure 3.18: ~~Sem~~ images of the cross section of a carbon fiber in gold braze produced using FIB. A platinum protective layer can be seen as is standard when creating cross sections in materials using FIB in order to protect the surface interface.

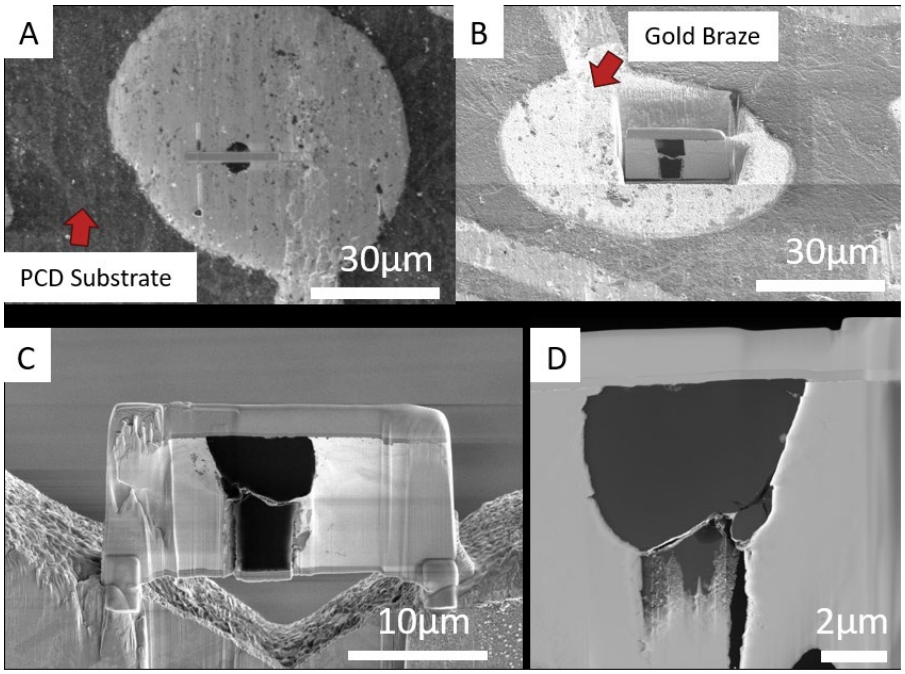

Figure 3.19: SEM image (looking straight down) showing the brazed hole in the PCD with carbon fiber (with platinum protective layer) in place (A.). SEM image (angled) of the TEM sample preparation using FIB (B. and C.). TEM image of the cross section of a carbon fiber in gold ~~B~~raze (D.).

b

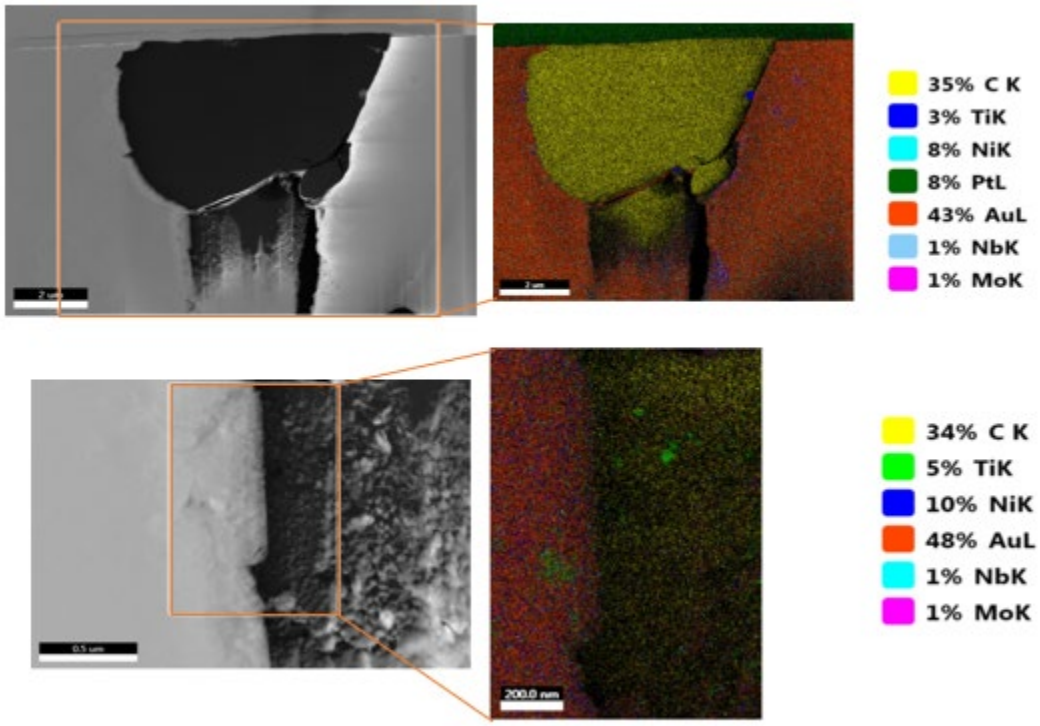

Figure 3.20: EDS performed showing the carbon fiber and braze interface. TEM images obtained (Left) with the EDS mapping (Middle) and elemental contents (Right).

To characterize the braze filling the holes surrounding the carbon fibers, multiple methods were employed. This involved firstly trying to optically observe the depth of the braze as well as determining how completely the braze filled the features. The braze cannot be visualized on the underside of the opaque TM100 PCD substrate due to the small hole and the carbon fiber blocking the view. The first method employed utilized the optical transparency of TM200 PCD to allow for the visualization of the features through the polished surface of the underside of the substrate. The same milling parameters were utilized, and the size and shape of the external features were consistent with the opaque PCD. The conical shape of the holes can be observed in Figure 3.21, as well as the gold and carbide layer that formed on the underside of the brazed features. From these images, the gold braze appears to fill roughly 100 µm into the holes. The carbide layer can still be seen at this depth. Due to reflections and the fact the inside of the holes is are obviously not polished flat, it is not possible to perform this to a higher magnification. The depth of the braze is also somewhat irrelevant if the connection to the carbon fiber is physically and electrically adequate and that the braze within the hole creates a hermetic seal for the implant. This could, however, be an area for improvement as it is assumed that a more complete filling will create a more optimal carbon fiber/braze/ PCD interface.

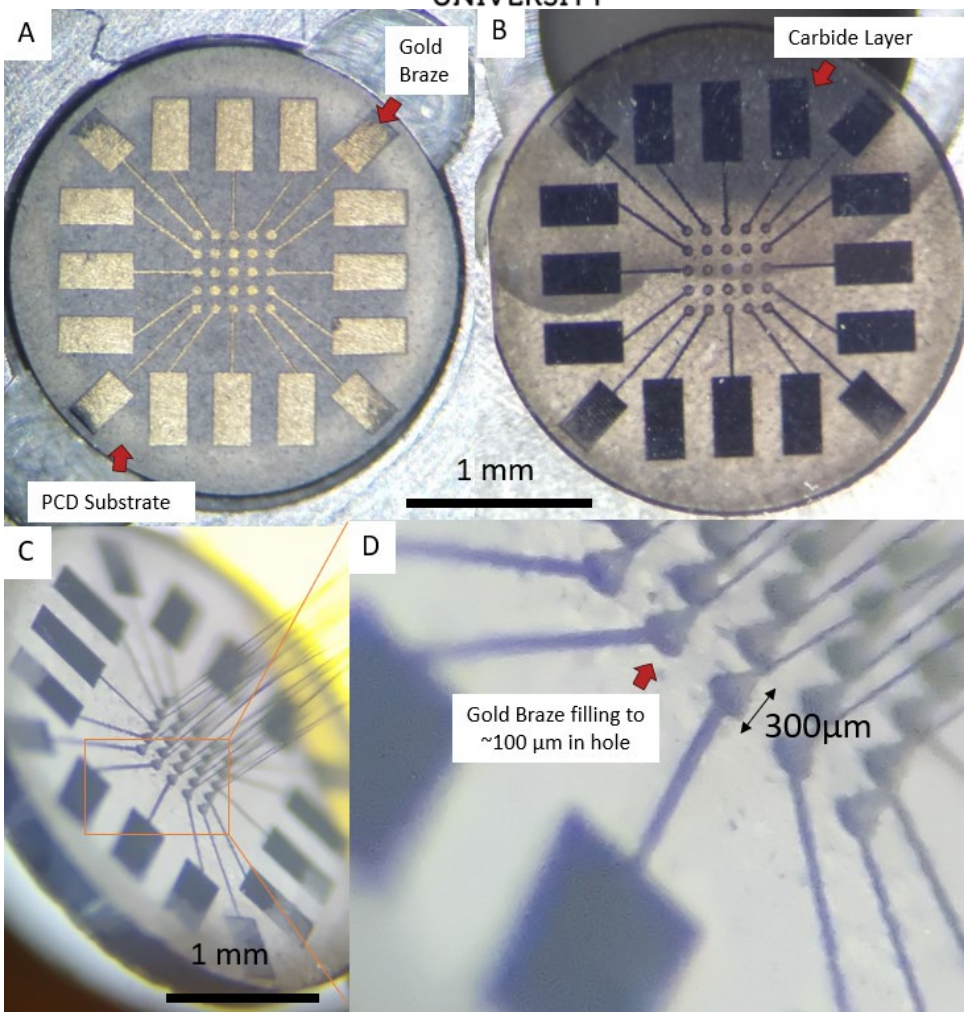

Figure 3.21: A fabricated Carbon Fiber Diamond Array using a transparent T200??? PCD substrate to visualise the braze filling and fiber orientation. The top (A) and bottom (B) sides of the brazed and polished sample can be seen with the carbide layer between the gold and diamond being visualised in black. The angled image (C and D) of the transparent underside of the array can be seen, showing the cone shape of the holes and the partial filling of the braze into the holes.

To further characterizing how the braze fills the hole beneath the surface, FIB was used on filled holes (Figure 3.22). This was performed both in the centre of the hole and at the location of where an electrical track meets the hole. The depth of this characterization was again limited due to the geometry constraints of the technique as only a 1:1 aspect ratio is possible with the FIB. The results showed complete filling to a depth of at least 100 µm as well as complete filling of the electrical tracks connecting to the holes, corroborating the images produced from the transparent PCD samples.

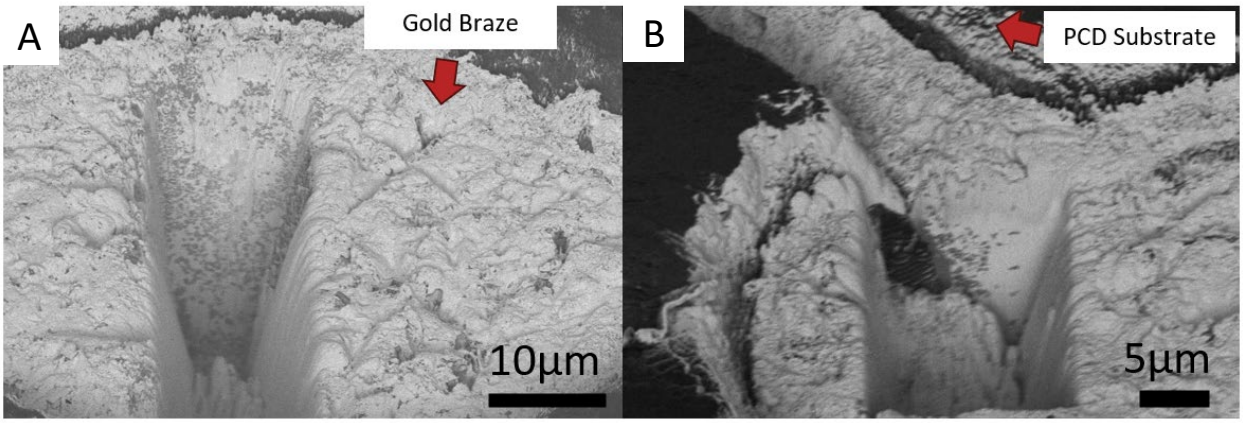

Figure 3.22: SEM images of trenches milled using FIB in the middle (A) of a brazed hole and edge of a hole connecting to a track (B) demonstrating braze filling at least 100 µm deep into the features.

The final step to validate the brazed feed-throughs was confirming the hermitic seal between the diamond, braze and carbon fibers. For this, samples were prepared that contained a 5×5 array of holes in the centre of 10×10 mm PCD plates, so that they would fit within the O-rings of the leak tester. The hermiticity tests were performed (Refer to 2.5.7) on samples with and without carbon fibers, and on 300 and 500 µm thick substrates. These were performed on the same set up as previously published work [174, 175]. These results showed no leaks for samples without carbon fibers for both thicknesses of substrates. This meant that the leak rate of the seal between the gold and the PCD was at least resistant to 1E-9 mbar l/s (the detection limit of the system). One sample that contained carbon fibers was able to achieve the same leak rate (Figure 3.23). Three other samples that contained the carbon fibers showed a small leak of 1E-7 mbar l/s. This indicates that the voids seen at the carbon fiber and braze interface could potentially extend through the brazed through hole, and this could be the source of the leak. The leak rate of 1E-7 would not be an issue for larger implants but would be problematic for this device as the dew point of smaller devices lower [177]. This leaking could not simply be mitigated by the parylene coating, as parylene does not meet the standards for implantable devices [171]. Further work into altering how the fiber sits within the gold could potentially create a reliable hermetic seal, wherein the fiber is pushed through the diamond to a point where the gold can create a complete seal over the entirety of the surface of the through hole. However, this was not explored further in this work.

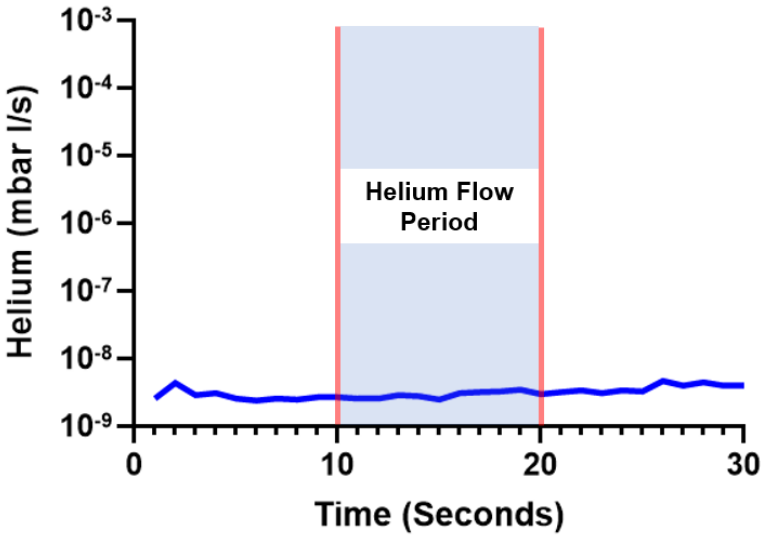

Figure 3.23: Graphical output of the helium leak tester. Test window of helium gas flow indicated no detection of helium within the limit of detection of the testing apparatus (10^{-9} mbar l/s).

3.4.2 Device Encapsulation

The parylene coating was an incredibly consistent process. Optical profiler and SEM images showed uniform coatings around 2.6 µm. No evidence was ever produced to indicate any leaks or issues with the coating, especially on the carbon fiber electrodes. The physical properties of the parylene were able to withstand the testing and fabrication procedures, as evident in every electrode imaged before implantation.

The fire deinsulation process produced consistent removal of parylene when exposed above the water surface. The deinsulation appeared complete in every sample assuming the length of the fibers were consistent. Some issues did arise during the deinsulation process, wherein clumping of the carbon fibers resulted in inconsistent deinsulation across the array (Figure 3.24). This occurred as this changed how the fibers protruded above the surface level of the water, meaning the fire was not evenly distributed among each of the fibers. In some cases, this also resulted in the fusing together of the parylene coating on adjacent clumped fibers. This produced inherent inconsistencies with some samples that needed to be accounted for during the insertion and *in vivo* testing.

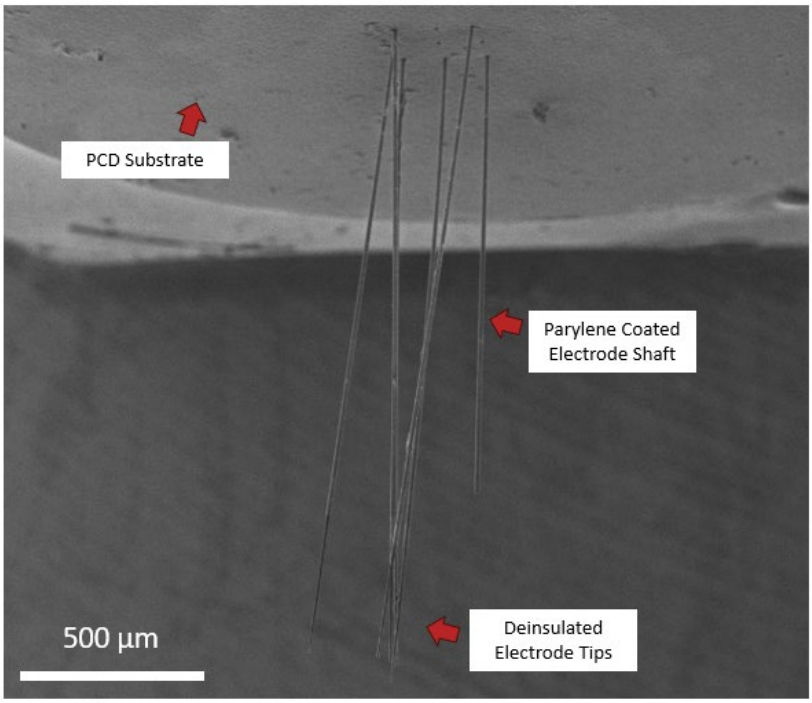

Figure 3.24. Clumping of adjacent electrodes during the fire deinsulation process.

subscript

The O2 plasma cleaning ~~used was shown to~~ successfully increase d the hydrophilicity of the fibers. Hydrophilicity was measured using glass slides coated in parylene placed within the chamber when coating electrodes. The coating used was already inherently hydrophilic, showing a contact angle of 61° ~~degrees~~ (Figure 3.25). This was reduced immediately after plasma etching to 26°~~degrees~~ and returned to 46°~~degrees~~ after a week of treatment. This ~~exhibited an~~ overall improvement ~~however showed that the effect~~ was somewhat transient. Using water droplet tests as a measure of hydrophilicity meant that the fibers themselves could not be tested. The slides were placed lying flat at the bottom of the plasma cleaner chamber. In this position the plasma ~~field~~ generated would be less intense than ~~what would be~~ that experienced by the fibers that protrude d up into the plasma, especially the tip of the electrodes. This means that the plasma effects would be different along the parylene coating of the electrodes. Thinner parylene films have been shown to produce more hydrophilic surfaces, if required, however these are too thin to ensure robustness and isolation of the electrodes [168, 183]. These works suggest a 2µm coating could exhibit the hydrophilicity properties required whilst still maintaining desired robustness for neural applications. The hydrophilicity and robustness of the parylene coating and subsequent treatments used were conducive to both the fabrication steps employed as well as the effectiveness of the array as a neural electrode (this is explored further in Chapter 4). These tests confirmed the choice of coating and surface treatment time were optimal for the design constraints of the device.

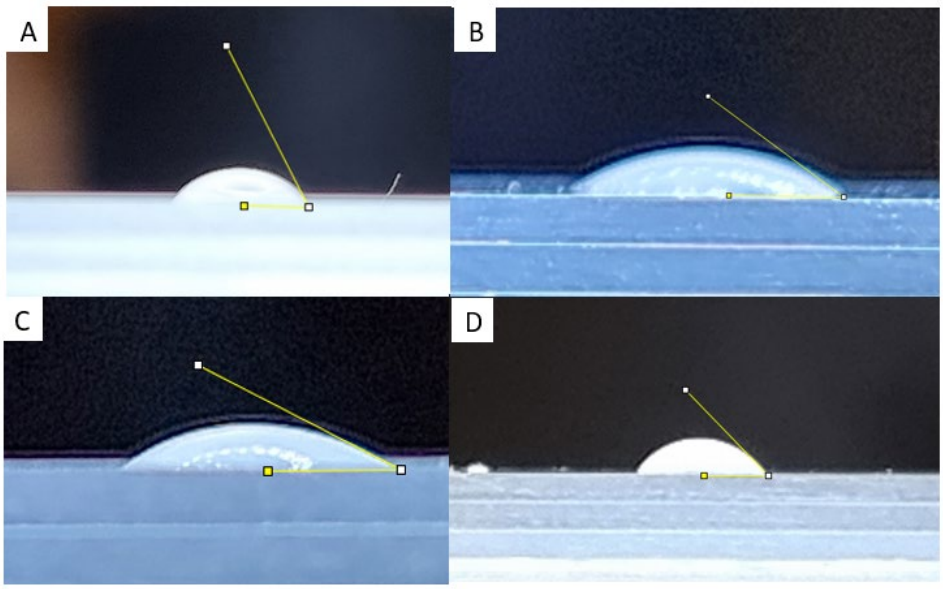

Figure 3.25. Water droplet hydrophilicity test. Water droplet on parylene coated glass slider before (61 degrees, A), immediately after (25 degrees, B), 24 hours after (26 degrees, C) and 1 week after (46 degrees, D) oxygen plasma treatment.

3.4.3 Electrical Performance

The electrical performance of both the diamond substrates and their connection to the PCBs were fully characterized. This involved the evaluation of the continuity through the brazed circuitry to the carbon fibers, the deinsulation and tip preparation as well as the external connection of the PCB to the substrates.

Firstly, isolated electrical connections were demonstrated between each electrode channel whilst showing complete electrical continuity from the brazed pads, through the holes to the carbon fibers. During the brazing process all channels become shorted due to the formation of a metal carbide layer on the diamond surface as a result of the braze [216]. This electrically shorts the entire surface in the kΩ range [216]. A graphite layer is also formed on the entirety of the diamond surface shorting each of the carbon fibers together on the underside of the PCD in the range of 5-10kΩ. The acid boiling technique used shows isolation on all diamond surfaces with impedance values in the GΩ range between channels. This is sufficient for neural signal transmission. The standard omnetics connector developed for neural signals exhibit isolation between channels in the GΩ range [217].

To achieve the continuity measurements a conductive agar solution using saline was used to electrically connect the carbon fibers to the potentiostat (Figure 3.26). The agar was used instead of a liquid saline solution to ensure that the saline did not wet the top surface of the substrate providing false continuity measurements for discontinuous channels. A probe was placed on each channel to determine the continuity from the pad through to the electrode tip. For this test, values in the kΩ range were deemed successful as this is the expected range for about 1mm of carbon fiber placed within a conductive saline solution. Through testing the desired kΩ range was achieved (values showed between 100-800 kΩ). It was determined that channels with visible gold braze filling the features provided electrical connections to carbon fibers that were still in place within the array.

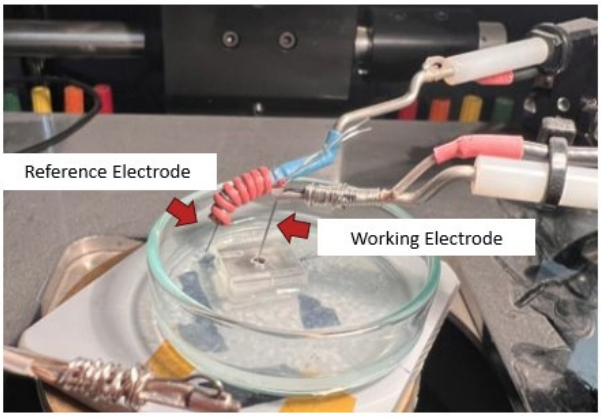

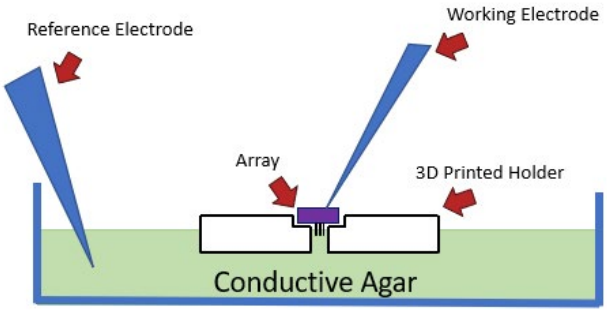

Figure 3.26. Experimental design for continuity measurements. Probes placed on the circuitry and in the conductive agar used to demonstrate the connection of the brazed pads to the fibers on the underside of the array.

Once the electrical properties of the substrate itself was verified, the complete package could be ~~created~~ assembled and tested. To facilitate this connection external PCBs were designed. The first and simplest of these can be seen in Figure 3.27. This iteration was a large, solid PCB with copper wires soldered to pins to allow connection through to the pads. These wires were attached with silver paste and all connections coated in an insulating epoxy. This design allowed for robust testing of continuity as well as areas ~~probable~~ accessible with a multi meter to test each separate connection for continuity. Once connected and insulated using epoxy on the exposed solder and wires, the continuity of the fibers through this ~~needed to be~~ was demonstrated. This was performed by placing the fibers in NaCl solution and electrically testing impedances on the electrodes. Similar to the agar tests performed, successful connection ~~would be~~ was indicated by kΩ resistance through the intact fibers and high MΩ in channels missing electrodes. The impedances detected through the channels with intact electrodes was between 100 kΩ and 900 kΩ. Channels connected to broken fibers showed MΩ impedances indicating no shorting between the channels. This simplified version was successful in proving the concept of the design. However, due to the size and rigidity of this design it was not appropriate for *in vivo* testing. ~~A~~ For this, a more compact flexible PCB design ~~would be~~ was required (Refer to Figure 3.8).

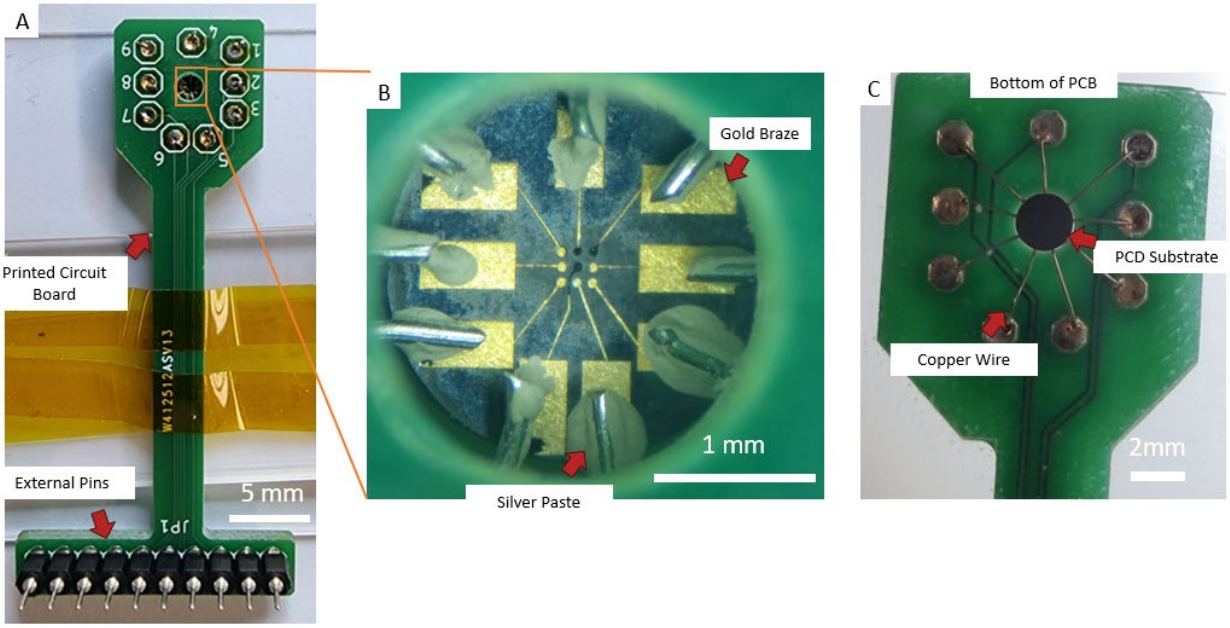

Figure 3.27 First iteration of the PCB connection design. This includes soldered pins on a solid PCB (A) and copper wires silver pasted to the gold pads (B). The underside of the PCB can be seen (C) with the wires protruding through the array from the PCB.

Now that the entirety of the external connection and the substrate have been verified, the tip preparation methods needed to be confirmed. The first step was to show the electrical deinsulation of the parylene from the carbon fibers. Figure 3.28A shows complete removal of the parylene under SEM. This is confirmed with the impedance (Figure 3.28C) being in the 100 kΩ range. This is representative of the majority of the electrodes produced, with slight variations seen for different exposure lengths of the carbon fiber. The CV application of the PEDOT appeared successful as the shape of the CV produced indicated polymerisation of the EDOT on the working electrode. The deposition was confirmed with SEM (Figure 3.28B) where a micron scale coating can be visually seen. Impedance values post PEDOT coating dropped down to as low as 2.7 kΩ. The value shown in Figure 3.28D is representative of majority of electrodes prepared. Once the complete characterisation of each electrode channel was conducted, arrays could be selected for the *in vivo* testing in Chapter 4.

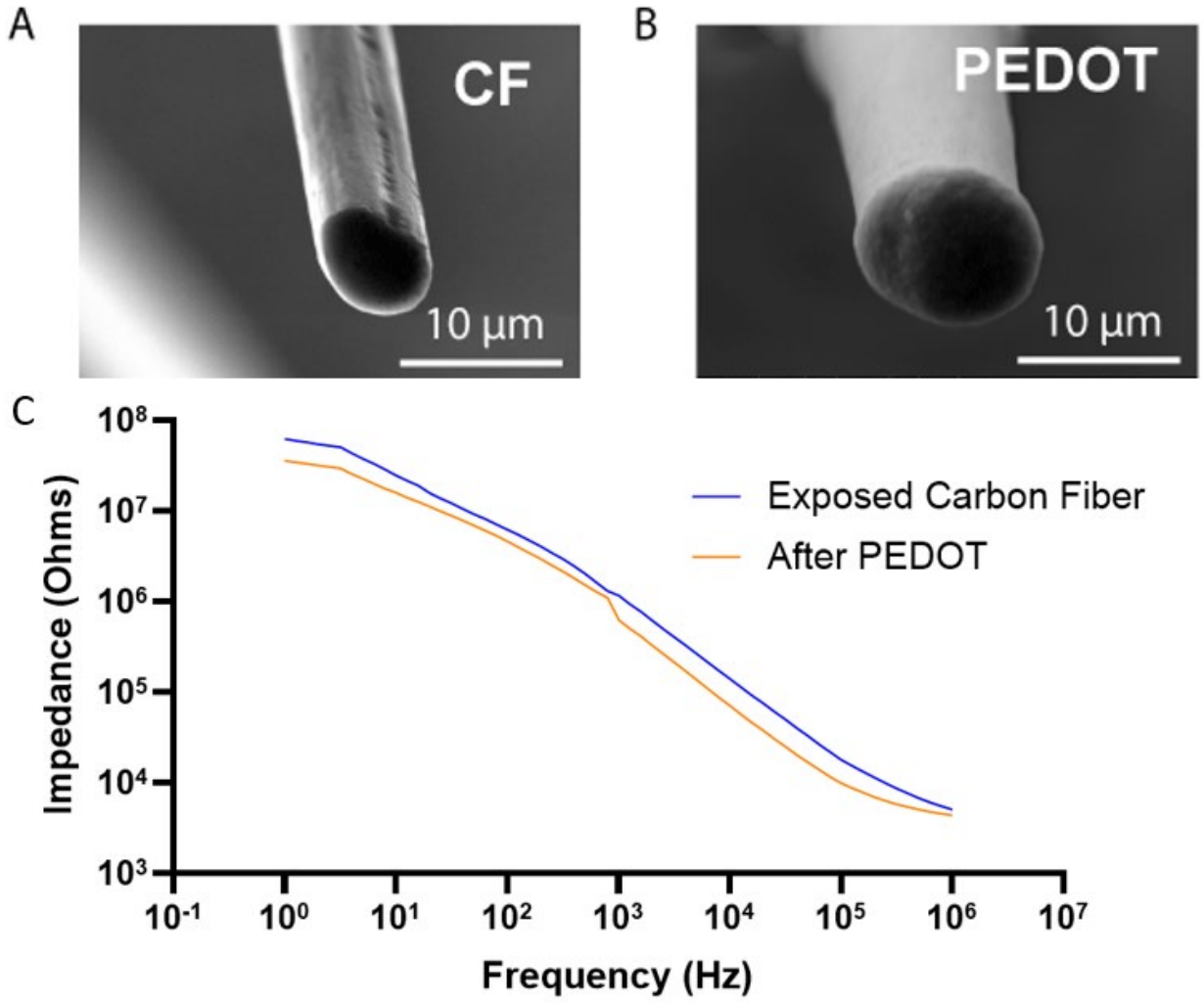

Figure 3.28: An example of a functional electrode tip on a working PCD substrate carbon fiber array. SEM images of the electrode tip before (A) and after PEDOT deposition (B). The associated impedance spectra of the electrode at these processing steps (C).

3.4.4 Limitations

The main limitations seen in this work were around the yields of devices. The yields in this work were very much a consequence of working at the size scale of the proposed device. This has been noted in previous works dealing with carbon fibers and other micro electrodes, however to successfully interface with neurons these are requirements. A major obstacle with the size constraints is the fact that many of the processes are working on the upper limits of the precision of some of the equipment. An issue encountered was with the laser cutter used. There was an upgrade to the system part way through the program that resulted in a changing of the beam characteristics. The spot size and power of the laser were enhanced which led to more precise surface milling. However, this had a drastic effect on the shape of the through holes produced (Figure 3.29). This was mitigated through further configuration but stands to highlight potential issues for reproducibility or issues when using new or different equipment.

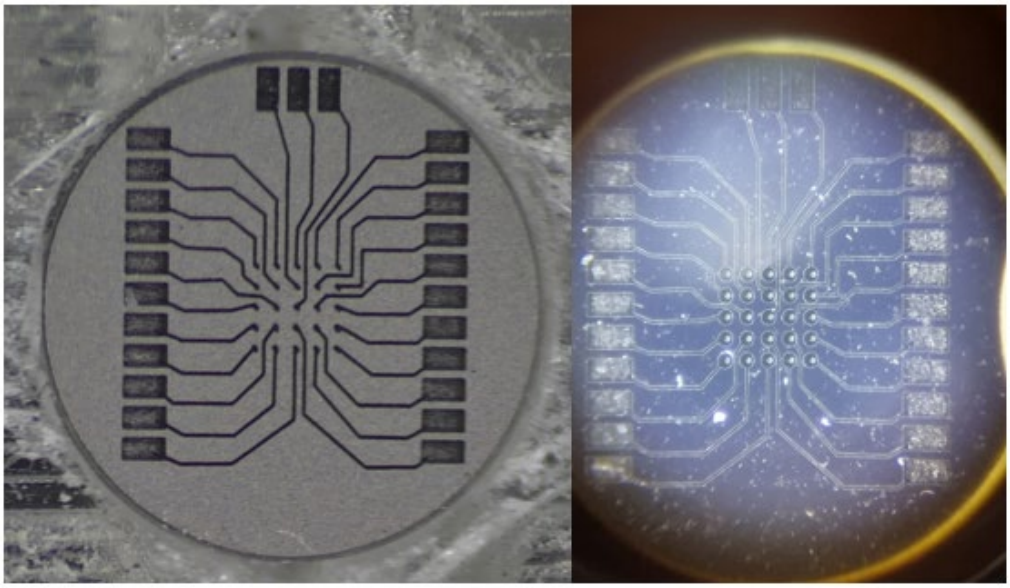

Figure 3.29: Examples of different through hole shapes before and after laser cutter equipment modifications.

where? Need arrows showing what you mean

The materials involved also presented some difficulties. These were unavoidable due to the biological requirements of a chronic device. The complexity of using gold to form the electrical hermetic feed-throughs presented challenges, specifically at the gold and carbon fiber interface. The introduction of the carbon fibers meant achieving hermeticity of the feed-throughs was more difficult. Adding additional elements to already complex processes showed to only retract from the effectiveness of these same processes. The presence of the carbon fibers also influenced every other processing step, as these fibers needed to be protected from either handling issues or the processes themselves. Lastly, improving the PCB connections to create electronics that can bond directly to the gold in a hermetic package would also be required for a final implant. Such a bonding could also work towards completing a reliable hermetic seal within the through hole. This was outside the scope of this work but would be beneficial for future work. Many promising steps were made to realise a complete device. More work is still needed to achieve a commercially available, chronically implantable neural implant.

reduced ir

3.5 Future Work

Considering the limitations of the proposed device, some avenues for improvement were explored to show potential increases in the viability of the design. This included working on thicker substrates to potentially improve yields, straightness of fibers and hermeticity. Work was also conducted to show the potential scalability of the design and how it could potentially compete with other higher electrode number arrays.

3.5.1 500 µm Diamond Substrates

Due to the evident cracking, yields of the carbon fibers and the hermeticity concerns, thicker PCD substrates were explored. PCD substrates were milled in the same configuration as shown using 0.5mm thick TM100 PCD. The major limitation for these samples was the ability to mill features deeper into the diamond. The shadowing effect of the substrate as the laser mills deeper results in larger feature sizes on the surface when creating through-holes. It was demonstrated that through-holes were possible even with

the thicker substrate and that carbon fibers could be housed within these (Figure 3.30). The next test was the brazing which also produced consistent results (Figure 3.31). No cracking was evident in any of the brazing runs conducted, indicating that the thicker substrate could potentially be useful for this reason alone.

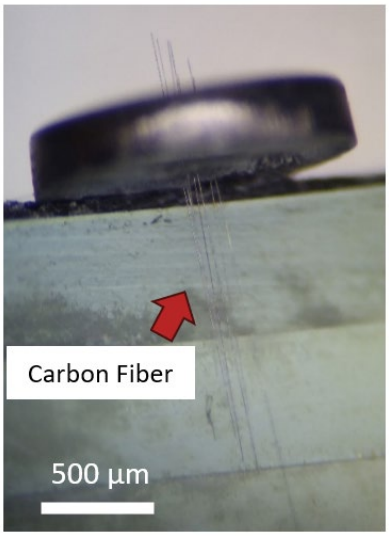

Figure 3.30: Shows a 500 µm thick PCD substrate with carbon fibers protruding through milled holes.

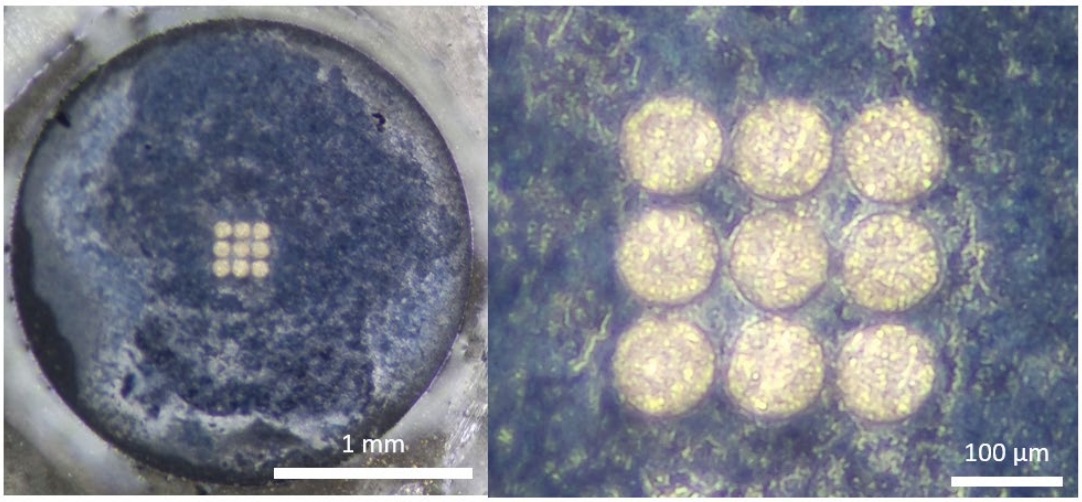

Figure 3.31: Gold brazed holes containing fibers in 500 µm thick PCD substrate.

The thicker substrates produced larger surface size holes meaning that creating tracks between channels is not possible for this electrode pitch (100 µm). The larger holes do provide a larger surface area to connect directly to the holes themselves for potential chip bonding solutions. Conductive agar tests were performed on these samples to again show continuity through the holes as well as isolation between channels (Figure 3.32). Similar to the 300 µm samples, the isolation was in the GΩ range with the continuity through the fibers being in the kΩ range. These tests indicated that the electrical performance of the arrays was achievable with the thicker substrates suggesting they would produce no extra issues for array construction.

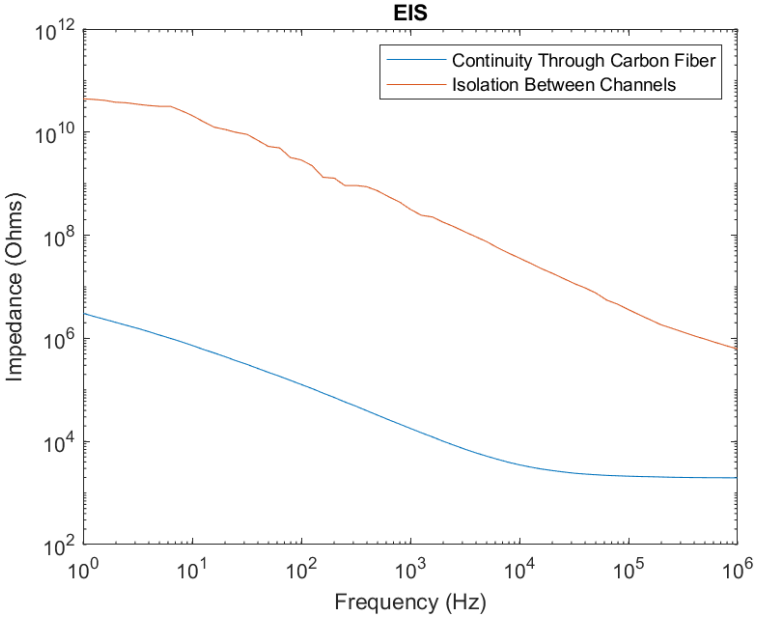

Figure 3.32: EIS data to show the continuity and isolation of the channels in the 500µm thick substrate samples.

3.5.2 Scalability

A limitation with single unit recording electrodes is that, while they provide detailed information on the behaviour of individual neurons, the spatial coverage of each individual electrode is very limited. The ability to scale single unit implants is incredibly vital to reaching the maximum number of neurons for the best picture of the overall neural activity. As each electrode is only capable of interacting with a very limited area, the only way to increase the spatial resolution of these implants is through increasing the number of electrodes available to the implant. This, in itself, brings in a number of its own limitations concerning scaling fabrication. Two iterations of arrays were fabricated but not electrically connected to demonstrate the feasibility of scaling the proposed implants. This included a 10×10 array housing 100 carbon fibers and a 32×32 array containing 1024 carbon fibers.

The first process of this is to demonstrate the ability to increase the milling of the features within the substrate to increase the number of electrodes that can be held. The modification of the milling program was simple, and the only constraint was time, as extra holes require extra milling time. This time increase is linear as no other parameters apart from number of holes needed to be altered. The placement of the fibers was a similar process to the smaller number of electrode versions. This too was linear as it was simply a matter of placing more carbon fibers within the substrate. The overall yield and straightness of the fibers was consistent, as the geometry of the holes did not change (Figure 3.33).

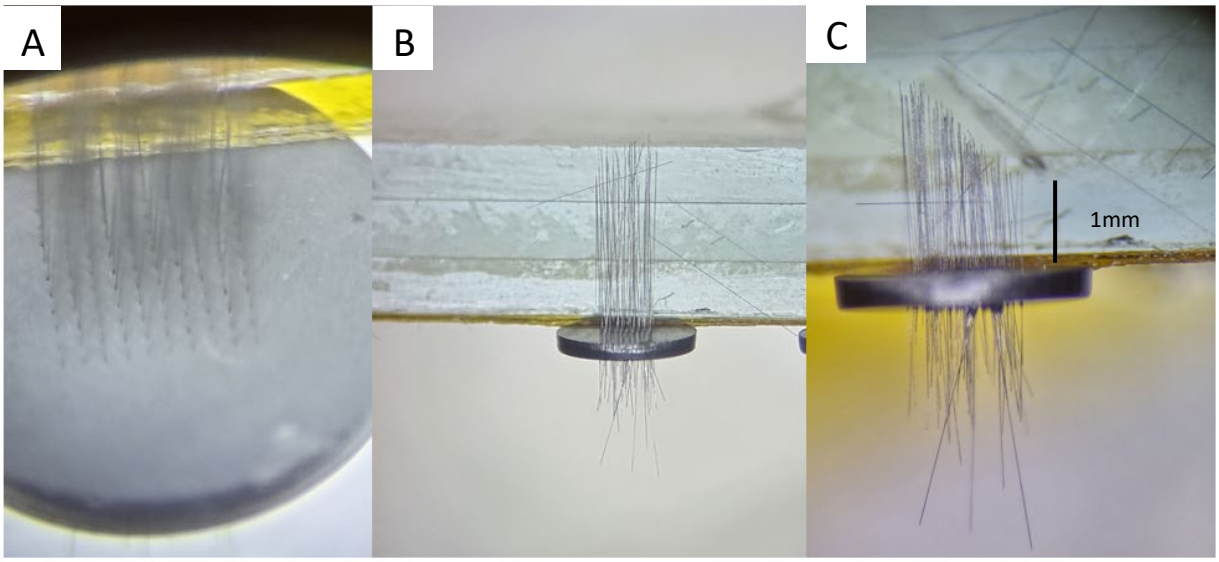

Figure 3.33: Microscope images of the PCD substrate holding the 100-carbon fiber in the 10 by 10 configuration. Bottom side of the substrate showing carbon fibers protruding through (A). Side view of the configuration showing before (B) and after (C) laser cutting of carbon fibers to length (1-2mm taper).

To accentuate the different possibilities available with increased electrode counts, the cutting of the carbon fibers was altered to highlight the possibilities of array geometries. The laser will cut each of the electrodes within a row, however this means that 3D geometries are possible by cutting the fibers along different planes. The simple taper demonstrated with all other fibers was expanded to include two sections of longer electrodes on each plane (Figure 3.34C). By doing this on the sample and rotating it by 90° degrees this was able to produce 4 sections of longer electrodes that culminate in an area of shorter length electrodes in the centre. More complex shapes could be created to optimize neural signals and array insertion in future work. The potential to insert longer fibers or geometries that are able to target specific layers of the cortex could be possible through such a method.

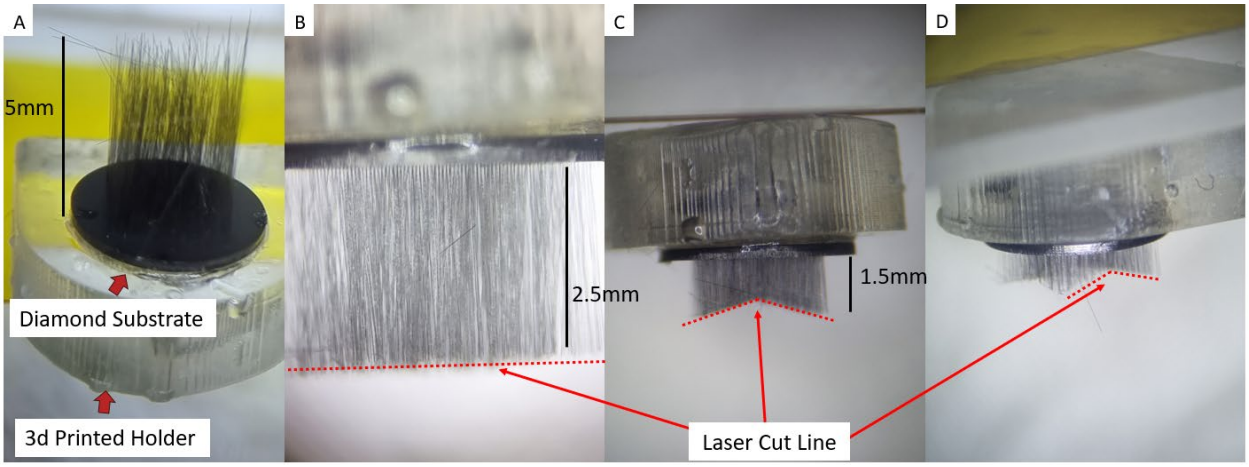

Figure 3.34: Microscope images of the PCD substrate holding the 1024-carbon fiber in the 32 by 32 configuration. The assembled array with the fibers secured in place (A). The transverse laser cutting of the fibers to length include a cut of all fibers to 2.5mm (B) followed by two separate sequential tapers creating 4 corner high points in the fiber geometry (C and D).

The processing steps that followed, again, showed no deviation from arrays with fewer electrodes, assuming the same configuration (i.e. tapered length, coatings and process order) remained the same. The fibers were cut to length, parylene coated and deinsulated in the same manner as the lower electrode number configurations. The final 100 and 1024 electrode array configurations can be seen in Figure 3.35 and 3.36, respectively.

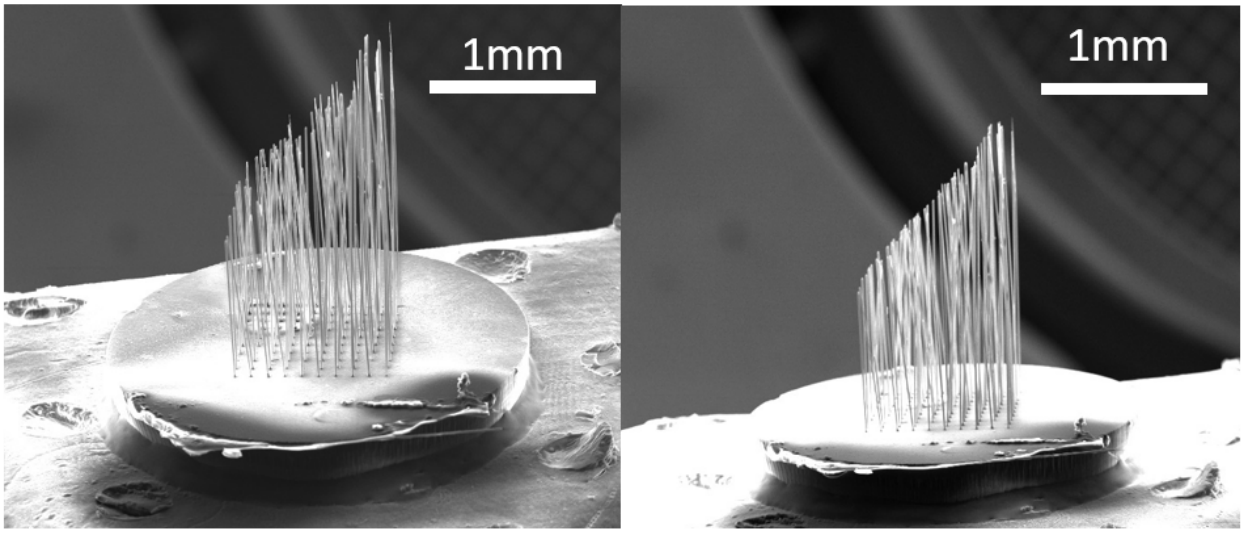

Figure 3.35: SEM images of the 10×10 grid 100 Carbon Fiber Array within a PCD substrate and Parylene coating.

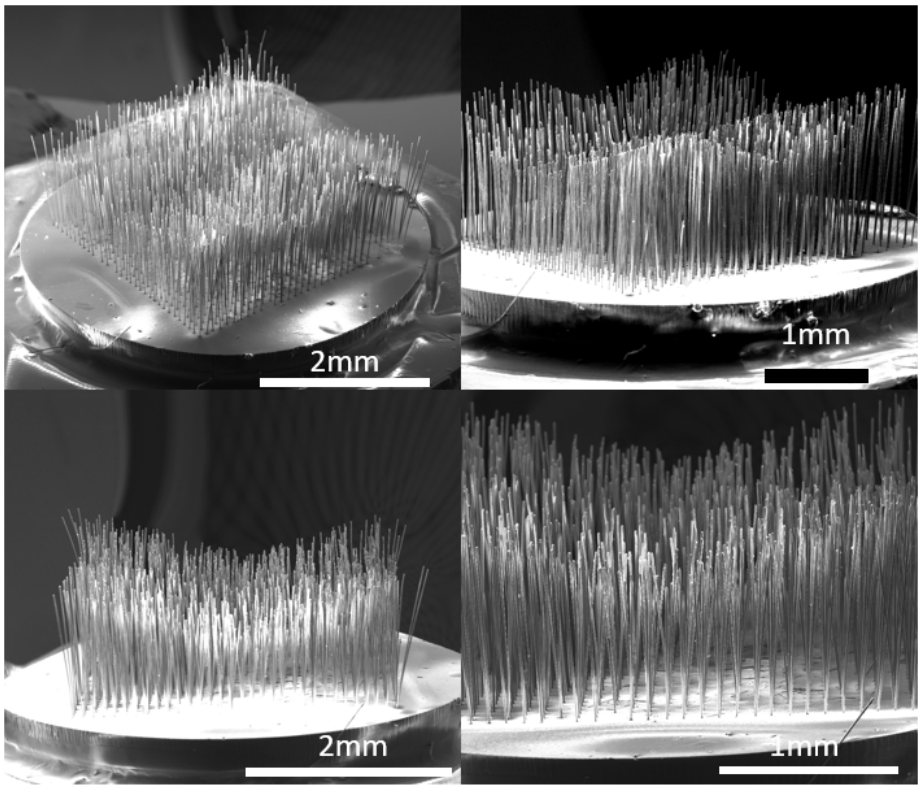

Figure 3.36: SEM images of the 32×32 grid 1024 Carbon Fiber Array within a PCD substrate and Parylene coating.

It appears that the largest limitation impacting the scalability of the implant would therefore be the external electrical connection to the implant. This could be mitigated by using a larger substrate to contain space for the larger number of pads required for connection to external recording devices. A larger electrode pitch would also allow for larger pads over each electrode for PCB stack designs or other solder bump technologies to connect to individual electrodes [218, 219]. It would also be possible to short multiple electrode channels together with large pads that would potentially allow for the stimulation of areas of the cortex as seen in other neuromodulation modes [220]. The fabrication methods do not appear to be the limiting factor when considering the scalability of the design.

Chapter 4: *In vivo* applications of Carbon Fiber Electrode arrays

4.1 Chapter Outline

This chapter will explore the *in vivo* implantation of carbon fiber arrays. This includes the immune-histological results, the implantation technique efficacy and the neural signal acquisition achieved.

4.1.1 Chapter Acknowledgements

The *in vivo* work conducted in this chapter was collaborative. The surgical development was conducted alongside Dr Sorel De Leon Vergara (RMIT University) and Dr Young Jun (The University of Melbourne). The insertion of the devices was optimized primarily by me, with Dr Jun performing much of the rest of the surgery. All of the passive devices utilized were created entirely by me. Some of the later stages of production of the active devices (PEDOT Application and Tip Optimization) were conducted by Dr Vergara. The tissue preparation for postmortem evaluation of the devices was performed by Dr Jun. The CT images were obtained and processed by Dr Yidan Shang (Monash University).

4.2 Chapter Introduction

To fully realise the implant as a neural recording device it needs to be trialled for in *in vivo* applications. This is to show how the characterisation performed translates to the practical use of the implant. This first involved investigating the implants effect on the neural tissue, both acutely and chronically. The tissue responses will also play an important role on the signal quality over time. The signal quality was ~~tested~~ extracted from electrically connected arrays that were implanted into the brain. Through this rigorous *in vivo* evaluation, the safety, longevity, and effectiveness of the proposed implant design ~~can be~~ was determined.

4.2.1 Array Implantation

Much of the performance of a neural implant is dictated by how the device is implanted within the neural tissue. The ability to insert the microelectrode is of particular importance for flexible neural probes. For the same reason that makes them beneficial by matching the mechanical properties of the implant to the neural tissue, these same properties hinder their ability to penetrate the tissue [88, 221-223]. Developing the correct insertion speeds and techniques will allow for the electrodes to be reliably implanted and able to interface with the tissue. This may also reduce tissue trauma upon implantation. This is important as signal quality in some implants can be directly related to the damage ~~on~~ to the tissue or device upon implantation [40, 52, 61, 62]. Flexible arrays aim to circumvent the tissue damage, however, are themselves more prone to damage due to their fragility. Insertion guides can aim to alleviate this issue. However, these have been shown to produce damage themselves and negate the benefits of using the flexible electrodes in the first place [77].

Carbon fibers find the balance between mechanical flexibility and mechanical strength ~~wherein~~ as they are able to be implanted with minimal damage to the implant or tissue [84, 164]. Previous work has indicated that carbon fiber lengths of 1.5 mm should be able to be consistently implanted into neural tissue [221]. This does not mean that the implantation of carbon fiber devices is trivial. There is a limit to the length of electrode that can be reliably inserted. This insertion still needs to be done in a controlled, slow manner.

Insertion speeds in the μms^{-1} range are typical for microwire implants [224]. These slower insertion speeds are also beneficial in that they have been proven to produce reduced tissue damage, even for larger silicon probes [59, 162, 225]. Removal of the dura will also benefit the implant as it aids implantation of the electrode without the tissue compressing and will grow back safely after implantation [226].

This tissue compression is often referred to as dimpling, where the tissue compresses to form a dimple. This occurs until the electrodes penetrate or the electrodes buckle, a mode of failure for flexible electrode insertion. This can be used to determine implantation success as after initial dimpling, the relaxation of the tissue as the electrodes penetrates can be often seen even when the microwires themselves cannot (due to constraints in the viewing angle of the electrodes within the tissue). This is less important for an electrically active implant as the signals themselves can be used to determine insertion success, either through signal acquisition or a reduction in electrical noise. This dimpling can also be compounded for Utah-like arrays, wherein the bed of nails effect will have an important role to play on the penetration of the electrodes into the tissue [227]. This is further exacerbated as the number of electrodes increases, as an increased number of electrodes or increase in density (reduction in electrode pitch) will lead to an even greater ~~amount of the~~ bed of nails effect.

No groups have developed a means to insert a Utah-style array of carbon fiber microelectrodes. The most similar work by Patel et al. and Kozai et al. all worked on planar arrays. Therefore, it ~~will be~~ is important to develop and verify the surgical implantation of the fabricated devices and hence show the effectiveness of the proposed design.

4.2.2 Signal Acquisition and Quality

The signals detected by the electrodes from the tissue ~~are able to be~~ were quantified to compare their performance to other devices. This ~~can be~~ was done using the spike rate or Signal-to-Noise Ratio (SNR). Spike rate refers to the number of spikes observed within a period of time, however this is heavily dependent on the location of the implant, general brain state at the time or any particular neural stimulus provided [228]. Due to the nature of *in vivo* recordings this may not always be a one-to-one comparison. This variation can also be seen in the SNR ~~of signals~~. SNR is usually calculated from comparing the ratio of the underlying noise bed to ~~the ratio of~~ the peak of the spike waveforms [229]. Commonly for single unit recordings the mean of the spike waveform is compared to the standard deviation of that same waveform's noise [230]. Many papers using these methods indicated an SNR of greater than 1.5 is deemed as acceptable for working electrodes [50]. Neural devices, including Utah, Michigan and carbon fibers have shown SNR levels as high as 5, however the average to sit closer to 2.5 [45, 213]. The spikes themselves are not the only determinant of SNR, as the ability to produce low noise signals will also have a direct effect on the retrieval of high SNR spikes. This is influenced by the electrode/implant itself, the electrode tissue interface as well as noise generated throughout the recording system or within the room. This is exacerbated by *in vivo* recordings where it can be much more difficult to isolate and remove sources of electrical noise from within the surgical set up.

These signals have been shown to change over time, sometimes for the better or worse depending on the electrode. Typically, stiff electrodes like that of the Utah array appear to improve over the period of time immediately following implantation as the tissue relaxes from the trauma experienced during insertion. This is less evident in microelectrode recordings where minimal trauma is experienced by the tissue. The stability of the signals will also affect the potential use of devices for BCI [231]. This suggest potential stability of signals over time could be as important as the signal quality itself [232]. Maximizing the signal quality and stability of the electrodes is key to proving the efficacy of the proposed implant.

4.2.3 Chronic Performance and Immunohistology

Evaluating the local tissue damage that is caused by the insertion of a neural implant is vital to fully understand the safety and ultimately efficacy of the device. Especially when dealing with the complex and important tissue within the brain, understanding and potentially reducing or limiting this is incredibly important. More so because the tissue damage from the implant is directly correlated to the chronic signal acquisition capabilities of a neural electrode and a primary failure mode for many devices [53, 225, 233-235]. An effective method to measure this damage is by performing post-mortem immunohistology on the implanted tissue. This is achieved by fixing the tissue at the implantation site to preserve the cells and architecture around the implant, to assess the local environment for the presence of inflammation or healthy neurons [64]. This involves preparing slices of this fixed tissue and using stains to test for particular inflammatory cells of interest. Glial Fibrillary Acidic Protein (GFAP) is one such commonly used stain target that is only found in astrocytes, which are a type of glial cell that is primarily responsible for the glial scarring of the FBR. Iba-1 (a protein expressed by microglia) is another typical stain target that is able to visualize microglia, another cell involved in this immune response [236]. Using this technique the amount of tissue damage can be quantified, as well as the extent of glial scarring that is occurring at the electrode-tissue interface. This interface scarring can be as thick as 100 µm [59, 108, 237]. This increases the impedance between the firing neurons and the electrode itself, reducing the signal quality of the electrode to the point of functional failure. Highlighting the importance in both reducing and quantifying any local inflammation of neural implants.

(This is a clause not a sentence)

This h s

4.3 Surgical Methods

4.3.1 Array Fabrication

All arrays used in this work were developed using the techniques and processes discussed in detail in Chapter 3. For clarity, there were two specific configurations used for these experiments. These included the Active and Passive arrays. Active arrays refer to electrically connected fully functional arrays. This includes the carbon fiber brazed into the diamond, connected to the PCB and encapsulated in Parylene-C with tip optimisation used (Figure 4.1A). Passive arrays involve the same carbon fibers, PCD substrate and encapsulation, however, lack the electrical connections (Figure 4.1B). The fibers were secured in place with cyanoacrylate as to reduce the complexity of fabrication to improve the efficiency of the experiments. This and allowed for the chronic experiments to be undertaken alongside the development of the active devices. The same tip preparation and tip treatments were used apart from the PEDOT, however there was no indication that the nanometre scale application of the coating impacted the insertion or immune-histological results shown.

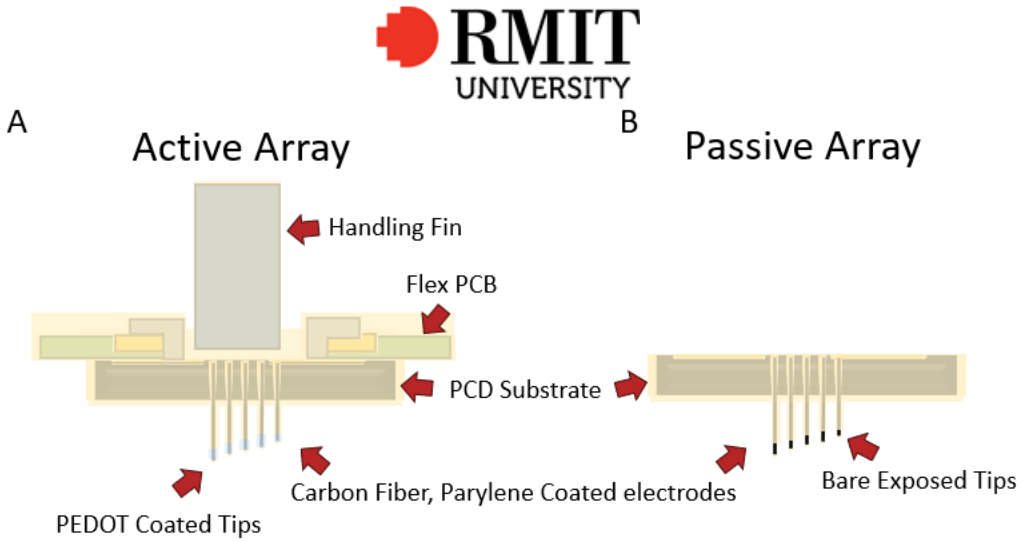

Figure 4.1: Visual diagrams of the active (A) and passive (B) arrays used for in vivo experimentation.

4.3.2 Animal Surgery technique

All experimental procedures were approved by the University of Melbourne Animal Ethics Committee (Ethics Approval #22494) and conformed to the policies of the National Health and Medical Research Council of Australia (NHMRC).

Animal experiments were performed on adult Long Evans Rats. Arrays were all inserted into the primary visual cortex (V1), typically in the right hemisphere. To achieve this, animals were anesthetized using 5% isoflurane in an induction chamber and transferred to a nose cone within a Harvard Surgical Frame. Maintenance anaesthesia was provided between 0.8% for recordings and 1.5% for the rest of the surgical process. A temperature pad was employed to ensure the animal remained stable and monitoring was performed to demonstrate no negative impacts on the animal. After the removal of the skin and cleaning of the skull using a scalpel blade, a 6 mm x 6 mm craniotomy was performed to expose the animal's neural tissue (Figure 4.2). Holes were drilled surrounding the craniotomy window to allow for stainless steel screws to be fixed for grounding during electrophysiology recordings and to aid in the head cap adhesion for the chronic recovery surgeries. The dura was removed with a fine needle to expose the pia and surface of the brain, with sterile saline saturated gel-foam being placed to keep the surface hydrated.

(explain these medical terms)

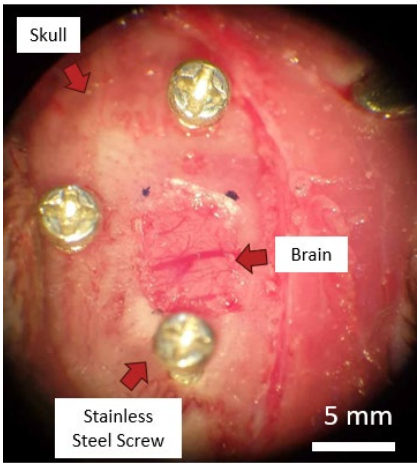

Figure 4.2. Surgical configuration of the incision, craniotomy window and the attachment/reference stainless steel screws.

4.3.3 Electrode Implantation

Arrays (sterilized with ethylene oxide) were fixed to controllable tweezers (mechanical or vacuum) for implantation. The tweezers were attached to a micromanipulator (Scientifica) and placed over the insertion window (Figure 4.3A). These were lowered until the fibers were directly adjacent to the surface of the brain. A camera with a macroscopic lens was used to visualize and record implantation. The fibers were inserted vertically into the brain from depths between 500 and 2000 µm at a speed of 7 $\mu m s^{-1}$. The success of the insertion was determined from the visuals provided by the camera where no excessive electrode bending, and retraction of the tissue dimpling was observed. For active arrays the devices were connected to a Blackrock systems head stage for signal recording using bespoke connectors (Figure 4.3E). For chronic surgeries the arrays were released from the tweezers and the manipulators removed. The chronic arrays were covered with silicone (Kwik-sil) and the entire craniotomy sealed with 3M UV curable dental cement (Figure 4.3C, D). The skin was sutured for complete encapsulation of the implant. Recovered animals were administered Buprenorphine and Meloxicam subcutaneously for analgesia for the first three days post-surgery. Animals were monitored twice daily for two weeks to ensure no adverse effects. Upon completion of experiments, animals were humanely killed using an intracardial overdose of sodium pentobarbital. The tissue was fixed via perfusion of 4% formalin and stored in refrigerators for postmortem analysis.

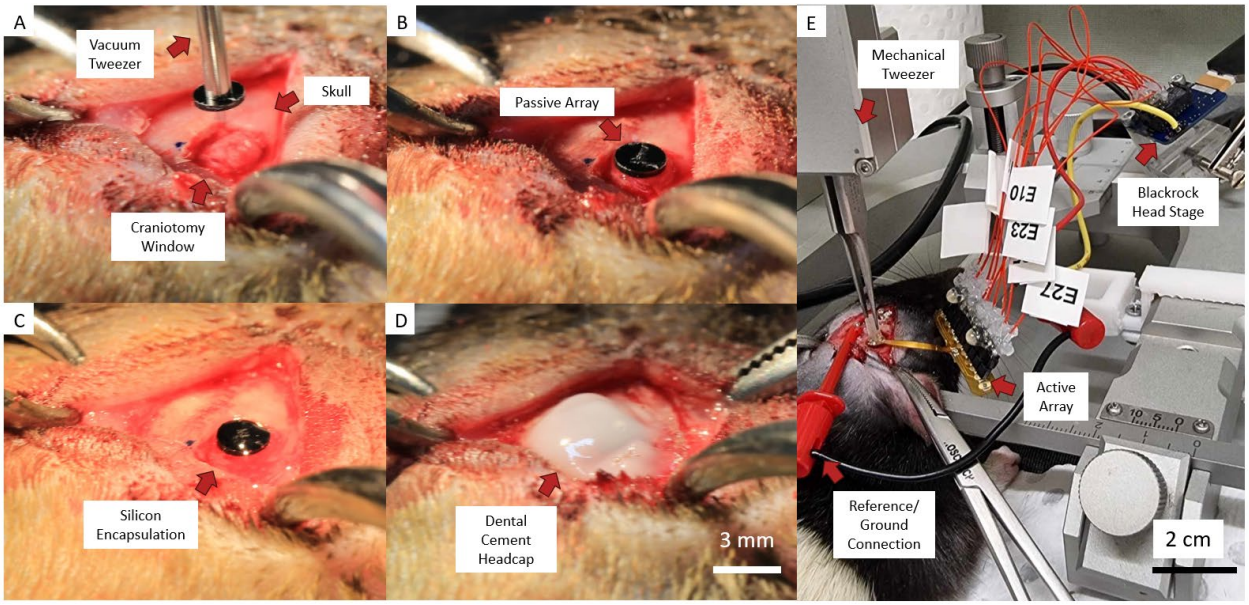

Figure 4.3. Passive array insertion using vacuum tweezers for Chronic Passive Array implantation into primary visual cortex (A, B). Subsequent silicon application (C) and dental cement headcap fixation (D). The active array insertion and recording set up including mechanical tweezer fixation for implantation and connector to Blackrock head stage (E).

4.3.4 Signal recordings

All signal recordings were acquired using a Ripple acquisition system (Ripple Neuro) at 30 kHz. These were displayed using Trellis so that signals could be evaluated at the time of experiment. The raw data collected underwent a high-pass filter above 300 Hz to remove any low-frequency noise. Kilosort was used as an automatic spike-sorting program to extract the spike waveforms of action potentials from the underlying baseline signal. Spike clusters were further processed by Phy to obtain known curated waveforms only. 10,000 random spike waveforms from each single cell were collected from the raw data trace. These were

(Trellis?)

Phy? Is this software?

made up of waveforms 1ms before and 2ms after spike time (-30 to 60 samples from the spike detection). These waveforms were averaged to normalize the baseline detected to equal 0. The signal-to-noise ratio (SNR) was calculated as the ratio between the mean waveform for a unit and twice the standard deviation (SD) of that waveforms noise [230].

4.3.5 Micro-CT Scanning

To visualize the position of the array upon completion of the chronic experiments, micro-CT was performed. Due to the fragility of the device and the surrounding tissue, it is not as simple as removing all of the fixings and encapsulation to observe the array and tissue postmortem. It would be impossible not to disturb array in the process of removal, and hence it would not produce an accurate assessment of how the array was contained within the tissue. Micro-CT allows visualization of the array, specifically the fibers as it sits *in vivo*. To achieve this the perfused rat's head was removed and placed within 4% formalin for 24 hours to fix the tissue. The entire head was scanned at low resolution (10.3 µm) to generate the bulk of the image (i.e. the skull and headcap). High resolution (3 µm) scans were used to image the carbon fibers still inside the neural tissue. The segmentation of these images was performed using 3D-Sliver (Version 5.2.2). Ansys SpaceClaim (Version 2021R2) was used on the high-resolution images to enhance the definition of the carbon fibers. These reconstructed 3D models were combined to create the final model produced.

4.3.6 Immuno-histological Staining

For immunohistology the headcap was removed from the tissue from animals post chronic implantation. Skull decalcification was performed by incubating the tissue in 0.25M EDTA solution at 5 degrees Celsius for 7 days as performed in [104]. A section of brain was removed from within where the craniotomy was located. Brain slices were obtained from the cleared tissue (tissue clearing kit ab243298, Abcam) as per manufacturer's instructions. Different antibodies were used for immunohistology. The primary antibodies were GFAB (chicken, ab4674, Abcam) and IBA 1 (rabbit, Fujifilm Wako). Goat anti-chicken Alexa Fluor 488 (ab150169, Abcam) and goat anti-rabbit Alexa Fluor 647 (ab150083, Abcam) were used as the secondary antibodies. The prepared samples were imaged using a z-stack scan on multiphoton and light sheet microscopes. ImageJ and MATLAB software were used to quantify GFAB and iBa1. The location of the electrodes was detected manually.

4.4 *In Vivo* Results

4.4.1 Electrode Array Insertion

Successful insertion of 25 electrode (tapered 1-1.5mm and straight 1.5mm) arrays was achieved repeatedly into the neural tissue of Long Evans Rats. This was confirmed optically and through the release of the arrays where they remained in place after release. All arrays used were imaged using SEM to confirm the tip morphology and straightness of electrodes were consistent to remove added variables. All arrays were inserted into similar areas of the cortex with the hydration level and condition of the tissue being kept as pristine as possible to limit these playing a role in the insertion success. Numerous animals (n=9) were used to account for any differences resulting from the *in vivo* nature of the experiment. The insertion speed of 7µms^{-1} was found to be the most viable for implant insertion success. This is conducive to previous work wherein slower insertion speeds have been indicated to produce more favourable insertions for flexible microelectrodes and provide less damage upon insertion [221, 225].

As stated previously, much work has been done on the insertion of carbon fiber and other various micro-electrode arrays into neural tissue, but no group has ever implanted a configuration of carbon fibers like those produced in this work. The 100 µm pitch of electrodes, number of electrodes and the Utah-like configuration of the device are all novel. The bed-of-nails effect that is seen on electrodes of this configuration would be a major problem that is not observed with the planar designs seen in related work on planar carbon fiber arrays [84, 104, 238]. There was no obvious damage to the electrodes or the PEDOT coating as could be seen in SEM images taken before and after implantation (Figure 4.4).

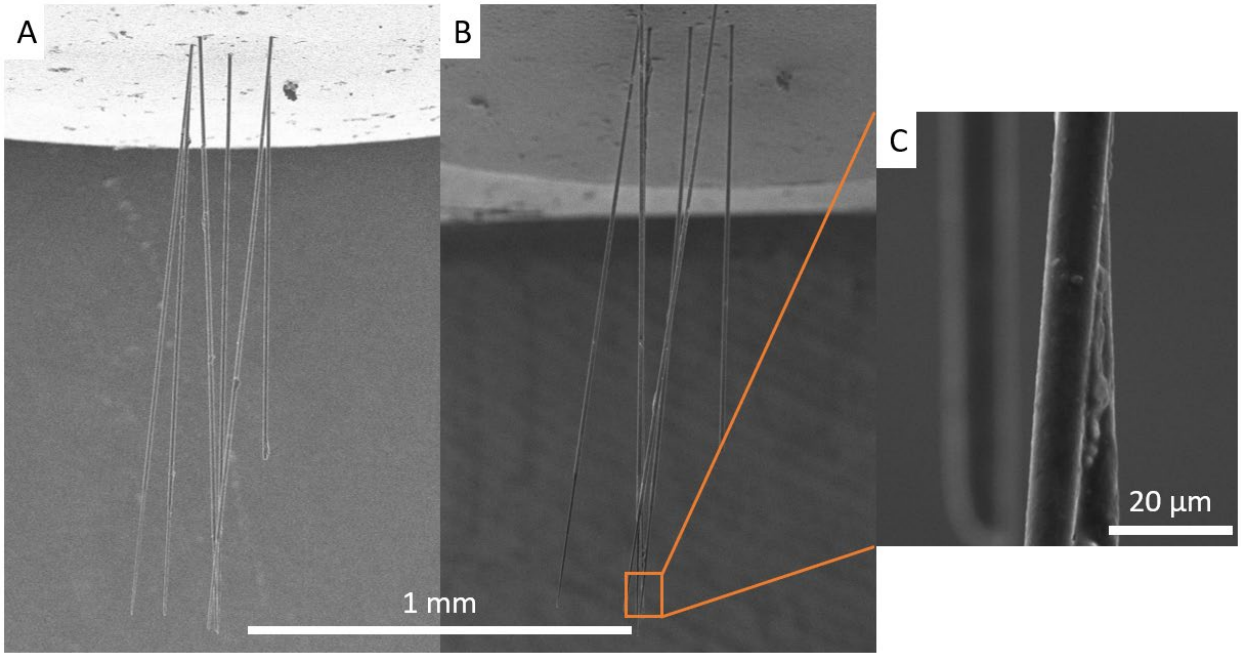

Figure 4.4. SEM images of carbon fiber electrode array before (A) and after (B) insertion into neural tissue. No obvious damage can be seen on the PEDOT coating as a result of the implantation (C).

Finding an effective method to verify the success of the insertion was a major challenge overcome. This was performed by viewing the electrodes during implantation and by observing the array after releasing. Force measurements of the insertion were considered to assess insertion viability. This was left for future work as the implantation of the equipment required proved too complicated for this stage of development. If the insertion was not successful, the spring force of the bending electrodes that have not penetrated would expel the array. This also informed some design choices for the Active Arrays and their connections (i.e. PCB designs). To this effect the camera set up used as well as releasing mechanisms were in combination a good indication of successful implantation. The camera utilized was able to record video and images of the insertion as seen in Figure 4.5. The depth of field and magnification available allowed for the viewing of most of the fibers throughout majority of the insertion. This was not without challenges as the line of site required to see the implantation proved difficult in some situations owing to the short length of the fibers and the presence of saline within the cranial window. The images do clearly show a successful implantation with the initial bending of electrodes, the dimpling of the tissue and the subsequent release of this dimple as the electrodes penetrate the tissue (Figure 4.5). Observing these key steps during the surgery is important as these moments occurred before the saline that was applied to the cranial window covered the entire array and removed the ability to observe final moments of the insertion. In instances where insertion was not successful, excessive bending of the electrodes was

evident and the dimpling would be drastic and not release before the point at which the line of site was lost.

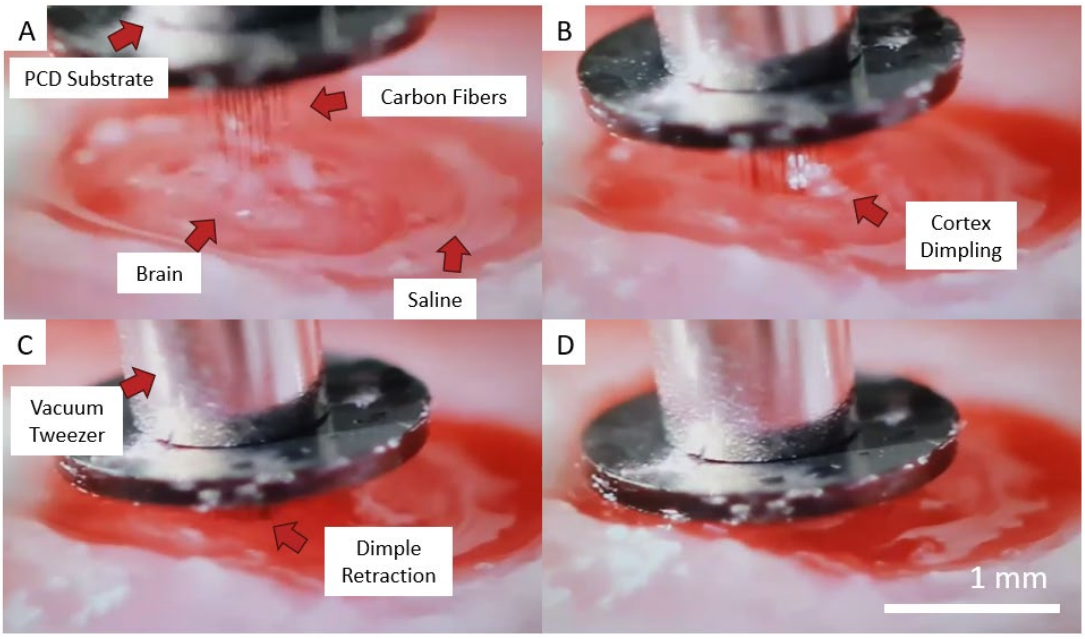

Figure 4.5. Passive carbon fiber array insertion for chronic implantation. Initial penetration of fibers into the neural tissue (A), dimpling of the cortical surface as the array is inserted (B), subsequent retraction of dimpling as the array is accepted into the neural tissue (C) and the complete insertion of the device (D).

Using the release of the arrays as a marker of successful indication provided somewhat mixed results. For much of the passive array implantation, vacuum tweezers were used to secure the flat topside of the arrays. This worked well to hold the arrays and provide the parallel force through the electrodes. However, some issues were encountered upon attempting to release the arrays. The presence of the saline and the seal that was created by the vacuum meant that the release was not as simple as turning the vacuum off. The back of the array had to be pressed on to disrupt the vacuum seal. This left some ambiguity on whether the array was being pulled out by the tweezers themselves or rejected by the tissue and bent electrodes. This issue was not seen later with mechanical tweezers, as the holding fins placed on the back of the arrays could be immediately released. The tweezers did allow for the retraction of the arrays if the device had not been released yet. This allowed for multiple insertion attempts for a single device with no damage to the arrays. In some instances, up to 4 attempts could be made with successful implantation.

To test the scalability of the array insertion, the 100 and 1024 passive electrode arrays (fabricated in Chapter 3.4.5) were also inserted into rat visual cortex (Figure 4.6 and 4.7, respectively). This was performed using mechanically controlled tweezers to hold the arrays and a linear manipulator at a speed of 7 μms^{-1} to control insertion. A larger 8×8 mm craniotomy window was opened for these tests to account for the larger footprint of these arrays and to still allow avoidance of blood vessels. For the 100-electrode carbon fiber array, the dimpling and tissue response observed appeared similar to the previously tested arrays with fewer electrodes (Figure 4.6B). Due to the size of the array and the associated difficulty with observing each electrode, the clear retraction of the dimpling was not able to be observed. The dimpling, however, appeared to hit a maximal deflection (Figure 4.6C). The fact it did not appear to increase past this point indicates the fibers were penetrating the tissue and not just bending. This was further confirmed by observing the positioning of the surrounding tissue upon complete penetration of the fibers (Figure 4.6D).

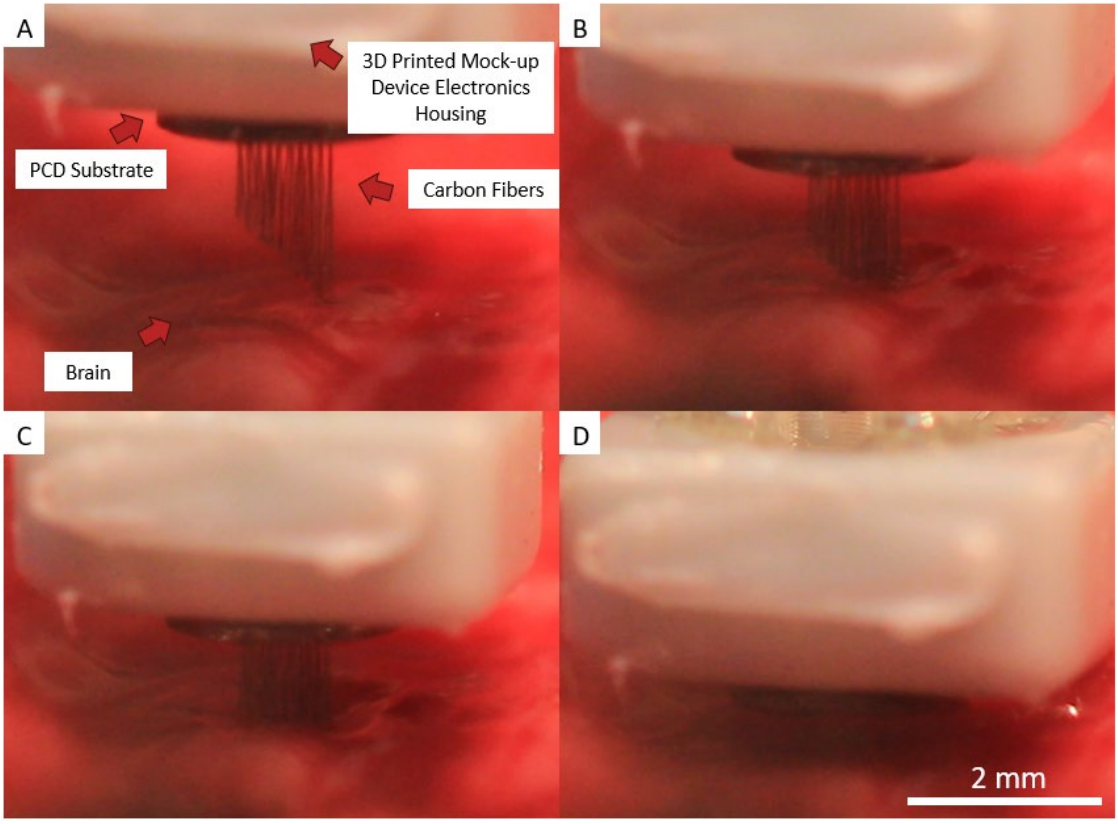

Figure 4.6. Passive insertion of the 100-electrode carbon fiber array. Electrode lengths were tapered from 2 mm to 1 mm (A). Some dimpling of the tissue can be seen (B and C) with the entire array appearing to successfully penetrate the tissue (D).

Similar to the 100-electrode array, the 1024-electrode array introduced some complexities when trying to visualise and assess the successful insertion of the implant. The increased electrode number resulted in restrictions to visibility of the implantation, as well as a vast increase in the accumulation of saline and fluids around the hydrophilic electrodes (Figure 4.7B). This made it difficult to see the individual electrodes and, as such, the tissue itself would be used to assess the success of the implantation. The fluid accumulation could, however, aid the insertion as it would help prevent the tissue from drying out during the process. A larger craniotomy window was successfully opened to accommodate the larger footprint of the electrodes (3.1×3.1 mm) and it appeared that minimal vasculature was present in this area to impede insertion (Figure 4.8). The before and after images of the tissue also do not show any overt signs of tissue damage or bleeding (Figure 4.8B). Dimpling was again observed during insertion (Figure 4.7C), however, like that seen in the 100-electrode array (Figure 4.6C), the dimpling appeared to hit a maximal deflection. The position of the tissue in Figure 4.7D indicates that the electrodes were able to penetrate after this point as the dimpling had not increased. Despite no evident bending of the electrodes, the fluid obscuring the view of the individual electrodes does still leave a level of ambiguity for the success of the insertion. At the very least, these results indicate the promise of using larger electrode numbers, as no catastrophic failure or adverse effects to the animal or tissue were observed. This indicates the requirement for further testing, building towards an increased electrode number of electronically active arrays.

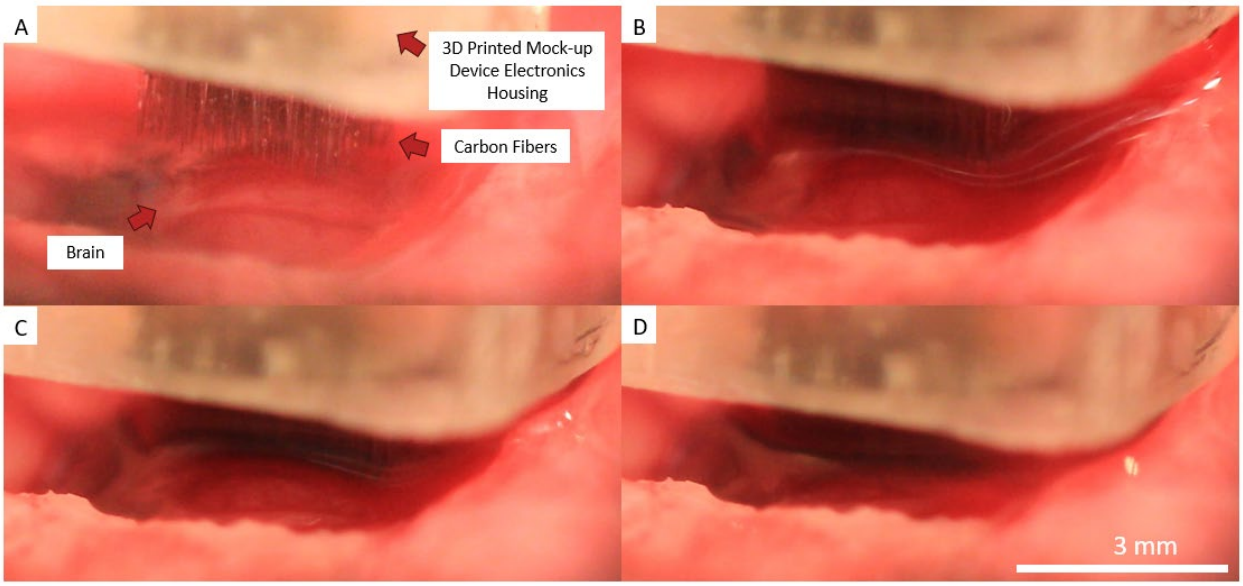

Figure 4.7. Passive insertion of the 1024-electrode carbon fiber array. Electrode lengths tapered from 1.5 mm to 1 mm in a unique geometrical pattern (A). Some dimpling of the tissue can be seen (B). The accumulation of saline and the size and geometry of the implant obscuring the final view of the electrodes upon complete insertion (C and D).

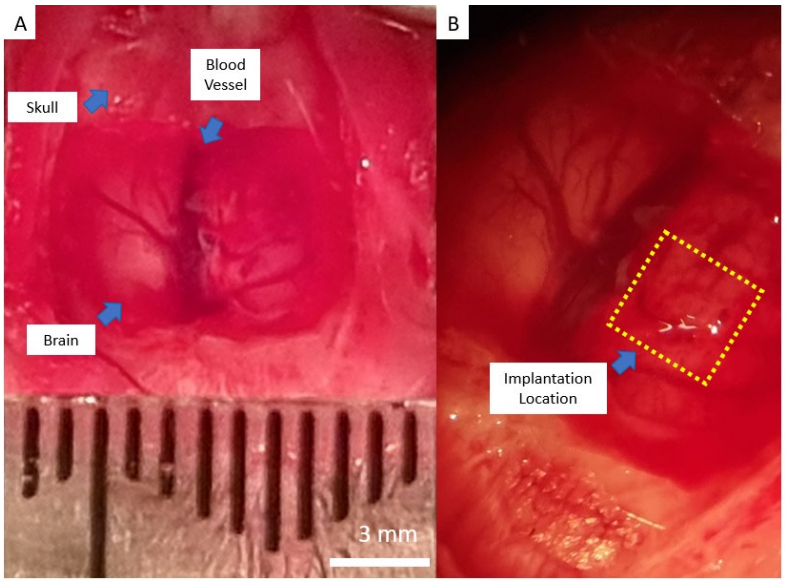

Figure 4.8. Craniotomy window for the insertion of the 1024-electrode array before (A) and after (B) insertion. Insertion location indicated by yellow dashed line, showing no obvious signs of tissue damage upon removal of the array.

Having demonstrated the correct procedures to insert the passive arrays, the insertion of the active arrays proved ~~minimal~~ to be a minor challenge (Figure 4.9). The configuration of the device with the PCB may have been different but due to thoughtful design considerations this had no impact on the insertion of the devices. This was aided by the fact that the electrical signals (be it the noise levels or the neural spiking) could be used to indicate successful insertion alongside visual observation of the electrodes. The size and flexibility of the PCBs were very conducive to the insertion techniques. They did not impact the acute surgery

protocol or the implantation. These would need to be reviewed for chronic implantation as the pins on the PCB were not biocompatible. This will be considered for future work.

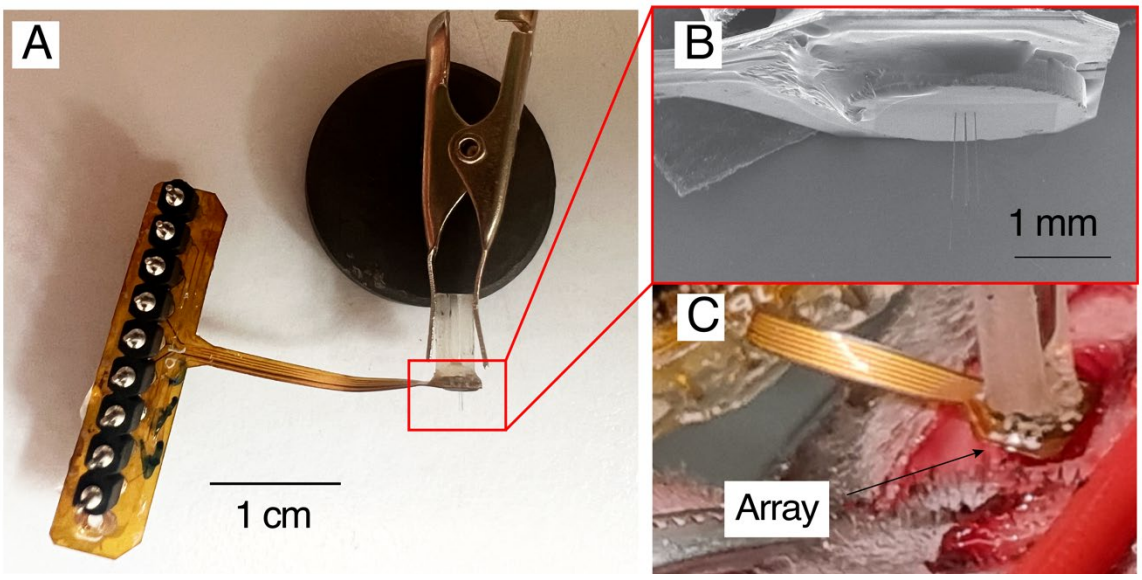

Figure 4.9. Active array implantation for acute neural recording. 9 channel array (optical image (A) and SEM (B)) that was inserted into the visual cortex through a craniotomy window (C).

4.4.2 Immuno-histological Results

Immuno-histological data was collected to show the extent of chronic inflammation caused by the implantation of the array. This was performed on passive arrays implanted for periods up to 6 months. The stained slices were able to successfully show the trajectory of the fibers through the neural tissue on both the coronal and sagittal planes (Figure 4.10). The staining showed the presence and distribution of microglia (Red IBA1 stained cells) and astrocytes (Green GFAP stained cells). The distribution in areas distal to the electrodes showed levels that would be expected in healthy tissue, indicating there was no issues with the staining. The glial scarring present at the electrode site was at most 20 µm. The minimal response seen is consistent with the work by Patel et al. for chronically implanted planar carbon fiber arrays [104]. This is drastically less than that seen in Utah Arrays or other stiffer alternative implantations where the thickness of scarring is greater than 100µm [59, 96]. This is significant as at this scale as distances greater than 50µm will greatly effect signal acquisition [239, 240].

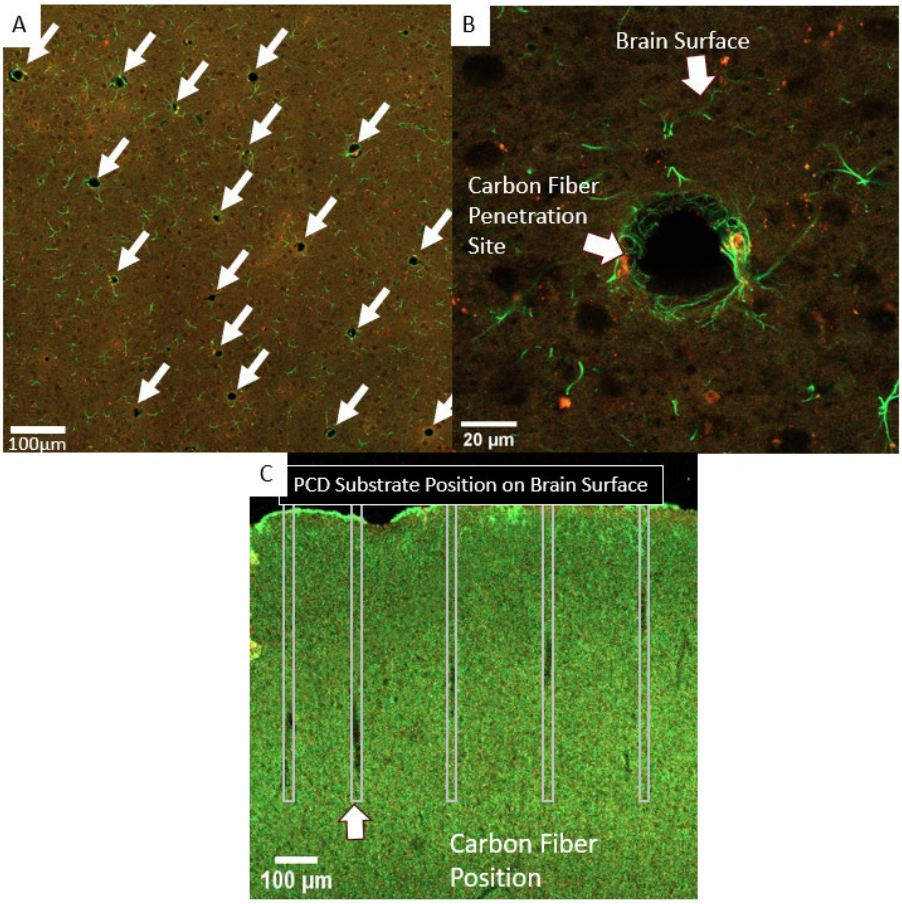

Figure 4.10. Immunohistology slices of the rat brain after 3 months of electrode implantation. A sagittal plane slice taken proximal to the surface of the tissue, arrays indicating the position of the fibers (A and B). Coronal plane slice to show the cross section of the length of the electrode within the neural tissue The GFAP and IBA1 maximal responses were only present within 20 µm from the electrode positions for all samples.

The distribution of the fibers in Figure 4.10A show that the fibers were not in the perfect alignment of the 100 µm pitch grid. This is not surprising as the SEM images of the devices showed some straightness issues. This is further exacerbated with any clumping of the electrodes upon insertion. The spacing between the fibers is still consistently close to 100µm, meaning that the overall coverage of the recording area would not necessarily be meaningfully impacted. The coronal slicing (Figure 4.10C) demonstrated that the electrodes maintained a straight trajectory upon insertion. The staining in this slice showed the level of FBR observed was not different along the length of the electrode. Samples for staining were not prepared from acute experiments. This was deemed unnecessary as it is primarily the chronic inflammation effects that were of concern. The presence of acute signals indicated that the level of acute inflammation was low enough to not disrupt signal acquisition. Meaning that if there was initial inflammation that occurred it dissipated quickly or had no meaningful impact on the functionality of the electrodes.

The CT scan performed was able to show the array while it was still in position. These reconstructions categorically showed that not only did the electrodes penetrate the tissue, but they also remained in place chronically. The carbon fibers seen in Figure 4.11A-C appear mostly straight. The general positioning of the fibers in the CT scan resembles how the array appeared before implantation using SEM (Figure 4.11D). The SEM image also shows that all of the electrodes remained intact during the entire process. One fiber can be seen to be missing in the CT scan; however, this same fiber had been broken during fabrication

and as is seen in the SEM. The PCD substrate seen in blue appears to be aligned with the skull as expected, meaning that it too did not move post-surgery.

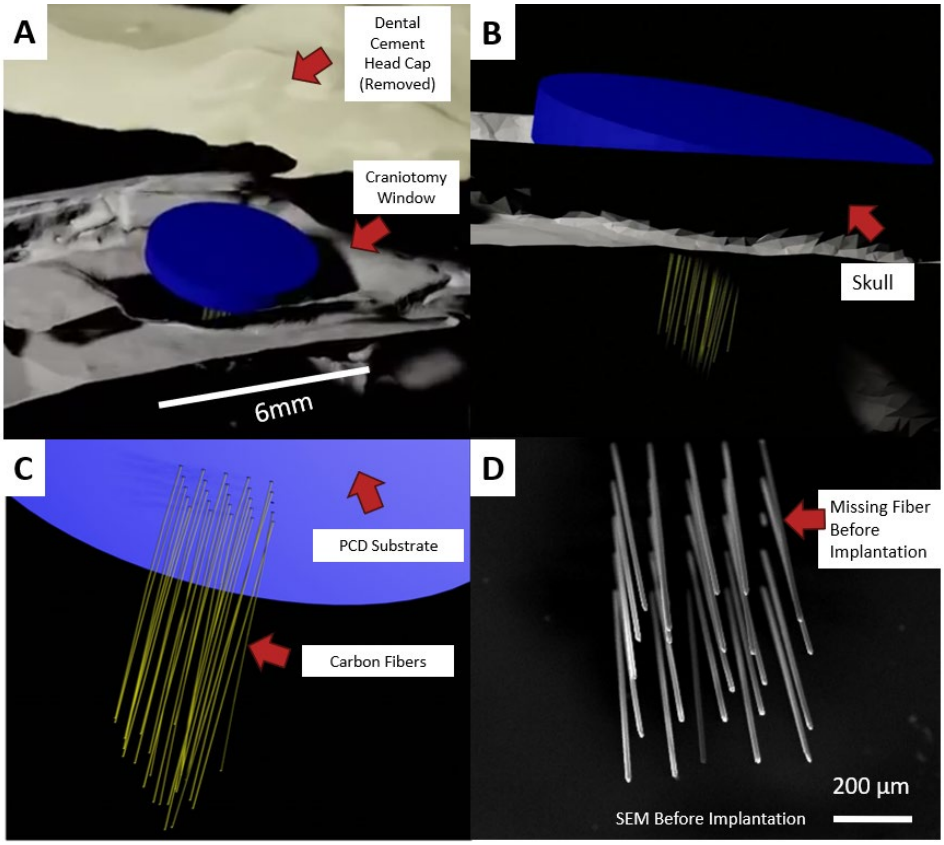

Figure 4.11. CT scan showing the position of a Passive Array within rat visual cortex 3 months post implantation (A). PCD substrate can be seen in blue, carbon fiber electrodes in yellow and the skull in grey. The position of the substrate relative to the skull cross section (B). The position of the electrodes within the tissue appears to be straight with successful implantation confirmed and maintained for this time period (C). SEM image of the same array before implantation showing consistent straightness as well as the missing fiber from the CT scan showing that this was not lost during implantation but rather during production (D).

4.4.3 Signal Acquisition

It's confusing to use the same symbol 'n' for 3 different values. I suggest you use subscripts, or different symbols, c for number of channels, d for devices, r for rats.

Electrical recordings were successfully obtained from live rat visual cortex. Spikes were observed across multiple channels (n=3), on multiple devices (n=6) and implanted in multiple rats (n=3). The signals detected contained signal to noise ratio between 2.4 and 5.4, with an average of 3.4. Examples of these spike wave forms and along with a 60-second recording of the raw trace can be seen in Figure 4.12. These results were very promising and show that the carbon fibers in this configuration perform at least, if not better than other comparable devices [45, 213]. Different electrodes in the same arrays were able to detect different neurons, as seen in the spike waveforms shown (Figure 4.12). This indicated that the coverage of the array over this spacing was adequate to potentially sample adjacent neurons, justifying the use of the high density 100µm pitch. Further testing is required to confirm this. The maximum number of channels that one array was able to record spikes from was 3. This was partly a manufacturing issue as well as a potential limitation to the electrode size and pitch. This array had 4 (out of a possible 9) functional channels when tested at the end of fabrication. The arrays were able to show recordings as shallow as 600µm and as deep as 1500µm (the full length of the electrodes). These results suggested that the core

concept of the design was successful and the electrical testing that was performed upon fabrication was validated through an *in vivo* model.

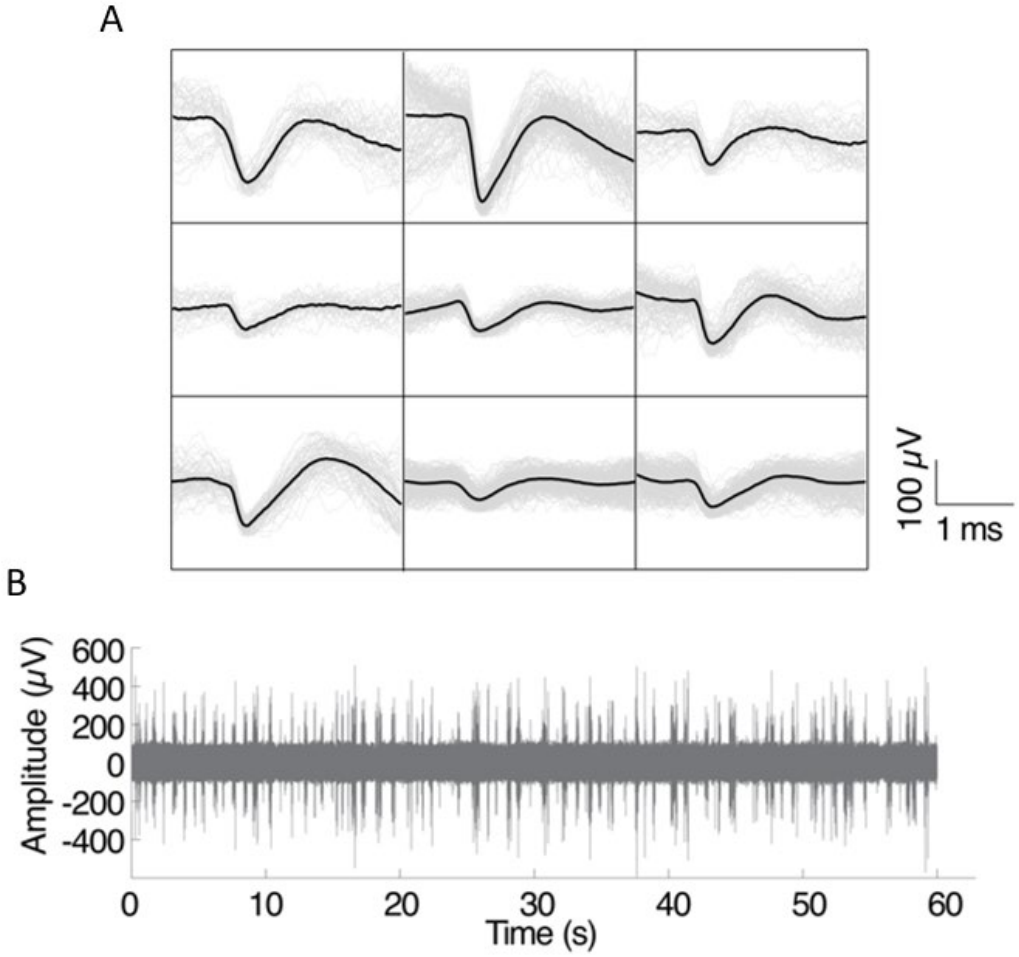

Figure 4.12. Representative neural spike waveforms from different channels recorded using various 9-channel carbon-fiber arrays (A). Unfiltered waveforms (grey) and the average waveform (black) are shown. Raw signal retrieved from one of these channels is shown (B) from a recording period of 60 seconds.

4.5 Future Work

The proposed device design showed the ability to be inserted into neural tissue, showed minimal chronic inflammation, and demonstrated an ability to record individual single-unit signals. More work is still required to completely validate this configuration of array for chronic recording with biocompatible electronics. This could also be expanded to include more channels; this would allow the electrical signals to confirm the successful insertion of the increased electrode number array. This was outside the scope of this work as there was not enough time for chronic recordings to be made after the laborious development process. This is why the Passive and Active Array works were delineated. The lack of chronic inflammation, the evidence suggesting the array remained intact and in place, as well as the acute recordings heavily indicated that this configuration of device would be viable for chronic use. Another area for further testing is the potential use of longer electrodes to reach different cortical layers and depths. More in-depth analysis of the recordings would also further add to the functionality of the devices.

why not?

Minimal analysis beyond spike shape, rates and size was performed on the data obtained. Using the devices to conduct neuroscience would give credence to the use of these electrodes for meaningful signal acquisition. Nonetheless, the fabricated devices showed an ability to produce signals in a configuration that had not been implemented before. Further improvements in the yields and manufacturing of these devices could provide much benefit in the field of neurological disease treatment and understanding.

Chapter 5: Deposition of Boron-Doped Diamond on carbon fiber bundles for Biosensing Applications

5.1 Chapter Outline

This chapter will describe the growth of a continuous and uniform coating of Boron Doped Diamond (BDD) carbon fibers for biosensing applications. This includes growth of diamond on carbon fibers, the fabrication of electrodes for electrochemical characterization as well as the physical characterization of diamond coated carbon fibers using techniques including SEM, TEM, Raman and EELS.

5.2 Chapter Introduction

To improve the effectiveness of the carbon fiber electrodes and expand on their list of potential uses, modification of the carbon fiber electrodes is usually required. An avenue for this is through the growth of carbon-based coatings on these electrodes to improve their electrochemical characteristics. These types of coating materials include carbon nano-walls and various forms of diamond. Previous work has shown successful growth of Nitrogen Doped Ultra-Nano Crystalline Diamond (NUNCD) and Boron Doped Carbon Nano-walls (B-CNW) [105]. This work will further explore the potential of a Boron-Doped Diamond (BDD) coating to explore an alternative coating that will elevate the utility of the carbon fibers for neural interfacing applications.

5.2.1 Current BDD Growths and Applications

Diamond presents many unique properties, such as biocompatibility, chemical inertness, and mechanical durability, making the material suitable for many biomedical applications. Diamond films can be deposited on various substrates using a process called chemical vapor deposition (CVD) [241]. CVD uses plasma to induce chemical growth onto the surface of a substrate, producing films with thickness in the nanometre to ~~micrometre~~ cm range (Figure 5.1A). Diamond growth on non-diamond substrates typically uses a form of CVD known as Microwave Plasma-enhanced Chemical Vapor Deposition (MP-CVD) to promote the nucleation of the diamond film required for diamond growth [242, 243]. Without this nucleation, the growth will be dominated by films other than diamond and show poor uniformity. Thin films in the nanometre to micrometre thickness range allow for surface modification of electrodes. Diamond and other forms of carbon have extensively shown a level of biocompatibility that has not been demonstrated with any other coatings [86, 244-246]. Conductive diamond coated electrodes also possess strong electrochemical stability, with a larger water window than other neural interfacing surface electrodes. For these reasons, conductive diamond ~~has presented~~ is a very promising electrode material for chronically implanted neural electrodes for recording and stimulation applications [247-249].

potential window in water

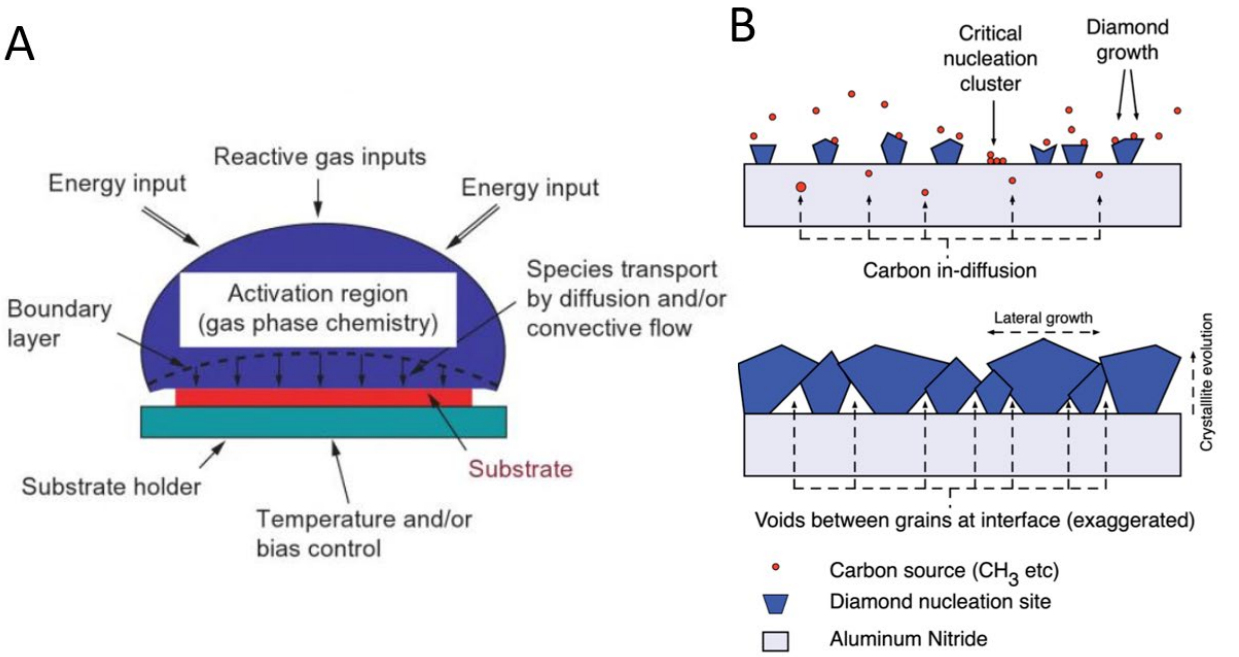

Figure 5.1. CVD plasma growth environment (A) [250]. Crystalline growth of nano and micro-diamond. Depicts the nature of void creation on a non-diamond substrate, highlighting the requirement for seeding as the critical nucleation cluster would be evenly distributed for a seeded sample (B) [251].

Diamond is innately an insulating material due to the sp^3 bonded carbon within the diamond crystal structure. The sp^3 bonding structure does not allow for the movement of electrons as they are each bonded within the dense lattice configuration. To enable electrical conductivity, the diamond film can be altered using different gases during the growth process. This modification of the film can enhance the electrical properties of an otherwise insulating diamond material via doping or changing the grain structure [252, 253]. A common means to achieve this is the use of nitrogen gas during the plasma growth to produce sp^2 graphitic rich grain boundaries between the diamond crystals [254, 255]. This sp^2 carbon bonding is conductive by virtue of the double bond present in the structure presenting an avenue for electron movement within the lattice.

Most forms of diamond growth contain crystals of varying sizes and orientations called Polycrystalline Diamond (PCD). Depending on the crystal size of PCD, it can be categorised into microcrystalline diamond (MCD) (crystal size in µm range), nanocrystalline diamond (NCD) (nm range) and ultra nanocrystalline diamond (UNCD) (<5 nm) [252, 256, 257]. The size difference is a result of the lateral growth within the crystals, a feature that is normally accentuated for larger film thicknesses (Figure 5.1B). However, if re-nucleation of diamond crystals is able to occur during the growth, the deposition of consecutive layers of smaller grain sizes is possible [258]. These different crystal sizes will produce different properties, both physically and electrically. Larger crystal grain sizes result in the diamond being less conductive as more of the film is in the insulating sp^3 bound diamond lattice [259]. Alterations in the films existing grain to boundary ratio ~~relationship~~ has been investigated for improving the capacitance of potential NUNCD films for electrochemical applications [253]. When boron is introduced during deposition, the diamond film becomes conductive due to the addition of holes to the binding structure, meaning the grains themselves are conductive and it is not just the grain boundary addition of sp^2 carbon producing electrical conductance [260]. The degree of doping is also another avenue to alter the growth mechanics and hence the characteristics of the produced film [261].

An alternative form of CVD grown carbon is Carbon Nano-Walls (CNW). CNWs are made of vertical graphitic sheets and grow outwards from the surface [262]. The growth mechanics of CNW begins with the adsorption of CH_3 radicals from the plasma onto the surface to create nucleation sites (Figure 5.2) [263]. Small graphene sheet propagation on carbon nano-islands leads to 2-Dimensional growth and eventually larger graphene sheets. These graphene sheets grow in multiple directions, however, larger sheets propagate vertically due to the growth mechanics favouring this orientation. CNW tend to grow preferentially at higher temperatures (greater than 1000 degrees Celsius) than diamond especially in growths containing higher levels of methane as a feed gas for the plasma [264, 265]. CNW elicit very low electrochemical impedances owing to their large effective surface area and therefore provide a promising alternative coating for neural electrode materials [266].

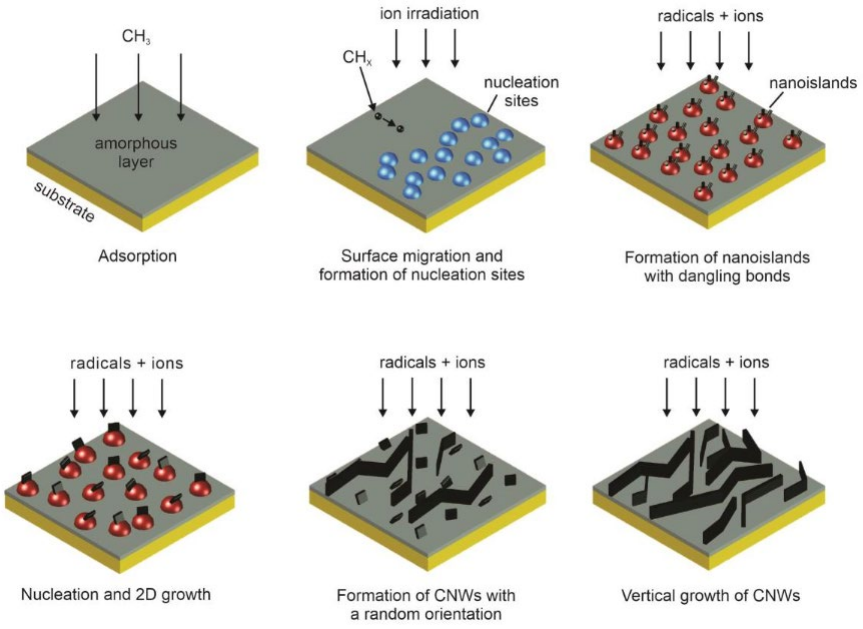

Figure 5.2. Visualised growth mechanisms of CNW [263], showing the adsorption of CH_3 leading to nucleation sites. The addition of ions from plasma leads to 2D growth into the eventual CNW formation. These CNW continue to grow vertically perpendicular to the substrate.

Alternative growth parameters may produce films with composites of diamond and other graphitic carbons with potentially tuneable electrochemical characteristics [267-272]. Many of these films include CNW and Diamond hybrid materials (Figure 5.3). These films may exhibit characteristics that combine the benefits of large geometric surface area and high conductivity from CNW morphologies with the electrical and chemical stability from diamond [188]. Sethy et al. produced growths that allow for increased current injection of NCD films with larger percentages of graphite [273]. Sobaszek et al. explores the increased charge storage capacity of sp^3-rich CNW-Diamond hybrids [268]. Silva et al. demonstrates the tuneable electro-wettability of hybrid Diamond-CNW made using a uniquely porous configuration consisting of a sacrificial substrate [274]. Zhoa et al. produced NCD growth on CNW sheets at different boron doping characteristics for electrochemical sensing [275]. The improved potential windows of the composite electrodes compared to other carbon-based films allowed for larger currents to be used for sensing and hence a larger signal to noise ratio for their measurements.

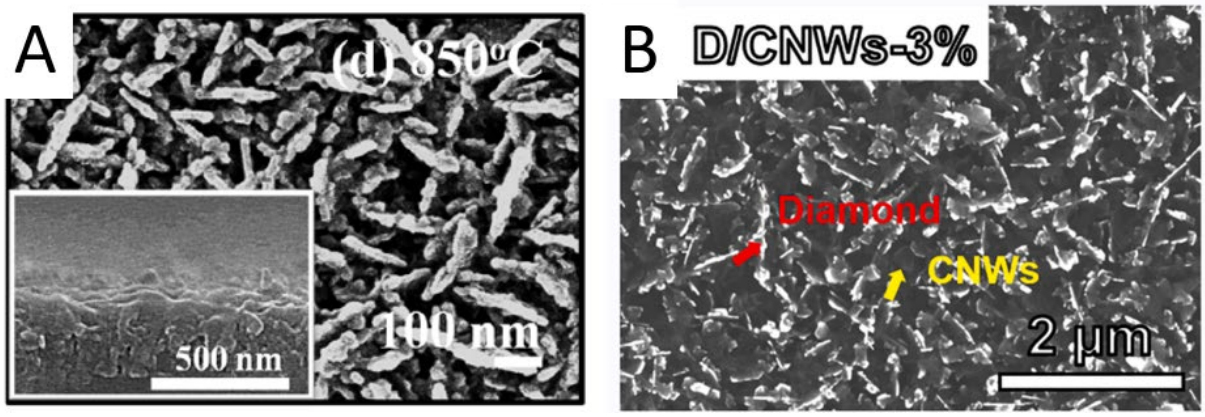

Figure 5.3. Examples of CNW and Diamond composite films. A depicts more graphitic like structured films [273]. B shows more conventional CNW films with ND surface coatings [275].

The creation of neural electrodes using CVD-grown thin carbon-based film is primarily limited by the parameters that are required for the growth of such films. In MP-CVD the process requires extreme growth temperatures exceeding 1000°C degrees Celsius. The substrate also needs to be exposed consistently to the highly reactive plasma within the CVD to allow for the appropriate chemical reactions to take place to grow consistent and reliable films (Figure 5.1A). Samples not made of diamond themselves require a nanodiamond seeding layer to propagate a uniform growth on these substrates. Many of the diamond coated arrays that have been developed for neural applications have been planar and utilize thicker substrates of silicon and diamond [247, 276]. Diamond coated microwires are a promising avenue to achieve such a device [170]. Boron doped UNCD has been used with microwires of 25-50 µm metals including Niobium, Tungsten and Tantalum in the past for both electrical and neurotransmitter detection [277, 278]. These electrodes have been further functionalised using a polymer coating of Parylene-C to provide an insulating layer to control functional electrode length. These electrodes required electrochemical treatment to remove the surface damage and polymer residue that arises from the laser deinsulation required to make them functional active electrodes. Another alternative microwire electrode material that is conducive to UNCD growth is Carbon Fiber. These have been explored with nitrogen doped UNCD and other forms of graphene for sensing applications [105].

5.2.2 Growth of BDD on Carbon Fiber

Previous work has demonstrated an ability to grow diamond and other carbon-based films on carbon fibers [105, 279-281]. Hejazi et al. successfully demonstrated the ability to uniformly grow nitrogen doped UNCD as well as a boron doped CNW on the surface of the carbon fibers. These electrodes were able to record single unit neural signals and exhibited improved stimulation capabilities compared to carbon fibers.

The nitrogen doped UNCD was susceptible to physical delamination, especially when compared to the CNW coated fibers. This indicates a potential physical benefit to a composite material or the attenuation of the growth to the fiber tips. Millan-Barba et al. created Diamond and CNW coated fibers that displayed uniform coating [279]. This group used a very large bundle consisting of a large number of carbon fibers and demonstrated that the coating improved the conductance of the fibers. Pereira et al. and Bennett et al. showed the capacity to produce Boron Doped Diamond (BDD) films, however none of these were able to uniformly coat the electrodes and showed limited suitability for electrochemical sensing [280].

Coating uniformity was greatly improved by seeding the carbon fibers with nano-diamonds. This can be further enhanced by electrochemically grafting functional groups onto the surface of the carbon fiber to allow for greater adhesion of the nano-diamond seeds to the fiber surface [105]. The orientation of the carbon fibers within the CVD growth chamber will also have a major impact on the growth characteristics. This is due to the fact that the microwave power, gas distribution and temperature that dictate the growth will be differentially distributed throughout the chamber [282]. These coatings also showed varying levels of carbon nano-wall and diamond growth that will also produce different film characteristics. Various groups have also demonstrated the ability to create a uniform growth of carbon nanotubes onto the surface of carbon fibers to improve the electrical conductivity of and altar the physical characteristics of the fibers [283, 284]. Therefore, there is benefit in exploring this coatings potential for use with carbon fiber. The growth of an improved and uniform coating over the carbon fiber could expand the potential of carbon fiber electrodes for neural interfacing.

5.2.3 Neurochemical sensing applications for NCD

Neurochemical sensing can be used for disease detection and potential treatments. Currently there is a lack of electrodes suitable for chronic neurochemical sensing. FSCV techniques for dopamine sensing using carbon fiber has been proven *in vivo* however has shown very limited chronic capacity [197, 285-287]. The Patel et al. device constructed for chronic implantation only successfully demonstrated dopamine sensing for 1 month post implantation [104]. Due to the constraints of FSCV (Refer to 2.4.4), electrode size and electrochemical properties will dictate the appropriateness of an electrode for high-sensitivity FSCV measurements. Carbon fibers are able to produce an ideal background current for FSCV due to the stability and magnitude of the background current aiding in analyte detection [286]. Carbon fiber electrodes have demonstrated sensitivities conducive to dopamine sensing at concentrations found in human neural tissue. Due to the voltage range required to perform the measurements outside the water window of carbon fiber, the surface degrades over time rendering the electrodes unable to perform chronic measurements. Biofouling adds to this issue, whereby proteins accumulate on the electrode surface after prolonged implantation resulting in even worse sensitivity over time. NCD coatings have been shown to remove both of these limitations in other configurations [255, 281, 288-290].

Another method for dopamine detection is Multiple Cyclic Square Wave Voltammetry (MCSWV) [158]. This method is able to detect tonic levels of dopamine and solves a potential limitation of FSCV. This is done using square-wave forms in conjunction with delayed holding potentials to manipulate the adsorption of dopamine to the electrode surface. This has many of the electrode constraints that FSCV does and like FSCV has been shown to be compatible with carbon fiber microelectrodes for acute experiments. Again, due to the voltages required and repeated cycles needed the carbon fiber is not applicable for chronic applications. No diamond-based electrodes have ever been used to obtain MCSWV dopamine results. Therefore, in this chapter, I propose to use a NCD coating to alleviate these chronic issues of electrochemical dopamine detection. The NCD is expected to maintain the electrode characteristics that make carbon fiber a suitable material for this purpose.

5.3 BDD Carbon Fiber Growth Methods

5.3.1 BDD Diamond Growth

To allow for optimal CVD growth with a continuous coating on the surface of the carbon fibers, pretreatment steps are required. The first step is the addition of amino phenyl groups to the carbon fiber surface using an electrochemical method [87]. The 3-electrode electrochemical cell (Refer to 2.4.3) was set up using a Gamry Potentiostat (Interface 1000E). An Ag/AgCl and a Glassy Carbon electrode were used as the reference and counter electrodes, respectively. Two separate solutions were used for these processes. Firstly, an acetonitrile solution containing 0.1 M of tetrabutylammonium tetrafluoroborate (purchased from Sigma) and 1mM nitrophenyl diazonium tetrafluoroborate (purchased from Sigma) was used. Five CV cycles were performed between 0.2 and -0.6 V at a scan rate of 200 mV/s to form a nitrophenyl film at the carbon fiber surface (Figure 5.4A)[185]. Samples were rinsed with acetone and DI water. The second solution used was 0.1M H_2SO_4. Five cycles were performed again with voltages between 0.5 V and -1.5 V at the same scan rate of 200 mV/s (Figure 5.4B). This left aminophenol groups at the surface of the carbon fiber. The samples were rinsed sequentially again in acetone and DI water.

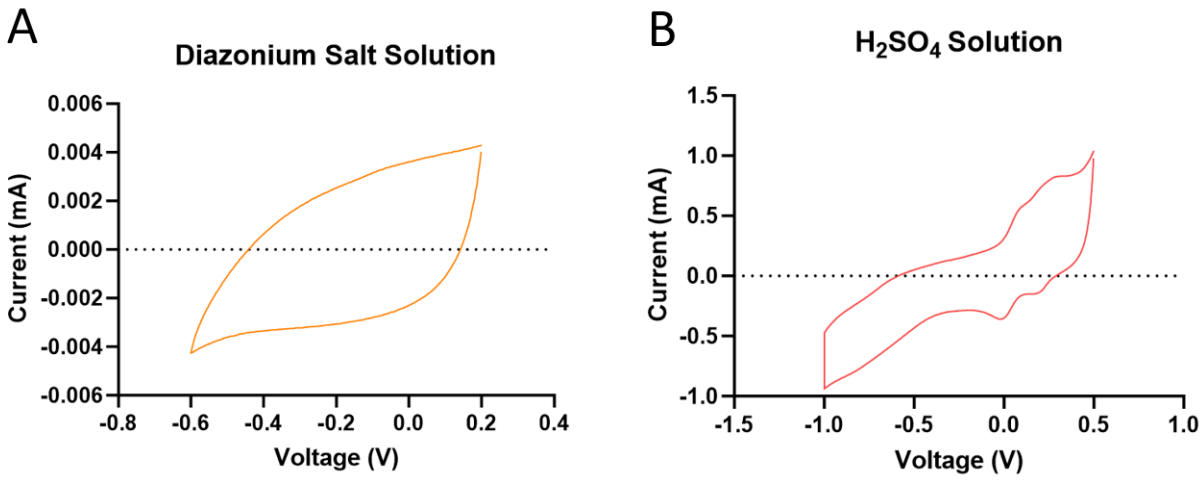

Figure 5.4. Cyclic voltammetry cycle from the diazonium salt solution (A) and H_2SO_4 solution (B) for the electrochemical seeding preparation.

The aminophenol groups added to the carbon fiber surface allow for the adhesion of seeded nanodiamonds required for CVD growth. The nanodiamond solution is described elsewhere and was prepared by a collaborator [186]. The solution contained a concentration of 8.47 x 10^7 particles/ml with an average particle size of 35-40 nm [105]. The pretreated fibers were soaked in the oxygen terminated nanodiamond solution for 24 hours within 48 hours of CVD growth. The fibers were rinsed with DI water and subsequently dried using nitrogen gas.

The bundle of fibers was placed on a molybdenum puck and secured between two further pucks (Figure 5.5). A 3D printed titanium cage was placed over the exposed end of the fibers with the bundle spread evenly throughout the cage. The titanium cage allows for the attenuation of the plasma evenly around the bundle of the fibers leading to more consistent growth mechanics. The separation between fibers in the bundle also allows for a more consistent growth as well as reducing the chance of the growth connecting adjacent fibers. A gas mixture of 95.5% H_2, 3% CH_4 and 1.5% trimethyl boron (TMB) was used

Check this value. This is huge! I'd expect the B conc in the gas to be around 1000ppm, not % levels.

to create Boron Doped Diamond (BDD). The deposition time was 60 minutes using a pressure of 40 torr and a microwave power of 1500 W. Samples were allowed to cool completely under turbo vacuum to ensure no degradation of the titanium cage.

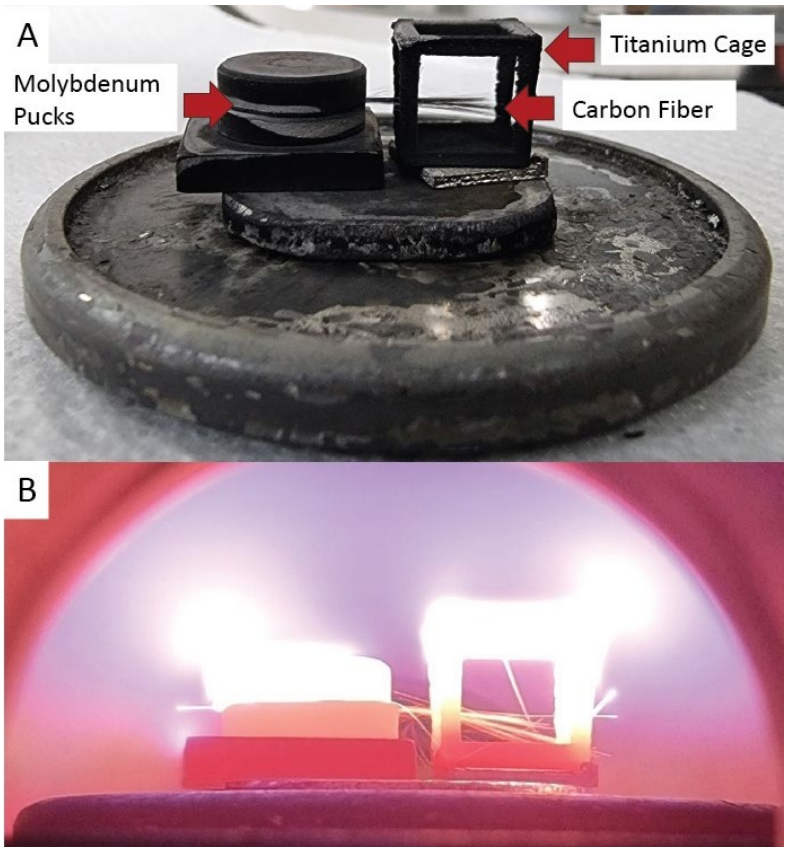

Figure 5.5. CVD set up with carbon fibers situated within a titanium cage held in place with molybdenum blocks post (A) and during growth (B).

5.3.2 Electrode Fabrication

To allow for the electrical characterisation of the coating, electrodes were fabricated using nitinol wire with polyimide insulation to allow for efficient characterisation. Individual coated and uncoated carbon fibers were isolated from the growth bundles, threaded into silica tubing, and secured with epoxy. One end of the fiber was connected to the nitinol wire using silver paste (Figure 5.6A). The paste was baked at 125 °C until cured and covered with a layer of epoxy. About 2 µm of Parylene C was deposited using a PDS 2010 LABCOTER™ 2 Parylene Deposition System to create an insulating layer over the length of the electrodes. 4.00g. To expose the electrode tip, the entire electrode was submerged in DI water with only around 200 µm of the fiber exposed above the surface of the water. A butane torch was applied briefly to burn the Parylene-C coating and expose the fiber tips (Figure 5.6B).

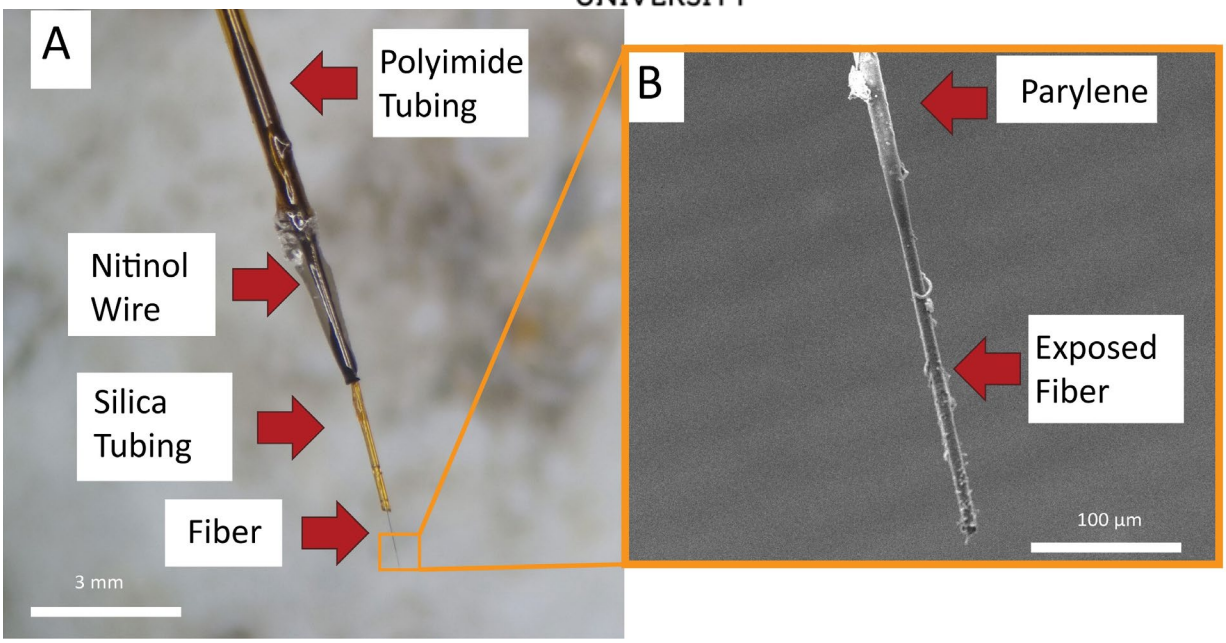

Figure 5.6. Functionalized nitinol wire electrode for electrochemical testing (A). The wire is insulated with various tubing and epoxy, as well as a layer of parylene. SEM image of the fiber tip including the insulating parylene coating and the deinsulated functional tip (B).

5.3.3 Electrode Characterisation

The electrochemical properties of the fabricated electrodes were investigated using a Gamry Potentiostat (Interface 1000E) with an Ag/AgCl reference electrode and a Glassy Carbon counter electrode. The capacitance of the electrodes was determined from the EIS using equivalent circuit models (CPE) fitted via the Levenberg-Marquardt Method to the Nyquists plots. Physical characterization of the growth films and electrode preparation was obtained using SEM, TEM, and Raman spectroscopy. SEM images were obtained with a FEI Quanta SEM (RMMF). TEM images and EELS were produced by a JEOL 2100F Transmission Electron Microscope. The TEM sample was prepared by cutting a cross section of a representative B-UNCD coated fiber. This sample was welded to a copper TEM sample stage using platinum and further thinned to 120nm. A Renshaw InVia Raman 532nm produced Raman spectra, specifically the D (1350 cm^{-1}) and G peaks (1580 cm^{-1}).

FSCV measurements were performed using fabricated electrodes to determine the sensitivity to dopamine *in vitro*. A 3D printed flow cell was designed to allow for controllable concentrations of dopamine to be added to the background measurements of PBS using a Pinnacle (exact model) FSCV system (Refer to 2.4.4) and a silver reference electrode. This allowed for the change in current to be measured for each electrode. This was normalized for the surface area of each electrode. Dopamine concentrations were prepared by mixing Dopamine (Sigma Aldrich) with PBS and aliquoting into further dilutions of PBS to allow for appropriate volumes required for the flow cell. The flow cell was rinsed with PBS thoroughly between each measurement and CV curves were produced to ensure no dopamine remained adsorbed to the electrodes.

5.4 Results and Discussion

5.4.1 Physical Morphological Characterisation

Completely uniform coatings were achieved on individual carbon fibers within the growth bundle. SEM images confirmed consistent coating along the length of the carbon fiber including fiber tips (Figure 5.7A-D). The coating contained diamond grains in the nano-crystalline scale (as small as 50nm) (Figure 5.7E and F). The size of the diamond grains did appear to be slightly different between fibers, however this is to be expected as the growth mechanics within the bundle will differ due to the placement of the carbon fibers. No etching or degradation of the carbon fibers was observed as a result of the exposure to the CVD conditions. The coating thickness was between 0.9-1.1 µm for all fibers.

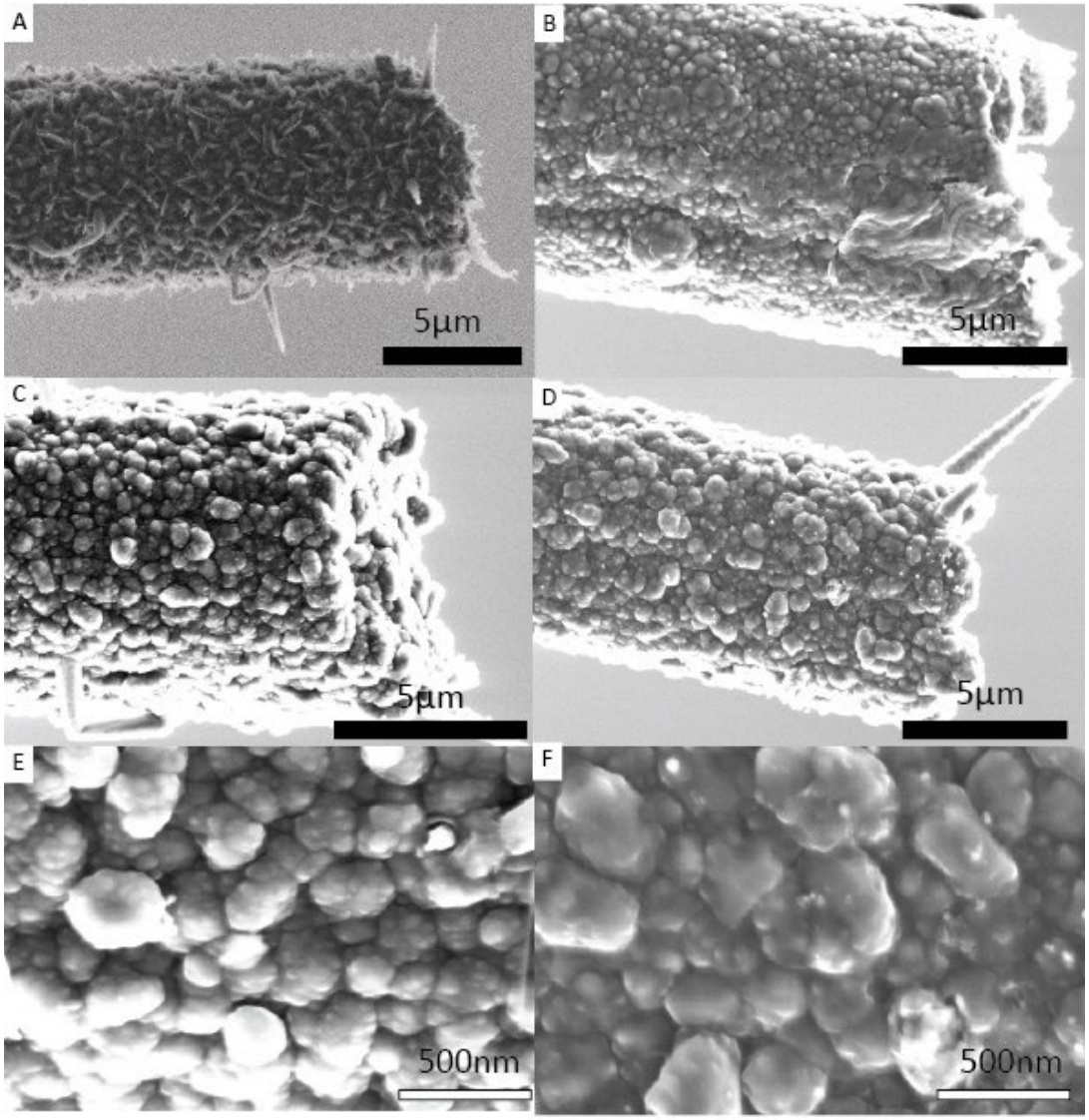

Figure 5.7. SEM images showing slightly different morphologies of NCD grown within the bundle.

The growth morphology did appear to differ throughout the bundle; however, this would be expected due to the non-uniformity of the plasma respective to each individual fiber. This, however, provides insight into the believed growth mechanics of this coating (outline in Figure 5.9). Some fibers displayed only CNW coating (Figure 5.8A), some with CNW sheets coated in Nanodiamond (ND) (Figure 5.8B). This suggests that within the bundle there is different growth conditions. This is evident by the plasma colouration in Figure 5.5B. The attenuation of the plasma and subsequent temperature would have an effect on the proportion of graphitic growth as well as the speed at which the coating grows. Previous work by Hejazi et al. showed CNW growth with a similar gas mixture as used here [105]. This growth used a lower proportion of methane feeder gas (3% compared to 8%) than that recipe, so it is expected that less graphitic growth would occur under those conditions. The set up used in this work was the same as the ones used in that work, including the molybdenum pucks and titanium cages were the same as the ones used.

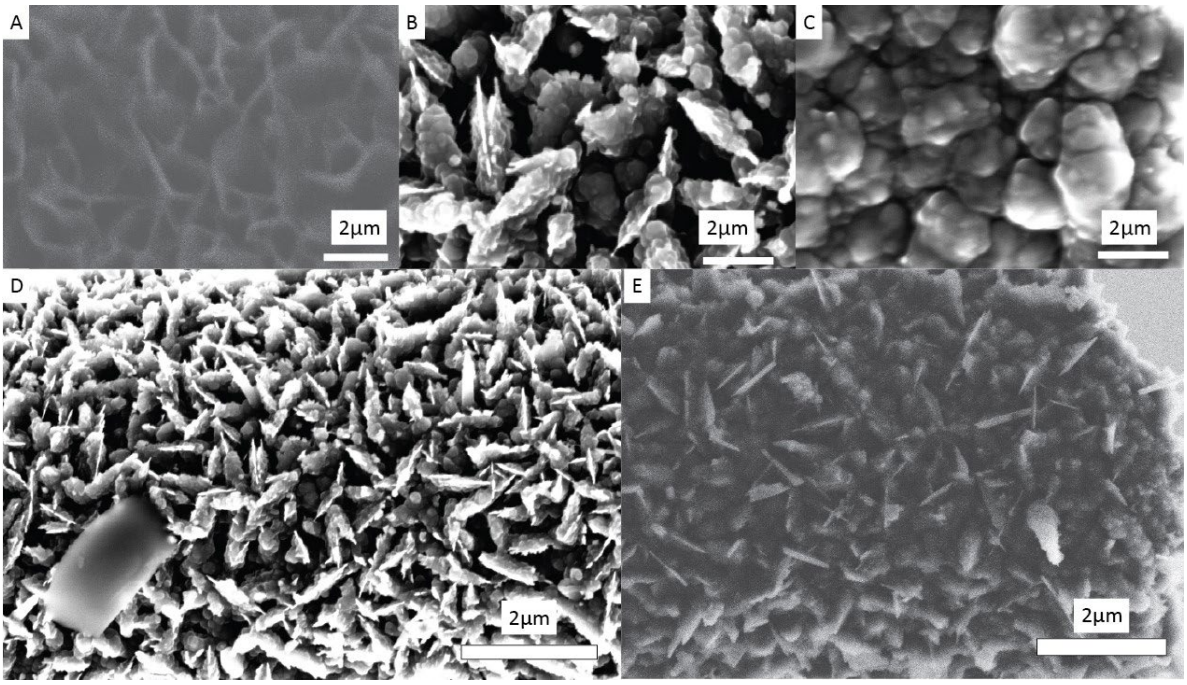

Figure 5.8. SEM images showing different stages of growth within the bundle. A. Carbon Nano-wall growth, B. Carbon Nano-wall growth covered in NCD and C. with NCD growing completely within the graphite matrix. D and E depict two electrodes with differing levels of NCD between the CNW matrices.

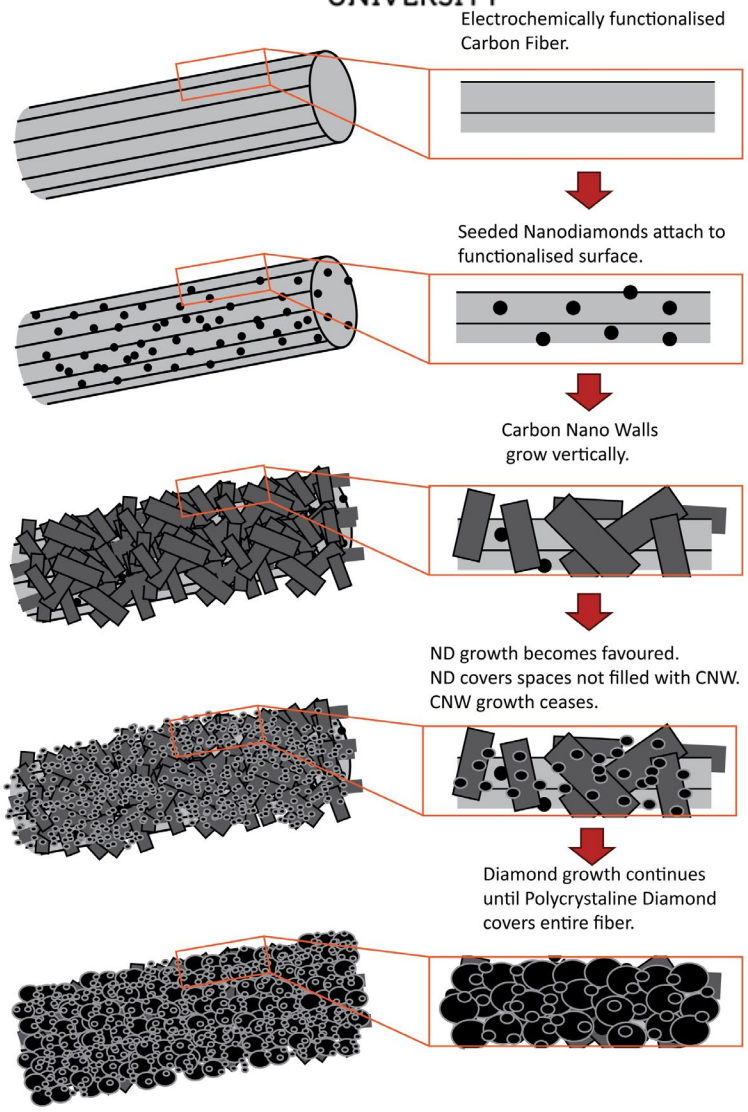

Figure 5.9. Proposed growth mechanics of the nanodiamond/CNW composite coating.

The coating morphology observed on the carbon fibers indicate that the initial stages of the deposition favoured growth of CNW. During much of the growth the pyrometer showed temperatures exceeding 1000 ~~degrees~~ °C, a result of the microwave power and stage heating temperatures used. The growth of CNW is favoured at temperatures above 1000 ~~degrees Celsius~~ °C. At some point during the growth, either due to the length of the CNW sheets, the plasma environment, or competitive etching between the radical addition for diamond growth and the plasma etching of graphene, the diamond phase becomes the dominant growth mechanism [264]. This results in ND and MD growth of diamond on the carbon fiber as well as the underlying graphitic layers. This results in the PCD filling in between CNW sheets until a uniform layer of diamond is observed (Figure 5.8C). The stages of this can also be seen in Figure 5.8D and 5.8E to varying extents where the graphitic sheets extend through the film as complete PCD coverage of the film has not yet been achieved. The ~~heavy~~ inclusion of graphite within the structure may not play a significant role in the electrochemistry of the coating surface, however, could have an impact on the mechanical properties.

Really? Evidence for this?

TEM images were taken to help characterize the crystal structure of the coating to help determine the presence of sp^2 and sp^3 carbon within the growth. This provides another insight into the presence of ND and CNW in the coating. The sample was successfully mounted on a TEM grid and further thinned to 120nm (Figure 5.10B). The sample was a representative ND sample as confirmed under SEM when performing the FIB preparation. Different crystals can be seen in Figure 5.10C, with the different areas of black and grey. Voids can also be seen in Figure 5.10C and 5.10D at the junction between the fiber and growth. This is to be expected as larger crystals grow outward from the surface. The number of voids in the coating was very low, indicating that the nano seeding methods used were successful. Diamond and Graphite can also be seen in the TEM cross sections at higher magnification. A mixture of graphitic and diamond carbon is present throughout the film, further corroborating the growth mechanics outlined above.

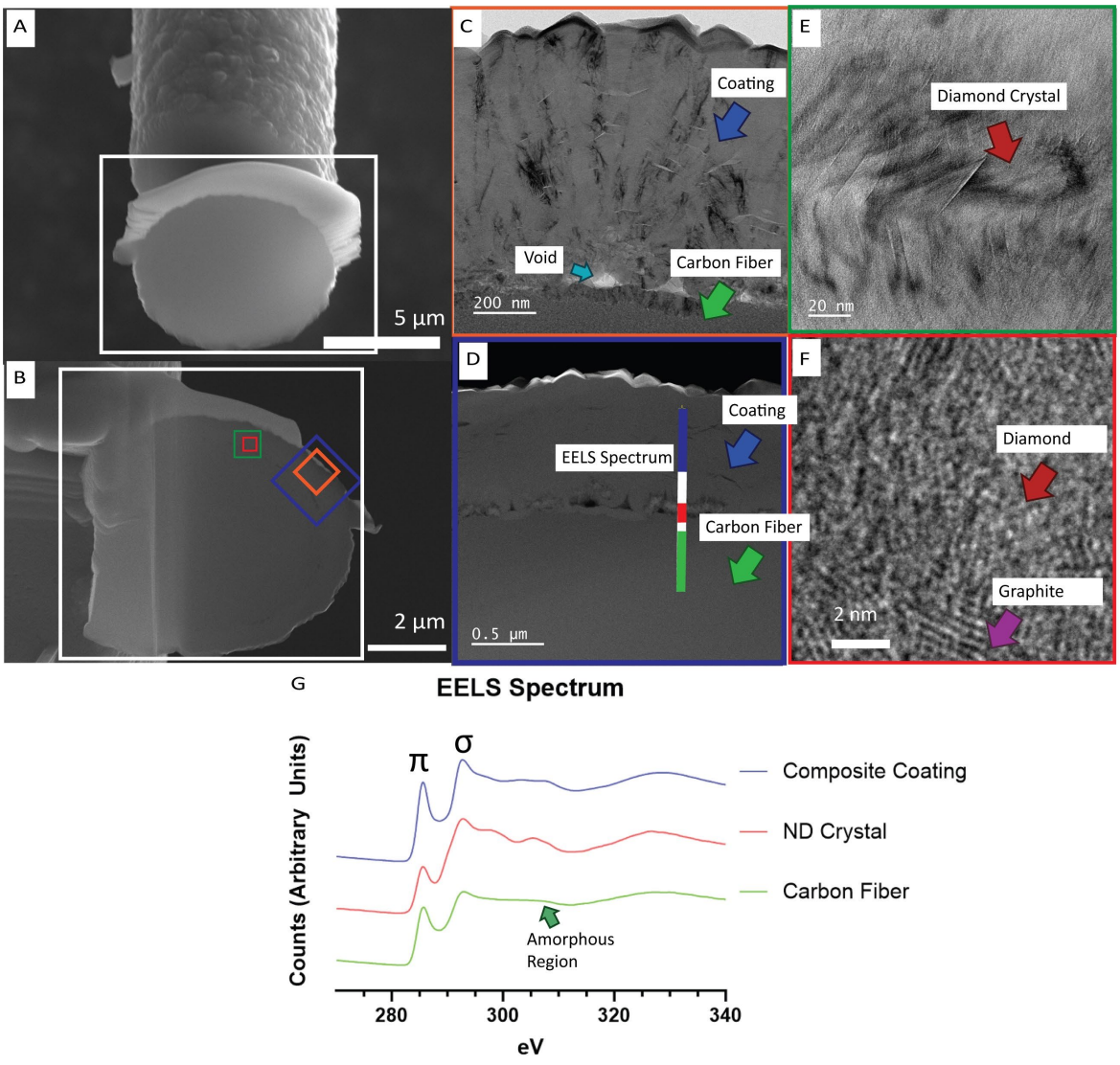

Figure 5.10. A and B show SEM of the fiber from which the TEM cross section sample was prepared. C-E show TEM images of the 120nm thick cross section produced by FIB. The carbon fiber (green arrow) and the coating (blue arrow). F shows graphitic (purple arrow) and diamond (red arrow) regions within the coating. G shows the EELS spectrum obtained from D. The bar on D and associated colours indicating where the EELS was extracted from, with the bulk composite coating (Blue), clear ND crystal (Red) and carbon fiber (Green).

The EELS spectra showed distinct differences between sections measured. The carbon fiber section (Figure 5.10G Green Curve) showed mostly amorphous carbon as indicated by the smooth curve past 300 eV with a relatively large peak at 285 eV [274]. The distinctive diamond crystal section (Figure 5.10G Red Curve) shows a lower peak at 285 eV (sp^2 peak) compared to the 290 eV (sp^3) peak. The presence of the peaks around 310 eV are also an indication of diamond growth. Comparing this section of the spectrum from the bulk coating measurement of the NCD coating (Figure 5.10G Blue Curve) to the other spectras shows a hybrid of the two, further indicating the growth of a diamond film with a graphitic content for the bulk of the coating [255].

To further understand the chemical composition of the coating, ~~we performed~~ was performed Raman spectroscopy on both coated and uncoated carbon fibers, ~~which is a powerful technique for characterizing the structure of carbon materials~~. Raman spectra for coated and uncoated carbon fiber are shown in Figure 5.11A and B, respectively. Despite the observed variability in the coating morphology, the Raman spectra remained remarkably consistent across the coated samples. Both coated and uncoated samples exhibit distinct sp^2-bonded carbon peaks, including D (at 1350 cm^{-1}) and G peaks (at 1580 cm^{-1}). The coated samples also contained a D' peak (at 1615 cm^{-1}), known to represent ordered graphite. This is another indication of CNW presence within the growth [274]. The 2D peak at 2690 cm^{-1} is also an indication of the ordered graphite and has been previously demonstrated in CNW/Diamond hybrid materials [274]. The BDD grown on carbon fibers by Millan-Barba et al. displayed Raman spectra for the BDD coating much more similar to the carbon fiber samples. These measurements were taken with a blue 488nm laser and could therefore have been sampling more of the underlying fiber than is demonstrated in these results. Quantitative assessment was performed by calculating the normalized intensity ratio of the G to D peaks for each sample. After the coating, there was a notable increase in this ratio, from 1 to 3, suggesting an augmented presence of ordered sp^2-bonded carbon within the coating matrix, as evidenced by the enhanced G peak. We did not observe the presence of the typical sp^3 carbon peak (at 1332 cm^{-1}) from any of the samples. This could be explained by the fact that Raman spectroscopy is much more sensitive for detecting sp^2-bonded carbon than sp^3-bonded carbon [291]. Additionally, considering the coatings are merely 1 µm thick, the Raman spectral data are likely augmented by the underlying carbon fiber substrate, which could skew the interpretation towards sp^2 carbon features.

Use proper prime symbol '

Really? check.

This is surprising. A blue laser should be sensitive to sp3 carbon, and 1um of diamond should be sufficient to detect, even if it's just a shoulder on the side of the D peak.

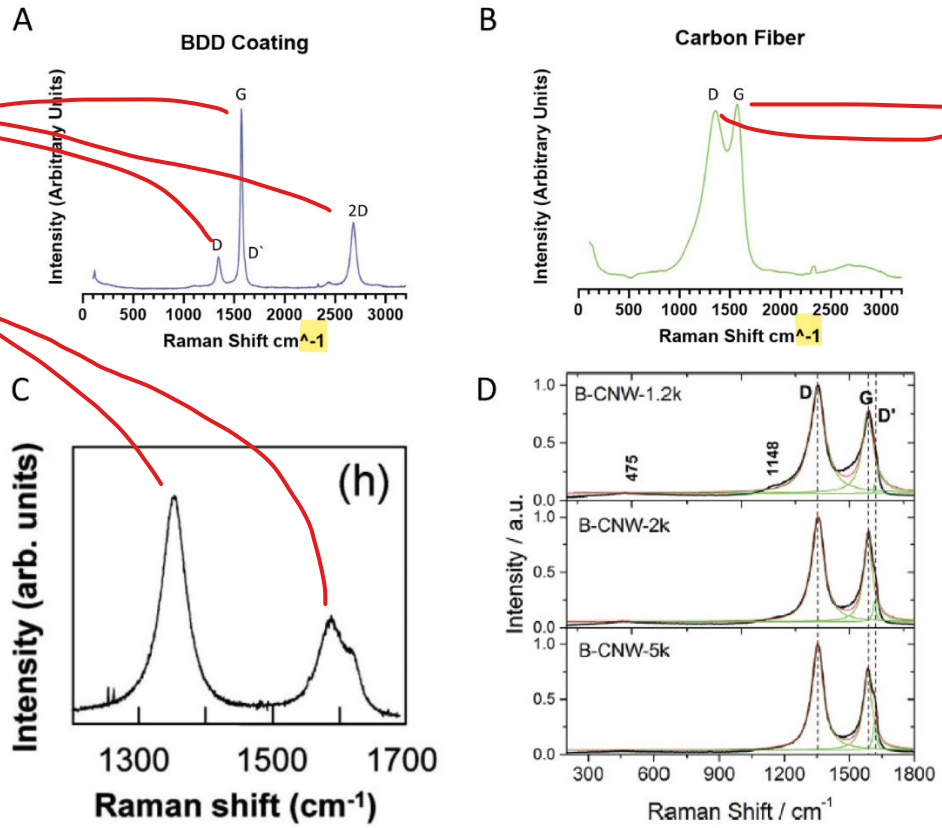

values of peak positions?

and again

Figure 5.11. Raman spectra of Diamond Coated Fibers (A. This work), Carbon Fiber (B. This work), CNWs (C. [265]) and Diamond Phase Rich CNWs (D. [268]).

5.4.2 Electrochemical Characterisation

In order to perform the electrochemical characterisation of the coating, electrodes were created. This included electrodes with BDD coated carbon fibers as well as carbon fiber micro electrodes with no coating (Figure 5.12). To achieve this, an insulating layer of parylene was used to allow for a controllable functional electrode surface area, as this is required to compare the normalization of the different coatings. This is also the same configuration used for the array that was developed, so will help to show the potential of this coating in incorporating into the array configuration. Firstly, it needed to be demonstrated that the flame deinsulation method used did not damage the coating. Figure 5.13 shows a BDD coated electrode before and after flame deinsulation, no obvious damage was observed on any electrode tested.

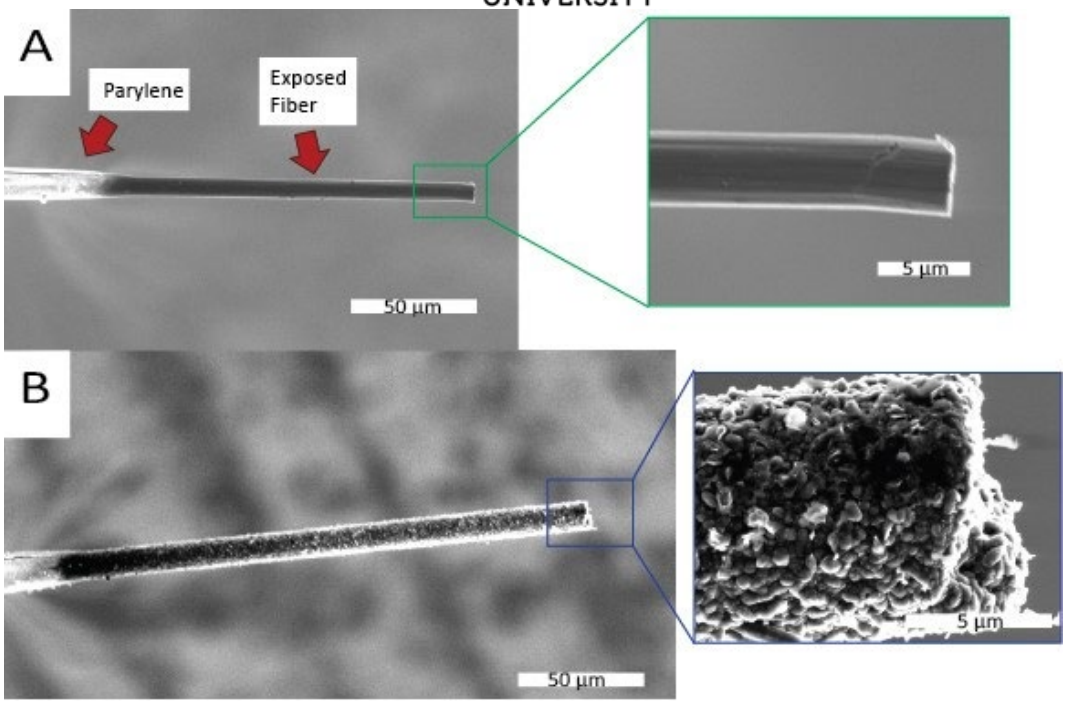

Figure 5.12. Functionalised carbon fiber (A) and BDD (B) electrodes prepared for electrochemical testing, showing the deinsulated region of the electrodes and their effective lengths.

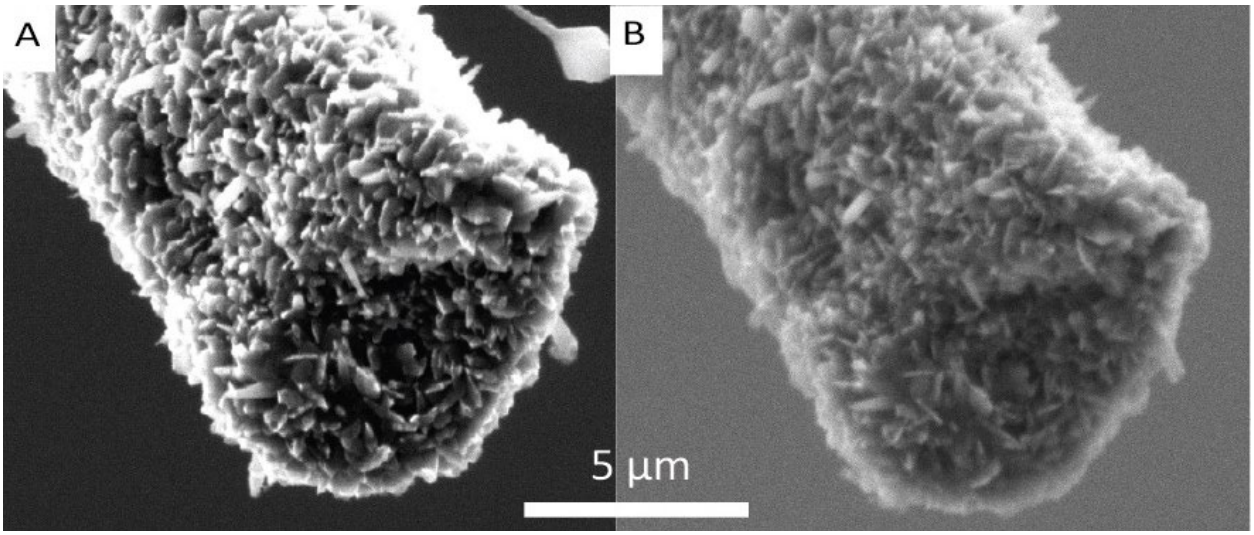

Figure 5.13. SEM images showing before (A) and after (B) parylene deinsulation using a butane torch (Scale bar 10µm).

Prior to testing the electrodes for dopamine sensing, we also performed electrochemical characterisation of the electrodes. Figure 5.14A shows the representative EIS spectrum of coated and uncoated carbon fiber electrodes. Figure 5.14B shows the average impedances at 1kHz of the coated and uncoated electrodes. The coated electrodes had lower impedance (9.82 GΩ/cm^2 after coating versus 17.23 GΩ/cm^2 before coating). The normalized 1kHz impedance for the electrodes created was 17.23 and 9.820 GΩ/cm^2 for the coated and uncoated fibers respectively. Using an equivalent circuit, we extract the double-layer

capacitance of the electrodes. The specific capacitance of the diamond coated and uncoated fibers are 16.1 and 93.9 µF/cm^2, respectively (Figure 5.14C).

The electrochemical characteristics of the fibers were compared. Figure 5.14A shows the representative EIS spectrum of coated and uncoated carbon fiber electrodes. The normalized capacitance of the BDD coated and uncoated fibers are 16.1 and 93.9 µF/cm^2, respectively (Figure 5.14C). The specific capacitance of the BDD coating is comparative to previous works using BDD [292, 293]. Lastly, the normalized impedance for the electrodes created was 17.23 and 9.820 GΩ/cm^2 for the coated and uncoated fibers, respectively. The lower diamond film resistances compared to bare carbon fibers observed was consistent with previous work that only looked at the resistance change in a similar growth on bundles of fiber [279]. This is also further evidence of the surface being dominated by the diamond coating and not CNW, as the impedance would be expected to be much lower if CNW or graphite was predominant on the surface [105].

Messy. Use proper superscripts and Greek symbols

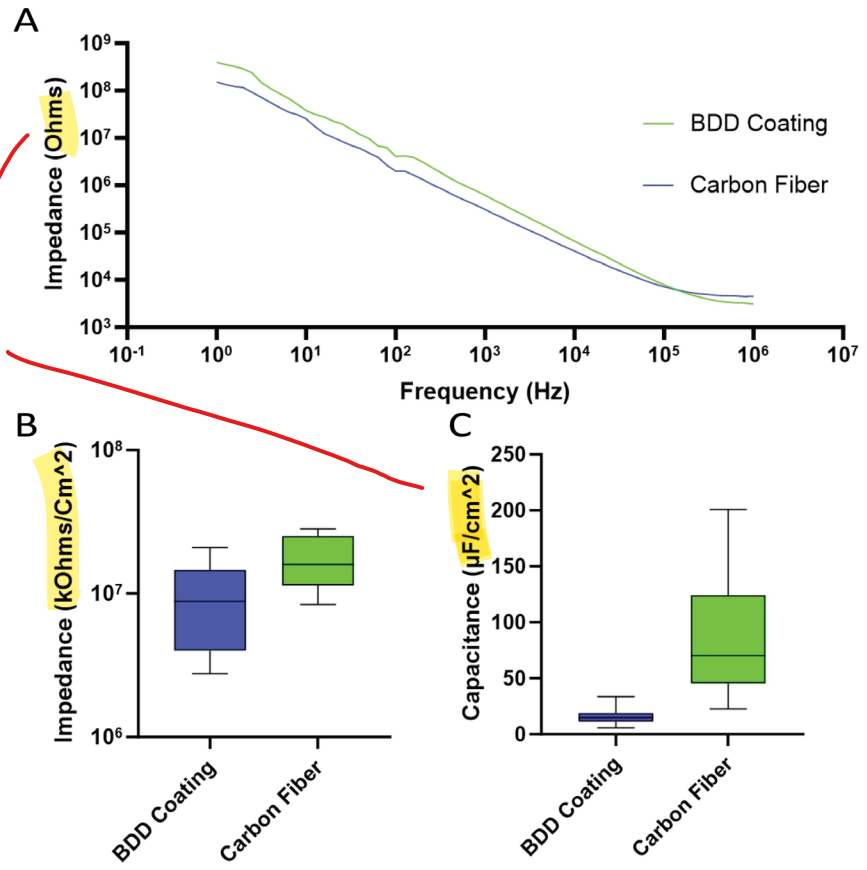

Figure 5.14. Electrochemical EIS of BDD and carbon fiber electrodes (A). Normalised impedance (B) and capacitance (C) for electrodes of known exposed surface area.

5.4.3 Neurochemical Sensing

To establish the effectiveness of the ability of the electrodes to detect phasic levels of dopamine, FSCV was used. The initial results obtained (Figure 5.15) indicated that the BDD coated fibers performed at least comparably to the bare carbon fiber electrodes. The sensitivity measured at 1µM of dopamine indicated

that these electrodes would be good candidates for further *in vivo* testing. Further electrodes were fabricated and distributed to a collaborator at the Mayo Clinic (their initial results can be seen in Figure 5.16) to undergo further *in vitro* and *in vivo* testing. These results also include the utilization of MCSWV for the detection of tonic levels of dopamine. These results will be completed and collated upon completion of this thesis.

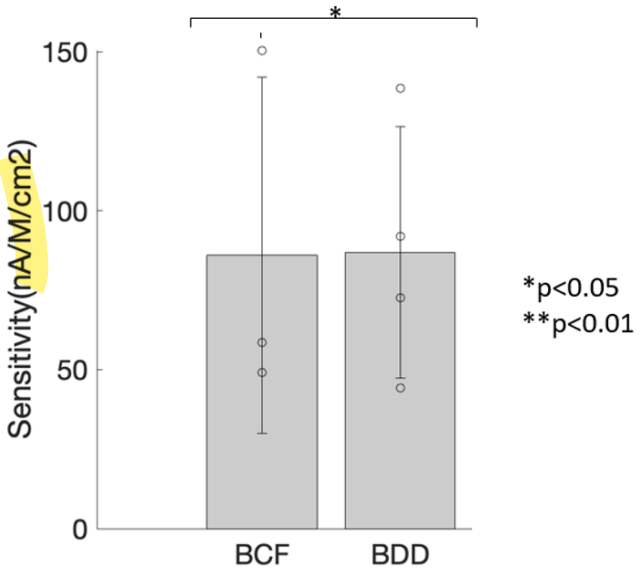

Figure 5.15. In vitro dopamine detection sensitivity comparison between Bare Carbon Fiber electrodes and BDD coated electrodes.

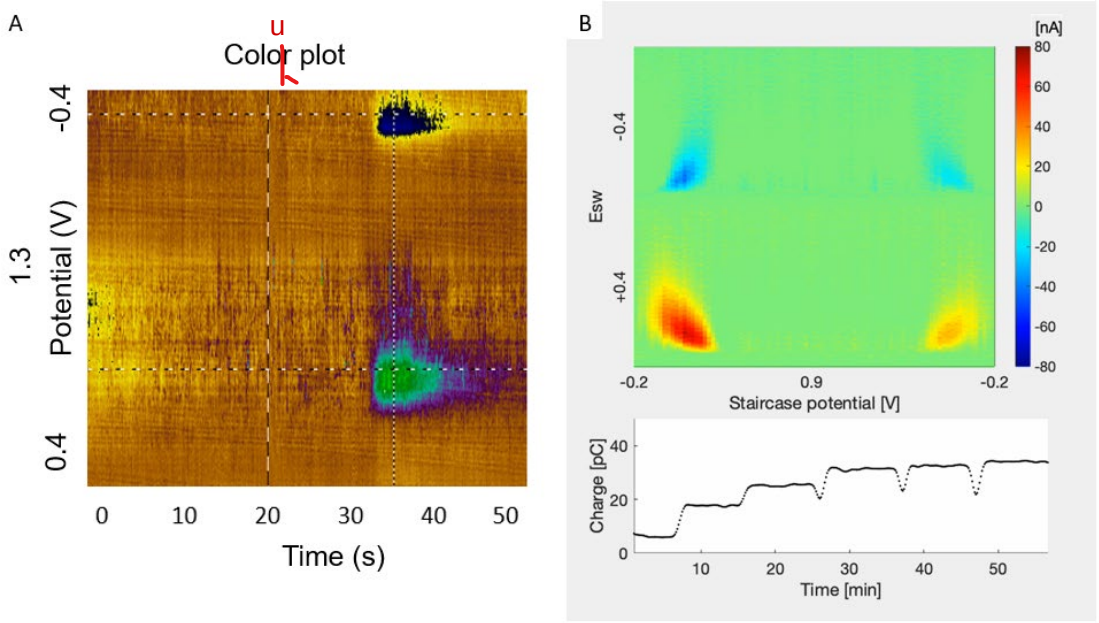

Figure 5.16. Initial successful in vitro dopamine detection sensitivity using fabricated BDD electrodes using FSCV (A) and MCSWV (B) performed by a collaborator at the Mayo Clinic.

5.4 Future Work

The coating produced in this works indicate a composite growth of CNW and ND with the latter coating predominately the surface. This is consistent with previous works and was verified using a number of different characterisation techniques. Future works required are still the chronic experiments to show the long-term stability of the electrodes which are the main benefits of producing such a coating. Further *in vivo* work is required to show how the testing in beakers translates to the measurement in neural tissue and achieve the potential of the coating to aid in disease treatment and detection. Alteration of the growth mechanics could also produce electrical properties in the coating that could be more conducive to an even more diverse range of applications. This could include growths at lower temperatures to limit CNW production and the inclusion of further Boron-doping to alter the electrical properties [273]. A means to produce electrodes more reliably from the variance seen within the growth bundle is also required. As this variance in coating will result in unreliability for clinical applications or a greater challenge in fabrication for this configuration of electrode.

Chapter 6: Growth of boron doped diamond onto carbon fiber arrays

6.1 Chapter Outline

This chapter will explore the potential of using Chemical Vapour Deposition (CVD) to coat carbon fiber arrays with conductive diamond. ~~I will evaluate~~ various growth conditions and techniques to direct plasma for preferential growth of diamond onto fiber tips. The overall aim is to prove the concept that a Nano-Crystalline Diamond (NCD) coating can be applied with spatial control, onto a configuration of individually addressable micro electrodes.

6.2 Chapter Introduction

Creating an array of individually addressed NCD coated carbon fibers is a difficult task. Simply copying any other array design that contains carbon fibers will not achieve consistently high yields. As shown with the CVD growth of diamond onto individual fibers in bundles, the coating across the bundle is variable (Chapter 5.4.1). This means it is difficult and unreliable to isolate individual fibers of the desired morphology to create a homogenous array. This would only be assessable either under Scanning Electron Microscopy (SEM) or electrochemically, which means that yields would not be known until later processing steps. This is not appropriate for a reproducible commercial device. The handling of the fibers to place them into the array during construction can also potentially damage the coating. Lastly, to ensure consistent length of electrodes it is common for carbon fibers to be cut to length, either using a scalpel blade or laser cutter. As this would damage the tip and expose the core of the carbon fiber this too is not conducive to the creation of a reliable and replicable array.

The use of the carbon fiber arrays brazed into Poly-Crystalline Diamond (PCD) (Chapter 3) opens possibilities for controlled deposition of diamond on carbon fibers. The use of the diamond substrate and the gold braze allows for the array to survive extreme temperatures and pressures of different manufacturing processes required for CVD diamond growth. CVD diamond growth requires the samples to experience temperatures up to 1000 degrees Celsius, vacuum pressure within the chamber as low as 10^{-3} torr and the complicated chemical conditions within the growth chamber. Therefore, the use of carbon fiber arrays presents an opportunity to control the plasma within the chamber, allowing for preferential growth of diamond on the carbon fiber tips.

The biggest challenge for growing NCD onto an array is ensuring growth only on the region of interest, being the active tips of the electrodes. By restricting the growth only to the tips of the electrodes the innate mechanical properties of the carbon fibers can be maintained maximising the effectiveness of the carbon fibers. Secondly, if the growth extends down onto the diamond substrate surface this will short all of the electrodes together. This could potentially be removed using masking techniques or with post processing methods, however a reduction in processes is ideal considering the many fabrication steps already required for such an array. This chapter will explore the creation of the 25-electrode carbon fiber coated NCD array and the novel strategies employed to enable growth directly onto the electrode tips.

6.2.1 Current NCD Arrays

Current diamond arrays are typically planar and are grown on stiff substrates [294-300]. Diamond or diamond coated electrodes on either diamond or silicon substrates capable of neural interfacing and

biosensing have been demonstrated. These have shown promise as retinal prosthesis, as a means of measuring activity in brain slices and have demonstrated an enhanced ability for neuronal cell growth on or around the array. In these applications a planar orientation is an advantage as the array can be placed directly onto the slice or retina that is also 2-dimensional so that each cell can be reached. However, this again highlights the lack of a penetrating array capable of chronic *in vivo* implantation. ~~One group in~~ Hess et al. ~~had~~ produced a shank polymer electrode that uses boron doped diamond capable of cortical implantation [301]. This device was similar to the configuration of the Michigan shank electrode and still contained a silicon backbone. Although capable of being inserted into the neural tissue, it still possesses all of the chronic limitations of the Michigan device. Being a shank electrode, it is also limited in recording area, as the lack of dimensionality means only layers can be interacted with. If the CVD growth ~~was able to be~~ were translated onto the proposed PCD substrate carbon fiber array, the benefits of the NCD growth could potentially be translated into a 3-dimensional chronically implanted neural interface.

6.2.2 CVD Plasma ~~Curation~~ Creation

As discussed previously in chapter 5, the growth produced from CVD is dictated heavily by a number of factors of the growth conditions [302-305]. This includes but is not limited to the microwave power, sample and chamber temperature, gases used, plasma attenuation and the chemical properties of the sample. For these reasons, utilising the same parameters as presented for the individual carbon fiber bundle growth will not necessarily yield the same growth mechanics and coating morphologies when translated to a different configuration. The growth rate as well as the NCD/CNW ratio could potentially be much different. It will also be important to be mindful of the unwanted effects that enhanced power and temperature could have on the sample substrate or electrical connections that were not present during previous growths. The plasma itself could be ~~curated~~ created in a way to promote the diamond growth on the carbon fibers and limit exposure of the substrate to the plasma and heightened temperatures. Current CVD grown diamond micro-arrays don't attempt to ~~curate~~ create the plasma but only attempt to pre-seed the areas of the array where the diamond will be required [204, 300, 301]. Typically, this results in diamond in ~~areas not desired~~ unwanted, and in many cases this coating could electrically short the electrodes. The excess coating then needs to be removed. This can be achieved using masks or by mechanically removing the excess using polishing or laser ablation. Masks would need to be added/removed to cover areas that do not need coating. Achieving this practically would be very difficult as it would affect other steps in the fabrication process or would cause damage to the carbon fibers themselves. This is the same for mechanically/chemically removing the unwanted areas as this would not be achievable without damage to the fibers. However, due to the geometry of the carbon fiber array there is potential to limit growth to only the carbon fibers by controlling the growth mechanics within the chamber during the process.

Previous work has shown that different aspect ratios of sample substrates will impact the growth mechanics. These works use molybdenum and titanium holders to reduce the edge effects of the substrate on the plasma for consistent and uniform growth rates [105, 306-308]. A plateholder design has the potential to both shield the substrate from the plasma as well as promote growth in the areas of interest [309]. It is proposed that a holder could be designed to limit temperatures on the substrate to below 1064 °C Degrees Celsius, the melting point of the gold braze. If the plasma were to be also ~~curated~~ created to only the tips of the carbon fibers, the mechanical properties of the fibers themselves would remain unchanged. ~~Providing~~ These all p e further potential to the creation of a fully implantable, chronic, ND coated microelectrode array.

6.3 BDD Coated Carbon Fiber Array Growth Methods

6.3.1 Holder Design

For the creation of the holder, 3D printed titanium was deemed the most appropriate. Titanium is a suitable material for surviving conditions of the CVD and could easily be manufactured into variable shapes to allow for more control over the plasma creation. The holder design involved a cut out section for the substrate to sit upon, with a well on the topside to align the lids, as the hole in any lid needed to be precisely situated directly over the fibers without damaging them (See Figure 6.1). By limiting the diameter of the hole, the amount of plasma exposure to the PCD substrate could be limited whilst also constraining the plasma exposure to the tips of the fibers.

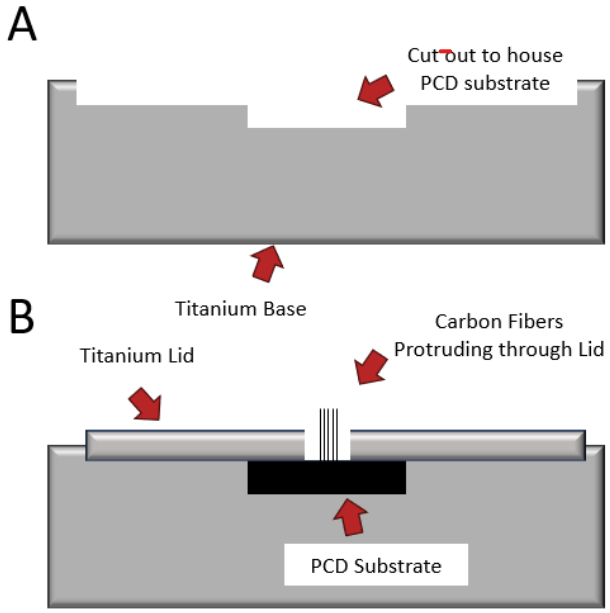

Figure 6.1: Schematic for the proposed 3D printed titanium holder without (A) and with (B) variable titanium lid for substrate protection and plasma attenuation to the carbon fiber tip.

A 100 × 100 mm square base with rounded edges was 3D printed using a SLM titanium printer (See Figure 6.2). This was further machined to ensure parts fit together as the proposed features in the print are on the limits of the resolution capable of this method. Jagged or protruding areas were sanded down and edges rounded to ensure minimal unwanted areas where the plasma would be inadvertently focused. The large surface area of the holder relative to the substrate maximises the distance between the edge of the holder and the substrate. This ensures that any plasma concentrated on the edge of the holder would be further away from the substrate, reducing the diamond substrate exposure to the plasma and higher temperatures. Different lid thickness ranging from 0.3 mm to 2.5 mm were used to control the growth mechanics at the electrodes.

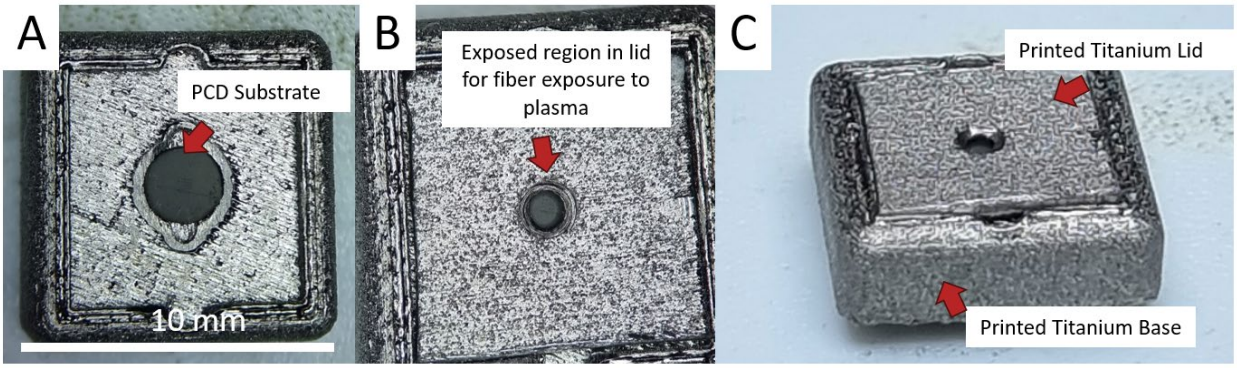

Figure 6.2: Titanium holder for attenuated plasma growth including the base for housing the PCD substrate (A). Printed titanium lid both acts to protect the bulk of the substrate from plasma whilst allowing for the exposure of the tips of the fibers to be exposed to the plasma field (B, C).

6.3.2 BDD Growth

The electrochemical pre-seeding and cleaning steps were performed as stated in Chapter 5.3.1. However, the set up required for this process was slightly different as electrically connecting the fibers to the working electrode of the potentiostat is not as simple as it was for a bundle of fibers. Firstly, by performing this on the array before the acid boiling step see Chapter (3.5.1.2) it is possible to connect to the back side of the array as each of the electrodes are still electrically shorted at this stage. Carbon tape was used for this purpose as it could be placed on a connected working electrode and would work to both physically and electrically connect the rear of the array to the working electrode. To aid in limiting the growth to the tips of the electrodes only the tips were placed within the seeding solutions (See Figure 6.3). This was performed using a manually operated linear manipulator. Care was taken to not wet the PCD surface with the solutions as this would both clump the electrodes and require further cleaning. The arrays were placed within a holder with a well filled with Oxygen terminated nanodiamond solution for 24 hours prior to the CVD growth. The fibers were rinsed with DI water and subsequently dried using nitrogen gas.

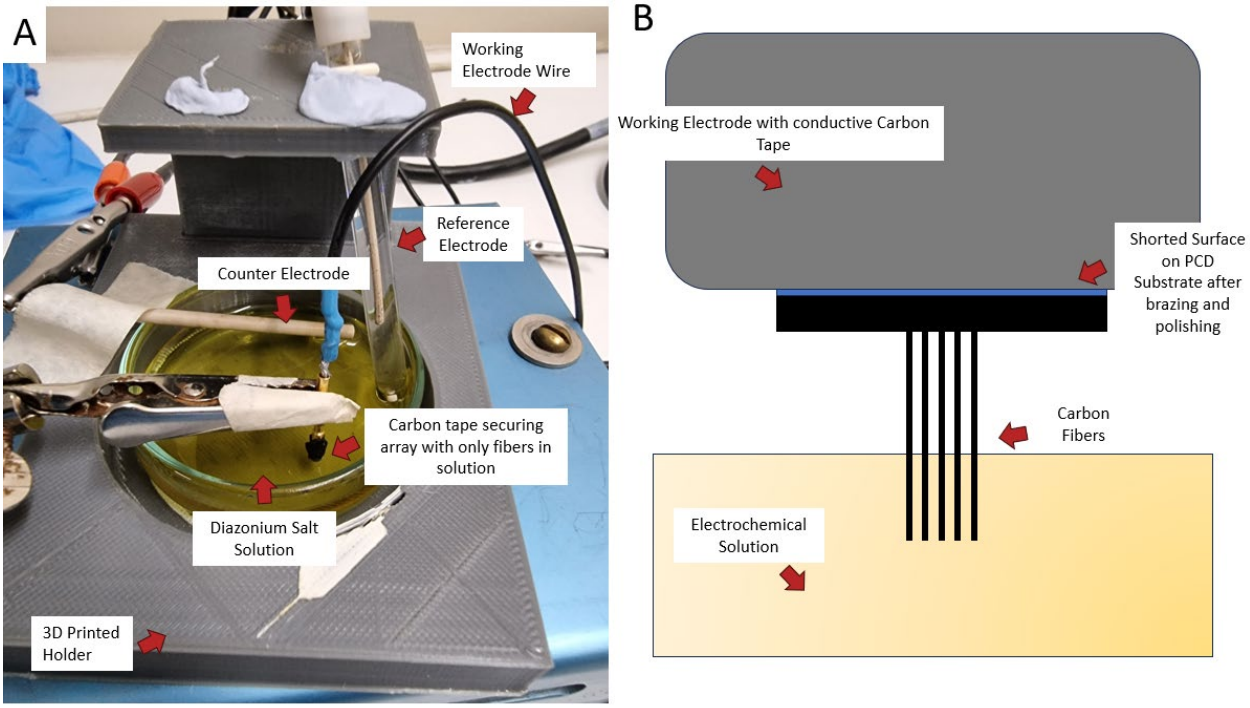

Figure 6.3: Electrochemical set up for nano diamond pre seeding (A). Carbon fiber suspended to ensure only the carbon fiber tips are pre-seeded within the solution, whilst the carbon tape allows for the electrical connection to the working electrode of the potentiostat (B).

The array was placed within the titanium holder with the fibers pointing up (See Figure 6.2A). Titanium lids were placed over the holder with the fibers protruding through a small hole. This configuration was positioned on a molybdenum puck and centred within the CVD chamber (see Figure 6.4). A gas mixture of 95.5% H_2, 3% CH_4 and 1.5% Trimethyl boron (TMB) was used to create CVD grown coatings on the carbon fiber arrays. The deposition time was 60 minutes using a pressure of 40 torr and a microwave power of 800 W. Samples were allowed to cool completely under turbo vacuum to ensure no degradation of the titanium holders. Once grown, the arrays were characterized using SEM and Raman Spectroscopy.

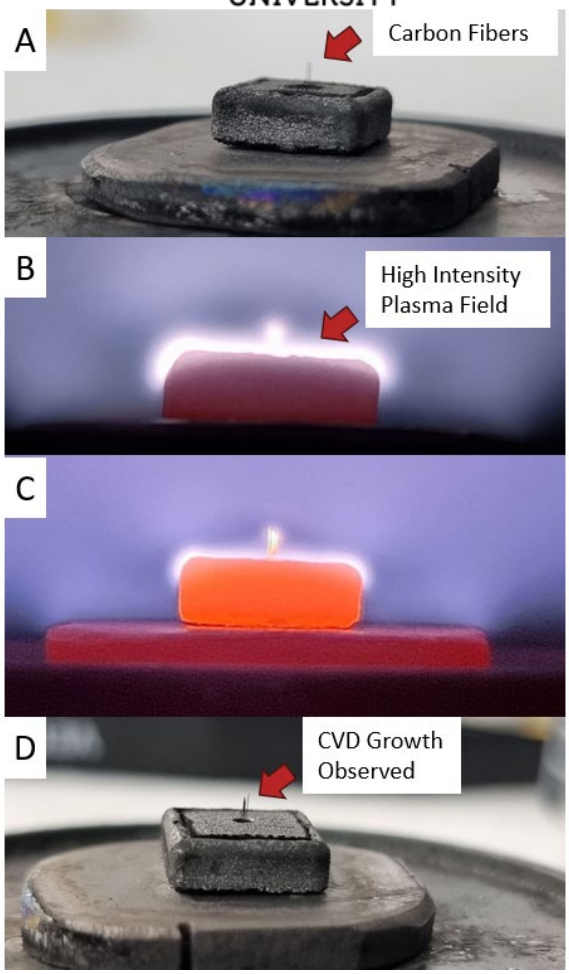

Figure 6.4: Sample configuration before growth with carbon fibers clearly protruding through the printed lid (A). Initial plasma conditions showing intense plasma attenuated around the exposed carbon fibers (B). Growth visibly forming on the fiber tips as the plasma is continually enhanced around exposed carbon fibers (C). Configuration post growth with no visible soot or growth on lid and the visible accumulation of CVD growth on the exposed carbon fiber (D).

6.4 BDD coated Carbon Fiber Array Discussion and Results

6.4.1 Carbon Fiber Array Growth Morphologies

The first attempted array growth was performed on a carbon fiber array with tapered electrode lengths ranging from 400-1200 µm using a 0.3 mm thick titanium lid (See Figure 6.5A). Post growth this sample displayed clearly defined regions of diamond-like and CNW morphologies (See Figure 6.5B-D). These coatings appeared to be around 1 µm thick and were comparable in morphology to those grown in this work previously on bundles of individual carbon fibers. The samples contained what appears to be NCD growth on the tips of most of the electrodes. This diamond region was not simply a gradient down the length of the tapered electrodes but shows a clear boundary region about 400 µm from the base of the fibers. This indicates that the plasma was attenuated by the holder meaning that the growth rate was enhanced above this distance from the substrate. Below this range CNW growth was observed. The CNW extended onto the PCD substrate and covered the entire substrate surface connecting onto each of the fibers. This is not ideal for device fabrication as this would electrically short each of the fibers to one

another meaning removal of this layer would be necessary. Oxygen plasma (See Chapter 2.3.5) was used in an attempt to remove this layer however this led to the complete destruction of the carbon fibers by the time the CNW was removed from the surface. The SEM characterisation of this sample provided a proof of concept that the plasma could be ~~curated to~~ located at the tips of the electrodes. This did not address the shorting or undesired growth areas that would be expected ~~for a growth without curation~~.

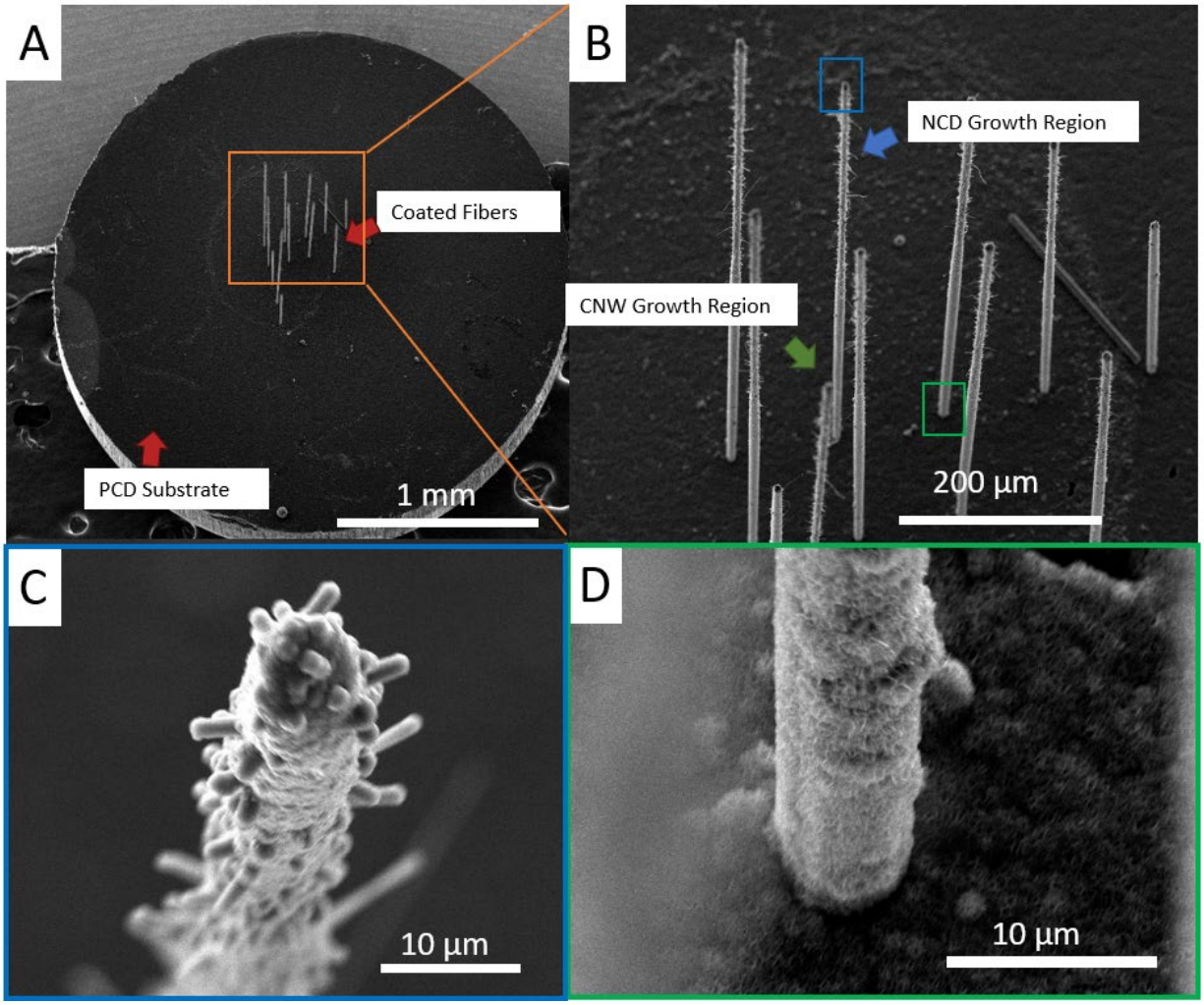

Figure 6.5: Carbon fiber array in diamond substrate with a thin 0.3 mm flat lid (A, B). NCD growth region can be seen on the top of the fibers (C) and CNW growth region on fiber base and PCD substrate (D).

At the completion of each growth, both the PCD substrate and gold braze circuitry remained intact (See Figure 6.6). The main difference in growth recipe used on this sample and that used for the carbon fiber bundles was a reduction in sample heating and microwave power. This was done to limit temperatures and plasma intensities experienced by the PCD substrates. This appears to not impact the overall growth mechanics, as the growth itself was still dominated by the power of the plasma. The high temperature of the growth still led to graphite formation on the PCD surface extending onto the brazed circuitry. This resulted in electrical shorting between all channels. This was removed using Oxygen Plasma Etching for 2 hours (See Chapter 2.3.5) by placing the array within a bespoke UV-curable 3D-printed resin holder to protect the fibers. A handheld multimeter was used to measure the conductivity of the surface post

treatment showing an open circuit indicating functional removal of the graphite. This means that a substrate would be able to functionally survive the growth conditions.

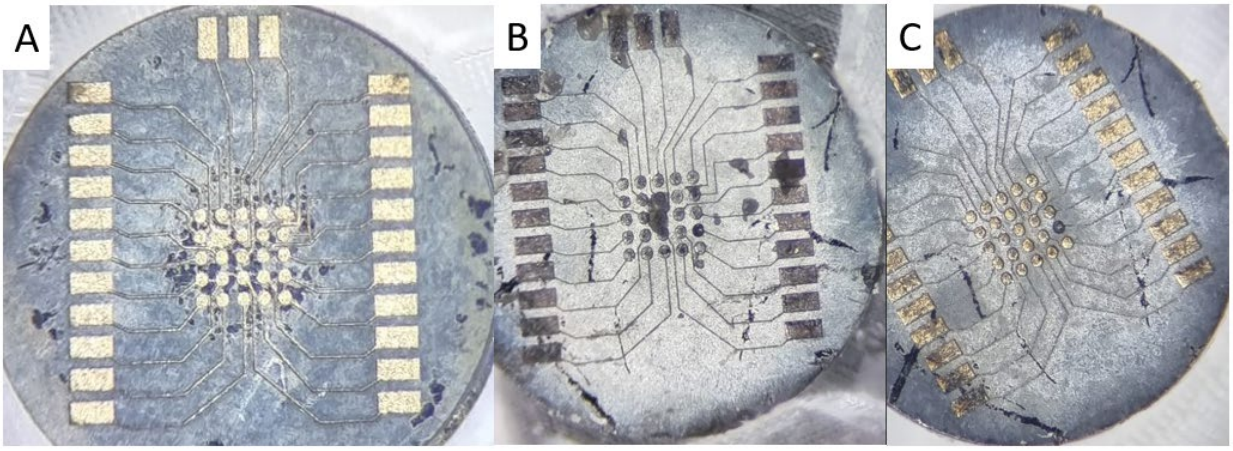

Figure 6.6: Array gold brazed circuitry before growth (A), post growth (B), right braze post 2 hours oxygen plasma to remove electrical shorting (C).

The next step was to control the growth mechanics in a way that allowed only ~~for the~~ NCD growth on the tips of the electrodes whilst limiting the CNW area of the growth to just the fibers themselves and not extending onto the PCD substrate. To achieve this goal, ~~I redesigned~~ the titanium holders and ~~tested~~ titanium lids of thickness varying between 0.3mm and 2.5mm. Figure 6.7 shows the CVD plasma during the growth using different titanium lid thickness. Figure 6.7 shows the growth where the plasma appears concentrated uniformly over the entire area over the top of the holder. The 1.5 and 2.5mm thick lids showed plasma attenuation further from the holder over the taller lids.

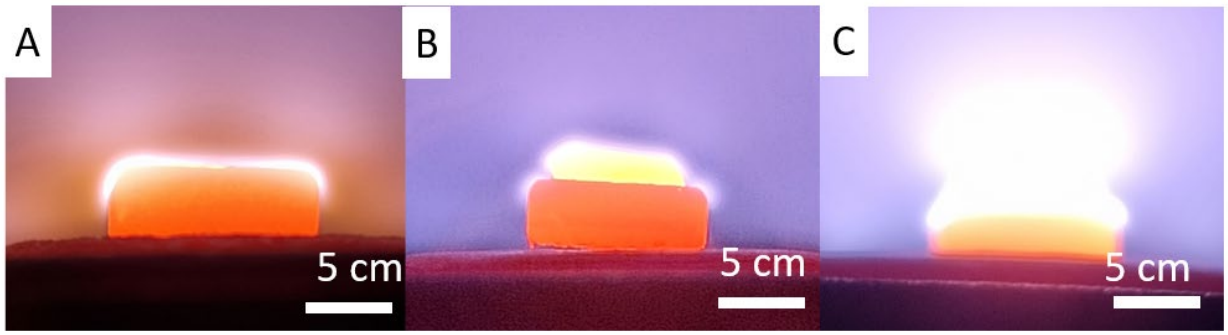

Figure 6.7: CVD plasma growth onto carbon fiber arrays within titanium holders. Different lid thickness 0.3mm (A), 1.5mm (B) and 2.5mm (C) resulted in different locations of plasma concentrations on the sample.

A growth using longer electrodes with a thicker lid in an attempt to inhibit any growth appearing on the PCD surface can be seen in Figure 6.8. This growth used 1.5mm long electrodes with a 1.5mm thick lid. The plasma during the growth can be seen in Figure 6.7B. Under this condition only a limited amount of CNW can be seen on the tips of the fibers with no evident ND observed (Figure 6.8B). This was successful in removing unwanted growth on the base of the fibers on the substrate (Figure 6.8 C and D respectively). The 2.5mm thick lid used in Figure 6.7C resulted in an even greater reduction in the amount of the fibers

covered by even the CNW. These results indicate that optimising the combination of fiber length and lid thickness would be required to achieve desired array morphology.

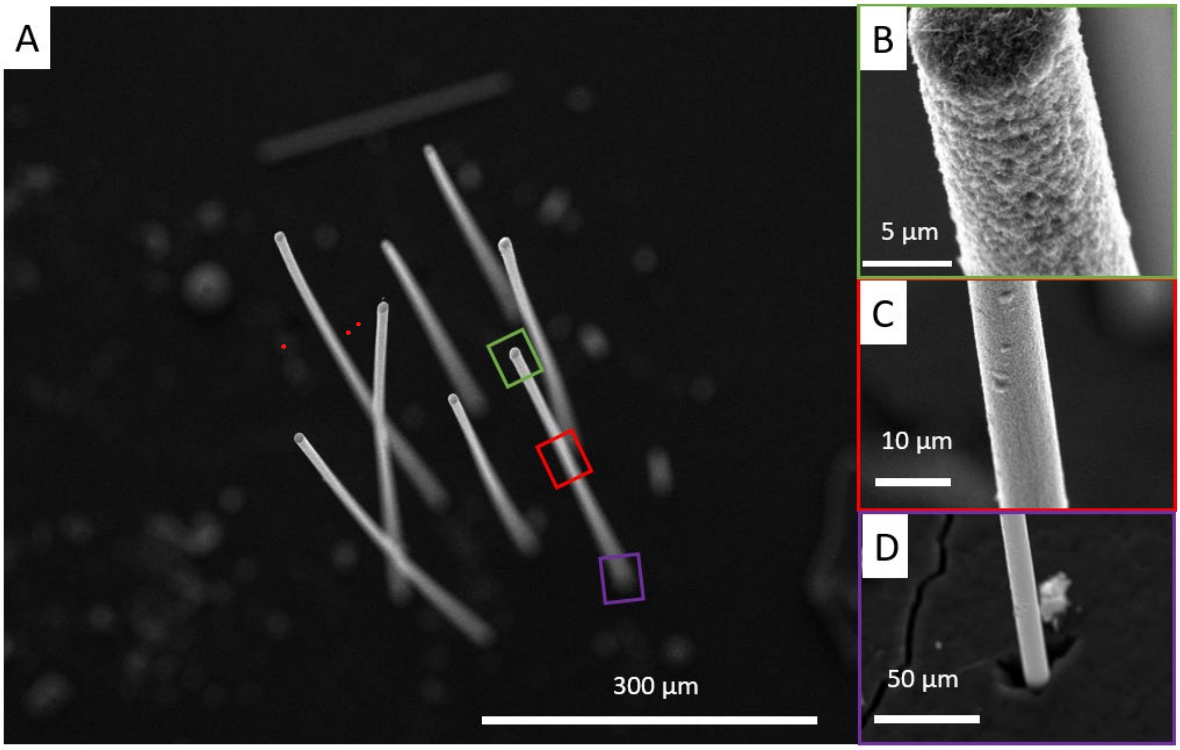

Figure 6.8: CVD plasma growth onto 1.5 mm long carbon fiber array (A) using a 1.5mm thick lid. CNW growth can be seen on the tips of the fibers (B) with growth ceasing partway down the fiber (C) with no change to the substrate surface (D).

To test the effect the fiber length on the plasma attenuation, 1.5mm long fibers were used in combination with the flat 0.3mm thick lid. The plasma dispersion and set up can be seen in Figure 6.9. This growth showed clear attenuation of the plasma around the fibers themselves. This resulted in optimal growth mechanics around this area as for the same duration growth produced a much thicker coating compared to the same set up with shorter fibers. The SEM images of this growth is seen below in Figure 6.9. This growth resulted in a very thick coating of Diamond on the tips of the electrodes with CNW appearing for a section down the length of the fiber (Figure 6.9 C and D, respectively). Raman spectra was later performed on the tips of the fibers and can be seen in Figure 6.10. This produced a similar spectrum to that grown and characterised on the bundle of individual fibers (Refer to Chapter 5, Figure 5.11A). SEM further confirmed that this coating was in fact the desired NCD. For this growth, no additional coating was observed on the base of the electrodes (Figure 6.9E), indicating that the desired growth mechanics had been achieved for this carbon fiber array configuration. A section of CNW is still evident some length down the electrodes (Figure 6.9D), but as this does not short the electrodes and has previously been shown not to disrupt the mechanical properties of the fibers [105]. As can be seen by the bulb in Figure 6.9C, the growth mechanics were highly concentrated at the tips of the electrodes. As the growth rate of the coating is mostly linear, an optimal thickness could be achieved simply by reducing the growth time. This is further evidence that this configuration to grow diamond on flexible neural arrays is the most appropriate in creating a chronically implantable neural interfacing array of NCD.

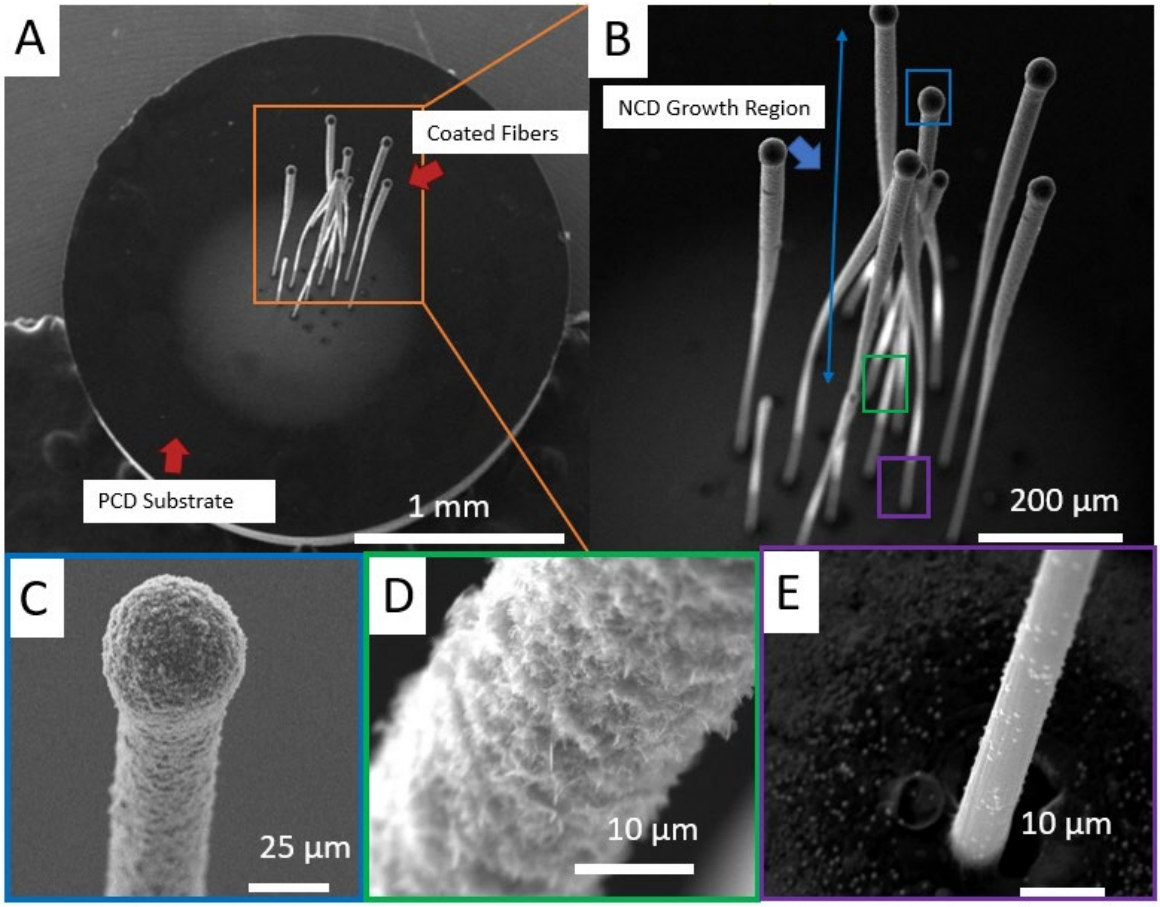

Figure 6.9: CVD plasma growth onto 1.5 mm long carbon fiber array (A) using a 0.3 mm thick lid. ND growth is observed in a region at the tips of the carbon fiber (B) with enhanced growth observed at the very tips of the fibers (C). CNW growth was observed part way down the fibers (D) with no growth observed on the substrate surface (E).

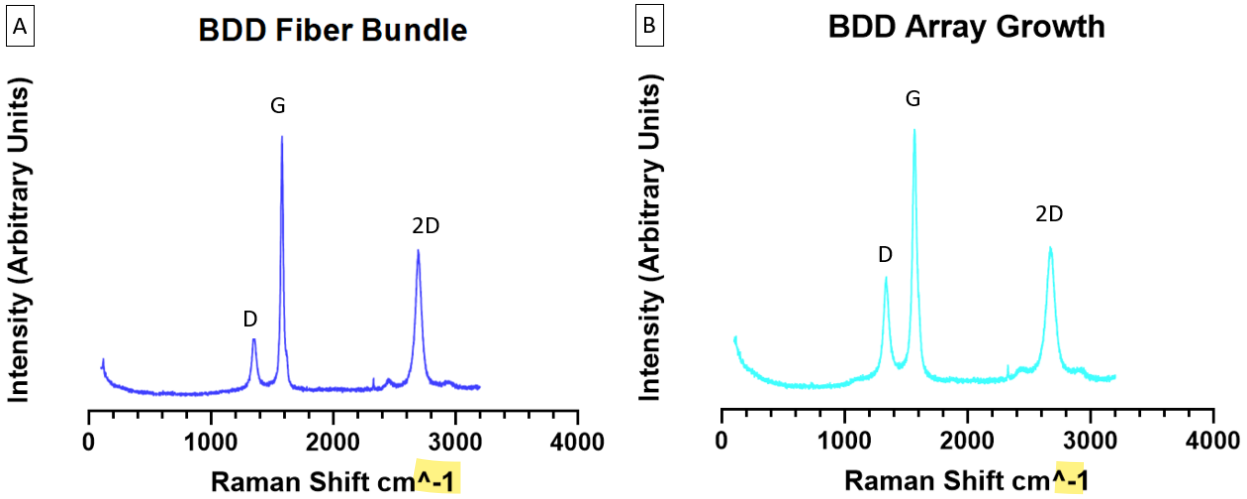

Figure 6.10. Raman spectrum indicating similar growth morphologies between the individual fiber growth (A) and the carbon fiber array growth (B).

6.5 BDD coated Carbon Fiber Array Limitations

Although a promising proof of concept has been developed, much work is still required for a fully functional and implanted device. The main limitation with this process is that it is adding another complicated process to an already complex array design with its own fabrication limitations. Any yield issues when creating an array for CVD growth are compounded by the yield issues outlined in the fabrication of the carbon fiber arrays. With more development this could be mitigated, and the highly promising chronically implantable NCD coated carbon fiber array could be achieved.

Creating consistent arrays and ensuring all alignment within the growth chamber is another issue encountered during this work. As CVD is a very complex process, repeatability is vitally important and difficult to achieve. The concept of growing directly onto the array and not individual fibers aims to mitigate this, however it is still a concern. The position of the holder within the chamber, the exact position of the substrate and fibers within the holder, the layout of the fibers within the array, as well as how the lids sit on the holder, will all impact the growth in some way. To add to this, the seasoning of the holders as well as debris or contamination within the chamber may also play some part. Constraining all of these variables will be vital when considering this concept for a functional and manufacturable device.

6.6 Future Work

Considering the limitations outlined, much work is still required. Future work will be required to produce a greater number of samples and achieve adequate levels of consistency and reliability. This would involve potentially finding the ideal length of fibers as well as growth time to produce a fully characterised NCD coating that is capable of neuromodulation in a meaningful capacity. Proving the chronic capabilities of the coating is also required. Lastly, this would need to produce an electrically connected device to show viability as well as to definitively prove that the materials used do all survive the CVD conditions in a way that is practically manufacturable. Much work has been done to unlock the capabilities of carbon fibers and NCD, however more work is needed to produce complete devices required for chronic implantation.

Chapter 7: Conclusions

The work presented has shown a broad, novel, and promising effort in furthering advances in neural interfacing. A complete array of carbon fibers was produced that was shown to not only achieve single unit recordings *in vivo* but were also implanted into animals long term in a manner that showed no chronic inflammation or adverse effects on the tissue or the implant itself. The scalability and future of these implants were explored. NCD coatings were used to improve the electrochemical characteristics and neurochemical sensing ability of carbon fibers. This work was validated and extended through collaborations and provides and avenue for creating a multipurpose neural interfacing material. This coating was successfully implemented onto the carbon fiber arrays in a configuration that could enable the implantation of these electrodes within the brain. A multipurpose, chronic neural interfacing implant would provide the understanding, diagnosis, and treatment opportunity potential for many neurological diseases. The results shown are all a positive step forward in achieving this aim.

This Chapter seems rather short. I'd have preferred this to be a long list of bullet points highlighting the major findings (positive and negative) from each chapter. It should also include a more general discussion about future work for the different types of array, summarising all the discussions from previous chapters, and providing a roadmap of where this research should go next.

References

[1] J. Vidal, "Real-time detection of brain events in EEG," *Proceedings of the IEEE,* vol. 65, pp. 633-641, 06/01 1977, doi: 10.1109/PROC.1977.10542.

[2] P. Konrad and T. Shanks, "Implantable brain computer interface: Challenges to neurotechnology translation," *Neurobiology of Disease,* vol. 38, no. 3, pp. 369-375, 2010/06/01/ 2010, doi: https://doi.org/10.1016/j.nbd.2009.12.007.

[3] T. O. Zander and C. Kothe, "Towards passive brain–computer interfaces: applying brain–computer interface technology to human–machine systems in general," *Journal of neural engineering,* vol. 8, no. 2, pp. 025005-025005, 2011, doi: 10.1088/1741-2560/8/2/025005.

[4] C. Guger *et al.*, "How many people are able to control a P300-based brain–computer interface (BCI)?," *Neuroscience letters,* vol. 462, no. 1, pp. 94-98, 2009, doi: 10.1016/j.neulet.2009.06.045.

[5] A. L. Benabid, "Neurosurgical giants: Feet of clay and iron," *Neuropsychologia,* vol. 25, no. 3, pp. 594-595, 1987, doi: 10.1016/0028-3932(87)90087-X.

[6] P. Blomstedt and M. I. Hariz, "Deep brain stimulation for movement disorders before DBS for movement disorders," *Parkinsonism & related disorders,* vol. 16, no. 7, pp. 429-433, 2010, doi: 10.1016/j.parkreldis.2010.04.005.

[7] M. Hariz, "Twenty-five years of deep brain stimulation: Celebrations and apprehensions," *Movement disorders,* vol. 27, no. 7, pp. 930-933, 2012, doi: 10.1002/mds.25007.

[8] A. M. Lozano *et al.*, "Deep brain stimulation: current challenges and future directions," *Nature Reviews Neurology,* vol. 15, no. 3, pp. 148-160, 2019/03/01 2019, doi: 10.1038/s41582-018-0128-2.

[9] J. Moss, T. Ryder, T. Z. Aziz, M. B. Graeber, and P. G. Bain, "Electron microscopy of tissue adherent to explanted electrodes in dystonia and Parkinson's disease," *Brain (London, England : 1878),* vol. 127, no. 12, pp. 2755-2763, 2004, doi: 10.1093/brain/awh292.

[10] M. Paff, A. Loh, C. Sarica, A. M. Lozano, and A. Fasano, "Update on Current Technologies for Deep Brain Stimulation in Parkinson's Disease," (in eng), *J Mov Disord,* vol. 13, no. 3, pp. 185-198, Sep 2020, doi: 10.14802/jmd.20052.

[11] N. Gravbrot, M. Saranathan, L. Nagae, J. Becker, and W. Kasoff, "Safety Profile of Infinity Deep Brain Stimulation Electrode Placement in a 1.5 T Interventional MRI Suite: Consecutive Single-Institution Case Series," *American Journal of Neuroradiology,* vol. 41, no. 12, pp. 2257-2262, 2020.

[12] P. Medtronic, "Green light for deep brain stimulator incorporating neurofeedback," *Nat. Biotechnol,* vol. 38, pp. 1014-1015, 2020.

[13] S. Stanslaski *et al.*, "Design and Validation of a Fully Implantable, Chronic, Closed-Loop Neuromodulation Device With Concurrent Sensing and Stimulation," *IEEE transactions on neural systems and rehabilitation engineering,* vol. 20, no. 4, pp. 410-421, 2012, doi: 10.1109/TNSRE.2012.2183617.

[14] K. A. Sillay *et al.*, "Perioperative Brain Shift and Deep Brain Stimulating Electrode Deformation Analysis: Implications for rigid and non-rigid devices," *Annals of biomedical engineering,* vol. 41, no. 2, pp. 293-304, 2013, doi: 10.1007/s10439-012-0650-0.

[15] J. K. Krauss *et al.*, "Technology of deep brain stimulation: current status and future directions," *Nature Reviews Neurology,* vol. 17, no. 2, pp. 75-87, 2021.

[16] F. Vitale, S. R. Summerson, B. Aazhang, C. Kemere, and M. Pasquali, "Neural Stimulation and Recording with Bidirectional, Soft Carbon Nanotube Fiber Microelectrodes," *ACS nano,* vol. 9, no. 4, pp. 4465-4474, 2015, doi: 10.1021/acsnano.5b01060.

[17] T. Lenarz, "Cochlear implant - state of the art," (in eng), *GMS Curr Top Otorhinolaryngol Head Neck Surg,* vol. 16, pp. Doc04-Doc04, 2018, doi: 10.3205/cto000143.

[18] D. Zahara, R. D. Dewi, A. Aboet, F. M. Putranto, N. D. Lubis, and T. Ashar, "Variations in Cochlear Size of Cochlear Implant Candidates," (in eng), *Int Arch Otorhinolaryngol,* vol. 23, no. 2, pp. 184-190, 2019, doi: 10.1055/s-0038-1661360.

[19] N. Swaddiwudhipong, C. Jiang, T. G. Landry, and M. Bance, "Investigating the Electrical Properties of Different Cochlear Implants," (in eng), *Otol Neurotol,* vol. 42, no. 1, pp. 59-67, Jan 2021, doi: 10.1097/mao.0000000000002861.

[20] D. Lemoine, E. Simon, G. Buc, and M. Deterre, "In vitro reliability testing and in vivo lifespan estimation of wireless Pixium Vision PRIMA photovoltaic subretinal prostheses suggest prolonged durability and functionality in clinical practice," *Journal of neural engineering,* vol. 17, no. 3, pp. 035005-035005, 2020, doi: 10.1088/1741-2552/ab8f70.

[21] J. Villalobos *et al.*, "A wide-field suprachoroidal retinal prosthesis is stable and well tolerated following chronic implantation," *Investigative ophthalmology & visual science,* vol. 54, no. 5, pp. 3751-3762, 2013, doi: 10.1167/iovs.12-10843.

[22] K. Kohler, J. A. Hartmann, D. Werts, and E. Zrenner, "Histological studies of retinal degeneration and biocompatibility of subretinal implants," *Der Ophthalmologe : Zeitschrift der Deutschen Ophthalmologischen Gesellschaft,* vol. 98, no. 4, p. 364, 2001.

[23] T. J. Oxley *et al.*, "Minimally invasive endovascular stent-electrode array for high-fidelity, chronic recordings of cortical neural activity," *Nature biotechnology,* vol. 34, no. 3, pp. 320-327, 2016, doi: 10.1038/nbt.3428.

[24] M. Mirowski *et al.*, "Termination of Malignant Ventricular Arrhythmias with an Implanted Automatic Defibrillator in Human Beings," *The New England journal of medicine,* vol. 303, no. 6, pp. 322-324, 1980, doi: 10.1056/NEJM198008073030607.

[25] N. F. Nolta, M. B. Christensen, P. D. Crane, J. L. Skousen, and P. A. Tresco, "BBB leakage, astrogliosis, and tissue loss correlate with silicon microelectrode array recording performance," *Biomaterials,* vol. 53, pp. 753-762, 2015, doi: 10.1016/j.biomaterials.2015.02.081.

[26] T. J. Oxley *et al.*, "Motor neuroprosthesis implanted with neurointerventional surgery improves capacity for activities of daily living tasks in severe paralysis: first in-human experience," *Journal of NeuroInterventional Surgery,* vol. 13, no. 2, p. 102, 2021, doi: 10.1136/neurintsurg-2020-016862.

[27] J. J. Han, "Synchron receives FDA approval to begin early feasibility study of their endovascular, brain-computer interface device," *Artificial organs,* vol. 45, no. 10, pp. 1134-1135, 2021, doi: 10.1111/aor.14049.

[28] M. Russo *et al.*, "Sustained Long-Term Outcomes With Closed-Loop Spinal Cord Stimulation: 12-Month Results of the Prospective, Multicenter, Open-Label Avalon Study," (in eng), *Neurosurgery,* vol. 87, no. 4, pp. E485-e495, Sep 15 2020, doi: 10.1093/neuros/nyaa003.

[29] M. Russo *et al.*, "Effective Relief of Pain and Associated Symptoms With Closed-Loop Spinal Cord Stimulation System: Preliminary Results of the Avalon Study," (in eng), *Neuromodulation,* vol. 21, no. 1, pp. 38-47, Jan 2018, doi: 10.1111/ner.12684.

[30] T. Deer *et al.*, "Safety Analysis of Dorsal Root Ganglion Stimulation in the Treatment of Chronic Pain," (in eng), *Neuromodulation,* vol. 23, no. 2, pp. 239-244, Feb 2020, doi: 10.1111/ner.12941.

[31] B. Fiani, T. Reardon, B. Ayres, D. Cline, and S. R. Sitto, "An Examination of Prospective Uses and Future Directions of Neuralink: The Brain-Machine Interface," *Curēus (Palo Alto, CA),* vol. 13, no. 3, pp. e14192-e14192, 2021, doi: 10.7759/cureus.14192.

[32] E. Musk and Neuralink, "An Integrated Brain-Machine Interface Platform With Thousands of Channels," (in eng), *Journal of medical Internet research,* vol. 21, no. 10, pp. e16194-e16194, 2019, doi: 10.2196/16194.

[33] L. Drew, "Elon Musk's Neuralink brain chip: what scientists think of first human trial," *Nature ~~(London),~~* 2024, doi: 10.1038/d41586-024-00304-4.

[34] N. A. Steinmetz, C. Koch, K. D. Harris, and M. Carandini, "Challenges and opportunities for large-scale electrophysiology with Neuropixels probes," *Current opinion in neurobiology,* vol. 50, pp. 92-100, 2018, doi: 10.1016/j.conb.2018.01.009.

[35] N. A. Steinmetz *et al.*, "Neuropixels 2.0: A miniaturized high-density probe for stable, long-term brain recordings," *Science ~~(American Association for the Advancement of Science),~~* vol. 372, no. 6539, p. 258, 2021, doi: 10.1126/science.abf4588.

[36] A. L. Juavinett, G. Bekheet, and A. K. Churchland, "Chronically implanted neuropixels probes enable high-yield recordings in freely moving mice," *eLife,* vol. 8, 2019, doi: 10.7554/eLife.47188.

[37] A. C. Paulk *et al.*, "Large-scale neural recordings with single neuron resolution using Neuropixels probes in human cortex," *Nature neuroscience,* vol. 25, no. 2, pp. 252-263, 2022, doi: 10.1038/s41593-021-00997-0.

[38] J. E. Chung *et al.*, "High-density single-unit human cortical recordings using the Neuropixels probe," *Neuron (Cambridge, Mass.),* vol. 110, no. 15, pp. 2409-2421.e3, 2022, doi: 10.1016/j.neuron.2022.05.007.

[39] J. Putzeys *et al.*, "Neuropixels Data-Acquisition System: A Scalable Platform for Parallel Recording of 10 000+ Electrophysiological Signals," *IEEE transactions on biomedical circuits and systems,* vol. 13, no. 6, pp. 1635-1644, 2019, doi: 10.1109/TBCAS.2019.2943077.

[40] K. C. Cheung, P. Renaud, H. Tanila, and K. Djupsund, "Flexible polyimide microelectrode array for in vivo recordings and current source density analysis," *Biosensors & bioelectronics,* vol. 22, no. 8, pp. 1783-1790, 2007, doi: 10.1016/j.bios.2006.08.035.

[41] K. L. Drake, K. D. Wise, J. Farraye, D. J. Anderson, and S. L. BeMent, "Performance of planar multisite microprobes in recording extracellular single-unit intracortical activity," *IEEE transactions on biomedical engineering,* vol. 35, no. 9, pp. 719-732, 1988, doi: 10.1109/10.7273.

[42] A. B. Schwartz, "Cortical neural prosthetics," *Annual review of neuroscience,* vol. 27, no. 1, pp. 487-507, 2004, doi: 10.1146/annurev.neuro.27.070203.144233.

[43] K. A. Ludwig, J. D. Uram, J. Yang, D. C. Martin, and D. R. Kipke, "Chronic neural recordings using silicon microelectrode arrays electrochemically deposited with a poly(3,4-ethylenedioxythiophene) (PEDOT) film," *Journal of neural engineering,* vol. 3, no. 1, pp. 59-70, 2006, doi: 10.1088/1741-2560/3/1/007.

[44] C. Kim, J. Jeong, and S. J. Kim, "Recent Progress on Non-Conventional Microfabricated Probes for the Chronic Recording of Cortical Neural Activity," (in eng), *Sensors (Basel, Switzerland),* vol. 19, no. 5, p. 1069, 2019, doi: 10.3390/s19051069.

[45] P. R. Patel *et al.*, "Chronic in vivo stability assessment of carbon fiber microelectrode arrays," *Journal of neural engineering,* vol. 13, no. 6, pp. 066002-066002, 2016, doi: 10.1088/1741-2560/13/6/066002.

[46] K. Woeppel *et al.*, "Explant analysis of Utah electrode arrays implanted in human cortex for brain-computer-interfaces," *medRxiv,* p. 2021.08.28.21262765, 2021, doi: 10.1101/2021.08.28.21262765.

[47] B. J. Black *et al.*, "Chronic recording and electrochemical performance of Utah microelectrode arrays implanted in rat motor cortex," *Journal of neurophysiology,* vol. 120, no. 4, pp. 2083-2090, 2018, doi: 10.1152/jn.00181.2018.

[48] P. J. Rousche and R. A. Normann, "Chronic recording capability of the Utah Intracortical Electrode Array in cat sensory cortex," *Journal of Neuroscience Methods,* vol. 82, no. 1, pp. 1-15, 1998/07/01/ 1998, doi: https://doi.org/10.1016/S0165-0270(98)00031-4.

[49] A. Branner *et al.*, "Neuronal ensemble control of prosthetic devices by a human with tetraplegia," *Nature (London),* vol. 442, no. 7099, pp. 164-171, 2006, doi: 10.1038/nature04970.

[50] C. Sponheim *et al.*, "Longevity and reliability of chronic unit recordings using the Utah, intracortical multi-electrode arrays," (in eng), *J Neural Eng,* vol. 18, no. 6, Dec 28 2021, doi: 10.1088/1741-2552/ac3eaf.

[51] J. Thelin *et al.*, "Implant size and fixation mode strongly influence tissue reactions in the CNS," *PloS one,* vol. 6, no. 1, pp. e16267-e16267, 2011, doi: 10.1371/journal.pone.0016267.

[52] M. P. Ward, P. Rajdev, C. Ellison, and P. P. Irazoqui, "Toward a comparison of microelectrodes for acute and chronic recordings," *Brain research,* vol. 1282, pp. 183-200, 2009, doi: 10.1016/j.brainres.2009.05.052.

[53] S. M. Wellman, L. Li, Y. Yaxiaer, I. McNamara, and T. D. Y. Kozai, "Revealing spatial and temporal patterns of cell death, glial proliferation, and blood-brain barrier dysfunction around implanted intracortical neural interfaces," *Frontiers in neuroscience,* vol. 13, no. MAY, pp. 493-493, 2019, doi: 10.3389/fnins.2019.00493.

[54] V. S. Polikov, P. A. Tresco, and W. M. Reichert, "Response of brain tissue to chronically implanted neural electrodes," *Journal of neuroscience methods,* vol. 148, no. 1, pp. 1-18, 2005, doi: 10.1016/j.jneumeth.2005.08.015.

[55] A. Sridharan, S. D. Rajan, and J. Muthuswamy, "Long-term changes in the material properties of brain tissue at the implant-tissue interface," *Journal of neural engineering,* vol. 10, no. 6, pp. 066001-066001, 2013, doi: 10.1088/1741-2560/10/6/066001.

[56] M. M. Holecko, J. C. Williams, and S. P. Massia, "Visualization of the intact interface between neural tissue and implanted microelectrode arrays," *Journal of neural engineering,* vol. 2, no. 4, pp. 97-102, 2005, doi: 10.1088/1741-2560/2/4/005.

[57] K. Yoshida, I. Lewinsky, M. Nielsen, and M. Hylleberg, "Implantation mechanics of tungsten microneedles into peripheral nerve trunks," *Medical & biological engineering & computing,* vol. 45, no. 4, pp. 413-420, 2007, doi: 10.1007/s11517-007-0175-0.

[58] A. A. Sharp, A. M. Ortega, D. Restrepo, D. Curran-Everett, and K. Gall, "In vivo penetration mechanics and mechanical properties of mouse brain tissue at micrometer scales," (in eng), *IEEE Trans Biomed Eng,* vol. 56, no. 1, pp. 45-53, Jan 2009, doi: 10.1109/tbme.2008.2003261.

[59] M. Welkenhuysen, A. Andrei, L. Ameye, W. Eberle, and B. Nuttin, "Effect of insertion speed on tissue response and insertion mechanics of a chronically implanted silicon-based neural probe," *IEEE Trans Biomed Eng,* vol. 58, no. 11, pp. 3250-9, Nov 2011, doi: 10.1109/TBME.2011.2166963.

[60] H. S. Sohal, G. J. Clowry, A. Jackson, A. O'Neill, and S. N. Baker, "Mechanical flexibility reduces the foreign body response to long-term implanted microelectrodes in rabbit cortex," *PloS one,* vol. 11, no. 10, pp. e0165606-e0165606, 2016, doi: 10.1371/journal.pone.0165606.

[61] R. Biran, D. C. Martin, and P. A. Tresco, "The brain tissue response to implanted silicon microelectrode arrays is increased when the device is tethered to the skull," *Journal of Biomedical Materials Research Part A,* vol. 82A, no. 1, pp. 169-178, 2007, doi: 10.1002/jbm.a.31138.

[62] S. Suner, M. R. Fellows, C. Vargas-Irwin, G. K. Nakata, and J. P. Donoghue, "Reliability of signals from a chronically implanted, silicon-based electrode array in non-human primate primary motor cortex," *IEEE transactions on neural systems and rehabilitation engineering,* vol. 13, no. 4, pp. 524-541, 2005, doi: 10.1109/TNSRE.2005.857687.

[63] T. Stöver and T. Lenarz, "Biomaterials in cochlear implants," (in eng), *GMS Curr Top Otorhinolaryngol Head Neck Surg,* vol. 8, pp. Doc10-Doc10, 2009, doi: 10.3205/cto000062.

[64] M. Gulino, D. Kim, S. Pané, S. D. Santos, and A. P. Pêgo, "Tissue Response to Neural Implants: The Use of Model Systems Toward New Design Solutions of Implantable Microelectrodes," (in eng), *Front Neurosci,* vol. 13, p. 689, 2019, doi: 10.3389/fnins.2019.00689.

[65] M. A. Erturk *et al.*, "Predicting in vivo MRI Gradient-Field Induced Voltage Levels on Implanted Deep Brain Stimulation Systems Using Neural Networks," *Frontiers in human neuroscience,* vol. 14, pp. 34-34, 2020, doi: 10.3389/fnhum.2020.00034.

[66] D. J. Di Lorenzo, K. W. Leyde, and D. Kaplan, "Neural state monitoring in the treatment of epilepsy: Seizure prediction—conceptualization to first-in-man study," *Brain sciences,* vol. 9, no. 7, p. 156, 2019, doi: 10.3390/brainsci9070156.

[67] Z. Tiganj and M. Mboup, "Neural spike sorting using iterative ICA and a deflation-based approach," *Journal of neural engineering,* vol. 9, no. 6, pp. 066002-066002, 2012, doi: 10.1088/1741-2560/9/6/066002.

[68] Z. Blumenfeld and H. Brontë-Stewart, "High Frequency Deep Brain Stimulation and Neural Rhythms in Parkinson's Disease," *Neuropsychology review,* vol. 25, no. 4, pp. 384-397, 2015, doi: 10.1007/s11065-015-9308-7.

[69] K. Chen, S. M. Wellman, Y. Yaxiaer, J. R. Eles, and T. D. Y. Kozai, "In vivo spatiotemporal patterns of oligodendrocyte and myelin damage at the neural electrode interface," *Biomaterials,* vol. 268, p. 120526, 2021/01/01/ 2021, doi: https://doi.org/10.1016/j.biomaterials.2020.120526.

[70] E. Patrick, M. E. Orazem, J. C. Sanchez, and T. Nishida, "Corrosion of tungsten microelectrodes used in neural recording applications," *Journal of neuroscience methods,* vol. 198, no. 2, pp. 158-171, 2011, doi: 10.1016/j.jneumeth.2011.03.012.

[71] V. Sankar, E. P. R. Dieme, J. C. Sanchez, A. Prasad, and T. Nishida, "Electrode impedance analysis of chronic tungsten microwire neural implants: Understanding abiotic vs. biotic contributions," *Frontiers in neuroengineering,* vol. 7, no. MAY, pp. 13-13, 2014, doi: 10.3389/fneng.2014.00013.

[72] K. Sahasrabuddhe *et al.*, "The Argo: A high channel count recording system for neural recording in vivo," *Journal of neural engineering,* vol. 18, no. 1, pp. 015002-015002, 2021, doi: 10.1088/1741-2552/abd0ce.

[73] G. E. Loeb, R. A. Peck, and J. Martyniuk, "Toward the ultimate metal microelectrode," *Journal of neuroscience methods,* vol. 63, no. 1, pp. 175-183, 1995, doi: 10.1016/0165-0270(95)00107-7.

[74] S. A. Desai, J. D. Rolston, L. Guo, and S. M. Potter, "Improving impedance of implantable microwire multi-electrode arrays by ultrasonic electroplating of durable platinum black," *Frontiers in neuroengineering,* vol. 3, pp. 1-11, 2010, doi: 10.3389/fneng.2010.00005.

[75] R. A. Frederick, I. Y. Meliane, A. Joshi-Imre, P. R. Troyk, and S. F. Cogan, "Activated iridium oxide film (AIROF) electrodes for neural tissue stimulation," *Journal of neural engineering,* vol. 17, no. 5, pp. 056001-056001, 2020, doi: 10.1088/1741-2552/abb9bf.

[76] T. D. Y. Kozai, A. S. Jaquins-Gerstl, A. L. Vazquez, A. C. Michael, and X. T. Cui, "Brain Tissue Responses to Neural Implants Impact Signal Sensitivity and Intervention Strategies," *ACS chemical neuroscience,* vol. 6, no. 1, pp. 48-67, 2015, doi: 10.1021/cn500256e.

[77] M. A. Arafat, L. N. Rubin, J. G. R. Jefferys, and P. P. Irazoqui, "A Method of Flexible Micro-Wire Electrode Insertion in Rodent for Chronic Neural Recording and a Device for Electrode Insertion," *IEEE transactions on neural systems and rehabilitation engineering,* vol. 27, no. 9, pp. 1724-1731, 2019, doi: 10.1109/TNSRE.2019.2932032.

[78] J. Shi and Y. Fang, "Flexible and Implantable Microelectrodes for Chronically Stable Neural Interfaces," *Advanced Materials,* vol. 31, no. 45, p. 1804895, 2019, doi: 10.1002/adma.201804895.

[79] S. P. Lacour *et al.*, "Flexible and stretchable micro-electrodes for in vitro and in vivo neural interfaces," *Medical & Biological Engineering & Computing,* vol. 48, no. 10, pp. 945-954, 2010/10/01 2010, doi: 10.1007/s11517-010-0644-8.

[80] Z. Zhao, E. Kim, H. Luo, J. Zhang, and Y. Xu, "Flexible deep brain neural probes based on a parylene tube structure," *Journal of micromechanics and microengineering,* vol. 28, no. 1, p. 15012, 2017, doi: 10.1088/1361-6439/aa9d61.

[81] R. Jalili *et al.*, "Scalable One-Step Wet-Spinning of Graphene Fibers and Yarns from Liquid Crystalline Dispersions of Graphene Oxide: Towards Multifunctional Textiles," *Advanced Functional Materials,* vol. 23, no. 43, pp. 5345-5354, 2013, doi: https://doi.org/10.1002/adfm.201300765.

[82] C. Chen, S. Ruan, X. Bai, C. Lin, C. Xie, and I.-S. Lee, "Patterned iridium oxide film as neural electrode interface: Biocompatibility and improved neurite outgrowth with electrical stimulation," *Materials Science and Engineering: C,* vol. 103, p. 109865, 2019/10/01/ 2019, doi: https://doi.org/10.1016/j.msec.2019.109865.

[83] E. J. Welle *et al.*, "Sharpened and Mechanically Durable Carbon Fiber Electrode Arrays for Neural Recording," *IEEE transactions on neural systems and rehabilitation engineering,* vol. 29, pp. 993-1003, 2021, doi: 10.1109/TNSRE.2021.3082056.

[84] P. R. Patel *et al.*, "Insertion of linear 8.4µm diameter 16 channel carbon fiber electrode arrays for single unit recordings," *Journal of Neural Engineering,* vol. 12, no. 4, p. 046009, 2015/06/02 2015, doi: 10.1088/1741-2560/12/4/046009.

[85] S. Park, G. Loke, Y. Fink, and P. Anikeeva, "Flexible fiber-based optoelectronics for neural interfaces," *Chem Soc Rev,* vol. 48, no. 6, pp. 1826-1852, Mar 18 2019, doi: 10.1039/c8cs00710a.

[86] S. K. Smart, A. I. Cassady, G. Q. Lu, and D. J. Martin, "The biocompatibility of carbon nanotubes," *Carbon,* vol. 44, no. 6, pp. 1034-1047, 2006/05/01/ 2006, doi: https://doi.org/10.1016/j.carbon.2005.10.011.

[87] D. J. Garrett *et al.*, "In vivo biocompatibility of boron doped and nitrogen included conductive-diamond for use in medical implants," (in eng), *J Biomed Mater Res B Appl Biomater,* vol. 104, no. 1, pp. 19-26, Jan 2016, doi: 10.1002/jbm.b.33331.

[88] S. Takeuchi, D. Ziegler, Y. Yoshida, K. Mabuchi, and T. Suzuki, "Parylene flexible neural probes integrated with microfluidic channels," *Lab on a chip,* vol. 5, no. 5, pp. 519-523, 2005, doi: 10.1039/b417497f.

[89] X. Xie *et al.*, "Long-term reliability of Al2O3 and Parylene C bilayer encapsulated Utah electrode array based neural interfaces for chronic implantation," *Journal of neural engineering,* vol. 11, no. 2, pp. 026016-026016, 2014, doi: 10.1088/1741-2560/11/2/026016.

[90] Y. Xie *et al.*, "Improving adhesion strength between layers of an implantable parylene-C electrode," *Sensors and actuators. A. Physical.,* vol. 260, pp. 117-123, 2017, doi: 10.1016/j.sna.2017.04.045.

[91] B. D. Winslow, M. B. Christensen, W.-K. Yang, F. Solzbacher, and P. A. Tresco, "A comparison of the tissue response to chronically implanted Parylene-C-coated and uncoated planar silicon microelectrode arrays in rat cortex," *Biomaterials,* vol. 31, no. 35, pp. 9163-9172, 2010, doi: 10.1016/j.biomaterials.2010.05.050.

[92] N. Tsierkezos *et al.*, "Boron-doped multi-walled carbon nanotubes as sensing material for analysis of dopamine and epinephrine in presence of uric acid," *Chemical Physics Letters,* vol. 710, 09/01 2018, doi: 10.1016/j.cplett.2018.09.007.

[93] M. Ecker *et al.*, "From softening polymers to multimaterial based bioelectronic devices," *Multifunctional Materials,* vol. 2, no. 1, p. 012001, 2018/12/11 2018, doi: 10.1088/2399-7532/aaed58.

[94] T. L. Massey, S. R. Santacruz, J. F. Hou, K. S. J. Pister, J. M. Carmena, and M. M. Maharbiz, "A high-density carbon fiber neural recording array technology," (in eng), *J Neural Eng,* vol. 16, no. 1, p. 016024, Feb 2019, doi: 10.1088/1741-2552/aae8d9.

[95] X. Fu *et al.*, "Carbon-Based Fiber Materials as Implantable Depth Neural Electrodes," (in eng), *Front Neurosci,* vol. 15, p. 771980, 2021, doi: 10.3389/fnins.2021.771980.

[96] J. G. Letner *et al.*, "Post-explant profiling of subcellular-scale carbon fiber intracortical electrodes and surrounding neurons enables modeling of recorded electrophysiology," (in eng), *J Neural Eng,* vol. 20, no. 2, Mar 17 2023, doi: 10.1088/1741-2552/acbf78.

[97] X. Luo, C. L. Weaver, D. D. Zhou, R. Greenberg, and X. T. Cui, "Highly stable carbon nanotube doped poly(3,4-ethylenedioxythiophene) for chronic neural stimulation," *Biomaterials,* vol. 32, no. 24, pp. 5551-5557, 2011, doi: 10.1016/j.biomaterials.2011.04.051.

[98] X. T. Cui and D. D. Zhou, "Poly (3,4-ethylenedioxythiophene) for chronic neural stimulation," (in eng), *IEEE Trans Neural Syst Rehabil Eng,* vol. 15, no. 4, pp. 502-8, Dec 2007, doi: 10.1109/tnsre.2007.909811.

[99] L. Groenendaal, F. Jonas, D. Freitag, H. Pielartzik, and J. R. Reynolds, "Poly(3,4-ethylenedioxythiophene) and Its Derivatives: Past, Present, and Future," *Advanced materials ~~(Weinheim)~~,* vol. 12, no. 7, pp. 481-494, 2000, doi: 10.1002/(SICI)1521-4095(200004)12:7<481::AID-ADMA481>3.0.CO;2-C.

[100] B. Roth *et al.*, "The Critical Choice of PEDOT:PSS Additives for Long Term Stability of Roll-to-Roll Processed OPVs," *Advanced energy materials,* vol. 5, no. 9, pp. 1401912-n/a, 2015, doi: 10.1002/aenm.201401912.

[101] A. N. Bezbaruah and T. C. Zhang, "Fabrication of Anodically Electrodeposited Iridium Oxide Film pH Microelectrodes for Microenvironmental Studies," *Analytical Chemistry,* vol. 74, no. 22, pp. 5726-5733, 2002/11/01 2002, doi: 10.1021/ac020326l.

[102] F. Deku, A. Joshi-Imre, A. Mertiri, T. J. Gardner, and S. F. Cogan, "Electrodeposited Iridium Oxide on Carbon Fiber Ultramicroelectrodes for Neural Recording and Stimulation," *Journal of The Electrochemical Society,* vol. 165, no. 9, pp. D375-D380, 2018, doi: 10.1149/2.0401809jes.

[103] X. Li, L. Zhou, and B. Su, "Iridium oxide nanoparticles modified carbon fiber microelectrodes for pH detection," *SCIENTIA SINICA Chimica,* vol. 51, pp. 383-387, 03/01 2021, doi: 10.1360/SSC-2020-0197.

[104] P. R. Patel *et al.*, "High density carbon fiber arrays for chronic electrophysiology, fast scan cyclic voltammetry, and correlative anatomy," (in eng), *J Neural Eng,* vol. 17, no. 5, p. 056029, Oct 15 2020, doi: 10.1088/1741-2552/abb1f6.

[105] M. A. Hejazi *et al.*, "High Fidelity Bidirectional Neural Interfacing with Carbon Fiber Microelectrodes Coated with Boron-Doped Carbon Nanowalls: An Acute Study," *Advanced functional materials,* vol. 30, no. 52, pp. 2006101-n/a, 2020, doi: 10.1002/adfm.202006101.

[106] "Multi-walled carbon nanotubes induce airway hyperresponsiveness in human bronchi by stimulating sensory C-fibers and increasing the release of neuronal acetylcholine," *Expert review of respiratory medicine,* pp. 1-9, 2021, doi: 10.1080/17476348.2021.1979395.

[107] S. Nimbalkar *et al.*, "Ultra-Capacitive Carbon Neural Probe Allows Simultaneous Long-Term Electrical Stimulations and High-Resolution Neurotransmitter Detection," *Scientific reports,* vol. 8, no. 1, pp. 6958-14, 2018, doi: 10.1038/s41598-018-25198-x.

[108] P. R. Patel *et al.*, "Utah array characterization and histological analysis of a multi-year implant in non-human primate motor and sensory cortices," (in eng), *J Neural Eng,* vol. 20, no. 1, Jan 18 2023, doi: 10.1088/1741-2552/acab86.

[109] E. R. Kandel, *Principles of neural science*, 5th ed. / edited by Eric R. Kandel ... [et al.] ; art editor, Sarah Mack. ed. New York: McGraw-Hill Medical, 2013.

[110] M. N. Rasband and E. Peles, "The nodes of Ranvier: Molecular assembly and maintenance," *Cold Spring Harbor perspectives in biology,* vol. 8, no. 3, pp. a020495-a020495, 2016, doi: 10.1101/cshperspect.a020495.

[111] J.-Q. He, Y. Ma, Y. Lee, J. A. Thomson, and T. J. Kamp, "Human Embryonic Stem Cells Develop Into Multiple Types of Cardiac Myocytes: Action Potential Characterization," *Circulation research,* vol. 93, no. 1, pp. 32-39, 2003, doi: 10.1161/01.RES.0000080317.92718.99.

[112] T. C. Sudhof, "The Molecular Machinery of Neurotransmitter Release (Nobel Lecture)," *Angewandte Chemie (International ed.),* vol. 53, no. 47, pp. 12696-12717, 2014, doi: 10.1002/anie.201406359.

[113] T. C. Sudhof, "The Presynaptic Active Zone," *Neuron ~~(Cambridge, Mass.)~~,* vol. 75, no. 1, pp. 11-25, 2012, doi: 10.1016/j.neuron.2012.06.012.

[114] D. J. Rossi and M. Hamann, "Spillover-mediated transmission at inhibitory synapses promoted by high affinity alpha(6) subunit GABA(A) receptors and glomerular geometry," *Neuron ~~(Cambridge, Mass.)~~,* vol. 20, no. 4, pp. 783-795, 1998, doi: 10.1016/S0896-6273(00)81016-8.

[115] K. J. Iremonger and J. S. Bains, "Asynchronous presynaptic glutamate release enhances neuronal excitability during the post-spike refractory period," *The Journal of physiology,* vol. 594, no. 4, pp. 1005-1015, 2016, doi: 10.1113/JP271485.

[116] J. C. Eccles, "The synapse: from electrical to chemical transmission," *Annual review of neuroscience,* vol. 5, no. 1, pp. 325-339, 1982, doi: 10.1146/annurev.ne.05.030182.001545.

[117] S. A. Bloomfield and B. Völgyi, "The diverse functional roles and regulation of neuronal gap junctions in the retina," *Nature reviews. Neuroscience,* vol. 10, no. 7, pp. 495-506, 2009, doi: 10.1038/nrn2636.

[118] "12.4 The Action potential." Rice University. https://openstax.org/books/anatomy-and-physiology/pages/12-4-the-action-potential (accessed 15 December, 2021).

[119] S. Herculano-Houzel, "The human brain in numbers: a linearly scaled-up primate brain," (in eng), *Front Hum Neurosci,* vol. 3, p. 31, 2009, doi: 10.3389/neuro.09.031.2009.

[120] R. W. Williams and K. Herrup, "The control of neuron number," (in eng), *Annu Rev Neurosci,* vol. 11, pp. 423-53, 1988, doi: 10.1146/annurev.ne.11.030188.002231.

[121] W. Lange, "Cell number and cell density in the cerebellar cortex of man and some other mammals," (in eng), *Cell Tissue Res,* vol. 157, no. 1, pp. 115-24, 1975, doi: 10.1007/bf00223234.

[122] G. Roth and U. Dicke, "Evolution of the brain and intelligence," (in eng), *Trends Cogn Sci,* vol. 9, no. 5, pp. 250-7, May 2005, doi: 10.1016/j.tics.2005.03.005.

[123] G. A. Martynov and R. R. Salem, *Electrical Double Layer at a Metal-dilute Electrolyte Solution Interface*, 1st ed. 1983. ed. (Lecture Notes in Chemistry, 33). Berlin, Heidelberg: Springer Berlin Heidelberg, 1983.

[124] F. Yang, "Size effect on electric-double-layer capacitances of conducting structures," *Physics Letters A,* vol. 383, no. 20, pp. 2353-2360, 2019/07/18/ 2019, doi: https://doi.org/10.1016/j.physleta.2019.04.051.

[125] D. A. Aikens, "Electrochemical methods, fundamentals and applications," *Journal of Chemical Education,* vol. 60, no. 1, p. A25, 1983/01/01 1983, doi: 10.1021/ed060pA25.1.

[126] J. M. Smulko, A. Szewczyk, and A. Lentka, "Noise in electrical double-layer capacitors (EDLCs)," 2019.

[127] L. Guo, "Perspectives on electrical neural recording: a revisit to the fundamental concepts," *Journal of Neural Engineering,* vol. 17, no. 1, p. 013001, 2020/02/25 2020, doi: 10.1088/1741-2552/ab702f.

[128] S. F. Cogan, "Neural stimulation and recording electrodes," (in eng), *Annu Rev Biomed Eng,* vol. 10, pp. 275-309, 2008, doi: 10.1146/annurev.bioeng.10.061807.160518.

[129] B. J. Venton and Q. Cao, "Fundamentals of fast-scan cyclic voltammetry for dopamine detection," *Analyst,* vol. 145, no. 4, pp. 1158-1168, 2020.

[130] D. A. Robinson, "The electrical properties of metal microelectrodes," *Proceedings of the IEEE,* vol. 56, no. 6, pp. 1065-1071, 1968, doi: 10.1109/PROC.1968.6458.

[131] E. S. Kappenman and S. J. Luck, "The effects of electrode impedance on data quality and statistical significance in ERP recordings," (in eng), *Psychophysiology,* vol. 47, no. 5, pp. 888-904, 2010, doi: 10.1111/j.1469-8986.2010.01009.x.

[132] A. V. Oppenheim and J. S. Lim, "The importance of phase in signals," *Proceedings of the IEEE,* vol. 69, no. 5, pp. 529-541, 1981, doi: 10.1109/PROC.1981.12022.

[133] V. Sankar, E. Patrick, R. Dieme, J. C. Sanchez, A. Prasad, and T. Nishida, "Electrode impedance analysis of chronic tungsten microwire neural implants: understanding abiotic vs. biotic contributions," *Front Neuroeng,* vol. 7, p. 13, 2014, doi: 10.3389/fneng.2014.00013.

[134] S. E. John *et al.*, "In Vivo Impedance Characterization of Cortical Recording Electrodes Shows Dependence on Electrode Location and Size," *IEEE transactions on biomedical engineering,* vol. 66, no. 3, pp. 675-681, 2019, doi: 10.1109/TBME.2018.2854623.

[135] E. K. Brunton *et al.*, "In vivo comparison of the charge densities required to evoke motor responses using novel annular penetrating microelectrodes," *Frontiers in neuroscience,* vol. 9, p. 265, 2015.

[136] J. E. Lisman, "Bursts as a unit of neural information: making unreliable synapses reliable," *Trends in neurosciences (Regular ed.),* vol. 20, no. 1, pp. 38-43, 1997, doi: 10.1016/S0166-2236(96)10070-9.

[137] S. E. Fox and J. B. Ranck, Jr., "Localization and anatomical identification of theta and complex spike cells in dorsal hippocampal formation of rats," (in eng), *Exp Neurol,* vol. 49, no. 1 Pt 1, pp. 299-313, Oct 1975, doi: 10.1016/0014-4886(75)90213-7.

[138] P. Charlesworth, E. Cotterill, A. Morton, S. Grant, and S. J. Eglen, "Quantitative differences in developmental profiles of spontaneous activity in cortical and hippocampal cultures," *Neural development,* vol. 10, no. 1, p. 1, 2015, doi: 10.1186/s13064-014-0028-0.

[139] R. M. Harris-Warrick, "Voltage-sensitive ion channels in rhythmic motor systems," *Current Opinion in Neurobiology,* vol. 12, no. 6, pp. 646-651, 2002, doi: 10.1016/S0959-4388(02)00377-X.

[140] N. V. Apollo *et al.*, "Soft, Flexible Freestanding Neural Stimulation and Recording Electrodes Fabricated from Reduced Graphene Oxide," *Advanced Functional Materials,* https://doi.org/10.1002/adfm.201500110 vol. 25, no. 23, pp. 3551-3559, 2015/06/01 2015, doi: https://doi.org/10.1002/adfm.201500110.

Author, proper title?

Incomplete

[141] D. Moran, "Evolution of brain–computer interface: action potentials, local field potentials and electrocorticograms," *Current opinion in neurobiology,* vol. 20, no. 6, pp. 741-745, 2010, doi: 10.1016/j.conb.2010.09.010.

[142] M. Teleńczuk, B. Teleńczuk, and A. Destexhe, "Modelling unitary fields and the single-neuron contribution to local field potentials in the hippocampus," *The Journal of physiology,* vol. 598, no. 18, pp. 3957-3972, 2020, doi: 10.1113/JP279452.

[143] N. W. Whitmore and S.-C. Lin, "Unmasking local activity within local field potentials (LFPs) by removing distal electrical signals using independent component analysis," *NeuroImage (Orlando, Fla.),* vol. 132, pp. 79-92, 2016, doi: 10.1016/j.neuroimage.2016.02.032.

[144] M. von Papen, H. S. Dafsari, E. Florin, F. Gerick, L. Timmermann, and J. Saur, "Phase-coherence classification: A new wavelet-based method to separate local field potentials into local (in)coherent and volume-conducted components," *Journal of neuroscience methods,* vol. 291, pp. 198-212, 2017, doi: 10.1016/j.jneumeth.2017.08.021.

[145] J. Bourien, F. Bartolomei, J. J. Bellanger, M. Gavaret, P. Chauvel, and F. Wendling, "A method to identify reproducible subsets of co-activated structures during interictal spikes. Application to intracerebral EEG in temporal lobe epilepsy," *Clinical neurophysiology,* vol. 116, no. 2, pp. 443-455, 2005, doi: 10.1016/j.clinph.2004.08.010.

[146] D. Cosandier-Rimele, J.-M. Badier, P. Chauvel, and F. Wendling, "A Physiologically Plausible Spatio-Temporal Model for EEG Signals Recorded With Intracerebral Electrodes in Human Partial Epilepsy," *IEEE transactions on biomedical engineering,* vol. 54, no. 3, pp. 380-388, 2007, doi: 10.1109/TBME.2006.890489.

[147] X. Li, C. Sun, and L. Shi, "Comparison of visual receptive field properties of the superior colliculus and primary visual cortex in rats," *Brain research bulletin,* vol. 117, pp. 69-80, 2015, doi: 10.1016/j.brainresbull.2015.07.007.

[148] S. H. Felix *et al.*, "Insertion of flexible neural probes using rigid stiffeners attached with biodissolvable adhesive," (in eng), *J Vis Exp,* no. 79, pp. e50609-e50609, 2013, doi: 10.3791/50609.

[149] Alex C. Kwan and Y. Dan, "Dissection of Cortical Microcircuits by Single-Neuron Stimulation In Vivo," *Current biology,* vol. 22, no. 16, pp. 1459-1467, 2012, doi: 10.1016/j.cub.2012.06.007.

[150] S. A. Mirbozorgi, H. Bahrami, M. Sawan, L. A. Rusch, and B. Gosselin, "A Single-Chip Full-Duplex High Speed Transceiver for Multi-Site Stimulating and Recording Neural Implants," *IEEE transactions on biomedical circuits and systems,* vol. 10, no. 3, pp. 643-653, 2016, doi: 10.1109/TBCAS.2015.2466592.

[151] R. Samba, T. Herrmann, and G. Zeck, "PEDOT-CNT coated electrodes stimulate retinal neurons at low voltage amplitudes and low charge densities," *Journal of neural engineering,* vol. 12, no. 1, pp. 016014-016014, 2015, doi: 10.1088/1741-2560/12/1/016014.

[152] Y. Yamamoto, M. Danhof, and E. C. M. De Lange, "Microdialysis: the Key to Physiologically Based Model Prediction of Human CNS Target Site Concentrations," *The AAPS Journal,* vol. 19, no. 4, pp. 891-909, 2017, doi: 10.1208/s12248-017-0050-3.

[153] A. A. El-Sherbeni, M. R. Stocco, F. B. Wadji, and R. F. Tyndale, "Addressing the instability issue of dopamine during microdialysis: the determination of dopamine, serotonin, methamphetamine and its metabolites in rat brain," *Journal of Chromatography A,* vol. 1627, pp. 461403-461403, 2020, doi: 10.1016/j.chroma.2020.461403.

[154] V. I. Chefer, A. C. Thompson, A. Zapata, and T. S. Shippenberg, "Overview of brain microdialysis," *Current protocols in neuroscience,* vol. 47, no. 1, pp. 7.1. 1-7.1. 28, 2009.

[155] Y. Deng, W. Wang, C. Ma, and Z. Li, "Fabrication of an electrochemical biosensor array for simultaneous detection of L-glutamate and acetylcholine," (in eng), *J Biomed Nanotechnol,* vol. 9, no. 8, pp. 1378-82, Aug 2013, doi: 10.1166/jbn.2013.1633.

[156] V. Biju, "Chemical modifications and bioconjugate reactions of nanomaterials for sensing, imaging, drug delivery and therapy," *Chem Soc Rev,* vol. 43, no. 3, pp. 744-64, Feb 7 2014, doi: 10.1039/c3cs60273g.

[157] J. E. Koehne *et al.*, "Carbon nanofiber electrode array for electrochemical detection of dopamine using fast scan cyclic voltammetry," *Analyst,* vol. 136, no. 9, pp. 1802-1805, 2011.

[158] Y. Oh *et al.*, "Tracking tonic dopamine levels in vivo using multiple cyclic square wave voltammetry," *Biosensors and Bioelectronics,* vol. 121, pp. 174-182, 2018.

[159] S. Negi, R. Bhandari, L. Rieth, R. Van Wagenen, and F. Solzbacher, "Neural electrode degradation from continuous electrical stimulation: Comparison of sputtered and activated iridium oxide," *Journal of neuroscience methods,* vol. 186, no. 1, pp. 8-17, 2010, doi: 10.1016/j.jneumeth.2009.10.016.

[160] R. Fiáth *et al.*, "Recording site placement on planar silicon-based probes affects signal quality in acute neuronal recordings," *Scientific Reports,* vol. 11, no. 1, p. 2028, 2021/01/21 2021, doi: 10.1038/s41598-021-81127-5.

[161] K. Wang *et al.*, "High-Performance Graphene-Fiber-Based Neural Recording Microelectrodes," *Advanced materials (~~Weinheim~~),* vol. 31, no. 15, pp. e1805867-n/a, 2019, doi: 10.1002/adma.201805867.

[162] C. S. Bjornsson *et al.*, "Effects of insertion conditions on tissue strain and vascular damage during neuroprosthetic device insertion," *Journal of Neural Engineering,* vol. 3, no. 3, pp. 196-207, 2006/06/21 2006, doi: 10.1088/1741-2560/3/3/002.

[163] N. Haj Hosseini, R. Hoffmann, S. Kisban, T. Stieglitz, O. Paul, and P. Ruther, "Comparative study on the insertion behavior of cerebral microprobes," *2007 29th Annual International Conference of the IEEE Engineering in Medicine and Biology Society,* pp. 4711-4714, 2007, doi: 10.1109/IEMBS.2007.4353391.

[164] T. Dong, L. Chen, and A. Shih, "Laser Sharpening of Carbon Fiber Microelectrode Arrays for Brain Recording," presented at the ASME 2020 15th International Manufacturing Science and Engineering Conference, 2020. [Online]. Available: https://doi.org/10.1115/MSEC2020-8479.

[165] G. Guitchounts, J. E. Markowitz, W. A. Liberti, and T. J. Gardner, "A carbon-fiber electrode array for long-term neural recording," (in eng), *Journal of neural engineering,* vol. 10, no. 4, pp. 046016-046016, 2013, doi: 10.1088/1741-2560/10/4/046016.

[166] T. Chung, J. Q. Wang, J. Wang, B. Cao, Y. Li, and S. W. Pang, "Electrode modifications to lower electrode impedance and improve neural signal recording sensitivity," *Journal of neural engineering,* vol. 12, no. 5, pp. 056018-056018, 2015, doi: 10.1088/1741-2560/12/5/056018.

[167] Z. Zhang, J. L. Wilson, B. R. Kitt, and D. W. Flaherty, "Effects of Oxygen Plasma Treatments on Surface Functional Groups and Shear Strength of Carbon Fiber Composites," *ACS Applied Polymer Materials,* vol. 3, no. 2, pp. 986-995, 2021/02/12 2021, doi: 10.1021/acsapm.0c01270.

[168] M. Gołda, M. Brzychczy-Włoch, M. Faryna, K. Engvall, and A. Kotarba, "Oxygen plasma functionalization of parylene C coating for implants surface: Nanotopography and active sites for drug anchoring," *Materials Science and Engineering: C,* vol. 33, no. 7, pp. 4221-4227, 2013/10/01/ 2013, doi: https://doi.org/10.1016/j.msec.2013.06.014.

[169] D. Kontziampasis *et al.*, "Effects of Ar and O2 Plasma Etching on Parylene C: Topography versus Surface Chemistry and the Impact on Cell Viability," *Plasma Processes and Polymers,* vol. 13, pp. 324-333, 03/01 2016, doi: 10.1002/ppap.201500053.

[170] Z. Shao, L. Wilson, Y. Chang, and B. J. Venton, "MPCVD-Grown Nanodiamond Microelectrodes with Oxygen Plasma Activation for Neurochemical Applications," *ACS sensors,* vol. 7, no. 10, pp. 3192-3200, 2022, doi: 10.1021/acssensors.2c01803.

[171] Z. You, L. Wei, M. Zhang, F. Yang, and X. Wang, "Hermetic and Bioresorbable Packaging Materials for MEMS Implantable Pressure Sensors: A Review," *IEEE sensors journal,* vol. 22, no. 24, pp. 1-1, 2022, doi: 10.1109/JSEN.2022.3214337.

[172] C. Li, M. Cauwe, L. Mader, D. Schaubroeck, and M. Op de Beeck, "Accelerated Hermeticity Testing of Biocompatible Moisture Barriers Used for the Encapsulation of Implantable Medical Devices," *Coatings*, vol. 10, no. 1, doi: 10.3390/coatings10010019.

[173] H. Yang, T. Wu, S. Zhao, S. Xiong, B. Peng, and M. S. Humayun, "Chronically Implantable Package Based on Alumina Ceramics and Titanium with High-density Feedthroughs for Medical Implants," in *2018 40th Annual International Conference of the IEEE Engineering in Medicine and Biology Society (EMBC)*, 18-21 July 2018 2018, pp. 3382-3385, doi: 10.1109/EMBC.2018.8513004.

[174] K. Ganesan *et al.*, "An all-diamond, hermetic electrical feedthrough array for a retinal prosthesis," *Biomaterials,* vol. 35, no. 3, pp. 908-915, 2013, doi: 10.1016/j.biomaterials.2013.10.040.

[175] S. G. Lichter *et al.*, "Hermetic diamond capsules for biomedical implants enabled by gold active braze alloys," *Biomaterials,* vol. 53, pp. 464-474, 2015/06/01/ 2015, doi: https://doi.org/10.1016/j.biomaterials.2015.02.103.

[176] L. Bisoni *et al.*, "Investigation on the hermeticity of an implantable package with 32 feedthroughs for neural prosthetic applications," (in eng), *Annu Int Conf IEEE Eng Med Biol Soc,* vol. 2016, pp. 1967-1970, Aug 2016, doi: 10.1109/embc.2016.7591109.

[177] T. Günther *et al.*, "Practical Aspects and Limitations of Hermeticity Testing of Microencapsulations Using Cumulative Helium Leak Detection for Miniaturized Implantable Medical Devices," *IEEE Transactions on Components, Packaging and Manufacturing Technology,* vol. 10, no. 3, pp. 351-359, 2020, doi: 10.1109/TCPMT.2020.2968126.

[178] H. R. Greenhouse, "Hermeticity of electronic packages," 2000.

[179] I. M. Taylor, E. M. Robbins, K. A. Catt, P. A. Cody, C. L. Happe, and X. T. Cui, "Enhanced dopamine detection sensitivity by PEDOT/graphene oxide coating on in vivo carbon fiber electrodes," *Biosensors & bioelectronics,* vol. 89, no. Pt 1, pp. 400-410, 2017, doi: 10.1016/j.bios.2016.05.084.

[180] K. Edalati *et al.*, "Improved wetting of gold active braze alloy on diamond for use in medical implants," *Diamond and Related Materials,* vol. 109, p. 108089, 2020/11/01/ 2020, doi: https://doi.org/10.1016/j.diamond.2020.108089.

[181] K. J. Brown, E. Chartier, E. M. Sweet, D. A. Hopper, and L. C. Bassett, "Cleaning diamond surfaces using boiling acid treatment in a standard laboratory chemical hood," *Journal of chemical health & safety (Online),* vol. 26, no. 6, pp. 40-44, 2019, doi: 10.1016/j.jchas.2019.06.001.

[182] T. Hoshino *et al.*, "Improvement of neuronal cell adhesiveness on parylene with oxygen plasma treatment," *Journal of bioscience and bioengineering,* vol. 113, no. 3, pp. 395-398, 2012, doi: 10.1016/j.jbiosc.2011.11.003.

[183] T. Trantidou, T. Prodromakis, and C. Toumazou, "Oxygen plasma induced hydrophilicity of Parylene-C thin films," *Applied surface science,* vol. 261, pp. 43-51, 2012, doi: 10.1016/j.apsusc.2012.06.112.

[184] J. S. Song, S. Lee, S. H. Jung, G. C. Cha, and M. S. Mun, "Improved biocompatibility of parylene-C films prepared by chemical vapor deposition and the subsequent plasma treatment," *Journal of Applied Polymer Science,* vol. 112, no. 6, pp. 3677-3685, 2009, doi: https://doi.org/10.1002/app.29774.

[185] W. Tong *et al.*, "Improved visual acuity using a retinal implant and an optimized stimulation strategy," *Journal of neural engineering,* vol. 17, no. 1, pp. 016018-016018, 2019, doi: 10.1088/1741-2552/ab5299.

[186] O. Shimoni *et al.*, "Development of a Templated Approach to Fabricate Diamond Patterns on Various Substrates," *ACS Applied Materials & Interfaces,* vol. 6, no. 11, pp. 8894-8902, 2014/06/11 2014, doi: 10.1021/am5016556.

[187] T. Nakai, K. Arima, O. Maida, and T. Ito, "High-quality diamond films grown at high deposition rates using high-power-density MWPCVD method with conventional quartz-type chamber," *Journal of crystal growth,* vol. 309, no. 2, pp. 134-139, 2007, doi: 10.1016/j.jcrysgro.2007.09.024.

[188] N. m. Elgrishi, K. J. Rountree, B. D. McCarthy, E. S. Rountree, T. T. Eisenhart, and J. L. Dempsey, "A Practical Beginner's Guide to Cyclic Voltammetry," *Journal of chemical education,* vol. 95, no. 2, pp. 197-206, 2018, doi: 10.1021/acs.jchemed.7b00361.

[189] J. P.S and D. S. Sutrave, "A Brief Study of Cyclic Voltammetry and Electrochemical Analysis," *International journal of chemtech research,* vol. 11, no. 9, pp. 77-88, 2018, doi: 10.20902/IJCTR.2018.110911.

[190] P. Chulkin and P. Data, "Electrochemical Impedance Spectroscopy as a Tool for Electrochemical Rate Constant Estimation," *Journal of visualized experiments,* no. 140, 2018, doi: 10.3791/56611.

[191] H. Wang and L. Pilon, "Physical interpretation of cyclic voltammetry for measuring electric double layer capacitances," *Electrochimica acta,* vol. 64, pp. 130-139, 2012, doi: 10.1016/j.electacta.2011.12.118.

[192] A. M. O'Mahony, D. S. Silvester, L. Aldous, C. Hardacre, and R. G. Compton, "Effect of Water on the Electrochemical Window and Potential Limits of Room-Temperature Ionic Liquids," *Journal of Chemical & Engineering Data,* vol. 53, no. 12, pp. 2884-2891, 2008/12/11 2008, doi: 10.1021/je800678e.

[193] Z. Wang *et al.*, "Activated carbon fiber paper with exceptional capacitive performance as a robust electrode for supercapacitors" Electronic supplementary information (ESI) available: Experimental section, SEM images of carbon fiber paper and activated carbon fiber paper, and CV curves of the activated carbon fiber paper. See DOI: 10.1039/c6ta02056a," vol. 4, no. 16, pp. 5828-5833, 2016, doi: 10.1039/c6ta02056a.

[194] D. L. Robinson, A. Hermans, A. T. Seipel, and R. M. Wightman, "Monitoring rapid chemical communication in the brain," (in eng), *Chem Rev,* vol. 108, no. 7, pp. 2554-84, Jul 2008, doi: 10.1021/cr068081q.

[195] B. J. Ostertag, M. T. Cryan, J. M. Serrano, G. Liu, and A. E. Ross, "Porous Carbon Nanofiber-Modified Carbon Fiber Microelectrodes for Dopamine Detection," *ACS applied nano materials,* vol. 5, no. 2, pp. 2241-2249, 2022, doi: 10.1021/acsanm.1c03933.

[196] B. D. Bath, D. J. Michael, B. J. Trafton, J. D. Joseph, P. L. Runnels, and R. M. Wightman, "Subsecond adsorption and desorption of dopamine at carbon-fiber microelectrodes," (in eng), *Anal Chem,* vol. 72, no. 24, pp. 5994-6002, Dec 15 2000, doi: 10.1021/ac000849y.

[197] R. L. McCreery, "Advanced Carbon Electrode Materials for Molecular Electrochemistry," *Chemical Reviews,* vol. 108, no. 7, pp. 2646-2687, 2008/07/01 2008, doi: 10.1021/cr068076m.

[198] Z. Luo, *A practical guide to transmission electron microscopy : fundamentals*, First edition. ed. (Materials characterization and analysis collection). New York, [New York] (222 East 46th Street, New York, NY 10017): Momentum Press, 2016.

[199] I. Utke, S. Moshkalev, and P. Russell, *Nanofabrication using focused ion and electron beams principles and applications* (Nanomanufacturing series ; v. 1). Oxford ;: Oxford University Press, 2011.

[200] C. J. Xiao, "Properties of nano-SiC/Ni composite coating on diamond surfaces," *Surface Engineering,* vol. 34, no. 11, pp. 832-837, 2018/11/02 2018, doi: 10.1080/02670844.2017.1376847.

[201] H. Xu, A. W. Hirschberg, K. Scholten, T. W. Berger, D. Song, and E. Meng, "Acute in vivo testing of a conformal polymer microelectrode array for multi-region hippocampal recordings," *Journal of neural engineering,* vol. 15, no. 1, pp. 016017-016017, 2018, doi: 10.1088/1741-2552/aa9451.

[202] F. Barz, V. Trouillet, O. Paul, and P. Ruther, "CMOS-Compatible, Flexible, Intracortical Neural Probes," (in eng), *IEEE Trans Biomed Eng,* vol. 67, no. 5, pp. 1366-1376, May 2020, doi: 10.1109/tbme.2019.2936740.

[203] E. Castagnola *et al.*, "Flexible Glassy Carbon Multielectrode Array for In Vivo Multisite Detection of Tonic and Phasic Dopamine Concentrations," *Biosensors ~~(Basel)~~,* vol. 12, no. 7, p. 540, 2022, doi: 10.3390/bios12070540.

[204] K. Ganesan *et al.*, "An all-diamond, hermetic electrical feedthrough array for a retinal prosthesis," (in eng), *Biomaterials,* vol. 35, no. 3, pp. 908-15, Jan 2014, doi: 10.1016/j.biomaterials.2013.10.040.

[205] K.-H. Yang and R. J. Narayan, "Biocompatibility and functionalization of diamond for neural applications," *Current Opinion in Biomedical Engineering,* vol. 10, pp. 60-68, 2019/06/01/ 2019, doi: https://doi.org/10.1016/j.cobme.2019.03.002.

[206] M. K. U. Sikder, J. Fallon, M. N. Shivdasani, K. Ganesan, P. Seligman, and D. J. Garrett, "Wireless induction coils embedded in diamond for power transfer in medical implants," *Biomedical Microdevices,* vol. 19, no. 4, p. 79, 2017/08/26 2017, doi: 10.1007/s10544-017-0220-1.

[207] F. Picollo *et al.*, "Realization of a diamond based high density multi electrode array by means of Deep Ion Beam Lithography," *Nuclear Instruments and Methods in Physics Research Section B: Beam Interactions with Materials and Atoms,* vol. 348, pp. 199-202, 2015/04/01/ 2015, doi: https://doi.org/10.1016/j.nimb.2014.11.119.

[208] K. Scholten and E. Meng, "Electron-beam lithography for polymer bioMEMS with submicron features," *Microsystems & Nanoengineering,* vol. 2, no. 1, p. 16053, 2016/11/07 2016, doi: 10.1038/micronano.2016.53.

[209] K. Edalati *et al.*, "Improved wetting of gold active braze alloy on diamond for use in medical implants," *DIAMOND AND RELATED MATERIALS,* vol. 109, ~~NOV~~ 2020, doi: 10.1016/j.diamond.2020.108089.

(lower case)

[210] N. V. Apollo *et al.*, "Brazing techniques for the fabrication of biocompatible carbon-based electronic devices," *Carbon,* vol. 107, pp. 180-189, 2016/10/01/ 2016, doi: https://doi.org/10.1016/j.carbon.2016.05.047.

[211] J. D. Urbano-Gámez *et al.*, "Biocompatibility study of a commercial printed circuit board for biomedical applications: Lab-on-PCB for organotypic retina cultures," *Micromachines ~~(Basel)~~,* vol. 12, no. 12, p. 1469, 2021, doi: 10.3390/mi12121469.

[212] L. Pauksch *et al.*, "Biocompatibility of silver nanoparticles and silver ions in primary human mesenchymal stem cells and osteoblasts," *Acta biomaterialia,* vol. 10, no. 1, pp. 439-449, 2014, doi: 10.1016/j.actbio.2013.09.037.

[213] Y. Huan *et al.*, "Carbon fiber electrodes for intracellular recording and stimulation," (in eng), *J Neural Eng,* vol. 18, no. 6, Dec 14 2021, doi: 10.1088/1741-2552/ac3dd7.

[214] R. Khmelnitskii and A. Gippius, "Transformation of diamond to graphite under heat treatment at low pressure," *Phase Transitions: A Multinational Journal,* vol. 87, 02/01 2014, doi: 10.1080/01411594.2013.807429.

[215] M. Seal, "Graphitization of Diamond," *Nature,* vol. 185, no. 4712, pp. 522-523, 1960/02/01 1960, doi: 10.1038/185522a0.

[216] K. Edalati *et al.*, "Effective removal of metal-carbide contamination from diamond circuit boards by reactive ion etching," *Diamond and Related Materials,* p. 110329, 2023.

[217] "Nano strip dual row NSD/NPD." Omnetics Connector Corporation. https://www.omnetics.com/products/micro-and-nano-strips/nano-nps-npd-series (accessed 1 September 2023.

[218] K. Katsura, T. Hayashi, F. Ohira, S. Hata, and K. Iwashita, "A novel flip-chip interconnection technique using solder bumps for high-speed photoreceivers," *Journal of lightwave technology,* vol. 8, no. 9, pp. 1323-1327, 1990, doi: 10.1109/50.59160.

[219] Y. Li and D. Goyal, *3D microelectronic packaging : from fundamentals to applications* (Springer Series in Advanced Microelectronics, 57). Cham: Springer International Publishing, 2017.

[220] R. A. Coker, E. R. Zellmer, and D. W. Moran, "Micro-channel sieve electrode for concurrent bidirectional peripheral nerve interface. Part B: stimulation," *Journal of neural engineering,* vol. 16, no. 2, pp. 026002-026002, 2019, doi: 10.1088/1741-2552/aaefab.

[221] S. P. Marshall, W. Lin, P. R. Patel, A. J. Shih, and C. A. Chestek, "Effects of geometry and material on the insertion oi very small neural electrode," in *2016 38th Annual International Conference of the IEEE Engineering in Medicine and Biology Society (EMBC)*, 16-20 Aug. 2016 2016, pp. 2784-2788, doi: 10.1109/EMBC.2016.7591308.

[222] A. Weltman, J. Yoo, and E. Meng, "Flexible, penetrating brain probes enabled by advances in polymer microfabrication," *Micromachines (~~Basel~~),* vol. 7, no. 10, p. 180, 2016, doi: 10.3390/mi7100180.

[223] S. Rezaei, Y. Xu, and S. W. Pang, "Control of neural probe shank flexibility by fluidic pressure in embedded microchannel using PDMS/PI hybrid substrate," *PloS one,* vol. 14, no. 7, pp. e0220258-e0220258, 2019, doi: 10.1371/journal.pone.0220258.

[224] C. Tian and J. He, "Monitoring Insertion Force and Electrode Impedance during Implantation of Microwire Electrodes," (in eng), *Conf Proc IEEE Eng Med Biol Soc,* vol. 2005, pp. 7333-6, 2005, doi: 10.1109/iembs.2005.1616205.

[225] R. Fiath *et al.*, "Slow insertion of silicon probes improves the quality of acute neuronal recordings," *Sci Rep,* vol. 9, no. 1, p. 111, Jan 14 2019, doi: 10.1038/s41598-018-36816-z.

[226] K. M. Scott, J. Du, H. A. Lester, and S. C. Masmanidis, "Variability of acute extracellular action potential measurements with multisite silicon probes," (in eng), *J Neurosci Methods,* vol. 211, no. 1, pp. 22-30, Oct 15 2012, doi: 10.1016/j.jneumeth.2012.08.005.

[227] I. N. McNamara *et al.*, "Electrode sharpness and insertion speed reduce tissue damage near high-density penetrating arrays," *Journal of neural engineering,* 2024.

[228] Z. Wan, T. Liu, X. Ran, P. Liu, W. Chen, and S. Zhang, "The influence of non-stationarity of spike signals on decoding performance in intracortical brain-computer interface: a simulation study," (in English), *Frontiers in Computational Neuroscience,* Original Research vol. 17, 2023-May-12 2023, doi: 10.3389/fncom.2023.1135783.

[229] G. Czanner *et al.*, "Measuring the signal-to-noise ratio of a neuron," *Proceedings of the National Academy of Sciences,* vol. 112, no. 23, pp. 7141-7146, 2015/06/09 2015, doi: 10.1073/pnas.1505545112.

[230] C. K. Ryan *et al.*, "Comparison of Recordings from Microelectrode Arrays and Single Electrodes in the Visual Cortex," *The Journal of Neuroscience,* vol. 27, no. 2, p. 261, 2007, doi: 10.1523/JNEUROSCI.4906-06.2007.

[231] C. Klaes, "Chapter 28 - Invasive Brain-Computer Interfaces and Neural Recordings From Humans," in *Handbook of Behavioral Neuroscience*, vol. 28, D. Manahan-Vaughan Ed.: Elsevier, 2018, pp. 527-539.

[232] J. M. Carmena, M. A. Lebedev, C. S. Henriquez, and M. A. Nicolelis, "Stable ensemble performance with single-neuron variability during reaching movements in primates," (in eng), *J Neurosci,* vol. 25, no. 46, pp. 10712-6, Nov 16 2005, doi: 10.1523/jneurosci.2772-05.2005.

[233] M. L. Cavuto and T. G. Constandinou, "Investigation of Insertion Method to Achieve Chronic Recording Stability of a Semi-Rigid Implantable Neural Probe," in *2019 9th International IEEE/EMBS Conference on Neural Engineering (NER)*, 20-23 March 2019 2019, pp. 665-669, doi: 10.1109/NER.2019.8717128.

[234] F. Lotti, F. Ranieri, G. Vadalà, L. Zollo, and G. Di Pino, "Invasive Intraneural Interfaces: Foreign Body Reaction Issues," (in eng), *Front Neurosci,* vol. 11, p. 497, 2017, doi: 10.3389/fnins.2017.00497.

[235] B. D. Winslow and P. A. Tresco, "Quantitative analysis of the tissue response to chronically implanted microwire electrodes in rat cortex," *Biomaterials,* vol. 31, no. 7, pp. 1558-1567, 2010/03/01/ 2010, doi: https://doi.org/10.1016/j.biomaterials.2009.11.049.

[236] A. Stankov, V. Belakaposka-Srpanova, N. Bitoljanu, L. Cakar, Z. Cakar, and G. Rosoklija, "Visualisation of Microglia with the use of Immunohistochemical Double Staining Method for CD-68 and Iba-1 of Cerebral Tissue Samples in Cases of Brain Contusions," (in eng), *Pril (Makedon Akad Nauk Umet Odd Med Nauki),* vol. 36, no. 2, pp. 141-5, 2015, doi: 10.1515/prilozi-2015-0062.

[237] P. A. Cody, J. R. Eles, C. F. Lagenaur, T. D. Y. Kozai, and X. T. Cui, "Unique electrophysiological and impedance signatures between encapsulation types: An analysis of biological Utah array failure and benefit of a biomimetic coating in a rat model," (in eng), *Biomaterials,* vol. 161, pp. 117-128, Apr 2018, doi: 10.1016/j.biomaterials.2018.01.025.

[238] T. D. Y. Kozai *et al.*, "Ultrasmall implantable composite microelectrodes with bioactive surfaces for chronic neural interfaces," *Nature Materials,* vol. 11, no. 12, pp. 1065-1073, 2012/12/01 2012, doi: 10.1038/nmat3468.

[239] D. A. Henze, Z. Borhegyi, J. Csicsvari, A. Mamiya, K. D. Harris, and G. Buzsáki, "Intracellular features predicted by extracellular recordings in the hippocampus in vivo," (in eng), *J Neurophysiol,* vol. 84, no. 1, pp. 390-400, Jul 2000, doi: 10.1152/jn.2000.84.1.390.

[240] G. Buzsáki, "Large-scale recording of neuronal ensembles," *Nature Neuroscience,* vol. 7, no. 5, pp. 446-451, 2004/05/01 2004, doi: 10.1038/nn1233.

[241] W. Yang *et al.*, "Relationship between substrate type and BDD electrode structure, performance and antibiotic tetracycline mineralization," *Journal of Alloys and Compounds,* vol. 890, p. 161760, 2022/01/15/ 2022, doi: https://doi.org/10.1016/j.jallcom.2021.161760.

[242] O. Auciello and A. V. Sumant, "Status review of the science and technology of ultrananocrystalline diamond (UNCD™) films and application to multifunctional devices," *Diamond and related materials,* vol. 19, no. 7, pp. 699-718, 2010, doi: 10.1016/j.diamond.2010.03.015.

[243] V. S. Vavilov, "Handbook of industrial diamonds and diamond films," *Physics Uspekhi,* vol. 41, no. 10, pp. 1045-1046, 1998, doi: 10.1070/PU1998v041n10ABEH000467.

[244] O. Auciello, S. Renou, K. Kang, D. Tasat, and D. Olmedo, "A Biocompatible Ultrananocrystalline Diamond (UNCD) Coating for a New Generation of Dental Implants," *Nanomaterials (~~Basel, Switzerland~~),* vol. 12, no. 5, p. 782, 2022, doi: 10.3390/nano12050782.

[245] R. Trouillon and D. O'Hare, "Comparison of glassy carbon and boron doped diamond electrodes: Resistance to biofouling," *Electrochimica Acta,* vol. 55, no. 22, pp. 6586-6595, 2010/09/01/ 2010, doi: https://doi.org/10.1016/j.electacta.2010.06.016.

[246] W. Tong, K. Fox, K. Ganesan, and S. Prawer, "Design of a Patterned Diamond Substrate for Ordered Neural Cell Adhesion," *Procedia Technology,* vol. 20, pp. 206-211, 2015/01/01/ 2015, doi: https://doi.org/10.1016/j.protcy.2015.07.033.

[247] Y. T. Wong *et al.*, "Feasibility of Nitrogen Doped Ultrananocrystalline Diamond Microelectrodes for Electrophysiological Recording From Neural Tissue," *Frontiers in bioengineering and biotechnology,* vol. 6, pp. 85-85, 2018, doi: 10.3389/fbioe.2018.00085.

[248] A. Voss *et al.*, "Influence of the surface termination of ultrananocrystalline diamond/amorphous carbon composite films on their interaction with neurons," *Diamond and related materials,* vol. 26, pp. 60-65, 2012, doi: 10.1016/j.diamond.2012.04.005.

[249] D. J. Garrett, K. Ganesan, A. Stacey, K. Fox, H. Meffin, and S. Prawer, "Ultra-nanocrystalline diamond electrodes: Optimization towards neural stimulation applications," *Journal of neural engineering,* vol. 9, no. 1, pp. 016002-1-10, 2012, doi: 10.1088/1741-2560/9/1/016002.

[250] O. A. Shenderova and D. M. Gruen, *Ultrananocrystalline diamond synthesis, properties, and applications* (Materials science and process technology series). Norwich, N.Y: William Andrew Pub., 2006.

[251] S. Mandal *et al.*, "Thick, Adherent Diamond Films on AlN with Low Thermal Barrier Resistance," (in eng), *ACS Appl Mater Interfaces,* vol. 11, no. 43, pp. 40826-40834, Oct 30 2019, doi: 10.1021/acsami.9b13869.

[252] J. Shalini *et al.*, "Ultra-nanocrystalline diamond nanowires with enhanced electrochemical properties," *Electrochimica acta,* vol. 92, pp. 9-19, 2013, doi: 10.1016/j.electacta.2012.12.078.

[253] S. Falahatdoost *et al.*, "Enhanced electrochemical capacitance of nitrogen-doped ultrananocrystalline diamond through oxygen treatment," *Applied surface science,* vol. 543, p. 148768, 2021, doi: 10.1016/j.apsusc.2020.148768.

[254] K. J. Sankaran, P. T. Joseph, H. C. Chen, N. H. Tai, and I. N. Lin, "Investigation in the role of hydrogen on the properties of diamond films grown using Ar/H2/CH4 microwave plasma," *Diamond and Related Materials,* vol. 20, no. 2, pp. 232-237, 2011/02/01/ 2011, doi: https://doi.org/10.1016/j.diamond.2010.12.018.

[255] J. Shalini, S. Jothiramalingam, C.-L. Dong, C.-Y. Lee, N.-H. Tai, and I. N. Lin, "In situ detection of dopamine using nitrogen incorporated diamond nanowire electrode," *Nanoscale,* vol. 5, 01/04 2013, doi: 10.1039/c2nr32939e.

[256] A. V. Sumant, O. Auciello, R. W. Carpick, S. Srinivasan, and J. E. Butler, "Ultrananocrystalline and Nanocrystalline Diamond Thin Films for MEMS/NEMS Applications," *MRS Bulletin,* vol. 35, no. 4, pp. 281-288, 2010/04/01 2010, doi: 10.1557/mrs2010.550.

[257] H.-F. Cheng, C.-C. Horng, H.-Y. Chiang, H.-C. Chen, and I. N. Lin, "Modification on the Microstructure of Ultrananocrystalline Diamond Films for Enhancing Their Electron Field Emission Properties via a Two-Step Microwave Plasma Enhanced Chemical Vapor Deposition Process," *The Journal of Physical Chemistry C,* vol. 115, no. 28, pp. 13894-13900, 2011/07/21 2011, doi: 10.1021/jp112131a.

[258] S. A. Linnik, A. V. Gaydaychuk, and E. Y. Baryshnikov, "Deposition of Polycrystalline Diamond Films with a Controlled Grain Size by Periodic Secondary Nucleation," *Materials Today: Proceedings,* vol. 3, pp. S138-S144, 2016/01/01/ 2016, doi: https://doi.org/10.1016/j.matpr.2016.02.024.

[259] N. Wiora *et al.*, "Grain boundary dominated electrical conductivity in ultrananocrystalline diamond," *Journal of Applied Physics,* vol. 122, p. 145102, 10/14 2017, doi: 10.1063/1.4993442.

[260] W. Gajewski *et al.*, "Electronic and optical properties of boron-doped nanocrystalline diamond films," *Physical Review B,* vol. 79, no. 4, p. 045206, 01/15/ 2009, doi: 10.1103/PhysRevB.79.045206.

[261] N. G. Ferreira, L. L. G. Silva, and E. J. Corat, "Electrochemical activity of boron-doped diamond electrodes grown on carbon fiber cloths," *Diamond and Related Materials,* vol. 11, no. 3, pp. 657-661, 2002/03/01/ 2002, doi: https://doi.org/10.1016/S0925-9635(02)00039-0.

[262] A. Vesel, R. Zaplotnik, G. Primc, and M. Mozetič, "Synthesis of Vertically Oriented Graphene Sheets or Carbon Nanowalls-Review and Challenges," (in eng), *Materials (Basel),* vol. 12, no. 18, Sep 12 2019, doi: 10.3390/ma12182968.

[263] "New Progress on Graphene Research," ed. Rijeka: IntechOpen, 2013.

[264] J. Chen, Z. Bo, and G. Lu, "PECVD Synthesis of Vertically-Oriented Graphene: Precursor and Temperature Effects," in *Vertically-Oriented Graphene: PECVD Synthesis and Applications*, J. Chen, Z. Bo, and G. Lu Eds. Cham: Springer International Publishing, 2015, pp. 35-54.

[265] M. Hiramatsu, K. Shiji, H. Amano, and M. Hori, "Fabrication of vertically aligned carbon nanowalls using capacitively coupled plasma-enhanced chemical vapor deposition assisted by hydrogen radical injection," *Applied Physics Letters,* vol. 84, no. 23, pp. 4708-4710, 2004, doi: 10.1063/1.1762702.

[266] Y. Yerlanuly *et al.*, "Physical properties of carbon nanowalls synthesized by the ICP-PECVD method vs. the growth time," *Scientific Reports,* vol. 11, no. 1, p. 19287, 2021/09/29 2021, doi: 10.1038/s41598-021-97997-8.

[267] Z. Zhai *et al.*, "Insight into the Effect of the Core–Shell Microstructure on the Electrochemical Properties of Undoped 3D-Networked Conductive Diamond/Graphite," *The Journal of Physical Chemistry C,* vol. 123, no. 10, pp. 6018-6029, 2019/03/14 2019, doi: 10.1021/acs.jpcc.8b11865.

[268] M. Sobaszek *et al.*, "Diamond Phase (sp3 -C) Rich Boron-Doped Carbon Nanowalls (sp2 -C): Physicochemical and Electrochemical Properties," *Journal of physical chemistry. C,* vol. 121, no. 38, pp. 20821-20833, 2017, doi: 10.1021/acs.jpcc.7b06365.

[269] C. Zhang *et al.*, "Nitrogen-doped carbon nanowalls/diamond films as efficient electrocatalysts toward oxygen reduction reaction," *Nanotechnology,* vol. 33, no. 1, p. 015401, 2021/10/20 2022, doi: 10.1088/1361-6528/ac2a84.

[270] D. V. Nechaev and A. F. Khokhryakov, "Formation of metastable graphite inclusions during diamond crystallization in model systems," *Geology of ore deposits,* vol. 56, no. 2, pp. 139-146, 2014, doi: 10.1134/S1075701514020044.

[271] M. Marton *et al.*, "Deposition of boron doped diamond and carbon nanomaterials on graphite foam electrodes," *Applied Surface Science,* vol. 312, pp. 139-144, 2014/09/01/ 2014, doi: https://doi.org/10.1016/j.apsusc.2014.05.199.

[272] H. Zanin *et al.*, "Porous Boron-Doped Diamond/Carbon Nanotube Electrodes," *ACS applied materials & interfaces,* vol. 6, no. 2, pp. 990-995, 2014, doi: 10.1021/am4044344.

[273] S. K. Sethy *et al.*, "Nitrogen-Incorporated Boron-Doped Nanocrystalline Diamond Nanowires for Microplasma Illumination," *ACS applied materials & interfaces,* vol. 13, no. 46, pp. 55687-55699, 2021, doi: 10.1021/acsami.1c16507.

[274] E. L. Silva *et al.*, "Direct Synthesis of Electrowettable Carbon Nanowall–Diamond Hybrid Materials from Sacrificial Ceramic Templates Using HFCVD," *Advanced Materials Interfaces,* vol. 4, no. 10, p. 1700019, 2017, doi: https://doi.org/10.1002/admi.201700019.

[275] C. Hua, J. Cai, L. Li, P. Pan, and J. Feng, "Controllable synthesis of diamond/graphite composite films with tunable dielectric properties for microwave attenuation," *Diamond and Related Materials,* vol. 138, p. 110242, 2023/10/01/ 2023, doi: https://doi.org/10.1016/j.diamond.2023.110242.

[276] A. E. Hadjinicolaou *et al.*, "Electrical stimulation of retinal ganglion cells with diamond and the development of an all diamond retinal prosthesis," *Biomaterials,* vol. 33, no. 24, pp. 5812-5820, 2012, doi: 10.1016/j.biomaterials.2012.04.063.

[277] M. C. Granger *et al.*, "Standard Electrochemical Behavior of High-Quality, Boron-Doped Polycrystalline Diamond Thin-Film Electrodes," *Analytical Chemistry,* vol. 72, no. 16, pp. 3793-3804, 2000/08/01 2000, doi: 10.1021/ac0000675.

[278] S. Siddiqui *et al.*, "A quantitative study of detection mechanism of a label-free impedance biosensor using ultrananocrystalline diamond microelectrode array," *Biosensors and Bioelectronics,* vol. 35, no. 1, pp. 284-290, 2012/05/15/ 2012, doi: https://doi.org/10.1016/j.bios.2012.03.001.

[279] J. Millán-Barba *et al.*, "Boron-doped diamond growth on carbon fibre: Enhancing the electrical conductivity," *Applied Surface Science,* vol. 615, p. 156382, 2023/04/01/ 2023, doi: https://doi.org/10.1016/j.apsusc.2023.156382.

[280] L. A. Pereira, A. B. Couto, D. A. L. Almeida, and N. G. Ferreira, "Singular properties of boron-doped diamond/carbon fiber composite as anode in Brilliant Green dye electrochemical degradation," *Diamond and Related Materials,* vol. 103, p. 107708, 2020/03/01/ 2020, doi: https://doi.org/10.1016/j.diamond.2020.107708.

[281] K. E. Bennet *et al.*, "A Diamond-Based Electrode for Detection of Neurochemicals in the Human Brain," (in eng), *Front Hum Neurosci,* vol. 10, p. 102, 2016, doi: 10.3389/fnhum.2016.00102.

[282] J. Weng, L. W. Xiong, J. H. Wang, S. Y. Dai, W. D. Man, and F. Liu, "Investigation of depositing large area uniform diamond films in multi-mode MPCVD chamber," *Diamond and related materials,* vol. 30, pp. 15-19, 2012, doi: 10.1016/j.diamond.2012.09.007.

[283] N. Yamamoto, R. Guzman de Villoria, and B. Wardle, "Electrical and thermal property enhancement of fiber-reinforced polymer laminate composites through controlled implementation of multi-walled carbon nanotubes," *Composites Science and Technology,* vol. 72, pp. 2009–2015, 11/16 2012, doi: 10.1016/j.compscitech.2012.09.006.

[284] N. De Greef *et al.*, "Direct growth of carbon nanotubes on carbon fibers: Effect of the CVD parameters on the degradation of mechanical properties of carbon fibers," *Diamond and Related Materials,* vol. 51, pp. 39-48, 2015/01/01/ 2015, doi: https://doi.org/10.1016/j.diamond.2014.11.002.

[285] P. S. Cahill, Q. D. Walker, J. M. Finnegan, G. E. Mickelson, E. R. Travis, and R. M. Wightman, "Microelectrodes for the measurement of catecholamines in biological systems," (in eng), *Anal Chem,* vol. 68, no. 18, pp. 3180-6, Sep 15 1996, doi: 10.1021/ac960347d.

[286] M. L. Huffman and B. J. Venton, "Carbon-fiber microelectrodes for in vivo applications," (in eng), *Analyst,* vol. 134, no. 1, pp. 18-24, Jan 2009, doi: 10.1039/b807563h.

[287] P. Takmakov *et al.*, "Carbon Microelectrodes with a Renewable Surface," *Analytical Chemistry,* vol. 82, no. 5, pp. 2020-2028, 2010/03/01 2010, doi: 10.1021/ac902753x.

[288] P. U. Arumugam, H. Zeng, S. Siddiqui, D. P. Covey, J. A. Carlisle, and P. A. Garris, "Characterization of ultrananocrystalline diamond microsensors for in vivo dopamine detection," *Applied physics letters,* vol. 102, no. 25, pp. 253107-253107, 2013, doi: 10.1063/1.4811785.

[289] S. Baluchová *et al.*, "Porous boron doped diamond for dopamine sensing: Effect of boron doping level on morphology and electrochemical performance," *Electrochimica acta,* vol. 327, p. 135025, 2019, doi: 10.1016/j.electacta.2019.135025.

[290] E. K. Purcell *et al.*, "Next-Generation Diamond Electrodes for Neurochemical Sensing: Challenges and Opportunities," (in eng), *Micromachines (Basel),* vol. 12, no. 2, Jan 26 2021, doi: 10.3390/mi12020128.

[291] W. Kulisch *et al.*, "Investigation of the nucleation and growth mechanisms of nanocrystalline diamond/amorphous carbon nanocomposite films," *Diamond and Related Materials,* Article vol. 17, no. 7-10, pp. 1116-1121, 2008, doi: 10.1016/j.diamond.2008.01.077.

[292] L. A. Hutton, J. G. Iacobini, E. Bitziou, R. B. Channon, M. E. Newton, and J. V. Macpherson, "Examination of the Factors Affecting the Electrochemical Performance of Oxygen-Terminated Polycrystalline Boron-Doped Diamond Electrodes," *Analytical chemistry (Washington),* vol. 85, no. 15, pp. 7230-7240, 2013, doi: 10.1021/ac401042t.

[293] T. Ohashi, W. Sugimoto, and Y. Takasu, "Catalytic roughening of surface layers of BDD for various applications," *Electrochimica Acta,* vol. 54, no. 22, pp. 5223-5229, 2009/09/01/ 2009, doi: https://doi.org/10.1016/j.electacta.2009.04.021.

[294] G. Piret *et al.*, "3D-nanostructured boron-doped diamond for microelectrode array neural interfacing," *Biomaterials,* vol. 53, pp. 173-183, 2015, doi: 10.1016/j.biomaterials.2015.02.021.

[295] F. Vahidpour *et al.*, "All-diamond functional surface micro-electrode arrays for brain-slice neural analysis," *Physica status solidi. A, Applications and materials science,* vol. 214, no. 2, pp. 1532347-n/a, 2017, doi: 10.1002/pssa.201532347.

[296] M. Bonnauron, S. Saada, L. Rousseau, G. Lissorgues, C. Mer, and P. Bergonzo, "High aspect ratio diamond microelectrode array for neuronal activity measurements," *Diamond and related materials,* vol. 17, no. 7, pp. 1399-1404, 2008, doi: 10.1016/j.diamond.2007.12.065.

[297] C. Hébert *et al.*, "Microfabrication, characterization and in vivo MRI compatibility of diamond microelectrodes array for neural interfacing," *MATERIALS SCIENCE & ENGINEERING C-MATERIALS FOR BIOLOGICAL APPLICATIONS,* vol. 46, pp. 25-31, 2015, doi: 10.1016/j.msec.2014.10.018.

[298] M. E. M. Stamp, W. Tong, K. Ganesan, S. Prawer, M. R. Ibbotson, and D. J. Garrett, "3D Diamond Electrode Array for High-Acuity Stimulation in Neural Tissue," *ACS applied bio materials,* vol. 3, no. 3, pp. 1544-1552, 2020, doi: 10.1021/acsabm.9b01165.

[299] E. Losero *et al.*, "Neuronal growth on high-aspect-ratio diamond nanopillar arrays for biosensing applications," *Scientific reports,* vol. 13, no. 1, pp. 5909-5909, 2023, doi: 10.1038/s41598-023-32235-x.

[300] M. McDonald, A. Monaco, F. Vahidpour, K. Haenen, M. Giugliano, and M. Nesladek, "Diamond microelectrode arrays for in vitro neuronal recordings," *MRS communications,* vol. 7, no. 3, pp. 683-690, 2017, doi: 10.1557/mrc.2017.62.

[301] A. E. Hess, D. M. Sabens, H. B. Martin, and C. A. Zorman, "Diamond-on-Polymer Microelectrode Arrays Fabricated Using a Chemical Release Transfer Process," *Journal of microelectromechanical systems,* vol. 20, no. 4, pp. 867-875, 2011, doi: 10.1109/JMEMS.2011.2159099.

[302] M. Schreck, S. Gsell, R. Brescia, and M. Fischer, "Ion bombardment induced buried lateral growth: The key mechanism for the synthesis of single crystal diamond wafers," *Scientific reports,* vol. 7, no. 1, pp. 44462-44462, 2017, doi: 10.1038/srep44462.

[303] V. S. Sedov, A. K. Martyanov, A. A. Khomich, S. S. Savin, E. V. Zavedeev, and V. G. Ralchenko, "Deposition of diamond films on Si by microwave plasma CVD in varied CH4-H2 mixtures: Reverse nanocrystalline-to-microcrystalline structure transition at very high methane concentrations," *Diamond and related materials,* vol. 109, p. 108072, 2020, doi: 10.1016/j.diamond.2020.108072.

[304] A. P. Bolshakov *et al.*, "Enhanced deposition rate of polycrystalline CVD diamond at high microwave power densities," *Diamond and related materials,* vol. 97, p. 107466, 2019, doi: 10.1016/j.diamond.2019.107466.

[305] I. Yagi, K. Tsunozaki, A. Fujishima, B. Ohtani, and K. Uosaki, "The effects of nitrogen and plasma power on electrochemical properties of boron-doped diamond electrodes grown by MPCVD," *Journal of the Electrochemical Society,* vol. 149, no. 1, pp. E1-E5, 2002, doi: 10.1149/1.1425795.

[306] S. Nad, Y. Gu, and J. Asmussen, "Growth strategies for large and high quality single crystal diamond substrates," *Diamond and Related Materials,* vol. 60, pp. 26-34, 2015/11/01/ 2015, doi: https://doi.org/10.1016/j.diamond.2015.09.018.

[307] E. E. Ashkihazi *et al.*, "Plateholder design for deposition of uniform diamond coatings on WC-Co substrates by microwave plasma CVD for efficient turning application," *Diamond and related materials,* vol. 75, pp. 169-175, 2017, doi: 10.1016/j.diamond.2017.04.011.

[308] V. Sedov *et al.*, "Effect of substrate holder design on stress and uniformity of large-area polycrystalline diamond films grown by microwave plasma-assisted cvd," *Coatings (Basel),* vol. 10, no. 10, pp. 1-10, 2020, doi: 10.3390/coatings10100939.

[309] A. Charris, S. Nad, and J. Asmussen, "Exploring constant substrate temperature and constant high pressure SCD growth using variable pocket holder depths," *Diamond and related materials,* vol. 76, pp. 58-67, 2017, doi: 10.1016/j.diamond.2017.04.010.